

**INVESTIGATION OF AN ADAPTABLE CRASH ENERGY
MANAGEMENT SYSTEM TO ENHANCE VEHICLE
CRASHWORTHINESS**

Ahmed Abd El-Rahman Khattab

A Thesis

in

The department

of

Mechanical and Industrial Engineering

Presented in Partial Fulfillment of the Requirements

for the Degree of Doctor of Philosophy at

Concordia University

Montreal, Quebec, Canada

October, 2010

© Ahmed Khattab, 2010

CONCORDIA UNIVERSITY
SCHOOL OF GRADUATE STUDIES

This is to certify that the thesis is prepared

By: **Ahmed Abd El-Rahman Khattab**

Entitled: **“Investigation of an adaptable crash energy management system to enhance vehicle crashworthiness, a conceptual approach”**

and submitted in partial fulfillment of the requirements for the degree of

DOCTOR OF PHILOSOPHY (Mechanical Engineering)

complied with the regulations of the University and meets the accepted standards with respect to originality and quality.

Signed by the final examining committee:

_____	Chair
Dr. B. Jaumard	
_____	External Examiner
Dr. F. Taheri	
_____	External to Program
Dr. K. Galal	
_____	Examiner
Dr. A. K. Waizuddin Ahmed	
_____	Examiner
Dr. I. Stiharu	
_____	Thesis Co-Supervisor
Dr. S. Rakheja	
_____	Thesis Co-Supervisor
Dr. R. Sedaghati	

Approved by

Dr. Wenfang Xie, Graduate Program Director

Dr. Robin A. L. Drew,
Dean, Faculty of Engineering and Computer Science

ABSTRACT

INVESTIGATION OF AN ADAPTABLE CRASH ENERGY MANAGEMENT SYSTEM TO ENHANCE VEHICLE CRASHWORTHINESS

Ahmed Abd El-Rahman Khattab, Ph.D.

Concordia University, 2010

The crashworthiness enhancement of vehicle structures is a very challenging task during the vehicle design process due to complicated nature of vehicle design structures that need to comply with different conflicting design task requirements. Although different safety agencies have issued and modified standardized crash tests to guarantee structural integrity and occupant survivability, there is continued rise of fatalities in vehicle crashes especially the passenger cars. This dissertation research explores the applicability of a crash energy management system of providing variable energy absorbing properties as a function of the impact speed to achieve enhanced occupant safety. The study employs an optimal crash pulse to seek designs of effective energy absorption mechanisms for reducing the occupant impact severity. The study is conducted in four different phases, where the performance potentials of different concepts in add-on energy absorbing/dissipating elements are investigated in the initial phase using a simple lumped-parameter model. For this purpose, a number of performance measures related to crash safety are defined, particular those directly related to occupant deceleration and compartment intrusion. Moreover, the effects of the linear, quadratic and cubic damping properties of the add-on elements are investigated in view of structure deformation and occupant's Head Injury Criteria (HIC).

In the second phase of this study, optimal design parameters of the proposed add-on energy absorber concept are identified through solutions of single- and weighted multi-objective minimization functions using different methods, namely sequential quadratic programming (SQP), genetic algorithms (GA) and hybrid genetic algorithms. The solutions obtained suggest that conducting multiobjective optimization of conflicting functions via genetic algorithms could yield an improved design compromise over a wider range of impact speeds. The effectiveness of the optimal add-on energy absorber configurations are subsequently investigated through its integration to a full-scale vehicle model in the third phase. The elasto-plastic stress-strain and force-deflection properties of different substructures are incorporated in the full-scale vehicle model integrating the absorber concept. A scaling method is further proposed to adapt the vehicle model to sizes of current automobile models. The influences of different design parameters on the crash energy management safety performance measures are studied through a comprehensive sensitivity analysis.

In the final phase, the proposed add-on absorber concept is implemented in a high fidelity nonlinear finite element (FE) model of a small passenger car in the LS-DYNA platform. The simulation results of the model with add-on system, obtained at different impact speeds, are compared with those of the baseline model to illustrate the crashworthiness enhancement and energy management properties of the proposed concept. The results show that vehicle crashworthiness can be greatly enhanced using the proposed add-on crash energy management system, which can be implemented in conjunction with the crush elements.

ACKNOWLEDGEMENT

First of all, I would like to give the ultimate thanks to Allah for everything you have given me in my life.

I wish to express the deepest appreciation to my supervisors Professor Subhash Rakheja and Doctor Ramin Sedaghati for their guidance, encouragement, and support throughout my study and for helping me complete my work. Their helpful suggestions have meant a lot to me and to my research. Their enthusiasm and unwavering support gave me the inspiration to undertake and complete this doctoral research. My deep and sincere appreciation goes to all them. The contributions and assistance of my committee members, Drs. A. K. W. Ahmed, I. Stiharu and K. Galal are also most appreciated and acknowledged. I would like to thank professors Metwally. M. Moussa and Mustafa El-Gendy for their support and assistance in the preparation of this thesis and the completion of my graduate work. Their insightful observations and ideas were responsible for some of the key developments of this work. I am deeply indebted to them for their help and encouragement. I would also like to extend my thanks to all of Concordia University's professors and administrative staff with whom I have had the opportunity to take courses or engage in discussions with. I would also like to thank all my lab-mates, LS-DYNA Forum groups, and all those who have helped me carryout my work. Finally, I would like to give special thanks and acknowledgement for the great and continuous help and encouragement that I received from my family throughout my years of study.

Table of Contents

LIST OF FIGURES	x
LIST OF TABLES	xx
NOMENCLATURE	xxiii
CHAPTER 1 LITERATURE REVIEW AND SCOPE OF DISSERTATION	1
1.1 Introduction.....	1
1.2 Review of Relevant Literature	4
1.2.1 Crashworthiness of Road Vehicles	4
1.2.2 Modeling Techniques.....	7
1.2.3 Dynamic Response Analysis of Vehicle Crash Models	16
1.2.4 Methods for Enhancing Structural Crashworthiness	26
1.2.5 Crash Energy Management (CEM) Techniques	28
1.3 Scope and Objectives of the Present Study.....	43
1.4 Thesis Organization	45
CHAPTER 2 ANALYSIS OF ADD-ON ENERGY ABSORBERS CONCEPTS.....	47
2.1 Introduction.....	47
2.2 Crash Energy Management through Add-on Energy Absorbers	48
2.2.1 Recent Trends of Variable Damping and Stiffness.....	52
2.2.2 Variable Damping/Stiffness Concept Implemented into Vehicle Crash Analysis.....	53

2.3	Development of Vehicle Models with Add-on Energy Absorbers /Dissipators...	54
2.3.1	Baseline Model	55
2.3.2	Vehicle Model with Integrated Energy Dissipator	57
2.3.3	Vehicle Model with Extended Energy Dissipators.....	59
2.3.4	Vehicle Model with Extendable-Integrated Dual Voigt absorbers (EIDV)....	60
2.3.5	Vehicle Model with Extendable Voigt and Integrated Energy Dissipators (EVIS).....	63
2.3.6	Vehicle Model with Integrated Voigt Structure (IV).....	64
2.4	Methods of Analysis and Performance Measures.....	65
2.5	Response Analyses of Vehicle Models with Add-on Energy.....	70
2.5.1	Comparison of Responses of Different Configurations of Add-on Absorbers	73
2.5.2	Sensitivity Analyses.....	76
2.6	Summary	88
CHAPTER 3 OPTIMAL ADD-ON ENERGY ABSORBERS CONFIGURATIONS		90
3.1	Introduction.....	90
3.2	Formulation of the Optimization Process	90
3.2.1	Single Objective Optimization.....	92
3.2.2	Combined Objective Optimization	97
3.2.3	Multi objective optimization.....	98
3.3	Illustrative Optimization Problems	100

3.4 Optimization Results.....	102
3.4.1 Optimization Results for Extendable-Integrated Dual Voigt (EIDV) Model.....	103
3.4.2 Optimization Results for Integrated Voigt (IV) Model	114
3.5 Performance Analysis and Comparison of the Results.....	120
3.6 Summary	126
 CHAPTER 4 CRASH ENERGY MANAGEMENT ANALYSES OF VEHICLES WITH ADD-ON ENERGY ABSORBES	 128
4.1 Introduction.....	128
4.2 Baseline Model Formulation and Validation	130
4.2.1 Method of Analysis.....	131
4.2.2 Validation of the Baseline Model	139
4.3 Baseline Vehicle Model with Occupant and Passive Restraint System	145
4.3.1 Occupant Responses to Frontal Barrier Impact	146
4.3.2 Vehicle Model with Occupant Seat Interactions	148
4.3.3 Response analysis of the Occupant-Seat System.....	149
4.4 Scaling of the Vehicle model.....	151
4.5 Analysis of Crash Energy Distribution of Vehicle-Occupant Model with Add-on Absorbers	156
4.6 Sensitivity analysis.....	166
4.7 Summary	171

CHAPTER 5 CRASH ENERGY MANGAMENT IMPLEMENTATION ON A FINITE ELEMENT MODEL USING LS-DYNA.....	172
5.1 Introduction.....	172
5.1.1 Nonlinear Finite Element Modeling for Crashworthiness	175
5.1.2 Method of Analysis and Performance Criteria	176
5.2 Validation of the Baseline FE Model.....	177
5.3 Modeling and Analysis of the proposed Extended-Integrated Dual Voigt (EIDV) Model	187
5.4 Optimization of the Modified FE Model	194
5.4.1 Metamodeling Techniques (Space Mapping Technique)	196
5.4.2 Optimization of the Surrogate Model	201
5.5 Summary	205
CHAPTER 6 CONCLUSIONS, CONTRIBUTIONS, AND FUTURE RECOMMENDATIONS.....	207
6.1. Highlight and Conclusions of Dissertation Research	207
6.2. Contributions.....	210
6.3. Recommendations for Future Works	211
APPENDEX-A	213
APPENDEX-B.....	216
REFERENCES	220

LIST OF FIGURES

Figure	page
Figure 1.1: Proportion of vehicles involved in traffic crashes [1]	5
Figure 1.2: Distribution of non-rollover vehicle crashes according to point of impact [25]	6
Figure 1.3: Distribution of in single- and multiple- vehicles crashes by initial point of impact [1]	7
Figure 1.4: Single-DOF lumped-parameter models for analysis of add-on energy absorbers; (a) baseline; and (b) integrated add-on [40]	10
Figure 1.5: Two-DOF lumped parameter model equipped with an extendable energy absorber [40]	10
Figure 1.6: Three-DOF lumped parameter model of a vehicle under barrier impact [43]	11
Figure 1.7: Multibody dynamic model of a vehicle [26]	13
Figure 1.8: Optimal crash pulse at 48 km/h with three deceleration phases [95]	24
Figure 1.9: Typical pattern of occupant deceleration pulse derived from the idealized kinematics models of the occupant [11]	24
Figure 1.10: Optimal decelerations pulse at three impact speeds [18]	25
Figure 1.11: Load paths of the car body structural members during frontal impact [28].	27
Figure 1.12: Energy distribution in a frontal car structure measured during frontal rigid and flexible barrier crash tests [108]	28
Figure 1.13: Variations in maximum decelerations for different mass ratios and at different closing velocities (120, 80 and 40 km/h) [112]	34
Figure 1.14: Cable supported telescopic longitudinal structure [18]	36
Figure 1.15: Schematic drawing of the proposed Magneto-Rheological (MR) impact bellows damper (a) before impact (b) after impact [90]	40
Figure 1.16: Five-DOF LMS mathematical model with the driver [90]	40

Figure 1.17: Three-DOF LMS model of the vehicle with an inflated bumper [19]	42
Figure 1.18: A pictorial view (left) and schematics (right) of expandable lattice structure: (a) U-shaped thin walled members; and (b) rectangular jagged members [19].....	43
Figure 2.1: Relationships among different measures of vehicle crash dynamic responses [18].....	52
Figure 2.2: Two-DOF baseline model of the vehicle and occupant subject to full frontal impact [36]	55
Figure 2.3: (a) Force-deformation; and (b) force-velocity curves of the restraint system [36].....	56
Figure 2.4: Two-DOF model of the vehicle-occupant system with integrated energy dissipative components (ID model)	58
Figure 2.5: Piecewise-linear representation of the rubber bump-stop spring	58
Figure 2.6: Vehicle-occupant model with energy dissipators in extended position (ED model)	60
Figure 2.7: Three-DOF model of the occupant-vehicle system in extendable-integrated Voigt elements (EIDV).....	61
Figure 2.8: Three-DOF model of the occupant-vehicle system with extendable-Voigt elements and integrated shock absorber (EVIS).....	64
4. Figure 2.9: Two-DOF model of the occupant-vehicle system in integrated Voigt element (IV model).....	64
Figure 2.10: Target deceleration pulses defined for rigid barrier impacts in 4 different speed ranges [18,96]	69
Figure 2.11: Comparison of occupant HIC and peak vehicle deformation responses with different arrangements of add-on absorbers at different impact speeds ($\lambda_2=0.1$; $\lambda_1=0.3$; $\mu_2= \mu_1=1.0$): (a) HIC; and (b) peak deformation.	74
Figure 2.12: Comparison of occupant HIC and peak vehicle deformation responses with different arrangements of add-on absorbers at different impact speeds ($\lambda_2=0.1$; $\lambda_1=0.3$; $\mu_2=1.7$; $\mu_1=1.5$): (a) HIC; and (b) peak deformation.	74

Figure 2.13: Comparison of vehicle deceleration responses of the baseline vehicle model with the three of models in the integrated (ID) and extended (ID) dampers, and integrated-extendable Voigt system (EIDV) and the target deceleration pulse ($v_0 = 48$ km/h).....	82
Figure 2.14: Comparison of response of different models subject to a 48 km/h frontal impact speed with the reported response [36]: (a) vehicle deformation and (b) occupant deceleration.....	83
Figure 2.15: Comparison design responses of the EIDV model with different models at different impact speeds: (a) occupant HIC and (b) peak vehicle deformation	84
Figure 2.16: Comparison of response of different models subject to a 55 km/h frontal impact speed: (a) vehicle deformation and (b) vehicle deceleration and (c) occupant deceleration	85
Figure 2.17: Comparison of response of different proposed models with the baseline model subject to a 55 km/h frontal impact speed: (a) vehicle deformation and (b) vehicle deceleration and (c) occupant deceleration	88
Figure 3.1: Effect of stiffness variation on both occupant HIC and peak vehicle deformation ‘Def’ at different impact speeds.	100
Figure 3.2: Three-DOF lumped-parameter EIDV model in a full frontal impact	102
Figure 3.3: Two DOF lumped-parameter IV model with integrated Voigt element	102
Figure 3.4: Convergence of optimization results using SQP technique for minimization of occupant HIC at an impact speed of 50 km/h using different initial starting points.	103
Figure 3.5: Comparison of DV (λ_2) values obtained from different optimization algorithms using HIC as an objective function for the EIDV model at different impact speeds	104
Figure 3.6: Comparison of DV (μ_2) values obtained from different optimization algorithms used in minimizing HIC for the EIDV model at different impact speeds.	105

Figure 3.7: Comparison of DV (λ_1) values obtained from different optimization algorithms HIC as an objective function for the EIDV model at different impact speeds	105
Figure 3.8: Comparison of DV (μ_1) values obtained from different optimization algorithms used in minimizing HIC for the EIDV model at different impact speeds.	105
Figure 3.9: Comparison of optimal HIC values and corresponding Def values obtained from different optimization algorithms using different objective functions for the EIDV model	106
Figure 3.10: Convergence of optimization results using SQP technique for optimal peak vehicle deformation ‘Def’ of the EIDV model at 80 km/h with different starting point.	106
Figure 3.11: Comparison of DV (λ_2) values obtained from different optimization algorithms used in minimizing peak deformation for the EIDV model at different impact speeds	107
Figure 3.12: Comparison of DV (μ_2) values obtained from different optimization algorithms used in minimizing peak deformation for the EIDV model at different impact speeds	108
Figure 3.13: Comparison of DV (λ_1) values obtained from different optimization algorithms used in minimizing peak deformation for the EIDV model at different impact speeds	108
Figure 3.14: Comparison of DV (μ_1) values obtained from different optimization algorithms used in minimizing <i>Def.</i> for the EIDV model at different impact speeds	108
Figure 3.15: Comparison of optimal peak deformation values and the corresponding values of HIC using different optimization algorithms for the EIDV model at different impact speeds.	109

Figure 3.16: Comparison between values of occupant HIC obtained from different optimization algorithms using different optimal targets for the EIDV model.....	110
Figure 3.17: Comparison between values of <i>Def</i> obtained from different optimization algorithms using different optimal targets for the EIDV Model.....	110
Figure 3.18: Comparisons of Pareto Front (PF) and Anti Pareto Front (APF) curves at a 50 km/h impact speed for the EIDV Model using four DVs	113
Figure 3.19: Comparison of Pareto Frontier 'PF' curve between the EIDV Model (DV _s : μ_1 and μ_2) and baseline model at different impact speeds using x-axis logarithmic scale	113
Figure 3.20: Comparison of the Anti-Pareto Frontier (APF) curves between for the EIDV Model (DV _s : μ_1 and μ_2) and the baseline model at different impact speeds	114
Figure 3.21: Convergence of optimization results using <i>SQP</i> technique with optimal occupant HIC using different initial starting points for IV model at 50 km/h impact speed.	115
Figure 3.22: Comparison of DV (λ_I) values obtained from different optimization algorithms used in minimizing HIC for IV model at different impact speeds.....	115
Figure 3.23: Comparison of DV (μ_I) values obtained from different optimization algorithms used in minimizing HIC for the IV model at different impact speeds..	116
Figure 3.24: Comparison of optimal HIC values and corresponding peak deformation obtained from different optimization algorithms for the IV model	117
Figure 3.25: Convergence of optimization results using <i>SQP</i> technique with optimal vehicle deformation using different initial starting points for the IV model at 50 km/h.	117
Figure 3.26: Comparison of DV (λ_I) values obtained from different optimization algorithms used in minimizing deformation for the IV model at different impact speeds	118

Figure 3.27: Comparison of $DV (\mu_I)$ values obtained from different optimization algorithms used in minimizing deformation for the IV model at different impact speeds	118
Figure 3.28: Comparison of optimal value of Def and corresponding value of HIC obtained from different optimization algorithms for IV model at different impact speeds	119
Figure 3.29: Comparison between PF and APF curves at different impact speed for the IV model using MOGA technique and baseline model.	120
Figure 3.30: Comparison between the PF and APF for EIDV model with the baseline model at different impact speeds using x-axis in logarithmic scale	121
Figure 3.31: Variations of design variables for the EIDV model at anchor points of PF curves at different impact speeds for EIDV model.....	122
Figure 3.32: Comparison between the PF and APF for EIDV model with the baseline model at different impact speed using two design variables: μ_1, μ_2	122
Figure 3.33: Comparison between the PF and APF of the IV model with the baseline model at different impact speeds using x-axis logarithmic scale.	124
Figure 3.34: Variations of design variables at anchor points of PF curves at different impact speeds for the IV model	125
Figure 3.35: Comparison between the Pareto Frontier (PF) curves of the EIDV and IV models with baseline model at different impact speeds in x-axis logarithmic scale	125
Figure 4.1: Three-DOF lumped-parameter model of the vehicle subject to an impact with a rigid barrier [38,44,177].....	131
Figure 4.2: Schematic of vehicle components illustrating different load paths in frontal car impact [177]	132
Figure 4.3: Generic dynamic load deflection characteristics [177]	134
Figure 4.4: Static load-deflection curve for the torque box structure (F_I) [38].....	136

Figure 4.5: Static load-deflection curve for the front frame structure (F_2) [38].	136
Figure 4.6: Static load-deflection curve for the driveline structure (F_3) [38].	136
Figure 4.7: Static load-deflection curve for the sheet metal structure (F_4) [38].	137
Figure 4.8: Static load-deflection curve for the firewall structure (F_5) [38].	137
Figure 4.9: Static load-deflection curve for the radiator structure (F_6) [38].	137
Figure 4.10: Static load-deflection curve for the engine mounts structure (F_7) in forward and rearward directions [38].	138
Figure 4.11: Static load-deflection curve for the transmission mount (F_8) in forward and rearward directions [38].	138
Figure 4.12: Comparison of dynamic responses of different bodies of the model with reported responses [38]: (a) displacement; (b) velocity; and (c) deceleration	140
Figure 4.13: Dynamic responses of different bodies of the model in a 56 km/h frontal impact with a rigid barrier: (a) displacement; (b) velocity; and (c) acceleration	141
Figure 4.14: Variation in dynamic force developed by various structural components in a 56 km/h frontal impact with a rigid barrier for structural members: (a) F_1 - F_4 , (b) F_5 - F_8	143
Figure 4.15: Dynamic force-deflection curves for different lumped masses of the baseline model at an impact speed of 56 km/h with a rigid barrier for structural members: (a) F_1 - F_4 , (b) F_5 - F_8 .	144
Figure 4.16: Four-DOF lumped mass model for baseline model equipped with a restrained occupant in full frontal impact	145
Figure 4.17: Dynamic responses of different bodies of the baseline model equipped with occupant in a 56 km/h frontal impact with a rigid barrier: (a) displacement; (b) velocity; and (c) acceleration.	147
Figure 4.18: Four-DOF lumped-parameter model of the vehicle with occupant-seat-restrained under full frontal impact	148
Figure 4.19: Piecewise-linear representation of the car seat cushion-metal spring	149

Figure 4.20: Comparison of the occupant mass response of the vehicle-occupant system model with restraint alone and with restraint and the seat system: (a) deceleration, (b) force-displacement.	150
Figure 4.21: acceleration responses of vehicle, engine and suspension to a 56 km/h impact with a rigid barrier.....	155
Figure 4.22: Mutli-DOF lumped-parameters representation of vehicle-occupant models with add-on absorber systems: (a) IV model, (b) EIDV model.....	157
Figure 4.23: Comparison of frontal barrier impact responses of the occupant mass with those of the vehicle, engine and suspension masses for the IV model at a 56 km/h impact speed: (a) displacement; (b) velocity; and (c) acceleration.....	159
Figure 4.24: Comparison of frontal barrier impact responses of the occupant mass with those of the vehicle, engine and suspension masses for the EIDV model at a 56 km/h impact speed: (a) displacement; (b) velocity; and (c) acceleration.....	161
Figure 4.25: Dynamic force-deflection curves for the add-on in extendable and integrated positions with vehicle structure for the EIDV model at 56 km/h impact speed	162
Figure 4.26: Comparison of occupant mass responses between the baseline and the EIDV models at an impact speed of 56 km/h with a rigid barrier.....	162
Figure 4.27: Distribution of percentage of absorbed energy by the structural members of the baseline model at different impact speeds	164
Figure 4.28: Comparison the percentage of absorbed energy over structural members between baseline and both the EIDV and IV models at different impact.....	165
Figure 4.29: Comparison of system performance between both EIDV and IV detailed model with the baseline model at different impact speeds.	165
Figure 4.30: Sensitivity of the peak vehicle deformation and maximum occupant deceleration to variations in μ_2 (EIDV model at 56 km/h)	167
Figure 4.31: Sensitivity of the occupant HIC to variations in μ_2 (EIDV model at 56 km/h).	167
Figure 4.32: Sensitivity of the specific energy absorption by the add-on to variations in μ_2 (EIDV model at 56 km/h).	167

Figure 4.33: Sensitivity of the peak vehicle deformation and maximum occupant deceleration to variations in μ_1 (EIDV model at 56 km/h)	168
Figure 4.34: Sensitivity of the occupant HIC to variations in μ_1 (EIDV model at 56 km/h)	168
Figure 4.35: Sensitivity of the specific absorbed energy by the add-on to variations in μ_1 (EIDV model at 56 km/h).	168
Figure 5.1: Isometric view of Geo-Metro FM model	178
Figure 5.2: Accelerometer locations	182
Figure 5.3: Comparison between the right rear seat deceleration of the Geo-Metro FE model with NCAC crash test results at 56.6 km/h.....	183
Figure 5.4: Comparison between the left rear seat deceleration of the Geo-Metro FE model with NCAC crash test results at 56.6 km/h.....	183
Figure 5.5: Comparison between top engine deceleration measured of the Geo-Metro FE model with NCAC crash test results at 56.6 km/h.....	184
Figure 5.6: Comparison between bottom engine deceleration of Geo-Metro FE model with NCAC crash test results at 56.6 km/h.....	185
Figure 5.7: Comparison between longitudinal rigid wall force of the baseline Geo-Metro FE model and both NCAC simulation and NCAP crash test results [195] at 56.6 km/h	185
Figure 5.8: Rigid-wall force of the baseline Geo-metro FE model at 56.6 km/h impact speed using two types of filters.....	186
Figure 5.9: Comparison of energy balance response between the baseline and NCAC simulation results, for Geo-Metro FE model at 56.6 km/h [195]	187
Figure 5.10: Modified Geo-metro model.....	188
Figure 5.11: Comparison between left rear seat deceleration signal of baseline model and modified Geo-Metro FE model at 56.6 km/h.....	190

Figure 5.12: Comparison between right rear seat deceleration signal of the baseline model and modified Geo-Metro FE model at 56.6 km/h.....	190
Figure 5.13: Comparison of upper engine deceleration signal between the baseline model and the modified Geo-Metro FE model at 56.6 km/h.....	191
Figure 5.14: Comparison of lower engine deceleration signal between the baseline model and the modified Geo-Metro FE model at 56.6 km/h.....	191
Figure 5.15: Comparison of the normal rigid wall force between the modified Geo-Metro and the baseline models at a 56.6 km/h impact speed.	192
Figure 5.16: Comparison of the car structural deformation (<i>Def</i>) between the modified Geo-Metro FE and the baseline models at a 56.6 km/h impact speed.....	192
Figure 5.17: Energy balance response of Geo-Metro extended FE model at 56.6 km/h	194
Figure 5.18: Comparison of the kinetic and internal energies between the baseline and extended FE Geo-Metro models at 56.6 km/h.....	194
Figure 5.19: Convergence of single objective function: occupant HIC using SQP optimization algorithm.....	202
Figure 5.20: Convergence of single objective function: peak vehicle deformation (<i>Def</i>) using SQP optimization algorithm.....	202
Figure 5.21: Comparison of system performance between MOO results of the surrogate FE and the initial design variables of the add-on configurations of the modified FE model at 56.6 km/h impact speed	204
Figure 5.22: Variations of design variables of the lower anchor point of the PF curve with iteration number at 56 km/h impact speed in logarithmic scale of the y-axis.	204

LIST OF TABLES

Table 2.1: The linear, quadratic and cubic damping constants leading to minimal occupant HIC and peak vehicle deformation.....	71
Table 2.2: Front barrier impact response of the baseline model at different impact speeds	80
Table 2.3: Identification of design variables of the EIDV model corresponding to minimal deformation, HIC, total deviation error at different impact speeds.....	81
Table 2.4: Comparison between HIC of the occupant for each model compared with the baseline model at 48 km/h impact speed	82
Table 3.1: Comparison of optimal <i>DVs</i> for different single objective functions for <i>EIDV</i> model at different impact speeds:	111
Table 3.2: Comparison of <i>DVs</i> for different single objective functions for <i>IV</i> model at different impact speeds:	119
Table 3.3: Comparisons of system performance at anchor points of PF and APF curves of the EIDV model with baseline model performance measures at different impact speeds using four design variables (μ_1, μ_2, λ_1 and λ_2) and two design variables (μ_1, μ_2).....	123
Table 3.4: Comparison of the system performance at anchor points of PF and APF curves of the IV Model with baseline model at different impact speeds	124
Table 3.5: Comparison between EIDV and IV models at both anchor points of Pareto Frontier curves with the baseline model and at different impact speeds	126
Table 4.1: Comparison of occupant restraint system responses subjected to frontal barrier impact at 48 km/h impact speed.....	151
Table 4.2: Scaling factors for different model properties	153
Table 4.3: design variables corresponding to the three chosen impact speeds for IV model	158
Table 4.4: Design variables at the three chosen impact speeds for IDEV model.....	160

Table 4.5: Comparison of simulation results of both EIDV and IV models with a baseline model at three impact speeds	163
Table 4.6: Comparison of the percentage of energy absorption for each structural member between different models at different impact speeds EIDV model	166
Table 4.7: Sensitivity analysis of system performance measures to variation in the, damping, variables at 56 km/h impact speed for EIDV model.....	170
Table 5.1: Comparison between FE model and test vehicle parameters of the vehicle model and benchmark data	179
Table 5.2: Design variables at the assigned impact speed for modified Geo-Metro model	189
Table 5.3: Percentage of enhancement of rear seat peak deceleration at 56.6 km/h	191
Table 5.4: Percentage of enhancement of the engine peak decelerations at a 56.6 km/h impact speed.....	192
Table 5.5: Percentage of enhancement of both the normal rigid wall force and peak vehicle deformation (<i>Def</i>) at a 56.6 km/h impact speed	193
Table 5.6: Design matrix of metamodel for the modified Geo model.....	199
Table 5.7: Comparison of the optimal HIC and Def values between the optimal and initial design variables.....	202
Table 5.8: Comparison between design criteria at the optimal sets obtained from LMS MOGA optimization and Metamodel MOGA optimization through LS-OPT at lower AP of Pareto Frontier curves.....	205
Table A.1: Identification of design variables of the EIDV model with configuration # 2 corresponding to minimal deformation, HIC, total deviation error at different impact speeds	213
Table A.2: Identification of design variables of the EVIS model corresponding to minimal deformation, HIC, total deviation error at different impact speeds	214
Table A.3: Identification of design variables of the IV model corresponding to minimal deformation, HIC, total deviation error at different impact speeds	215

Table B.1: Pareto Frontier (PF) results at four selected impact speeds over the specified range of impact speeds using multiobjective optimization using GA for the EIDV model (extended-integrated voigt elements) using only two design variables (μ_2, μ_1)	216
Table B.2: Anti-Pareto Frontier (APF) results at four selected impact speeds over the specified range of impact speeds using MOGA for the EIDV model (extended-integrated voigt elements) using only two design variables (μ_2, μ_1)	217
Table B.3: Pareto Frontier (PF) results at four selected impact speeds over the specified range of impact speeds using multiobjective optimization using GA for the EIDV model (extended-integrated voigt elements) using the four design variables ($\lambda_2, \lambda_1, \mu_2, \mu_1$)	218
Table B.4: Anti-Pareto Frontier (APF) results at four selected impact speeds over the specified range of impact speeds using MOGA for the EIDV model (extended-integrated voigt elements) using the four design variables ($\lambda_2, \lambda_1, \mu_2, \mu_1$)	219

NOMENCLATURE

Roman symbols

Symbol	Description
AIA:	Adaptive Impact Absorption
AIS:	Abbreviated Injury Scale
CEM:	Crash energy management
CFC:	Channel frequency class
CIP:	Crash initiation pulse
COR:	Coefficient of restitution
CGS:	Chest acceleration criteria
CRUSH:	Crash Reconstruction Using Static History.
CSI:	Vehicle crash severity index.
DoE:	Design of experiments
EA:	Energy absorber
DOF	Degree-of-freedom
FARS:	Fatality Analysis Reporting System
FMVSS:	Federal Motor Vehicle Safety Standard Testing
IIHS:	Insurance institute for highway safety.
HIC:	Head Impact Criteria.
LMS:	Lumped mass spring model
MBD:	Multi-body dynamics
MDB:	Moving Deformable Barrier.
MOO:	Multi-objective optimization technique

MRF:	Magneto-rorheological fluid
NASS/CDS:	National automotive sampling system crashworthiness data system.
NCAP:	New Car Assessment Program.
NHTSA:	National Highway Traffic Accident Administration.
OEM:	Original equipment manufacturer.
ODB:	Offset deformable barrier.
OSI:	Overall severity index
RIR:	Relative injury risk
RSM:	Response surface method
SCF:	Structural collapse force
SUV:	Sport utility vehicle
VOR:	Vehicle-occupant-restraint system
VTB/VTV:	Vehicle-to-barrier/Vehicle-to-vehicle impact.

Greek symbols

α, β, γ	Linear, quadratic and cubic term of the shock absorber damping force
B	Geometric scaling factor
C_{1L}, C_{2L}	Linear damping coefficients of add-on energy absorbers in integrated and extendable positions with the vehicle structure, respectively.
C_{1NL}, C_{2NL}	Nonlinear damping coefficients of add-on energy absorbers in integrated and extendable positions with the vehicle structure, respectively.
C_{sL}, C_{sNL}	Linear and cubic damping coefficients of the seat cushion, respectively.
d_L, d_{NL}	Nominal linear and nonlinear damping constant of the add-on elements, respectively.

- $F_{str}, F_{rest}, F_{seat}$ Developed force due to structural deformation restraint system, respectively.
- F_{d_p}, F_{d_s} Developed force by the dissipative hydraulic damper in integrated and extended positions, respectively.
- F_{v_1}, F_{v_2} Dissipation-absorption force in Voigt system implemented in integrated and extendable positions, respectively.
- F_{stop_i}, F_{stop_e} Developed force due to the elastic end stop in the integrated and extended Voigt elements, respectively
- k_o, c_o Linear stiffness and damping coefficients of the occupant restraint system.
- k_L, k_{NL} Linear and nonlinear stiffness coefficients of vehicle structure for the simplified lumped-parameter model.
- $k_{r1}^i, k_{r1}^e, k_{r2}^i, k_{r2}^e$ Linear and bilinear stiffness coefficients of elastic stop of the hydraulic damper in integrated and extended arrangement.
- K_{eqv} Nominal stiffness value of the add-on energy absorbers.
- K Dynamic load factor
- k_s, k_{sI} Linear and bilinear seat stiffness under low level and high deformation, respectively.
- δ_{oc} Initial slack distance of the occupant restraint system.
- δ_{0i}, δ_{0e} Deformation limit for initiation the elastic stop of hydraulic damper in integrated and extendable position, respectively.
- δ_{1i}, δ_{1e} Deformation limit for initiation the bilinear stiffness of the elastic stop of hydraulic damper in integrated and extendable position, respectively.

$\Delta_{i_limit}, \Delta_{i_limit}$	Available hydraulic damper travel in integrated and extendable position, respectively.
δ_s	Static pre-stress deflection in the seat cushion.
Δ_{cush}	Seat cushions thickness.
$\mu_1, \mu_2, \lambda_1, \lambda_2$	Damping and stiffness multiplication factors of the integrated and extended Voigt elements, respectively.
m_v, m_b	vehicle body and bumper masses in the simplified lumped-parameter model, respectively.
m_o	Occupant masses in the lumped-parameter model simulation.
m_{FE}	Vehicle mass of the FE model.
m_1, m_2, m_3	vehicle body, engine and cross member masses in the detailed lumped-parameter model, respectively.
S_i	Slope of the elastic loading and unloading curve of the i^{th} structural member.

CHAPTER 1

LITERATURE REVIEW AND SCOPE OF DISSERTATION

1.1 Introduction

Enhancement of crashworthiness of road vehicles is among the most important development issues considering the increased traffic intensity together with legislations requiring developments in fuel-efficient automobiles. Although strict safety standards and well-designed energy absorbing vehicle structures have contributed to improved passenger compartment integrity and occupant safety, the social and economic costs of crash injuries in motor vehicle crashes continue to be excessive. A recent report from Centers for Disease Control and Prevention (CDC) estimates nearly 161,000 fatalities associated with crash-related injuries in the United States, and the annual costs for medical care and productivity loss exceed \$ 117 billion [1]. Consequently, design methodologies leading to improved passengers/driver safety, particularly the crashworthiness, have been of intense concern in the recent years.

The crashworthiness of a road vehicle is defined by the vehicle structure's ability to absorb impact energy in a controlled manner while maintaining an adequate interior survivable space and providing protection to its occupants [2,11]. This can be achieved through preventing compartment intrusion and limiting the force or deceleration transmitted to the occupant. Vehicle designs with enhanced passenger safety need to address crash prevention in the first stage, crash severity reduction in the second stage and occupant injury mitigation in the third stage.

Concepts in active pre-crash avoidance systems such as enhanced brake assist, driver warning system, blind spot monitors, and stability control have always been developed to prevent or reduce the likelihood of a collision [4-7]. Such systems, however, cannot entirely eliminate vehicle crashes. Considerable advancements have been made in enhancing the crash energy absorbing properties of vehicle through structure design, alternate smart materials and integration of crush elements [3,8-10], to reduce of the crashes severity deemed unavoidable by the pre-crash avoidance systems. A number of innovative designs in vehicle occupant restraints (VOR) such as active air bags, steering column with a collapsible mechanism and advanced seat belts have been developed to reduce the severity of occupant injuries by limiting peak deceleration and intrusion [12-16]. Owing to the growing demands for light-weight fuel-efficient automobiles, crash energy management (CEM) through structure design and VOR continues to be the primary challenges.

A few studies have suggested that the crashworthiness of road vehicles could be considerably enhanced through distribution and absorption management of crash energy that could be realized via: (i) modification in the vehicle structure involving strengthening of load paths or additional load paths; (ii) implementation of passive add-on energy absorbers (EA) known as crush elements; and (iii) implementation of adaptable add-on EA systems. The effectiveness of CEM systems have been evaluated using crash tests and numerical analysis of the vehicle structures, using a wide range of performance measures such as peak occupant deceleration, occupants' head injury criteria (HIC), total vehicle deformation and absorbed energy. While there seems to be little agreement on a generally acceptable measure of crashworthiness of a vehicle, the different performance

measures often pose conflicting design requirements. For instance, a lower HIC value demands a soft structure design, while a stiffer structure is desirable to reduce the compartment intrusion. The desirable properties of a vehicle structure and energy absorbers depend upon the total energy encountered during crash, which relies on many factors in a highly complex manner. These include the types of crash (vehicle-to-vehicle ‘VTV’ or vehicle-to-barrier ‘VTB’ impact), impact speed, car mass and angle of impact. The passive energy absorbers and specific structure design may thus yield effective crash energy management over a narrow range of crash conditions [17]. Concepts in adaptable add-on energy absorbers system that yield variable stiffness properties may thus be considered desirable [18,19].

This dissertation research concerns the optimal designs of the add-on of passive and adaptable energy absorbers for effective management of the crash energy. Passive and adaptable energy absorbers, characterized by their linear stiffness and nonlinear damping parameters, are integrated to the vehicle structure for analysis of the energy absorption and management. For this purpose, an idealized lumped parameter model of an automobile is formulated together with multi-objective functions of different conflicting measures. Multi-parameter optimization methods are applied to determine optimal designs of passive and adaptable energy absorbers over a wide range of impact speed. Selected configurations of the CEM system with optimal design parameters are applied on a detailed vehicle model using scaling techniques to prove the possibility of implementing the proposed system with the optimal design parameters on different car sizes. The proposed CEM model with optimal design is subsequently implemented to a validated FE model using LS-DYNA software to assess its effectiveness in enhancing

crashworthiness. Optimal design of the add-on elements is also identified from the finite-element model using LS-OPT optimization package based on the design-of-experiments (DoE) via a surrogate model. The results of the study are discussed to demonstrate the effectiveness of the proposed concepts in enhancing crashworthiness of road vehicles.

1.2 Review of Relevant Literature

The enhancement and analysis of crashworthiness of vehicles encompasses numerous challenges and thorough understanding in vehicle structures, add-on energy absorbers, modeling of vehicle structure and occupant restraint, crash performance measures and requirements, and methods of analysis and optimization. The relevant reported studies in these subjects are thus reviewed to build essential knowledge and the scope of the dissertation research. The reviewed studies, grouped under related subjects, are discussed in the following sections.

1.2.1 Crashworthiness of Road Vehicles

Accidents involving vehicle crashes have been associated with high rates of fatalities and extensive social and economic costs. The vehicle occupant safety is of prime concern considering the growing traffic volume, demands for light weight “green” vehicles, and growth in the large size cargo vehicles. According to World Health Organization (WHO), road crashes kill nearly 1.2 million people every year and injure or disable another 50 million throughout the world [2]. According to Canadian motor vehicle traffic collision statistics road crashes in 2005 resulted in nearly 3,000 fatalities and serious injuries among 17,529 people, in Canada [21]. The annual cost related to vehicle collisions in Canada was estimated in the order of \$62.7 billion, which

represented about 4.9% of Canada's 2004 GDP [3]. The impact severity in a collision depends on different design and operational factors such as impact speed, vehicle weight, type of collision, and incompatibility issues between colliding vehicles. Among all the factors affecting the impact severity, the collision speed is known to be the most important factor, followed by the type of crash and vehicle weight [2]. The severity of a potential injury in a high-speed crash could be up to 25 times greater than that incurred in relatively mild or low speed crashes. Another study reported that more than 27% of the total fatalities could be attributed to urban road crashes in the range of 56 to 64 km/h, while on highways at speeds in the order of 80 km/h accounted for 43% of the fatalities [22]. It has been further reported that passenger cars represent about 57% of the total number of fatal crashes (Figure 1.1) [1]. Additionally, passenger cars have been reported as a high percentage in casualties as they represent 61% of the total killed in vehicle crashes according to Fatality Analysis Reporting System (FARS) 2005 [24].

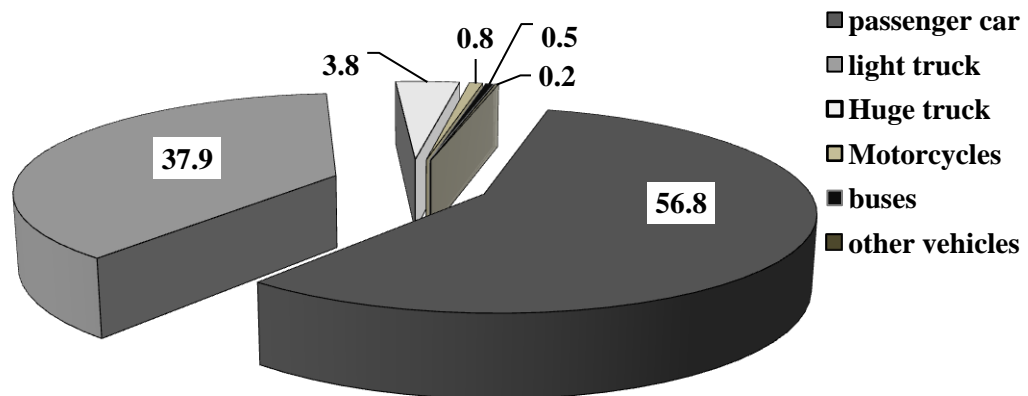


Figure 1.1: Proportion of vehicles involved in traffic crashes [1]

The severity of a collision involving road vehicles also depends upon the type of collision and the angle of impact. Figure 1.2 illustrates the distribution of non-rollover

crashes with the angle of attack frontal impacts [20,25]. Frontal impacts constitute a higher percentage of high severity crash accidents for all vehicle categories in single- or multiple-vehicle crashes, as shown in Figure 1.3 [1]. Frontal crashes also account for greatest proportion of 43% to 67% of the total types of non-rollover crashes irrespective of the angle of impact. Poor structural interaction and mass ratios of up to 1.6 of the mating vehicles are the main reasons for higher ratio of fatalities in vehicle-to-vehicle frontal impacts [26,27]. The impact speed, however directly relates to the severity of the crash and thus the risk of a fatality. Wood et al. [28] investigated the effect of impact speed on the crash severity in vehicle-to-vehicle frontal impacts using a relative injury risk (RIR) index, a function of the relative absorbed energy, masses, and overall lengths of colliding vehicles. The study concluded that impact speed has a primary effect on the RIR and energy distribution, and suggested relative safety of small/light cars could be improved by modifying structural collapse force characteristics (SCF) through enhancing their structural stiffness. It was shown that RIR could vary from 2.0 at low speeds to 11.3 at high speed collisions of vehicles with a mass ratio (M_r) of 2.

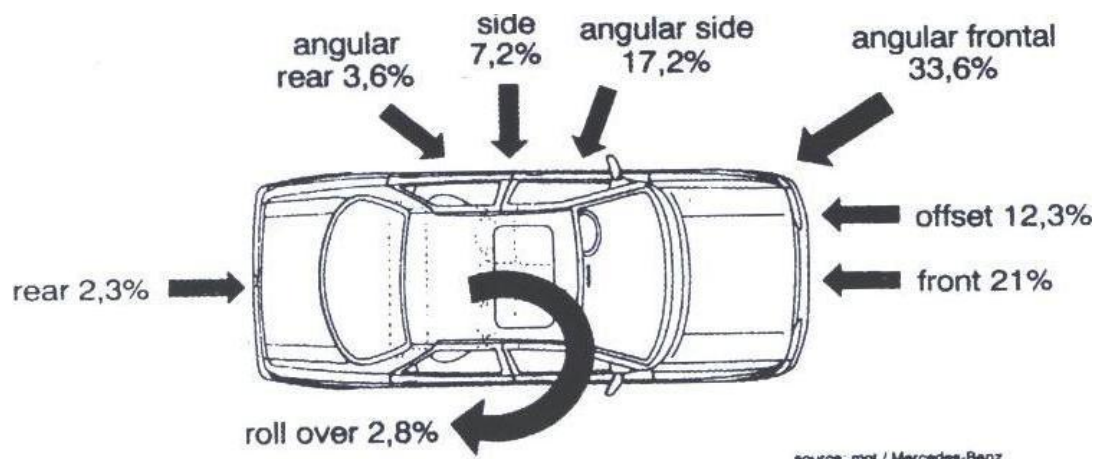


Figure 1.2: Distribution of non-rollover vehicle crashes according to point of impact [25]

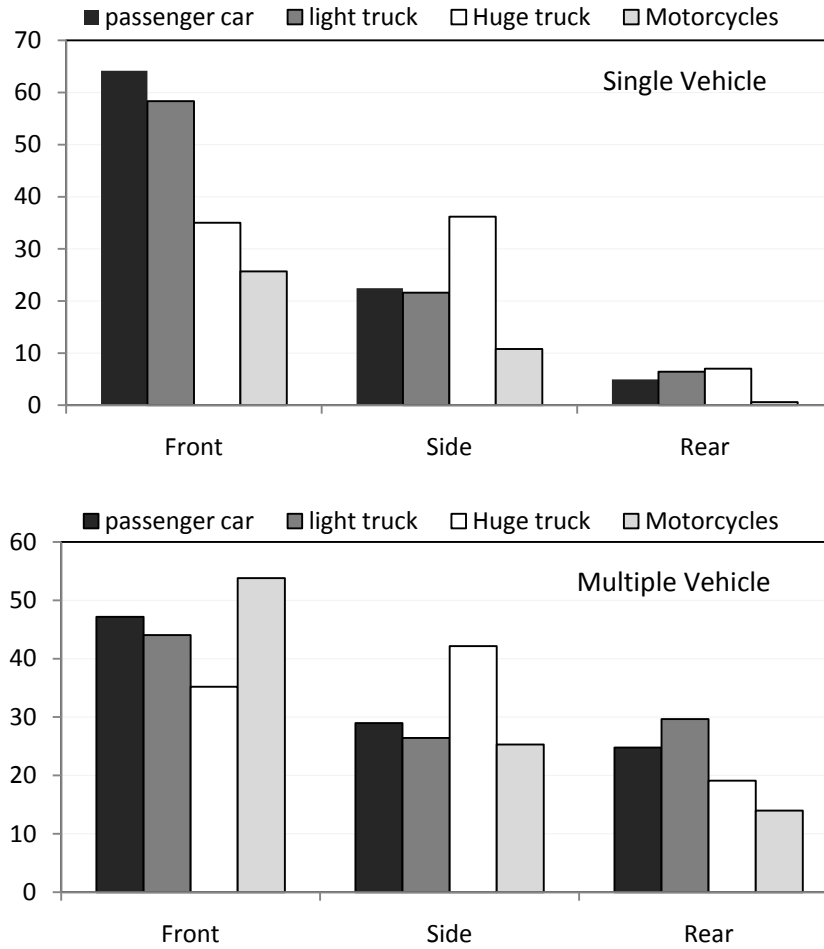


Figure 1.3: Distribution of in single- and multiple- vehicles crashes by initial point of impact [1]

1.2.2 Modeling Techniques

The crashworthiness of different vehicles has been extensively evaluated through experimental and analytical means. While the experimental methods yield most valuable data, they are known to be extremely costly, with costs ranges from \$25,000 to \$200,000 for a full crash test. Furthermore, experimental methods are time consuming and do not always yield definitive information, while the data is limited only for specific impact conditions [28,30]. Alternatively, a number of computational models have emerged to simulate the response of vehicle structures under crash events. In this section, different

crashworthiness analysis methods are discussed. The discussions are mostly limited to design and analysis for frontal crashes since these are considered to be responsible for more traffic fatalities and injuries than any other crash mode. The reported studies on analysis of structural behavior under impact have employed a wide range of analytical models of varying complexities, which can be classified in four main categories on the basis of the modeling approach, namely: lumped-parameter models (LMS); multi-body dynamic (MBD) models; finite element (FE) models; and hybrid models.

The finite element analysis (FEA) is most widely used for crash analyses of vehicle structures at different design stages in order to minimize the number of crash test trials. Large scale finite element models, however, are required considering the nonlinear behavior of vehicle structures undergoing large magnitudes of plastic deformations, which are generally demanding on human and computational resources. The applications of such large-scale detailed FE models are generally limited to final design and assessment stages, while these are known to pose extreme complexities for designs involving iterative or optimization processes [31-33]. Alternatively, a large number of relatively simpler and computationally efficient impact models have been employed for analyses of vehicle structures and concepts in energy absorbing elements [26,27,34,35]. Specifically, lumped-parameter models have emerged as effective tools for analysis of add-on energy absorbers at the conceptual design stages [36-38].

Lumped-Parameter (LMS) Models

Lumped-parameter models describe structure by rigid lumped masses interconnected by deformable structural members representing the energy-absorbing structural elements (springs and/or dampers), whose properties are generated from crush

tests. The vast majority of the reported lumped-parameter models describe vehicle structure by idealized linear or nonlinear stiffness characteristics [11,13]. Such models are considered most appropriate for parametric studies in crash analysis especially at the conceptual design stages to identify desirable structure modification and for assessments of add-on EA components. These models often have many advantages such as simplicity and greater computational efficiency, while their validity under large magnitude plastic deformations is limited [11]. The lumped mass-spring models, however, can yield effective predictions of deceleration transmitted to the passenger compartment and vehicle deformation during impact simulations [36]. Linear and nonlinear lumped-parameter models of varying degree-of-freedom (DOF) have been widely reported for evaluating different concepts in EA elements under frontal barrier impacts.

Simple single-DOF models have been extensively used to evaluate crashworthiness enhancement of vehicles by using add-on EA elements [36,40-42]. The vehicle body in such models is represented by a rigid mass, as shown in Figure 1.4, where the primary load bearing members are described by linear or nonlinear springs with or without a linear or nonlinear damper. The occupant, which is coupled with the vehicle structure via the restraint, is also represented by an additional DOF, as shown in the figure. Nonlinear lumped-parameter models with two- or multi-DOF have also been reported for analyses of EA and structure deformation responses under barrier impact loads. Mooi and Huibees [43] proposed a two-DOF vehicle model to study incompatibility issues in vehicle-to-vehicle (VTV) or vehicle-to-movable deformable barrier impacts. The model has also been applied to study the crashworthiness enhancement by using extendable EA elements

by Elmarakbi and Zu [36,40-42], as shown in Figure 1.5. The model comprises two extendable energy absorbers or dissipators (c_1 and c_2).

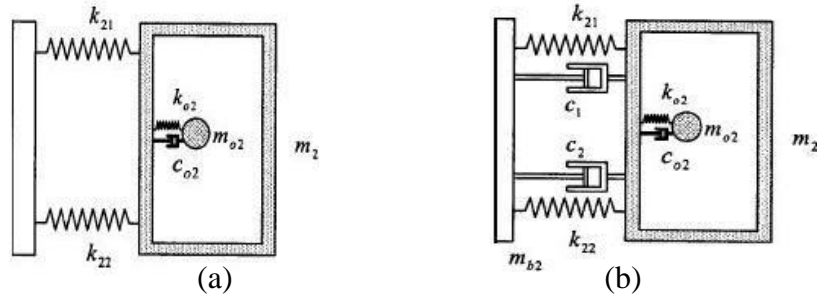


Figure 1.4: Single-DOF lumped-parameter models for analysis of add-on energy absorbers; (a) baseline; and (b) integrated add-on [40]

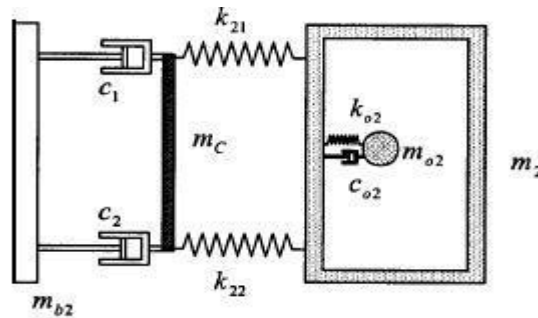


Figure 1.5: Two-DOF lumped parameter model equipped with an extendable energy absorber [40]

Kamal [44] proposed a comprehensive three-DOF lumped parameter model of the vehicle comprising nonlinear stiffness properties of various structural members such as radiator, firewall, engine cradle, engine mounts and cross members (Figure 1.6). The stiffness properties of the structural members were established through extensive crash tests performed for each component. Such models have also been applied to investigate the influence of various design parameters on the vehicle structural behavior. These parameters could include the element thickness, representing structural elements coupled with different types of EA elements and the inertia effect of the intermediate components [45-48].

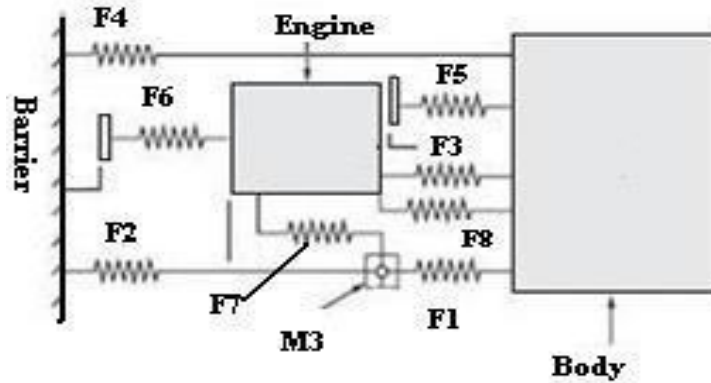


Figure 1.6: Three-DOF lumped parameter model of a vehicle under barrier impact [43]

While lumped-parameter models have been widely used to assess effectiveness of different concepts in EA elements, these require thorough characterization of various structural members. Such models, however, are one-dimensional models, while they assign identical dynamic load factor (DLF) for all the structural elements [44]. These models could thus lead to noticeable differences between the model and test results. The lumped-parameter models also exhibit a number of important shortcomings that are briefly summarized below:

- The models generally require deep understanding and characterizations of structural behavior under severe impacts.
- The models require prior knowledge of element crash characteristics, and thus cannot be applied to a new structural element [3].
- The models cannot describe the contributions due to compliances of different joints.
- The models cannot account for kinematics of the components due to their one-dimensional nature.

Multi-Body Dynamic (MBD) Models

The multi-body dynamics (MBD) models are constructed upon discretizing the structure into rigid bodies as in the case of lumped-parameter models. The rigid bodies, unlike lumped-parameters, are coupled by various joint types with varying DOF. Such

models also provide a unified methodology for the simulation of structural systems together with biomechanical representation of the occupant, and design optimization of the integrated systems. It could also be used to measure different occupant-related crashworthiness issues such as injury scaling, whole body tolerance to impact, and performance analyses of occupant restraints [39]. A number of multi-body dynamic (MBD) models have been developed to study different aspects of crash energy management (CEM). Schram et al. [27] developed a MBD model of a vehicle to assess effectiveness of EA elements in reducing an acceleration severity index (ASI) and the HARM factor (the average estimated cost for injury in thousands of dollars) at different crash speeds for various offset ratios in vehicle-to-vehicle (VTV) incompatible impacts. The study concluded that the deviation between the vehicle deceleration pulse and a target deceleration pulse could be reduced by defining additional nodal constraints.

Schram et al. also [27] developed a MBD model of a vehicle subframe to analyze the occupant injury potential in a full frontal impact (Figure 1.7). A number of large-order MBD models have also been developed and analyzed to study the influences of important design parameters. These studies have shown that they could enhance structural ability to sustain greater crash force and reduce occupant peak decelerations under incompatible impacts [28,49]. The MBD models also offer significant advantages in defining complex kinematic relations, not only for different structural components, but also for the human occupant [11], while permitting greater computational efficiency compared to the FE models. The MBD models, however, require accurate characterization of joints and their compliances, while considering kinematics of a pair of bodies, which may be quite complex.

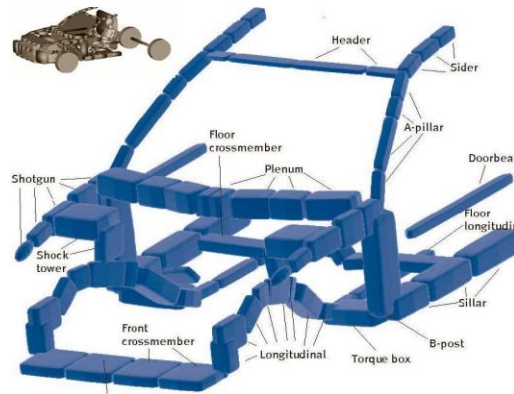


Figure 1.7: Multibody dynamic model of a vehicle [26]

Nonlinear Finite Element (FE) Models

During an impact, the vehicle structural components experience high impact loads leading to large progressive elastic-plastic deformations and thereby large deformations and rotations of the contacting bodies together with high stresses. The primary advantages of the FE models lie in their capability to describe local/total structural deformations, stress distributions and vehicle deceleration-time history, which permits for analyses of potential occupant injuries, identifications of critical structural elements, design refinements and structural optimization [3]. The crashworthy analyses of vehicle structures have been mostly performed using FE models of varying sizes and complexities. Such models, unlike the MBD and the lumped-parameter models, permit considerations of structural components with specific geometries and material properties, and characteristics of various joints and couplings [3]. Furthermore, such models permit considerations of high nonlinear stress behaviors of components with different collapse modes and effects of rate of loading that may occur under severe collision conditions [50-52].

The reported studies of crash analyses of vehicle structures have widely employed various finite-element software codes. Implicit software such as ANSYS and NASTRAN,

however, are not well-suited for short duration crash loading of structures with various nonlinearities associated with the geometry, material properties and boundary conditions [3,53,54]. Explicit nonlinear dynamic finite element codes, such as LS-DYNA, PAM-CRASH and RADIOSS, have been developed and widely used to solve for crash responses of structures subject to large magnitude elastic-plastic deformation [54-57]. The LS-DYNA is a nonlinear FE codes that has been widely used in vehicle crash simulations [33,58,59].

The reported studies have implemented widely different FE models of various vehicles to study different methods of improving vehicle structural integrity and enhancing structural crashworthiness during impacts [54,60,61]. A number of studies have also employed optimization methods to realize optimal structural characteristics, while the methodologies and design objectives differ considerably. Some studies have focused on defining new load paths or strengthening selected local areas of most probable bending initiation modes [49,54,62], while others are based upon crashworthiness enhancement using add-on EA elements or mechanisms [18,63]. Different FE models have been used to assess effectiveness of stiffeners on the overall structural stiffness [12,64]. Vehicular structural optimization studies have employed either single or multi-objective functions of widely different crashworthiness performance measures such as occupant deceleration, target deceleration pulses, maximum intrusion and/or energy absorption. Duddeck [65] performed a single objective structural optimization using response surface method (RSM) to create a surrogate model applicable for multidisciplinary optimization using different crash situations, and noise, vibration and harshness (NVH) as objective functions.

Owing to conflicting design requirements of different measures, many studies have considered multi-objective structural optimization using different approximation methods to enhance both occupant safety and structural crashworthiness [31,60,66-68]. The design vectors in these studies are generally limited to geometric and material properties of the most critical load carrying members. Structural optimization using nonlinear FE models, however, impose excessive demands on computational recourses. A number of studies have thus focused on deriving reduced order FE models for effective and efficient crash analyses by simply replacing main load carrying members in FE model by beam-spring elements to reduce the run time to almost 85%, while maintaining relative error less than 15% compared with the original FE model [34,69].

Hybrid Models

Hybrid models are characterized by combination of simplicity of the lumped-parameter modeling approach, and the flexibility and accuracy of the FE models. Such models can thus overcome some of the limitations of the lumped-parameters models and MBD models and help reduce the computational demands of the FE models. Owing to the high computational demands of nonlinear FE models, a few studies have proposed hybrid vehicle model for efficient crash analysis and occupant-level design optimization [34,69,70]. The hybrid models, however, are load-path dependent; the model structure thus depends on the loading direction and the boundary conditions. The hybrid models also require formulations of essential relations between lumped bodies and the finite elements during the collapse mode, which could be significantly altered by the internal loads and crush properties of the elements.

From the above discussions on different types of modeling techniques, it can be deduced that lumped-parameter models could be effectively applied for assessments of add-on EA elements. Such a model would permit detailed parametric studies and design optimization in a highly efficient manner. The performance assessment of the resulting design could then be performed through a detailed FE model of the vehicle structure.

1.2.3 Dynamic Response Analysis of Vehicle Crash Models

Different studies have addressed widely differing aspects of crashworthiness of road vehicles that involve varying performance measures, models, inputs and analysis methods. The primary goals of the reported studies, however, are generally consistent in that they involve enhancement of crashworthiness of the vehicle subject to limit constraints on the vehicle weights and dimensions. The dynamic responses of the reported crash models tend to differ considerably due to the considerations of widely different inputs and target performance measures. The inputs and responses considered in the reported studies are thus thoroughly reviewed and discussed below in order to identify desirable performance measures and inputs.

1.2.3.1 Types of Inputs

The inputs to a crash model vary depending upon the crash situation. These include the input speed, impact load, angle of impact, etc., apart from the vehicle model properties. The inputs to a crash model may be classified into two categories, namely, force/motion inputs and collision condition inputs. The collision inputs relate to the type of impact (e.g. fixed barrier or and vehicle-to-vehicle) and angle of impact. Reported studies have mostly emphasized response analysis to force/motion inputs, particularly for situations involving frontal barrier impacts [71,72]. The vehicle speed is known to be

main input factor affecting the crash responses, since it relates to the strain rate. This is also evident from the specifications defined for different standardized crash test methods and safety regulations, namely:

- FMVSS 208 [73] describes the test specifications for full-scale vehicle full frontal impact test against a rigid barrier. The method requires the test to be performed at 48 km/h and it employs a lap and shoulder seatbelt or airbag with free moving occupant.
- CAP test method [74] is a full-scale vehicle full frontal impact test against a rigid barrier for assessing the occupant safety. The standard specifies the impact speed of 56 km/h with lap/shoulder belts in addition to the passive airbag.
- IIHS test method [75,76] is a frontal impact with 40 % offset deformable barrier (ODB) to be conducted at an impact speed of 64 km/h. The test is performed with a Hybrid III dummy in the driver's seat and the test method provides guidelines to evaluate overall safety rating based on measured performances of the structural and safety cage, injury measures, and restraints and dummy kinematics.

The reported studies on the simulation of crash models also consider the impact speed within the ranges stipulated by the standardized methods generally 48 to 56 km/h for vehicle-to-rigid barrier full frontal impact, and 60 to 64 km/h vehicle-to-vehicle offset frontal impacts [1,43,77]. A number of simulation studies, particularly those on energy absorbers, have also considered relatively higher impact speeds, up to 100 km/h [27,77-79]. Apart from the impact speed, a few studies have defined initial impulsive load, mainly as the primary input. These studies, however, are focused at the component level, to study the effects of type of material, beam thickness, cross-sectional properties and joint welding specifications on the component responses [25,77]. However, it is generally agreed that the impact speed or the strain rate are equally important factors at the

component levels as well as the total vehicle levels. Different performance criteria that have been selected will be investigated in the following subsection.

1.2.3.2 Performance Measures

The crashworthiness of vehicle structures have been measured using a wide range of performance measures depending on the purpose of the study. These include the target deceleration pulse, head injury criteria, occupant chest decelerations, energy absorbed, occupant compartment intrusion, structural deformation etc. Some of the performance measures used in the reported studies are summarized below:

Vehicle deceleration pulse: The crashworthiness of vehicle structures have been widely assessed in terms of a target deceleration response, deemed to be the limiting deceleration value for occupant safety, and often referred to as ‘the crash pulse’ [11,80]. The majority of the studies employing either MBD or FE models consider the vehicle deceleration response at the lower part of the B-pillar as recommended by standardized tests, such as FMVSS and IIHS [27,47,77]. Some of the studies have evaluated crashworthiness by the deceleration pulse at the driver location on the seat cross-member [77,81] and at the passenger seat [19,81,83].

Occupant peak deceleration: The occupant injury risk in crash analyses of lumped-parameter models is often related to the peak deceleration of the mass representing the occupant [40-42,84]. The occupant mass in such models is coupled to the rigid bodies representing the vehicle structure or the load path through the restraint system.

Passenger compartment and total structural deformation (dynamic crush): The magnitude of dynamic crush of vehicle structure has been directly related to the passenger compartment intrusion and consequently to the occupant injury in crash accidents

[49,85]. The passenger compartment intrusion is the result of deformation of various substructures in the load path denoted as the total vehicle structure deformation. The total deformation is strongly influenced by many vehicle design and operational parameters such as structural stiffness of load carrying members, available space, stack up of non-crushable power-train components, impact speed and vehicle mass [18]. Many studies also consider total structural deformation as a measure of the impact energy absorption properties of the vehicle [36-43,84,87,87].

The occupant compartment intrusion, measured in terms of toe-pan/board deformation is largely affected by the total vehicle deformation and the inertia of the bulk mass components such as the engine and transmission [47,78]. Different methodologies, however, have been employed to describe the compartment intrusion. These include the changes in the longitudinal distance between the rear end of the structure and the lower corner of the A-pillar, especially in an offset crash [66] and the intrusion at the toe pan into the driver's compartment [77].

Occupant chest deceleration and head injury criterion: The occupant injury risk during a crash event has been directly associated with the deceleration of the occupant head and chest [88,89]. Consequently, the majority of the crash test standards assess the crashworthiness in terms of peak chest acceleration, expressed as the head injury criterion (HIC) [73,75]. In recent years, crashworthiness of vehicles have been specified by their 'star ratings' by the safety organization, which is based on Abbreviated Injury Scale (AIS), a function of both Chest-G and HIC. Both, the Chest-G and HIC are most widely used to assess the crashworthiness of road vehicles [19,47,77], and to evaluate the

relative performance potentials of structural modifications [18,88] and add-on energy absorbing elements [85,90].

The head injury criteria (HIC) is defined as a measure of the severity of an impact on the occupant's head and is related to the deceleration magnitude and its duration. The current FMVSS code [73] recommends a constant duration of 15 ms of the deceleration pulse, while its earlier version employed a duration of 45 ms. The HIC_{15} value for a 15 ms duration is computed from:

$$HIC_{15} = (t_2 - t_1) \left[\frac{1}{(t_2 - t_1)} \int_{t_1}^{t_2} a(t) dt \right]^{2.5} \quad (1.1)$$

where $a(t)$ is the resultant occupant deceleration at the center of mass (cg) of the occupant's head expressed in g units, and (t_1, t_2) defines the continuous time duration of the pulse over which HIC attains a maximum value. The HIC value is computed in the vicinity of the peak deceleration and over the entire event for constant pulse duration $(t_2 - t_1)$ of 15 ms. The resulting HIC value is taken as the maximum value of HIC attained over the entire event. The threshold value of HIC has been defined on the basis of AIS, which provides a ranking of the injury risk in accordance with potential damages to organs sustained during a trauma. The AIS provides a measure of injury risk over a scale of 0 to 6, where '0' refers to negligible injury risk [91]. The FMVSS [73] code recommends a threshold value of HIC of 1000, while a HIC value of 700 is recommended for preservation of occupant safety, which refers to AIS of 2 indicating moderate injury risk.

Crash tests and regulations also relate the potential injury risk to the peak deceleration and its duration measured at the chest of the dummy. The FMVSS code

[11,73] states that the chest deceleration must not exceed 60 g, except when the duration of the peak deceleration event is less than 3 ms. Apart from the most commonly used chest deceleration and HIC measures, many different measures of crash severity have been used in the reported studies. These include the peak occupant head deceleration together with the chest deceleration [19,46,77], a Vehicle Crash Severity Index (VCSI) as a function of the crash deceleration [81], an Overall Severity Index (OSI), defined as a weighted function of various crash measures such as HIC, Chest-G, Chest deformation, Femur load and Neck moments [18,92].

Specific absorbed energy: The crashworthiness of a vehicle structure has been directly related to the energy absorption property of the structure, which is a function of the plastic deformations of the structure and energy absorbed/dissipated into the add-on energy absorbers [85,92]. The energy absorbed by a vehicle structure depends upon the stress-strain properties of the material and the strain rate [83,90]. The specific energy absorption measures have been widely used to assess performance potentials of different concepts in add-on energy absorbers [37,8537]. The absorbed energy is often normalized with respect to the vehicle mass, termed as specific absorbed energy, in order to perform relative evaluations of vehicles of comparable total mass [5,85]. Greater specific energy absorption is achieved by employing crush elements and light-weight materials [8,93-95].

Optimum Vehicle deceleration pulse: Considering the direct association between the deceleration or vehicle crash pulse and the potential injury risks, many studies have proposed shape of desired deceleration pulse, namely the peak deceleration and duration [95,18-102]. Such crash pulses have been proposed in order to reduce the injury potential in consideration of the mechanical properties of the biomechanical structure of the human

occupant. The primary goal of defining a desired or optimal crash pulse is to identify desirable properties of the vehicle structure or add-on energy absorbing elements. Kral [97] proposed two optimal deceleration pulses that ensure peak occupant chest deceleration below 60 g assuming a constant vehicle deformation during each interval of the predominant deceleration peak. The proposed pulses comprise the dominant deceleration events over different durations, while the deceleration level diminishes to zero during the intermediate intervals. Such pulses are difficult to achieve in real vehicle structures. Alternately, Cheng and Pelletiere [98,99] proposed a vehicle optimal deceleration pulse corresponding to a 56 km/h impact speed. The proposed optimal crash pulse is similar to an impulse at the time of crash followed by a gradual decay in the deceleration. The realization of such a pulse, however, necessitates a greater interior space, and thus aims at achieving lower peak occupant deceleration by providing more free interior space. The proposed pulse could be realized only through structural modifications and would be difficult to attain through add-on energy absorbers.

Motozawa and Kamei [100] and Motozawa et al [101] proposed an optimal crash pulse through formulation and analysis of a two-mass model of the vehicle structure. The two masses correspond to those of vehicle body in contact with the occupant and the vehicle frame, which are separated by a gap, while the pulse is defined on the basis of the vehicle body deceleration response. The optimal pulse exhibits a positive peak decaying deceleration initially and is followed by a sudden negative decaying pulse in second interval. The practical applicability of such a pulse is highly questionable considering the vehicle structure separation by two discrete masses. Wu and Nusholtz [102] proposed an optimal deceleration pulse that reduces occupant relative velocity at a 56 km/h impact

speed from a conceptual design perspective. The optimal pulse describes two step-like constant deceleration intervals. The study investigated the ratio of the deceleration magnitudes during the two intervals under a constant vehicle crush distance and constant pulse durations, and proposed an optimal deceleration ratio in the 0.7 to 1.3 range.

An optimal deceleration pulse was proposed by Brantman [95] on the basis of accepted HIC and Chest-G levels and injury potentials. The deceleration pulse designed for the B-pillar and shown in Figure 1.8 has been widely accepted for design of vehicle structures with enhanced crashworthiness [26,92,103] on the basis of the occupant deceleration response at a 48 km/h frontal impact. The pulse defines three distinct deceleration intervals corresponding to crash initiation, airbag deployment (onset) and occupant contact with respective magnitudes of 13, 6.5 and 26 g. The study involved simulation of a crash sensor and a passive airbag system together with experimental results, and analysis of effects of the airbag system on the occupant injury measures to adapt to the vehicle crash pulse. The study suggested that the acceptable pulse would fall between the upper and lower bounds (Figure 1.8), which were determined based on limiting injury measures, namely, the HIC value of 350 and peak chest deceleration of 40 g. Figure 1.9 illustrates typical occupant deceleration response variations pulse during the three intervals, derived from an idealized and kinematic occupant models [11].

Considering that the crash response varies significantly with the impact speed, the optimal deceleration pulse proposed by Brantman [95] was further explained by Witteman and Kriens [55,104] in order to derive optimal deceleration pulses at three different impact speeds of a full frontal impact with a rigid barrier, namely 32, 56 and 64 km/h. The resulting deceleration pulses (Figure 1.10) were obtained on the basis of the

overall severity index (OSI) proposed by Witteman [18] as a weighted function of HIC, chest-G, chest-deformation, Femur load and neck moment. The proposed optimal pulses have been judged to be more feasible since they comprise three intervals that are consistent with occupant behavior during a collision [18,55,104]. Furthermore, a number of studies have shown that such deceleration pulses could be obtained, to a certain extent, by controlling the crushing behavior of the vehicle structure and by using add-on energy absorbing elements [95,105].

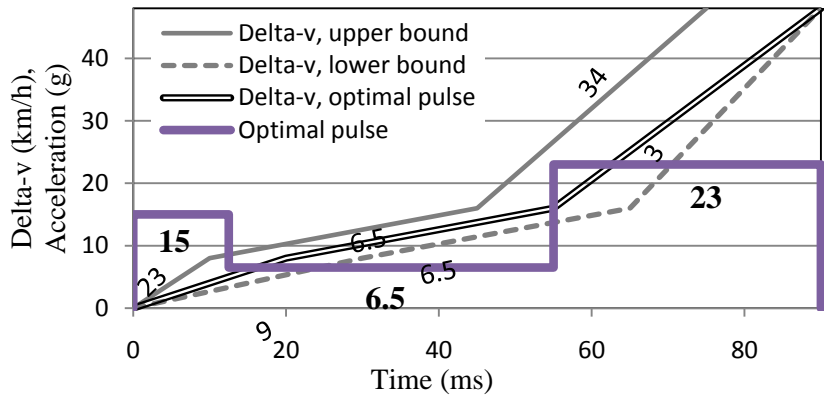


Figure 1.8: Optimal crash pulse at 48 km/h with three deceleration phases [95]

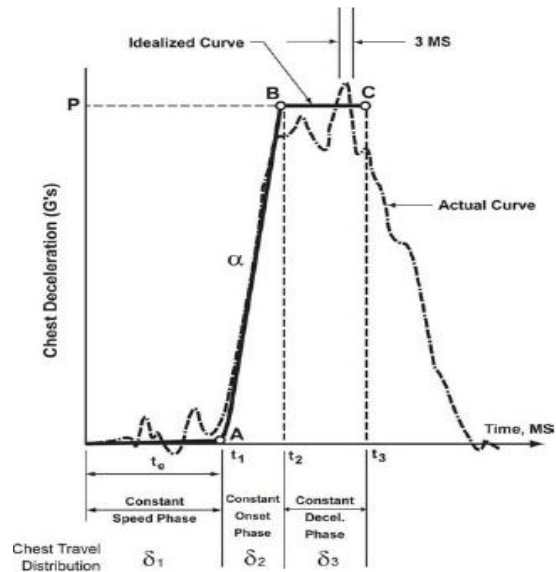


Figure 1.9: Typical pattern of occupant deceleration pulse derived from the idealized kinematics models of the occupant [11]

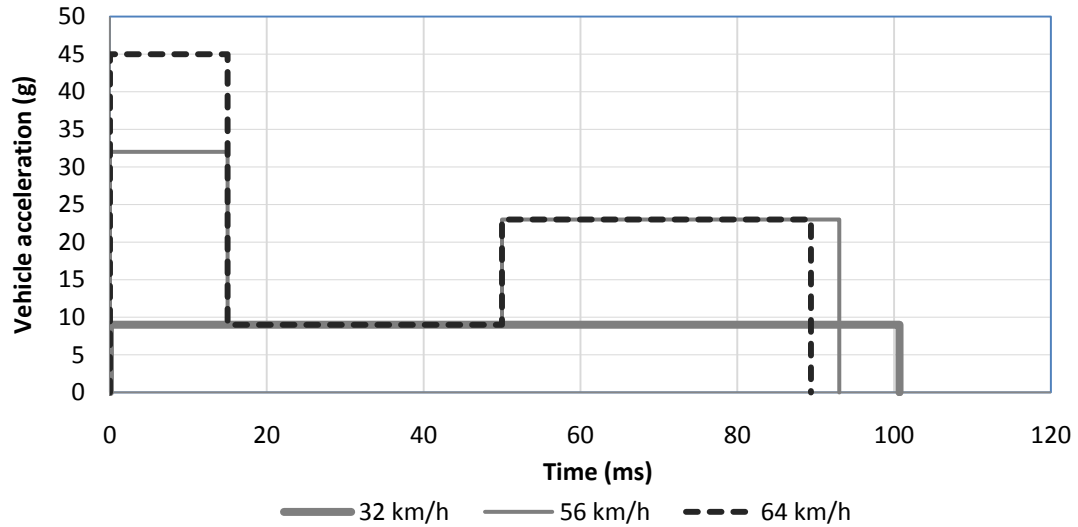


Figure 1.10: Optimal decelerations pulse at three impact speeds [18]

1.2.3.3 Critical discussion on the performance measures

From the above discussions, it is evident that the crashworthiness of vehicle structures and effectiveness of energy absorbers have been evaluated using a wide range of performance measures such as peak vehicle deceleration, total deformation, peak occupant head and chest decelerations, HIC, ASI, RIR and compartment intrusion. There seems to be little consensus on a generally acceptable performance measures among the published studies, while the test and assessment standards have converged to common measure of HIC and Chest-G apart from femur load, neck moment and chest deflection [73,74]. Irrespective of the measure used, the reported studies have proposed the measures with a common goal to reduce the severity of the crash and the associated injury potentials. The optimal deceleration pulses proposed in different studies also differ significantly. The deceleration pulse proposed by Brantman [95] was further refined by Witteman [18]. The reported pulses are considered to correlate well with three phases of the occupant interaction with the vehicle and restraint system under impact conditions [10,103,104,106]. Furthermore, the proposed optimal pulses comprise a crash initiation

phase in which the occupant moves under the initial impact speed but remains mostly unaffected by the vehicle deceleration. The occupant deceleration pulse increases rapidly as the occupant interacts with the vehicle or restraint system in the second phase.

1.2.4 Methods for Enhancing Structural Crashworthiness

In the design stages, a vehicle structure is designed to satisfy a target deceleration pulse and to limit the crush distance below the available frontal crumple zone. This is generally achieved by selecting and attaining a desired crush sequence and failure modes of the main load carrying members [50,54,107]. The designs of structures of various vehicles have converged to these common features for effective energy crash management. These include the designs with greater stiffness of the occupant compartment, controllable and progressive crush or deformation with limited intrusion, and enhanced energy absorption properties of the structure [11]. The vast majority of the studies on crashworthiness of vehicles have shown the benefits of occupant compartment design with higher stiffness in preserving the occupant safety during collisions. A stiff occupant compartment necessitates higher load capacity to support the energy absorbing structures so as to limit the vehicle deceleration and structural deformation during a crash [3,18]. The frontal structure is generally designed to yield progressive deformations or collapse of different substructures. The frontal structure is thus designed to achieve three crush zones in a sequential manner: (i) a soft front zone to reduce the collision aggressiveness; (ii) a primary stiff crush zone that is composed of the main energy absorbing structure; and (iii) a secondary stiff crush zone that involves the structural elements between the energy absorber and the passenger compartment extending to the dash panel and toe-board area [85]. The structure designs, however, are realized under

constrained structure weight so as to achieve enhanced specific energy absorption capabilities of the main load carrying members [33].

Crashworthiness of a vehicle structure strongly depends on the properties of the primary load carrying members, namely, the materials properties, shape and cross-sections in addition to the continuity of different load paths. Figure 1.11 illustrates different load paths in a typical automotive frontal-structure [28]. The data obtained from extensive frontal crash tests, conducted by New Car Assessment Program (NCAP) in US and Europe, suggested that the longitudinal rails (longerons) absorb most of the impact energy, as evident in Figure 1.12 [108]. The data in the figure were obtained by US-NCAP during full frontal impact with a rigid barrier at 56 km/h, and by Euro-NCAP under a 40% offset frontal impact against a deformable barrier at 64 km/h. The primary load path, the longitudinal rails can undergo both bending and axial compression collapse modes, while the compressive mode is most desirable to achieve maximum energy absorption in a continuous manner prior to failure. Consequently, the primary load path must be designed to limit the bending modes [79,108].

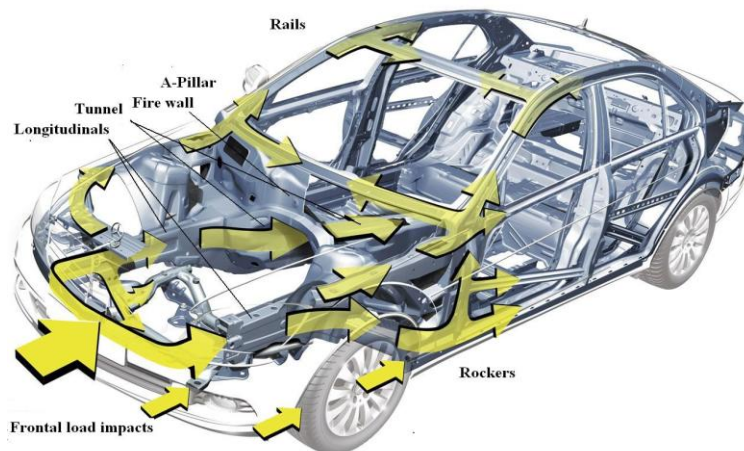


Figure 1.11: Load paths of the car body structural members during frontal impact [28]

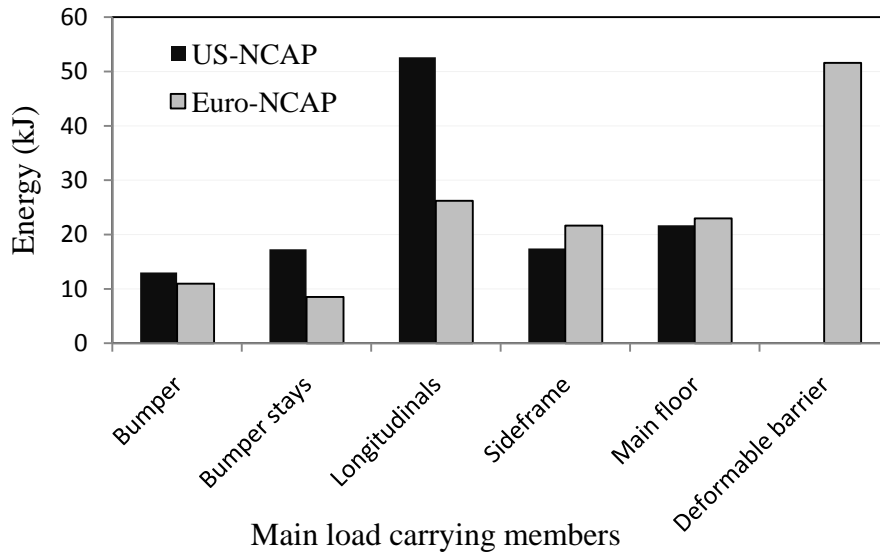


Figure 1.12: Energy distribution in a frontal car structure measured during frontal rigid and flexible barrier crash tests [108]

While the reported studies have emphasized the above stated three common requirements of the structure design, widely different methods have been adapted to realize the goals. Irrespective of the methods used to enhance CEM, the designs and/or identifications of the primary load paths of a vehicle structure form the essential basis. This is attributed to the fact that the impact load is transmitted through these paths and absorbed by different load carrying members in a specified sequential manner thereby reducing the impact load transmitted to the occupant compartment. Additionally, a thorough understanding of the crash dynamics leads to identifications of essential developments in CEM to improve the crashworthiness.

1.2.5 Crash Energy Management (CEM) Techniques

The injury risk of an occupant involved in a frontal impact could be attributed to two primary response quantities: (i) a physical contact injury caused by intrusion of frontal structural components' into the occupant compartment [109,110]; and (ii) injury

due to impact load attributed to high deceleration transmitted to the occupant. Owing to the greater energy absorption properties of the primary load path, a number of designs have either introduced or proposed several additional load paths and structural enhancements for improved crash energy management. Different CEM methods can be categorized into three broad categories according to the type of enhancement, namely: (i) modification of vehicle structure characteristics (ii) implementation of crush elements; and (iii) implementation of adaptable add-on energy absorption systems. These methods are summarized in the following subsections, followed by general conclusions.

1.2.5.1 Enhancement of the Structural Stiffness

Many studies have investigated crashworthiness enhancement of vehicle structures by selecting optimal material and geometrical properties (thickness/cross-section) of the main load carrying members or by introducing additional load paths to the structure. Considering the growing demands for lighter and more fuel-efficient vehicles, a large number of studies have focused on the usage of lightweight materials together with optimal structural design to preserve and enhance occupant safety [25,26,110]. These have been realized under constraints of maintaining the ultimate strength, and have invariably suggested aluminum alloys structural components for enhanced high specific energy absorption. The resulting structure designs could provide weight reductions up to 40% or more with enhanced crash performance compared with the steel structures [93,97]. Various studies employing structural optimization have thoroughly investigated crash initiation pulse (CIP) by considering different types, shapes and locations of the primary load path [25,111]. These have provided important design guidance of longitudinal rails for enhanced energy absorption at different impact speeds [25,26].

Additionally, some studies have also investigated the effects of cross-section characteristics of longitudinal rails on minimizing and controlling the bending moment modes at the anticipated plastic hinge locations [18,47]. A few studies have investigated effects of reinforcing the connections between different load paths to enhance crashworthiness [49,50,54]. These have concluded that an increase in the coupling stiffness between the upper and lower load paths up to 10% of a light vehicle could reduce the likelihood of pitching moment in case of incompatible impact against a medium size vehicle. Such modifications also reduce the hocking effect due to incompatible impacts [49,112].

Hamza and Saiou [31] and Hamza [67] presented a new non-gradient based optimization method referred to as the equivalent mechanism (EM) approximation method to configure structural overall deformation sequences or crash modes in an efficient manner. The method was considered an efficient tool to perform critical assessments at early design stages.

1.2.5.2 Passive Add-on Energy Absorber Elements

A large number of studies have investigated the effectiveness of add-on energy absorbers or crush elements for absorption of energy in the vicinity of impact zone. The use of aluminum metal-foam or aluminum honeycomb crush elements as passive EA elements in vehicle crashes has been widely suggested to increase specific energy absorption capacity [113,114]. The design of EA elements in crumple zone are realized on the basis of three fundamental requirements, namely: (i) high-energy absorption capacity with uniform compressive stress; (ii) lightweight; and (iii) withstand different collapse modes in a predictable manner [115]. Various studies have proposed a wide

range of crush elements or alternate structure design modifications to realize effective crush properties and crash energy management. Sohn et al. [116] showed that by replacing a conventional bumper stays with hydroformed EA tubes reduced the bumper's weight by about 34% and enhanced absorption capabilities up to 16.7 km/h crash speed to comply with FMVSS 215. Heyerman [115] proposed lightweight aluminum structure filled with aluminum metallic foam alloy to achieve an increase in specific energy absorption of 40 - 60% for different foam densities, ranging from 3 to 10%. Lehmus [117] proposed a new trend in metal-sponge foam design, called the advanced pore morphology (APM) foams, to be used as crush elements in automotive industry with enhanced specific energy absorption. Walters [106,118] investigated the use of Kagome as an EA material because of its high specific energy density with maximum compressive strain that can reach 75% under both static and dynamic loads up to 56 km/h impact velocity. Scarpa and Ruzzene [8] proposed the application of shape memory alloy (SMA) and developed a smart honeycomb structure with the capability to retain its original shape, to a certain extent, after the impact load diminishes. However, inclusion of honeycomb in frontal car bumper should be studied carefully since it may increase the tendency of pitching moment and yield to the hocking effect due to contact point mismatch [15].

The effectiveness of EA elements in reducing the severity of frontal collisions have been extensively investigated using different vehicle models, ranging from simple single-DOF to elaborate FE models. Schram [27] and van der Zweep et al. [49] employed multibody dynamic models to study the effectiveness of EA elements in the frontal vehicle substructure in reducing the injury level in incompatible vehicle-to-vehicle

impact as a part of the on-going European project named vehicle crash compatibility (VC-compatibility) [27,49]. The studies showed that the front substructures equipped with energy absorbers could considerably enhance crashworthiness of vehicles by lowering peak longitudinal deceleration under combinations of impact speed and overlap ratio. An acceleration severity index (ASI) was used to obtain a HARM score that represented the average estimated cost measured in thousands of dollars associated with a potential crash. The HARM score was related to ASI, as:

$$\text{HARM} = 13.401 \text{ ASI}^{1.54} (10^3 \$) \quad (1.2)$$

where ASI is determined from deceleration response at the occupant location such that:

$$\text{ASI}(t) = \left[\left(\frac{\bar{a}_x}{\hat{a}_x} \right)^2 + \left(\frac{\bar{a}_y}{\hat{a}_y} \right)^2 + \left(\frac{\bar{a}_z}{\hat{a}_z} \right)^2 \right]^{\frac{1}{2}} \quad (1.3)$$

In the above relation, \bar{a}_x , \bar{a}_y and \bar{a}_z are the average occupant decelerations over a 50 ms duration and \hat{a}_x , \hat{a}_y and \hat{a}_z represent the limiting values with typical values of ($\hat{a}_x = 12 \text{ g}$, $\hat{a}_y = 9 \text{ g}$, $\hat{a}_z = 10 \text{ g}$) [107]. A number of studies on elastic or visco-elastic energy absorbers/dissipations have concluded that performance of such members is severely limited by permissible space and thus limited travel of the visco-elastic impact absorbers [18,63,118,119]. Lee [19] investigated the impact force transmitted to the load path by considering an extended spring-mass bumper with linear spring stiffness characteristics with a large stroke and low stiffness ratio compared to vehicle structural stiffness. The results attained under a 48 km/h vehicle-to-vehicle impact revealed oscillatory impact force transmitted to the load path, while the peak magnitude was lower than that of the baseline model. The implementation of such an extended absorber, however, would be prohibitive in vehicles. Balike [48] proposed a damped under-ride

guard to reduce the passenger intrusion under a truck in car-truck collisions, while maintaining peak deceleration below the assigned limit at a 50km/h impact speed. The study showed the benefit of using spring/damper system in enhancing crashworthiness by absorbing a portion of the impact energy. The hydraulic dampers, however, may yield hydraulic lock up under high speed impacts, which was not considered in the study.

The reported studies on passive add-on energy absorbers have demonstrated considerable benefits of such elements, although the analyses have been limited to a few impact speeds. Furthermore, crush elements exhibit limited abilities under offset and oblique severe impact conditions. Consequently, a few studies have proposed concepts in adaptable add-on EA systems with variable absorption characteristics.

1.2.5.3 Adaptable Add-on Energy Absorber System

The effects of variations in the structure stiffness on the peak deceleration and deformation under front impact have been investigated by Wägström et al. [61,112]. The study investigated the vehicle-to-vehicle (VTV) and vehicle-to-barrier (VTB) frontal impacts at three-impact speeds and different weight ratios, and concluded that the peak deceleration over the impact speed range could be significantly reduced by introducing variable stiffness structures. The results obtained for VTB impacts revealed that a lower stiffness is desirable under low speed impacts, while an enhanced stiffness reduces the peak deceleration under high speed impacts. The study proposed an adaptive algorithm to vary the structure stiffness prior to the impact in order to reduce peak decelerations of the mating vehicles. Figure 1.13 shows noticeable reductions in the peak decelerations of colliding vehicles with different mass ratio (low, medium, and high) of vehicles equipped with adaptive stiffness. The study concluded that increasing structural stiffness causes the

absorbed energy to increase considerably in the initial deformation zone, while the peak deceleration remains lower than the baseline model with constant stiffness. The energy absorbing potentials of adaptable frontal energy absorbers have been investigated in a few studies. In review of the CEM approach, the adaptable EA concepts employed in these studies could be classified into four main categories: (i) splitting the impact energy between the primary load bearing and the least affected load carrying members; (ii) add-on EA absorbers; (iii) add-on EA dissipation systems; and (iv) active safety devices.

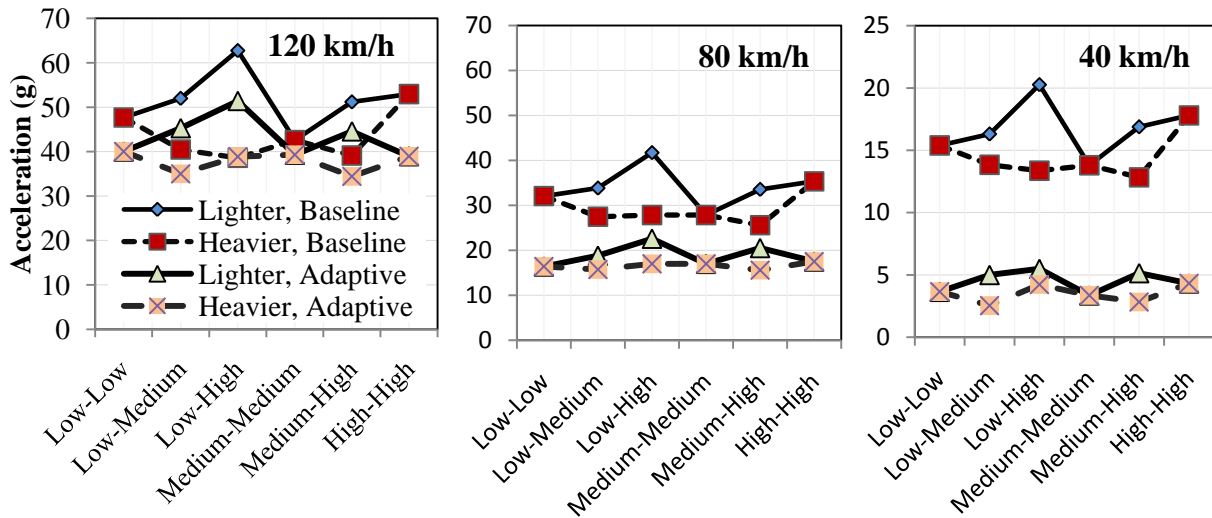


Figure 1.13: Variations in maximum decelerations for different mass ratios and at different closing velocities (120, 80 and 40 km/h) [112]

Distribution of Impact Energy

A few studies have proposed splitting the impact energy in order to utilize energy absorption properties of structural components that are mostly unaffected by the impact loads. This allows for enhanced energy absorption of the total vehicle structure and thereby reduces the severity of a frontal impact. Tarazona and Castjon [62] investigated crash energy management through splitting of the impact energy between the front and rear primary load carrying members by implementing a rope-pulley transmission

mechanism. The proposed mechanism comprised of using a flexible element to produce a time lapse before the rear structure member undergoes deformation so as to reduce the peak deceleration. The implementation of such a conceptual design, however, necessitates considerations and analyses of various design parameters, namely controlling the sequential load distribution, the effects of transmission mechanism on the pitch moment and hocking effect in frontal impacts. Sharpe et al. [105] described the enhancement of structural crashworthiness via multi-stage load paths to sustain impact loads of different orientations. The concept permitted crash load distribution among different structural parts under the constraints of total weight reduction. The study also proposed a ‘three ringed concept’ as an anti-hooking mechanism and thereby offered greater degree of occupant protection under impacts up to 65 km/h.

Adaptable Add-on Energy Absorption Systems

A number of studies have shown that a lower structural stiffness is preferable under low speed impacts, while a higher stiffness is desirable under high speed impacts. The adaptable energy absorption systems have been proposed for effective crash energy management through adaptive variations in overall structural stiffness characteristics in accordance with some of the impact conditions. The reported studies have investigated different methods to adjust structural stiffness under varying impact conditions. Ostrowski et al. [119,120] used electronically-controlled additional detachable stiffeners connected to the longitudinals to achieve a dual-stage structural stiffness during an offset or incompatible frontal impact. Witteman [18] proposed an adaptable frontal structural system able to withstand frontal impacts at different collision speeds. The proposed add-on energy absorption/dissipation system comprising telescopic longitudinal members

controlled by a wire-drum brake hydraulic system with variable braking force to realize variable energy absorption depending on the crash situation (Figure 1.14).

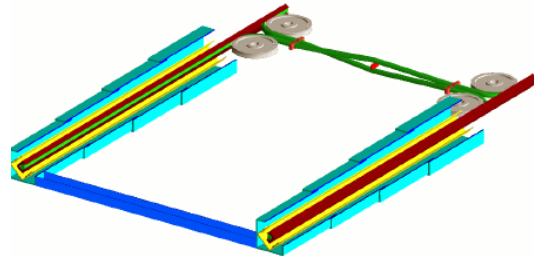


Figure 1.14: Cable supported telescopic longitudinal structure [18]

Witteman and Kriens [104] further proposed relatively stiff U-tubes structures with sliders under the main floor panel and an active brake system was introduced to control the movements of the U-tubes. The proposed structure was implemented to replace the longitudinal rails for enhanced energy absorption. The analyses under offset and oblique impacts revealed that the proposed system could help reduce vehicle peak deceleration by regulating hydraulic pressure in the brake system [18,121]. The study, however, did not explore various design issues such as the effect of movable longitudinal rails on loads transmitted to different fixation points with the underbody assembly of the vehicle structure. Beek [103] further proposed replacing the longitudinal rails by three controllable interconnected members together with integrated shock absorbers integrated within the mid-layer member. The results obtained under three different speeds (32, 56 and 64 km/h) revealed lower peak decelerations. Pipkorn and Håland [122] compared the behaviors of two different pressurized tubes, one with a telescopic shape and the other with a constant-diameter tube, under frontal impacts. The study showed that the telescopic structure could absorb the same amount of impact energy with reduced peak force and increased crush distance. It was further concluded that the impact energy

capacity and the endurance limit of the tube could be enhanced by increasing the inside pressure.

Active structural strengthening technology has been proposed to adjust the dynamic behavior of structural members and consequently prevent initiation of bending modes under impact loads, which would increase absorption capability while attaining stronger and lighter structure [128-128]. Deshmukh and McKinley [123] demonstrated that inclusion of piezo-ceramic actuators (PZT) could increase load-bearing capability by a factor of 5.6. PZT actuators can be used in the locations of the anticipated bending of primary load carrying members to increase load-bearing capability during impact loads [123-128], while the identification of optimal locations would be a challenging task.

Add-on Energy Dissipation Systems

Energy dissipators within the frontal structure could help dissipate a portion of the impact energy to minimize both the total vehicle deformation and peak occupant deceleration. A number of studies have investigated the performance potentials of add-on energy dissipation devices with either fixed or variable damping characteristics. The concept of adaptive impact absorbers (AIA) evolved from oleo-pneumatic struts employed in landing gears and emergency landing applications together with a controller so as to change structure characteristics to minimize the transmission of impact loads to the primary structure using minimal activation power [83,126-128]. Bielecki et al. [129,129] and Holnicki [126] investigated the effectiveness of a conceptual adaptive car bumper equipped with energy dissipators (structural fuses) under 35 km/h frontal impact for a 1100 kg vehicle. The proposed absorbers comprised dampers controlled by electro-magnetic or piezo-magnetic valves that were activated prior to the crash event. The

studies, however, did not explore the buckling of the structural fuses or the active truss members on the overall structure performance and the effect of high impact speed on the structural fuses.

Shock absorbers with variable orifice openings are currently used as standard equipments in rail cranes and rail bumpers to reduce the impact energy and minimize the bumper end force and deceleration at low impact speeds up to 12 km/h [131]. Different studies investigated the applicability of shock absorbers in different arrangements with vehicle structure to reduce the effect of impact. Jawad [37] concluded that extended shock absorbers with relative lower damping factors could reduce vehicle deformation significantly with slight increase in peak deceleration in vehicle-to-vehicle frontal impacts at low- and mid-speeds (32-64 km/h). It was further suggested that the adaptability of impact absorbers could be achieved by controlling the orifice size opening in the dampers. Owing to the limited available space, Wang [85] proposed an extendable/retractable-bumper system equipped with electrical motor actuators with self-locking mechanisms to reduce the impact energy by 10%. It was concluded that an extendable bumper could help reduce peak vehicle deceleration by 9%. The study used short-range radar sensors for actuators' activation before the crash. Elmarakbi and Zu [4036,40] investigated the effect of an extendable shock absorber in full frontal/offset impacts at a 48 km/h impact speed in vehicle-to-barrier and vehicle-to-vehicle impacts for enhancement of crashworthiness of vehicles. These studies employed a lumped-parameter vehicle model that was solved using an incremental harmonic balance method (IHBM) and the results demonstrated that dampers with either integrated or extendable mechanisms offer merits in reducing both the occupant peak deceleration and vehicle

deformation. The studies also investigated the performance potentials of shock absorbers with fixed damping characteristics in vehicle-to-vehicle frontal impacts with incompatible mass and stiffness properties, and concluded that only slight reductions in the vehicle deformation and occupant deceleration could be attained [84].

A few recent studies have investigated the applications of magneto-rheological (MR) fluids for impact energy absorption because of their high dynamic range, fast response and ability to react in a rapid and reversible manner to external stimuli [132-136]. Woo et al. [90] proposed extendable MR fluid bellows to be integrated within the frontal vehicle structure to provide semi-actively controlled damping during the three intervals of an optimal pulse (Figure 1.15). The performance potential of the proposed concept was evaluated using a five-DOF lumped parameter model (Figure 1.16) subject to a barrier impact in the 25 to 60 km/h range. The results suggested considerable reduction in vehicle deformation, occupant deceleration and crash severity index (CSI) over the entire range of impact speeds considered. Such a concept, however, would require further investigation on the required deployable length to achieve energy dissipation by the MR damper. A MR damper encased between two blocks of honeycomb crush elements was proposed to enhance crash energy management by Browne et al. [9,114]. The study evaluated the energy absorption through experiments under impacts up to 36 km/h speed and concluded that the effect of the magnetic field intensity on the energy absorption was very small at high speeds. It was suggested that the MR fluid dampers could be effective under high impact speeds. Kim et al. [132] investigated the applicability of active impact absorbers in gun recoil mechanisms to sustain high impact loads over a very short response time using a fuzzy control algorithm to realize control of

fluid flow rate in the absorber. The study showed a slight improvement in the recoil displacement, while the power demand of active hydraulic system was very high, in the order of 427 HP.

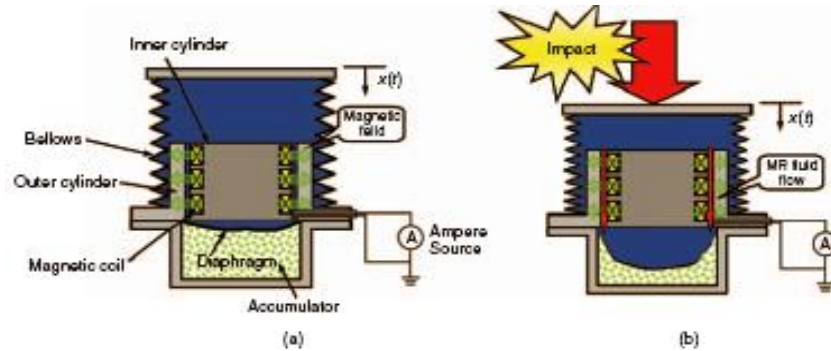


Figure 1.15: Schematic drawing of the proposed Magneto-Rheological (MR) impact bellows damper (a) before impact (b) after impact [90]

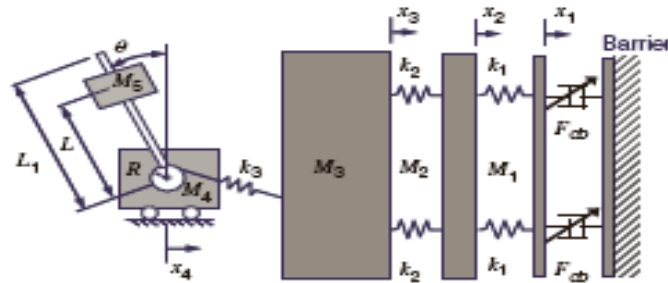


Figure 1.16: Five-DOF LMS mathematical model with the driver [90]

Active Safety Devices:

The active safety devices for enhanced crash energy management refer to mechanisms designed for accident prevention or as pre-crash avoidance systems, or stability control and anti-skid braking system, or for reducing the effects of a crash such as an airbag. An extendable energy absorber supported by a rapidly inflatable device can also be considered as an active safety device since it can reduce the severity of impact loads transmitted to vehicle structure by dissipating or absorbing a portion of the energy induced due to the impact [139,140]. A few studies have proposed concepts in extendable airbag systems to be integrated within the front end structure. The first trial was

conducted under a project named Research Safety Vehicles (RSVs), sponsored by NHTSA in the 1970's, to design and build vehicles capable of withstanding large magnitude of impact forces. This study used a two-chamber airbag in the bumper that was designed to inflate prior to a potential crash ahead of a vehicle in anticipation of impact [110,139]. The proposed airbag bumper absorbed about 19% of the impact energy under a 48 km/h frontal impact.

The use of an airbag bumper, however, necessitates developments in detection methods and sensors for detecting onset of a potential crash and mechanisms for rapid inflation of the airbags. An extendable active energy absorber is also required to satisfy three primary simple packaging principles (SPP) relevant to occupant's protection, as proposed by De Haven [140]. These include the abilities of the device to withstand and resist expected impact forces and transmit the impact loads to the primary load path, while the absorber must be deployed only in case of an impact, and the airbag must be shielded by stiffer shell to protect the bag and distribute the impact forces. The energy absorption potentials and packaging features of an inflatable airbag have been investigated in light and heavy rail crashes under different impact scenarios such as rail-to-road vehicle crashes [142]. The effectiveness of the SPP principle has also been investigated for a rotorcraft crash test, under a project referred to as: Rotorcraft External Airbag Protection System (REAPS). The REAPS comprised an adaptive external airbag inflating systems for emergency landing to avoid direct collision with the ground at a speed of 36 km/h [143]. Lee et al. [81], Wang [85] and Lee [19] proposed a new conceptual design of an inflatable bumper called the 'I-Bumper Concept', which

comprised external airbags (Figure 1.17) and a lattice structure (Figures 1.18) and a locking mechanism to be deployed before an impact.

The simulation results obtained for a three-DOF vehicle model showed 40% reduction in peak vehicle deceleration. The study used longitudinal rails filled with a granular material to enhance their energy absorption property and implemented TNT (Trinitrotoluene) explosives to realize rapid deployment of the bumper assembly with controlled discharge rate. The practical implementation of such an inflatable bumper would be highly questionable, considering the use of explosives. The reported studies on add-on energy absorber whether passive or active, suggest that such absorbers cannot meet the requirements of target deceleration pulses under impacts at different speeds [37,145]. This is partly attributed to the limited energy absorption properties of structural members of the compact energy absorbers [85]. Furthermore, integration of such elements into vehicle frontal substructure may require various modifications and strengthening of the load carrying members that may violate some of the specifications defined by the original equipment manufacturer (OEM) [63].

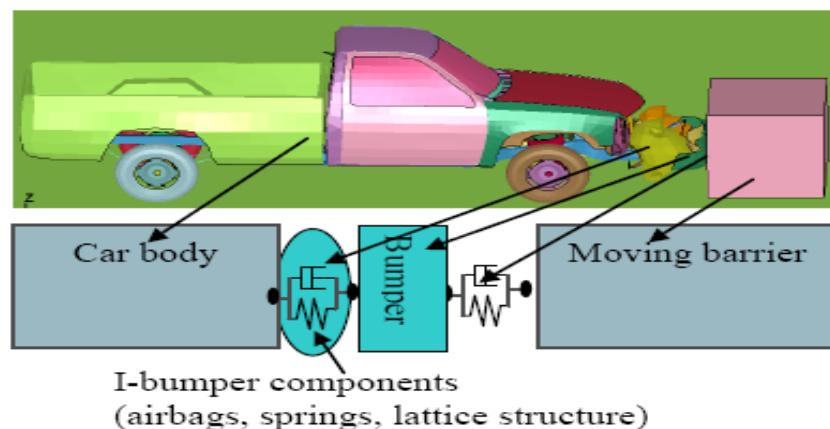


Figure 1.17: Three-DOF LMS model of the vehicle with an inflated bumper [19]



Figure 1.18: A pictorial view (left) and schematics (right) of expandable lattice structure: (a) U-shaped thin walled members; and (b) rectangular jagged members [19]

1.3 Scope and Objectives of the Present Study

The review of the literature suggests that effective crash energy management approaches are desirable to ensure occupant safety in a crash event. Furthermore, the management of crash energy of a vehicle through structure modifications is a highly challenging task for the vehicle designers. This in-part can be attributed to the contribution of different design and operational factors to the distribution of the crash energy. From the review of literature, it is also evident that the crash energy management of vehicle structures has been attempted using three approaches, namely: (i) modifications of the vehicle structures by introducing new load paths and enhancement of the stiffness; (ii) designs of add-on energy dissipators and absorbers (crush elements); and (iii) conceptual design of adaptable add-on EAs controlled in a semi-active or active manner. The effectiveness of these approaches and proposed concepts however have not been thoroughly evaluated in terms of their benefits or limitations in occupant protection. Whereas the concepts in extendable energy absorbers appear to be quite promising, additional efforts are needed to assess their absorption and dissipation properties.

The growing demands for light weight vehicles with enhanced fuel efficiency together with reduced frontal area for improved aerodynamic performance have caused greater concerns related to their crashworthiness apart from the additional constraints on

the structural design. There exists a need to explore alternative crash energy management approaches to ensure occupant safety in a crash event. Furthermore, a given structural design cannot provide effective energy management under different crash loads arising from different impact speeds and impact conditions. Further analyses of adaptive add-on absorbers are thus meritorious for designs of effective crash energy management systems. Such absorbers can dissipate a portion of the impact energy and reduce the impact loads imposed to the occupant, while reducing the degree of occupant compartment intrusion. The design of an adaptive absorber, however, poses most significant challenges involving identification of design parameters and their ranges to achieve optimal crash energy management under a wide range of impact speeds. Furthermore, the assessment of concepts in CEM systems requires evaluation of both the occupant injury criterion and vehicle deformation.

The primary objective of the dissertation research is formulated to undertake systematic investigations on optimal crash energy management through comprehensive analyses of concepts in adaptable add-on energy absorbers. The specific objectives are briefly described below:

- Evaluate energy absorption effectiveness of passive add-on energy absorbing elements using a one-dimensional lumped-parameter model of the vehicle-occupant system subject to frontal impact; and investigate influences of absorber parameters on structural deformation and occupant HIC.
- Perform analyses of different concepts in add-on energy absorbers with variable stiffness and damping characteristics to seek effective crash energy management under impacts at different speeds, while ensuring minimal influence on the structure stiffness during normal operating conditions.
- Evaluate energy absorption potentials of adaptive energy absorbers using the lumped parameter vehicle-occupant model and seek solutions for a multi-parameter

optimization problem to achieve acceptable compromise in occupant HIC and peak vehicle deformation over a range of impact speeds.

- Investigate performance potentials of adaptive add-on energy absorbers in conjunction with a detailed nonlinear model of a full scale automobile using a scaling technique based on the mass ratio.
- Investigate performance potentials of the energy absorber in conjunction with elasto-plastic finite element model of an automobile, and examine validity of the model on the basis of the available crash data.
- Formulate and solve optimizations problem using a surrogate model to define an optimal set of design variables of the adaptive absorbers identified from the simple lumped-parameter model.

1.4 Thesis Organization

This thesis consists of six chapters. The present chapter (Chapter 1) provides a literature review of the most recent research that is closely related to the field of study, together with problem formulation and objectives of the study. In Chapter 2, a lumped-mass vehicle model is used for the analysis of energy absorption potentials of passive hydraulic dampers in extendable and integrated arrangements under a rigid barrier impact. Different configurations of add-on energy absorbers/dissipators are presented and investigated to attain lower occupant HIC and total vehicle deformation. Sensitivity analyses are conducted to determine desirable optimal design variables for the proposed configurations through simulations.

Chapter 3 presents the formulations of optimization problem for the proposed model and explores solutions using different optimization techniques. Single- and multi-objective optimization functions are defined and solved to configure Pareto Frontier curves that provide the designer with the add-on energy absorber. In addition, Anti-Pareto

front (APF) is obtained to give the designer an overall picture of a set of design variables to be avoided.

Chapter 4 conducts the application of the proposed CEM system to a large-scaled detailed lumped-parameter vehicle model to investigate the effects of the proposed CEM system using a detailed elasto-plastic vehicle model. This chapter is also used to validate the implementation of the proposed system on different vehicles with varying masses by applying scaling techniques. Sensitivity analyses are conducted to investigate stability of the system over relatively small variations in design variables.

Chapter 5 investigates the performance potentials of the proposed CEM system using a comprehensive FE model of a small passenger car. The validity of the FE model demonstrated on the basis of available crash data. The performance characteristics of the add-on absorber are evaluated and an optimal design is identified through optimization using response surface method and metamodel based iteration approach.

Finally, the major conclusions, the most significant outcomes and contributions and suggestions for the future works are briefly described in Chapter 6.

CHAPTER 2

ANALYSIS OF ADD-ON ENERGY ABSORBERS CONCEPTS

2.1 Introduction

The management of crash energy in vehicles has been mostly explored through enhancement of load paths and the structure [18,21,62]. Add-on energy absorbers offer considerable potential in managing the crash energy due to frontal impacts by dissipating/absorbing a portion of the total energy. A few studies have investigated the energy absorption properties of either fixed or adaptable add-on energy absorbers in frontal impacts under selected ranges of impact speeds [36,61,85,112]. These have invariably concluded that design requirements of energy absorbers vary considerably with the impact speed, while the analyses have been generally limited to peak deceleration of the vehicle body or the occupant mass [27,36,47,146]. It has also been shown that the design of an energy absorber to satisfy a given target deceleration pulse over a range of impact speeds is extremely complex.

Reported studies have employed different vehicle models, ranging from simple single-DOF model to elaborate FE models to evaluate the energy absorption properties of the add-on energy absorbers [40-145,144,145]. Simple lumped parameter models of occupant-vehicle system, however, could be conveniently applied to assess relative performance potentials of absorbers in a highly efficient manner [36,37]. Such models could also permit relative analyses in terms of most relevant measures such as occupant injury criteria and intrusion of the occupant compartment, and help identify optimal design parameters in an efficient manner.

In this chapter, different concepts in add-on energy absorbers are considered and described by nonlinear lumped-parameter models. A two-DOF baseline vehicle model integrating a single-DOF representation of the occupant and the restraint system is formulated to study the response characteristics of add-on energy absorbers in terms of potential occupant injury risk and vehicle body deformation. The occupant-seat interactions during a crash event are also described by a model integrating visco-elastic properties of the seat cushion together with the restraint system. The vehicle-absorber models are subsequently analyzed under different impact speeds. A comprehensive parametric study is conducted to identify desirable parameters and configuration of the add-on energy absorbers on the basis of different measures such as peak occupant deceleration, peak intrusion, head injury criteria (HIC) and error relative to a target deceleration pulse.

2.2 Crash Energy Management through Add-on Energy Absorbers

The crashworthiness of a vehicle relates its ability to manage the crash energy associated with an impact through controlled vehicle deformations or via distribution of crash energy among the load paths, while maintaining adequate interior space for the occupant. The residual crash energy is further managed by the restraint system to minimize the crash load transfer to the vehicle occupants. The designs of crash energy management systems are obtained using a number of generally accepted fundamental design principles and goals [3,18,96]. These are briefly summarized below:

- (a) *Sufficient Occupant Protection Performance*: A number of studies have identified a family of optimal crash pulses or vehicle crash signatures that satisfy specific injury criteria and thus ensure sufficient occupant protection in the event of a crash [18,96-102]. Although, a general agreement on the desired deceleration pulse is not evident,

it has been shown that a crash deceleration pulse with an initial peak in time followed by a gradual decay would be more beneficial for protection of a restrained occupant. This is mostly attributed to delay between the vehicle body and the occupant response [18,96,97]. The proposed deceleration pulses can thus be used to define objective criteria for the CEM system, including the add-on energy absorbers.

- (b) *Stiff Cage Structural Concept*: Vehicle structures must be designed to provide protection for the occupants in all modes of survivable collisions with minimal intrusion [3,147]. This implies a design principle for the occupant passenger compartment that must withstand the peak impact load and support the energy absorbing members without exhibiting excessive deformation or intrusion.
- (c) *Controlled Progressive Crush with Limited Intrusion*: During a collision, the vehicle structure may undergo two main structural collapse modes, the bending and the axial modes, or a combination of the two. The axial collapse mode is most efficient in managing or absorbing the crash energy. The front/rear substructures of vehicles are thus designed with primary and secondary crush zones, with the primary crush zone being relatively soft to yield uniform and progressive structural normal collapse [18,27,49]. The secondary crush zone is designed to yield additional progressive energy absorption structure and distribution of the impact energy.
- (d) *Weight Efficient Energy Absorbing Structures*: Vehicle structural topology or the architecture of the structural frame must be realized in conjunction with the packaging constraints. Selection of a topology would depend on the energy absorption ability of the primary crush zones during the crash event. The design loads of different structural members (energy absorbers and support frames) are subsequently determined on the basis of the baseline structure design, while the total structure weight must be constrained.

Apart from the above principles, the following are the additional design requirements of an effective system that would permit uniform energy absorption in a progressive manner:

- In case of a full frontal impact with a rigid barrier, the vehicle structure stiffness should be proportional to both the vehicle weight and the impact speed to achieve

the required energy absorption capability, while reducing both the vehicle deformation and the peak deceleration [18,112].

- In case of an offset impact with a rigid barrier with offset ratio less than 70%, the affected longitudinal rail must have double its original stiffness to absorb the impact energy and prevent excessive compartment intrusion [18,36,121]. In case of an oblique impact with angle of attack in the -30° to $+30^\circ$ range, the structure is required to absorb impact energy with limited yaw rotation of the vehicle [18].
- In case of a vehicle-to-vehicle frontal impact or an impact with a deformable barrier, the vehicle structure is required to possess variable energy absorption capability depending on its compatibility with the mating vehicle. This could reduce the severity risk for the occupant of the lighter vehicle. Furthermore, in case of a vehicle-to-vehicle offset impact, the loaded longitudinal rail should exhibit variable stiffness to prevent occurrence of large magnitude deceleration, which could reach 2.5 times the designed deceleration limits [18].

The above design requirements are quite difficult to realize with structures and energy absorbers with fixed parameters. A crash energy management (CEM) system with variable stiffness, where the desired variation in structural stiffness could be achieved prior to a collision using active control mechanisms and crash detection devices, would be highly desirable.

A CEM system is generally composed of one or more energy absorbing elements or techniques that depend upon a number of factors such as the degree of protection to be achieved, impact conditions and design goals. An add-on energy absorber forms an integral part of a CEM system to provide dissipation and absorption of impact energy via

energy dissipative and restoring elements. Furthermore, these devices would yield only minimal effect on the total structural stiffness specified by the OEM during normal modes of operation. Several studies have implemented and investigated the usage of shock absorbers as add-on EA systems using different arrangements such as integrated or extendable hydraulic dampers to enhance crashworthiness in frontal impact situations [37,40-42,65,85]. The design of such absorbers involves two primary challenges: (i) generation of sufficient damping force to maximize the energy dissipation; and (ii) packaging space to ensure sufficient stroke of the absorber. Moreover, the design involves a satisfactory compromise between the two contradicting design criteria associated with minimal total vehicle deformation and peak occupant deceleration below the occupant endurance limit. Apart from the above, different crash situations require different structural stiffness and crash energy management. In particular, structures with variable stiffness are required to attain effective crash energy management at different frontal impact speeds.

Considering that the kinetic energy increases with the square of the impact speed, the total energy absorption property of the absorbers needs to be varied with the impact speed, which is related to deformations of the load carrying members and the impact force that directly relates to the peak deceleration. This implies that the deformation or intrusion can be limited with increase in the impact force and thus the average vehicle deceleration. A reduction in the deceleration can be achieved with greater vehicle deformation that can cause physical injuries to the occupant. Adaptive structures and absorbers with variable properties are thus desirable to ensure occupant protection over the range of impact speeds [1,2,20-22]. Figure 2.1 illustrates relationships among the

input energy, deformation, impact force and speed [18], which clearly shows conflicting variations in the force and deformation. The figure also illustrates the influences of vehicle mass and structural stiffness.

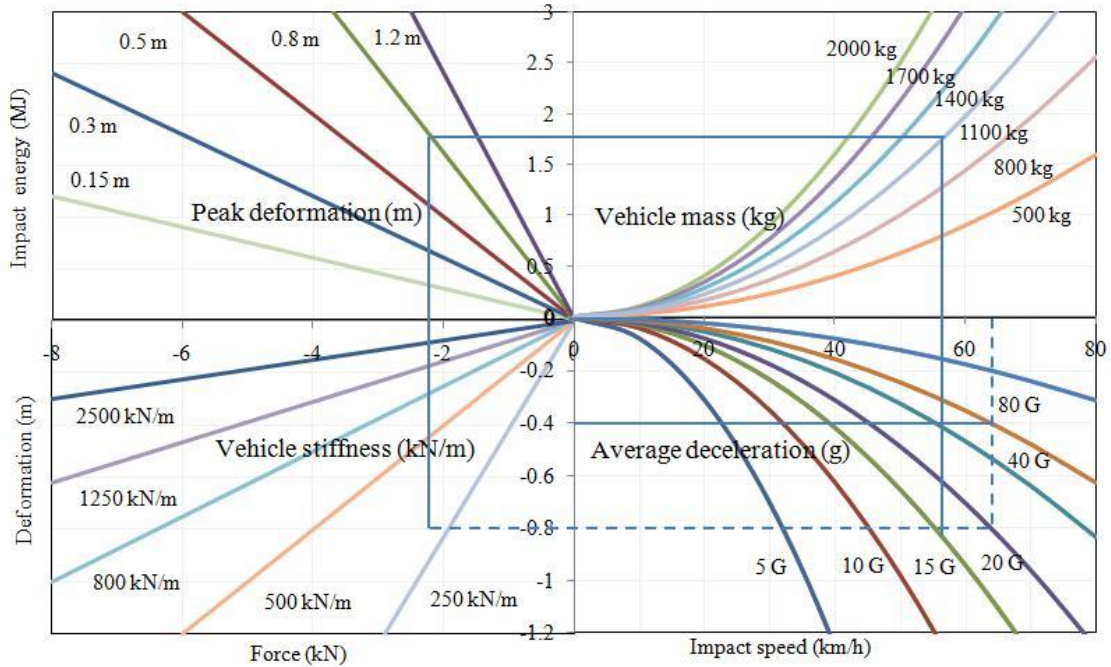


Figure 2.1: Relationships among different measures of vehicle crash dynamic responses [18].

2.2.1 Recent Trends of Variable Damping and Stiffness

As mentioned in chapter 1, variable energy absorption capabilities of vehicle structures at different impact conditions are desirable for enhanced crashworthiness in frontal impacts. A number of variable stiffness controllable dampers concepts have been proposed for vibration control, including the semiactive or active control systems [64,147-150]. Controllable MR fluid dampers have also been proposed to achieve higher equivalent stiffness up to four times the nominal value, while providing significant variation in the damping characteristics [64,148,149]. Such devices are represented by a Voigt element with continuous variable characteristics (VECVC). These studies

concluded that the equivalent stiffness variation could be achieved by changing the damping ratio of the Voigt element in extended position, while maintaining low stiffness ratio. The equivalent damping could be varied by varying the damping ratio of the integrated damper [148]. These studies have demonstrated improved vibration transmissibility of both the base- and forced-excited systems through using semi-active control. The equivalent variable stiffness, however, is always lower than or equal to the nominal stiffness suggesting that such a device cannot be applied to achieve increase in structural stiffness. Alternatively, hydro-pneumatic devices with different controllers have been proposed to achieve continuous variations in both the stiffness and damping characteristics by varying the internal pressure and/or orifice opening [150]. Such variable stiffness and damping devices could also be applied as add-on energy absorbers for effective crash energy management.

2.2.2 Variable Damping/Stiffness Concept Implemented into Vehicle Crash Analysis

The implementation of a variable parameter energy absorber in crash energy management would require relatively lower stiffness of the structure. A relatively high damping coefficient of the Voigt element may be essential to attain total stiffness equal to the structure stiffness during normal operations. Consequently, alternative design methodologies need to be investigated to increase the original structural stiffness during collisions that could be achieved by activating the Voigt element used in an extendable position prior to the crash event as [37,85]. In order to implement the concepts mentioned in the previous subsection, various design postulations have to be thoroughly investigated to satisfy the required variations of the original structural stiffness. Additional shock

absorber/Voigt elements, connected in integrated position, are investigated to support vehicle structure during impact and increase the energy absorption capability. Moreover, wide ranges of damping ratio are investigated to utilize the merit of the extendable part to absorb a significant portion of impact energy before reaching the main load carrying members of vehicle structure.

Variable stiffness and damping elements, represented by Voigt elements, can be implemented in integrated position only without a need of extendable part to vary its equivalent stiffness and work as energy dissipaters. However, this may not afford the same degree of crashworthiness enhancement that a model with extendable absorbing/dissipation system can offer since it does not have the sequential dissipation effect. In the following section, different concepts in variable stiffness and damping elements, represented by different Voigt elements arrangements are considered to investigate their contribution of enhancing crashworthiness.

2.3 Development of Vehicle Models with Add-on Energy Absorbers /Dissipators

The energy absorption/dissipation potentials of the add-on energy absorbers can be effectively evaluated using simple two-dimensional lumped-parameter models of the vehicle-occupant system. The add-on energy absorbers are characterized by their linear and nonlinear stiffness and damping characteristics and integrated to the vehicle model for analyses under frontal impacts at different speeds. The baseline model, proposed by Elmarakbi and Zu [36,40-36] is initially reformulated and subsequently enhanced to investigate the absorption/dissipation properties of alternate concepts in nonlinear add-on absorbers.

2.3.1 Baseline Model

Figure 2.2 illustrates the baseline vehicle model integrating occupant-restraint, as proposed by Elmarakbi [36]. In the model, the vehicle structure is represented by a rigid mass m_v coupled to the bumper through structure stiffness represented by a linear and a nonlinear springs, k_L and k_{NL} . Henceforth, this baseline model will be denoted as ‘BL model’. The occupant is represented by a rigid mass m_o , while the occupant restraint system is characterized by linearly varying stiffness and damping properties with a slack. The restraint system is engaged only when the occupant movement relative to the vehicle exceeds the initial occupant slack in the restraint system. Figure 2.3 illustrates the force-deflection and force-velocity characteristics of the restraint system. The dead zone in the force-deflection curve corresponds to the available slack δ_{oc} .

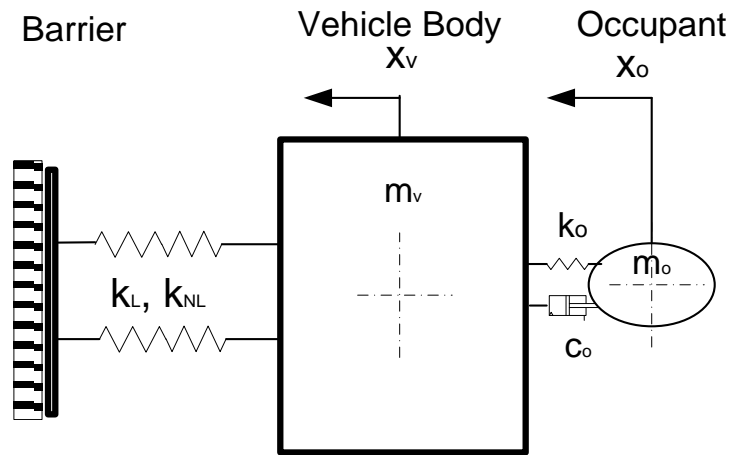


Figure 2.2: Two-DOF baseline model of the vehicle and occupant subject to full frontal impact [36]

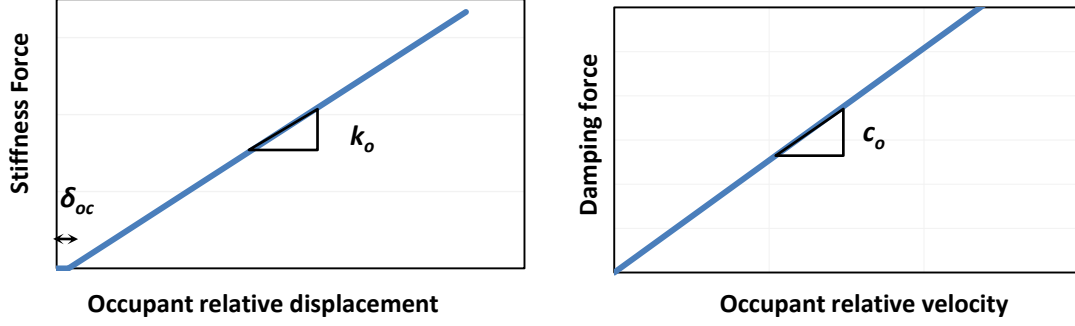


Figure 2.3: (a) Force-deformation; and (b) force-velocity curves of the restraint system [36]

The differential equations describing the motions of the vehicle and the occupant masses during the primary and secondary impact stages are described considering a full frontal impact characterized by the initial impact velocity:

$$m_v \ddot{x}_v + F_{str} - F_{rest} = 0 \quad (2.1)$$

$$m_o \ddot{x}_o + F_{rest} = 0 \quad (2.2)$$

where F_{str} and F_{rest} are the forces developed due to structural deformation and restraint system, respectively. x_v and x_o define the displacements of m_v and m_o , respectively. The vehicle structure is assumed to exhibit nonlinear stiffness properties with negligible damping such that:

$$F_{str} = k_L x_v + k_{NL} x_v^3 \quad (2.3)$$

where k_L and k_{NL} are the linear and nonlinear stiffness coefficients. The force developed by the restraint system is derived upon considering the slack in the restraint, and linear stiffness and damping characteristics such that:

$$F_{rest} = \begin{cases} k_o (x_o - x_v - \delta_{oc}) + c_o (\dot{x}_o - \dot{x}_v) & \text{for } (x_o - x_v) \geq \delta_{oc} \\ 0 & \text{for } (x_o - x_v) < \delta_{oc} \end{cases} \quad (2.4)$$

where, k_{oi} and c_{oi} are the linear stiffness and damping coefficients of the restraint system, respectively, and δ_{oc} is the slack clearance in the restraint system. The solutions of Eqns. (2.1) and (2.2) would yield responses to a full frontal barrier impact in terms of peak occupant deceleration \ddot{x}_o , intrusion $(x_v - x_o)$ and energy absorption.

2.3.2 Vehicle Model with Integrated Energy Dissipator

Apart from the energy absorption characteristics of the vehicle structure, as in the case of the baseline model, energy dissipative elements may also be integrated to enhance the crash energy management. The energy dissipation could be realized by integrating dampers as proposed in [36,40-36] or structural materials with enhanced damping properties. Figure 2.4 illustrates the vehicle model with nonlinear energy dissipating elements in integrated position, henceforth will be called as '*ID model*'. While the equation of motion of the occupant mass is identical to Eqn. (2.2), the equation of motion of the vehicle mass subject to frontal barrier impact is written as:

$$m_v \ddot{x}_v + F_{str} - F_{rest} + F_{d-p} = 0 \quad (2.5)$$

where F_{d-p} is the nonlinear damping force due to the dissipative element that is assumed to follow linear and cubic relations with the velocity. The hydraulic dampers would encounter interactions with the bump stop, particularly under severe impact [151,152]. The bump-stop stiffness is characterized by piece-wise linear stiffness constants as shown in Figure 2.5. The total force developed by the dissipative elements can be expressed as:

$$F_{d-p} = \begin{cases} c_{IL} \dot{x}_v + c_{INL} \dot{x}_v^3 & \text{for } x_v < \delta_{oi} \\ c_{IL} \dot{x}_v + c_{INL} \dot{x}_v^3 + k_{r1}^i (x_v - \delta_{oi}) & \text{for } \delta_{oi} \leq x_v < \delta_{li} \\ c_{IL} \dot{x}_v + c_{INL} \dot{x}_v^3 + k_{r1}^i (\delta_{li} - \delta_{oi}) + k_{r2}^i (x_v - \delta_{li}) & \text{for } \delta_{li} < x_v \leq \Delta_{i_limit} \end{cases} \quad (2.6)$$

where c_{1L} and c_{1NL} are the linear and nonlinear damping coefficients, respectively, Δ_{i_limit} is the total permissible travel of the integrated damper, δ_{0i} is the available damper travel prior elastic bump contact, k_{r1}^i is the stiffness constant of the elastic stop under low level deformations ($x_v < \delta_{1i}$) and ($k_{r2}^i > k_{r1}^i$) is the stiffness constant under higher deformations ($x_v > \delta_{1i}$).

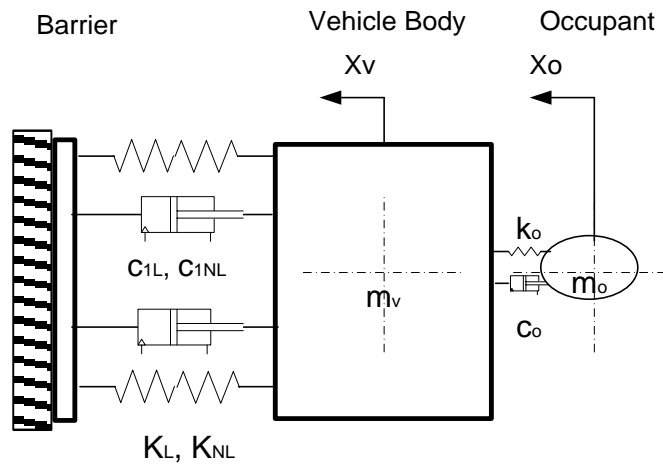


Figure 2.4: Two-DOF model of the vehicle-occupant system with integrated energy dissipative components (ID model)

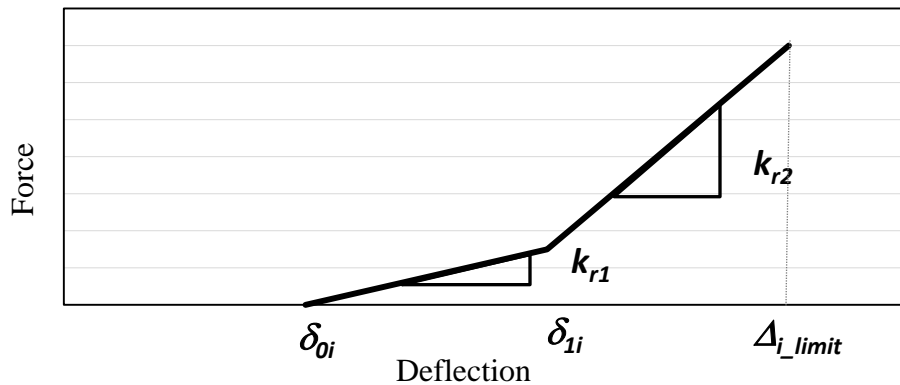


Figure 2.5: Piecewise-linear representation of the rubber bump-stop spring

The solutions of Eqns. (2.2) and (2.5) would yield the crash response properties of the vehicle structure with integrated nonlinear energy dissipating elements.

2.3.3 Vehicle Model with Extended Energy Dissipators

The energy dissipation potential of an integrated energy dissipator (Figure 2.4) is generally limited due to limited travel. A concept in extendable dampers was proposed to realize sufficient damper stroke and thus sufficiently large damping forces and energy dissipators [37,37-42]. The extended damper concept, however, would require a crash detection system and a rapid deployment mechanism. Figure 2.6 illustrates the baseline vehicle-occupant model coupled with extended dampers beyond the front structure, referred to as '*ED model*'. The equations of motion for the vehicle and the bumper masses are given below, while that for the occupant mass is identical to that described in Eqn. (2.2).

$$m_v \ddot{x}_v + F_{str} - F_{rest} = 0 \quad (2.7)$$

$$m_b \ddot{x}_b - F_{str} + F_{d_ext} = 0 \quad (2.8)$$

$$F_{str} = k_L (x_v - x_b) + k_{NL} (x_v - x_b)^3 \quad (2.9)$$

where m_b is the bumper mass and F_{d_s} is the damping force developed by the extended dampers. Assuming that the damping force is related to linear and cubic velocity, F_{d_s} is formulated as:

$$F_{d_s} = \begin{cases} c_{2L} \dot{x}_b + c_{2NL} \dot{x}_b^3 & \text{for } x_b < \delta_{0e} \\ c_{2L} \dot{x}_b + c_{2NL} \dot{x}_b^3 + k_{r1}^e (x_b - \delta_{0e}) & \text{for } \delta_{0e} \leq x_b \leq \delta_{1e} \\ c_{2L} \dot{x}_b + c_{2NL} \dot{x}_b^3 + k_{r1}^e (\delta_{1e} - \delta_{0e}) + k_{r2}^e (x_b - \delta_{1e}) & \text{for } \delta_{1e} < x_b \leq \Delta_{e_limit} \end{cases} \quad (2.10)$$

where c_{2L} , and c_{2NL} are the linear and cubic terms of the damping force; respectively, with inclusion of the rubber modeled as a piecewise linear stiffness elements with coefficients k_{r1}^e and k_{r2}^e , Δ_{e_limit} is the total extended damper travel, δ_{0e} is the available damper travel before contact with the elastic bump. It should be mentioned that the damping

coefficients in both the *ID* and *ED* models are assigned to be equal to the nominal values of linear and nonlinear damping constant for both arrangements, proposed by Elmarakbi [36].

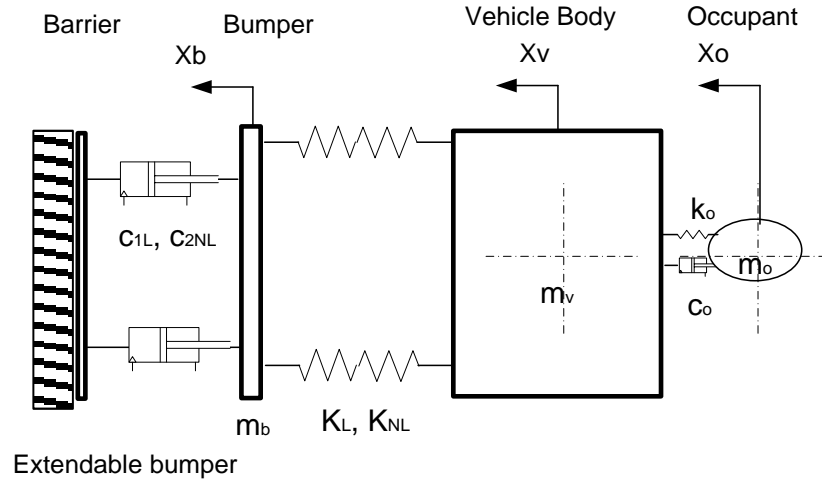


Figure 2.6: Vehicle-occupant model with energy dissipators in extended position (ED model)

2.3.4 Vehicle Model with Extendable-Integrated Dual Voigt absorbers (EIDV)

Apart from the extendable energy absorbing structure, the integrated damped structures may be employed to increase the energy absorption of the add-on elements. This is described by a Voigt element replacing the integrated dampers in the vehicle-occupant model, as shown in Figure 2.7. Both the integrated and extendable Voigt structures could provide enhanced stiffness for the vehicle structure and help in limiting the vehicle deformation and the occupant deceleration. The equations of motion for the vehicle and bumper masses of the model, denoted as ‘EIDV’, under a full frontal impact are given below, while that for the occupant mass is identical to that described in Eqn. (2.2).

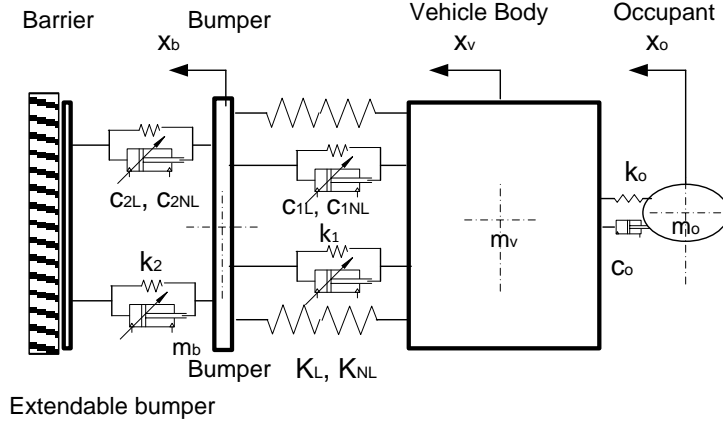


Figure 2.7: Three-DOF model of the occupant-vehicle system in extendable-integrated Voigt elements (EIDV).

$$m_v \ddot{x}_v + F_{str} + F_{v_i} - F_{rest} = 0 \quad (2.11)$$

$$m_b \ddot{x}_b - F_{str} - F_{v_i} + F_{v_e} = 0 \quad (2.12)$$

where m_v and m_b are the vehicle and bumper masses, and F_{v_i} and F_{v_e} are the dissipation-absorption forces due to Voigt systems implemented in the integrated and extendable positions with the vehicle structure, respectively, expressed as:

$$F_{v_i} = k_1 \Delta x + c_{1L} \Delta \dot{x} + c_{1NL} \Delta \dot{x}^3 + F_{Stop_i} \quad (2.13)$$

$$F_{v_e} = k_2 x_b + c_{2L} \dot{x}_b + c_{2NL} \dot{x}_b^3 + F_{Stop_e} \quad (2.14)$$

where $\Delta x = x_v - x_b$ and $\Delta \dot{x} = \dot{x}_v - \dot{x}_b$, k_1 and k_2 are the linear stiffness constants of the integrated and extended elements, and c_{1L} , c_{1NL} , and c_{2L} , c_{2NL} are the linear and nonlinear damping coefficients of the integrated and extended Voigt structures, respectively. F_{stop_i} and F_{stop_e} are the forces due to elastic end stops in the integrated and extended Voigt elements, respectively, which are derived in a manner similar to that in Eqs (2.6) and (2.10), as:

$$F_{stop_i} = \begin{cases} 0 & \text{for } x_b < \delta_{0i} \\ k_{r1}^i (\Delta x - x_{0i}), & \text{for } \delta_{1i} \leq x_b < \delta_{0i} \\ k_{r1}^i (\Delta x - x_{0i}) + k_{r2}^i (\Delta x - \delta_{1i}) & \text{for } x_b \geq \delta_{1i} \end{cases} \quad (2.15)$$

$$F_{stop_e} = \begin{cases} 0 & \text{for } x_b < \delta_{0e} \\ k_{r1}^e (\Delta x - x_{0e}), & \text{for } \delta_{1e} \leq x_b < \delta_{0e} \\ k_{r1}^e (\Delta x - x_{0e}) + k_{r2}^e (\Delta x - \delta_{1e}) & \text{for } x_b \geq \delta_{1e} \end{cases} \quad (2.16)$$

where δ_{0i} and δ_{0e} are the available free travel of the integrated and extendable Voigt element, k_{r1}^i and k_{r1}^e are the linear stiffness constants of the elastic stops of the integrated and extended elements, respectively, corresponding to initial deformations ($x_b \leq \delta_{1i}$), similarly, k_{r2}^i and k_{r2}^e are the linear stiffness constants of the integrated and extendable Voigt elements, when displacements exceed δ_{1i} and δ_{1e} , respectively. The extendable bumper is allowed to extend to 0.4 m before the event of an impact.

Additionally, the stiffness and damping coefficients used in Eqns. (2.13) and (2.14) are defined as functions of their respective nominal values, such that:

$$k_1 = \lambda_1 k_{eqv}; \quad k_2 = \lambda_2 k_{eqv} \quad (2.17)$$

$$c_{1L} = \mu_1 d_L; \quad c_{1NL} = \mu_1 d_{NL} \quad (2.18)$$

$$c_{2L} = \mu_2 d_L; \quad c_{2NL} = \mu_2 d_{NL} \quad (2.19)$$

where μ_1 , μ_2 , λ_1 , and λ_2 are the damping and stiffness multiplication factors of the integrated and extended Voigt elements, respectively, d_L and d_{NL} are the nominal linear and nonlinear damping constants of the add-on elements, respectively, K_{eqv} defines the equivalent stiffness constant of the vehicle structure as the nominal value of the add-on energy absorbers. The resisting force resulting from structural deformation of the nonlinear stiffness is the same as defined in Eqn. (2.9).

It should be mentioned that the EIDV model is investigated for two design configurations: (i) restraining the upper limit of the damping factor μ_1 to a value of 2.0 coupled with relatively higher upper limit of the damping factor μ_2 with a value of 5.0, denoted as ‘Config₁’, (ii) relaxing the upper limit of the damping factor μ_1 to a higher value of 5.0 together with reducing the upper limit of the damping factor μ_2 to 1.5, denoted as ‘Config₂’. In both configurations, the stiffness factors λ_1 and λ_2 are restrained to the value of 0.3 and all the design variables are allowed to be varied with a 0.1 increment step.

2.3.5 Vehicle Model with Extendable Voigt and Integrated Energy Dissipators (EVIS)

Structures or damping elements extended beyond the bumper could yield improved crash energy management and effectively limit the vehicle body deformation and occupant deceleration. The extendable structure, characterized by Voigt elements with nonlinear stiffness and damping properties are thus considered to be employed in the vehicle model with integrated energy dissipators (Figure 2.8) to study their potential performance in view of crash energy management. While the equation of motion for the occupant mass remains the same, the equations of motion for the vehicle and the bumper masses are derived as:

$$m_v \ddot{x}_v + F_{str} + F_{d_in} - F_{rest} = 0 \quad (2.20)$$

$$m_b \ddot{x}_b - F_{str} - F_{d_p} + F_{v_e} = 0 \quad (2.21)$$

where F_{v_e} is the force developed by the extended Voigt elements given in Eqn. (2.14) and F_{d_p} is the force developed by the integrated damper given denoted in Eqn (2.22).

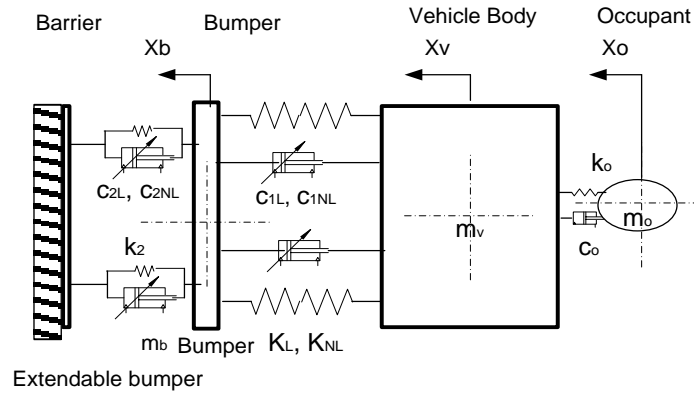
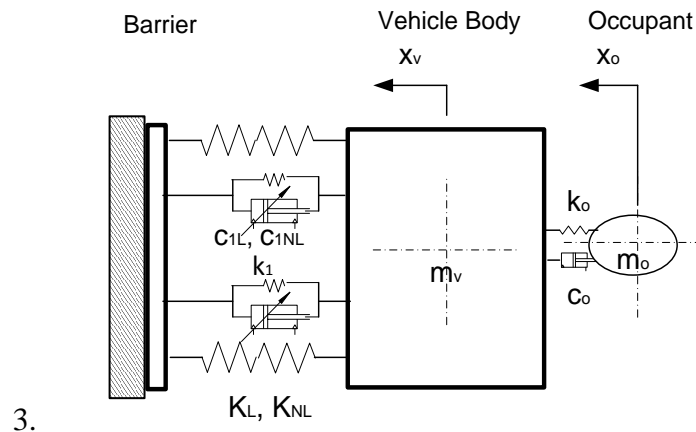


Figure 2.8: Three-DOF model of the occupant-vehicle system with extendable-Voigt elements and integrated shock absorber (EVIS)

$$F_{d-p} = \begin{cases} c_{1L}(\Delta\dot{x}) + c_{1NL}(\Delta\dot{x})^3 & \text{for } \Delta x < \delta_{0i} \\ c_{1L}(\Delta\dot{x}) + c_{1NL}(\Delta\dot{x})^3 + k_{r1}^i(\Delta x - \delta_{0i}) & \text{for } \delta_{0i} \leq \Delta x < \delta_{1i} \\ c_{1L}(\Delta\dot{x}) + c_{1NL}(\Delta\dot{x})^3 + k_{r1}^i(\Delta x - \delta_{0i}) + k_{r2}^i(\Delta x - \delta_{1i}) & \text{for } \delta_{1i} < \Delta x \leq \Delta_{i_limit} \end{cases} \quad (2.22)$$

2.3.6 Vehicle Model with Integrated Voigt Structure (IV)



4. Figure 2.9: Two-DOF model of the occupant-vehicle system in integrated Voigt element (IV model)

An occupant-vehicle systems model is also formulated with an integrated add-on absorber with sufficient damping property. The model, shown in Figure 2.9 and denoted as ‘IV’, illustrates the integrated add-on absorber as nonlinear Voigt elements. Such an add-on absorber would be considered more practical compared to the extendable

absorbers, and would yield enhanced structure stiffness. The equation of motion of the vehicle mass can be expressed as:

$$m_v \ddot{x}_v + F_{str} + F_{v_i} - F_{rest} = 0 \quad (2.23)$$

2.4 Methods of Analysis and Performance Measures

The equations of motion for the models, presented in section 2.3, are solved for full frontal impact at speeds ranging from 35 to 80 km/h, which are taken as the initial system velocities. The results are attained for different arrangements and properties of the add-on energy absorbers/dissipators so as to realize improved crash energy management. The stiffness and damping coefficients of the add-on elements are the primary design variables. The variations in design variables are realized by define scale factors that describe the variation about the nominal values of the linear and nonlinear damping and linear stiffness constants, defined in Eqns (2.17) to (2.19). The energy absorption/dissipation properties of different configurations of the add-elements are evaluated at different impact speeds.

The responses are compared with those of the baseline model to assess the performance potentials of various concepts. For this purpose, the responses are expressed by a number of crash injury related performance measures. Although a range of measures have been defined to assess the injury risk of a vehicle collision, very little agreement exists on a set of generally-accepted measures [18,36,61,85]. The reported measures, however, consistently associate various injury measures to occupant deceleration and occupant compartment intrusion. Dennis [110] suggested that the human occupant can withstand peak deceleration up to 40 g for 3 ms and onset rate up to $\dot{x}' \leq 1000$ (g/sec) without severe injury [11,80,110]. The effectiveness of the add-on energy absorbers are

assessed using a set of selected performance measures described in section 1.2.5.2. These are further summarized below:

Occupant Head Injury Criteria (HIC)

The head injury criteria (HIC) has been most widely used to assess severity and thus the injury risk of vehicle crashes. The HIC relates to acceleration of the occupant head over a continuous duration of 15 ms and is often denoted as HIC₁₅ [12,18,92,150], such that:

$$HIC_{15} = \left[\frac{1}{t_2 - t_1} \int_{t_1}^{t_2} a(t) dt \right]^{2.5} (t_2 - t_1) \quad (2.24)$$

where $a(t)$ is the head deceleration measured in g units and $(t_2 - t_1)$ defines the duration of the acceleration event, which is limited to 15 ms. The HIC₁₅ measure is thus computed over several 15 ms intervals within the acceleration-time history of the impact response. The current crash safety regulations state that the peak HIC₁₅ value over a continuous 15 ms interval should not exceed 1000 [3,73,153,154]. The European Union Road Federation (ERF) [89] has further defined an abbreviated injury index scale (AIS) as an exponential function of the HIC. The study proposed an AIS threshold of 1.5 for minimal injury that corresponds to HIC₁₅ of 350. It was found that AIS is exponentially proportional to the occupant HIC after the AIS threshold value [155].

Magnitude of specific vehicle deformation ‘ μ_d ’

The vehicle deformation, expressed by maximum dynamic crush of the frontal structure, has been greatly associated with the degree of occupant compartment intrusion [85,155]. The specific deformation magnitude is defined as the peak deformation, $(x_c)_{\max}$, normalized by the vehicle total length (L), such that :

$$\mu_d = \frac{(x_c)_{max}}{L} \quad (2.25)$$

where μ_d is the specific deformation magnitude that describes the degree of total crushing and it could be used as an indication of the degree of compartment intrusion. The frontal car structure should not be allowed to deform more than certain value, which is usually less than 0.7 m. A deformation beyond this value will cause an intrusion of the passenger compartment. In this study, since the overall length of the lumped-parameter model is unknown, the total deformation is used for measuring the compartment intrusion.

Normalized energy absorbed ' μ_E '

The performance potential of an add-on energy absorber may also be assessed by the total amount of energy absorbed. A normalized measure of the energy absorbed, depends on the ratio of the total absorbed energy and the total kinetic energy, has been proposed to evaluate effectiveness of the add-on EA systems. For the integrated and extendable add-on energy absorbers considered in the study, the normalized absorbed energy (μ_E) may be expressed as:

$$\mu_E = \frac{\int F_{v_e} d(x_v - x_b) + \int F_{v_i} dx_v}{0.5 m_v \dot{x}_v^2} \quad (2.26)$$

where F_{v_i} and F_{v_e} are the damping forces due to integrated and extended absorbers, respectively, given by:

$$\begin{aligned} F_{v_i} &= c_{1L} (\dot{x}_v - \dot{x}_b) + c_{1NL} (\dot{x}_v - \dot{x}_b)^3 \\ F_{v_e} &= c_{2L} \dot{x}_b + c_{2NL} \dot{x}_b^3 \end{aligned} \quad (2.27)$$

The energy absorbed by the structures is generally negligible compared to that by the damped add-on EA elements. Therefore, the percentage of energy absorbed by the EA elements thus may not yield meaningful information on the potential performance

process. This criterion, however, is included in the evaluation process to assess relative performance potentials of different configurations of EA elements.

Total deceleration deviation ' Δ_{Err} '

This measure defines the deviation between the acceleration response of the vehicle and the desired deceleration pulse, which serves as the target acceleration response for selecting design parameters of the add-on elements so as to reduce the potential injury risk. In this study, the total deceleration deviations are obtained using four optimal deceleration pulses corresponding to different speed ranges: less than 48 km/h; 48 to 56 km/h; 56 to 64 km/h; and greater than 64 km/h, as shown in Figure 2.10. These were derived on the basis of those reported in [18,18] for rigid barrier impacts at 48, 56 and 64 km/h. The defined pulses are used to identify design variables of the add-on energy absorbers on the basis of total deviation between the models' response and the target pulse. It should be noted that the optimal deceleration pulse corresponding to 64 to 80 km/h impact was established through extrapolation of the reported pulses for three lower speeds. This was realized by representing the time-acceleration history in three intervals based on the occupant interactions with the vehicle, namely: (i) a crash initiation phase; (ii) airbag deployment phase; and (iii) the ride-down phase [11,18,96]. The reported studies on crash-related injuries have recommended that vehicle deceleration in the second and third phases should be relatively low, as shown in Figure 2.10, in order to minimize the impact on the occupant who is in direct contact with the vehicle via the restraint system. The peak acceleration during the initiation phase, however, can be relaxed since the occupant is not completely involved with the vehicle in the initial phase. The magnitudes of the desired decelerations during the second and third phases are thus

limited to those defined for optimal pulse at 64 km/h impact with values of 9 and 23 g, respectively. The peak deceleration in the first phase is estimated as 57 g corresponding to 75 km/h impact speed over impact duration of 85 ms. This limiting value is assumed to be applicable over the 65 to 80 km/h impact speed range. The total deviation (Δ_{Err}) between the optimal and actual deceleration pulses is computed as the sum of the root mean squared (RMS) errors over each interval, such that:

$$\Delta_{Err} = \sum_{j=1}^m \left(\sum_{i=1}^n (a_v - a_{opt})_i^2 / n \right)^{1/2} \quad (2.28)$$

Where a_v , and a_{opt} refer to the vehicle and the optimal decelerations corresponding to the i^{th} interval of the crash pulse, n defines the number of subintervals considered over each interval i ($i=1, \dots, m$) and m is the total number of intervals considered ($m=3$).

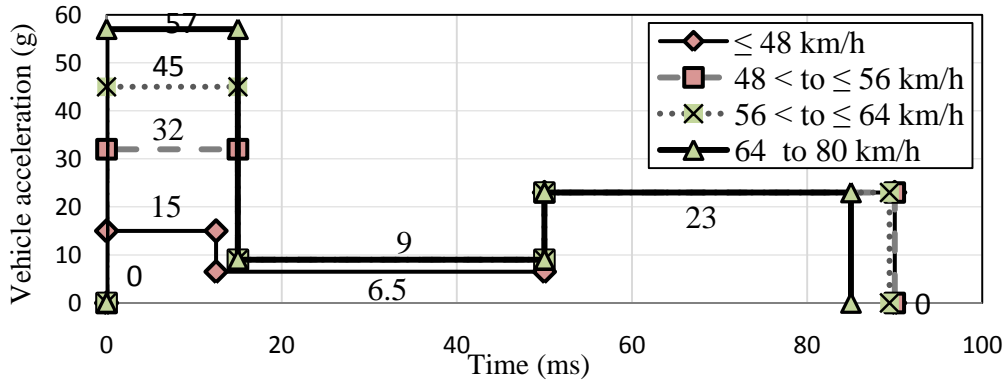


Figure 2.10: Target deceleration pulses defined for rigid barrier impacts in 4 different speed ranges [18,96]

The vehicle deceleration response is computed by considering nonlinear stiffness of the vehicle structure represented as linear and cubic functions of the deformation to resemble the elasto-plastic behavior of structural elements during a collision. The impact energy is assumed to be entirely absorbed by deformations of the crumple zone of the frontal substructure, add-on EA systems or by the occupant restraint system, i.e. there is no rebound motion of the structure. The simulation models also involve further

simplifying assumptions, including: (i) absence of hydraulic lock effect of dampers at high impact speeds; (ii) negligible restoring force of dampers at high impact speeds considering negligible effect of compliance or the gas spring; and (iii) linear characteristics of the occupant-restraint system, although with a clearance due to slack.

2.5 Response Analyses of Vehicle Models with Add-on Energy

The response characteristics of the vehicle models with different configurations of add-on energy absorbers are initially evaluated to study relative contributions of design variables related to the damping properties. The initial analyses are performed for an impact speed of 48 km/h as recommended in FMVSS 208 [73] for both the *ED* and *ID* models presented in sections 2.3.2 and 2.3.3. Different values of linear and nonlinear damping parameters are considered for the analysis. Furthermore, a nonlinear quadratic function is introduced in the damping forces to study its effect on the selected measures. For this purpose, the damping force, F_d , due to integrated or extendable dampers is expressed as:

$$F_d = \alpha d_L \dot{v} + \beta d_2 \dot{v}^2 + \gamma d_{NL} \dot{v}^3 \quad (2.29)$$

where α , β and γ are linear, quadratic and cubic damping scaling factors, respectively, d_2 is the nominal quadratic damping coefficient and v is the relative velocity.

The relative influences of linear, quadratic and cubic damping terms are investigated by varying α , β and γ in the 1 to 25 range, while selected models are analyzed to determine the important measures such as HIC and vehicle deformation. Each damping constant was varied with an increment of 0.5, which resulted in a total of 117,649 simulation runs. The initial simulations were performed for the baseline damping constant, namely: $d_L=8000$ Ns/m, $d_2= 100$ Ns²/m² and $d_{NL}= 20$ Ns³/m³. The baseline

simulation parameters are taken as: $m_v=1500$ kg, $m_o=65.7$ kg; $m_b=50$ kg; $k_o=98.1$ kN/m; $c_o=2.54$ kNs/m; $\delta_{oc}=0.005$ m; $k_L=50$ kN/m; $k_{NL}=1000$ kN/m³; $d_L=800$ Ns/m; $D_{NL}=20$ Ns³/m³; $\Delta_{e_limit}=0.4$ m; $\delta_{0e}=0.35$ m; $\delta_{1e}=0.3$ m; $\Delta_{i_limit}=0.7$ m; $\delta_{0i}=0.65$ m; $\delta_{1i}=0.6$ m; $k_{eqv}=220.6$ kN/m, $k_{r1}=1500$ kN/m; and $k_{r2}=15$ MN/m.

The simulation results were analyzed to identify near optimal damping parameters that would yield minimum values of both the occupant HIC and the peak vehicle deformation. These responses are compared with those corresponding to those reported by Elmarakbi [36] for the baseline model and the two vehicle-occupant models comprising extendable (ED) and integrated (ID) dampers. Table 2.1 presents the damping coefficient values that could yield minimal occupant HIC and minimal peak vehicle deformations. The Table also present the HIC and deformation values corresponding to nominal parameters ($\alpha=1$, $\beta=0$, and $\gamma=1$).

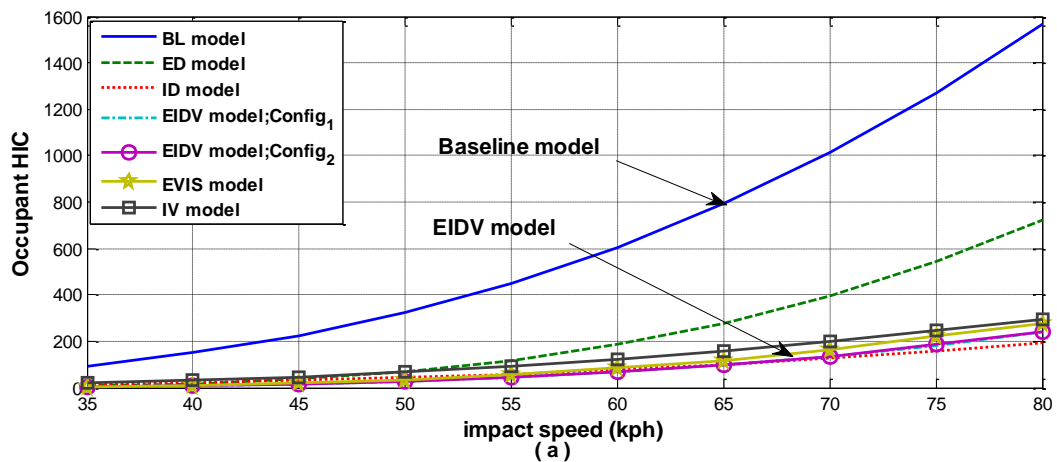
Table 2.1: The linear, quadratic and cubic damping constants leading to minimal occupant HIC and peak vehicle deformation

	nominal parameters [36]	Damping parameters leading to minimal HIC and peak deformation			
		without quadratic damping; $\beta=0$		with quadratic damping	
		Minimal deformation	Minimal HIC	Minimal deformation	Minimal HIC
ED-model					
	$\alpha=1.0;$ $\beta=0; \gamma=1.0$	$\alpha=2.187;$ $\gamma=0.75$	$\alpha=2.735;$ $\gamma=0.75$	$\alpha=2.065;$ $\beta=1; \gamma=0.5$	$\alpha=2.3125;$ $\beta=1; \gamma=0.5$
Peak deformation	0.584	0.4907	0.4974	0.4912	0.4981
Occupant HIC	514.4	279.89	276.41	281.9	277.44
		Minimal deformation	Minimal HIC	Minimal deformation	Minimal HIC
ID-model					
	$\alpha=1.0;$ $\gamma=1.0$	$\alpha=3.125; \gamma=12.5$	$\alpha=0.125; \gamma=12.5$	$\alpha=3.125;$ $\beta=10; \gamma=12.5$	$\alpha=0.125;$ $\beta=24; \gamma=0.5$
Peak deformation	0.498	0.2231	0.396	0.1990	0.3943
Occupant HIC	312.2	255.01	170.94	260.8	172.3

The results attained from the sensitivity analysis suggest that nonlinear scaling factors (α , β and γ) should be adjusted to attain optimal occupant HIC and peak deformation. A variation in the linear viscous damping factor (α) from 2.1875 to 2.375, could help achieve minimal values of both the occupant HIC and vehicle deformation, while the corresponding variation in the of cubic term (γ) factor appears to be in the 0.5 to 0.75 range for the ED model, as shown in Table 2.1. Both the linear and cubic terms scale factor yield minimum vehicle deformation and minimum HIC in the ID model. However, the effects were most significant for the factors in the 0.125 to 3.125 and 12 to 12.5 ranges, respectively. These suggest that the effectiveness of an integrated add-on energy dissipator would strongly depend up on the nature of damping. Furthermore, the inclusion of quadratic term in the damping force revealed negligible effect on HIC and deformation, especially for the ED model for the range of β values considered. A higher value of β , however, could yield lower peak deformation of the ID model, while the effect on HIC was very small. The simulation results also show that the variations in damping could yield considerably lower HIC and deformation compared to those derived from the baseline parameters [40,40-144]. The results further suggest that variations in nonlinear damping parameters could help achieve lower HIC and deformation, which are contradictory measures. Furthermore, the quadratic damping term has only little effect on both the measures over the range considered. The subsequent analysis are thus conducted considering $\beta = 0$. It should be noted that the nonlinear damping force with linear and cubic terms can be obtained by using a damper with a variable orifice opening or equipped with a compressed gas chamber, whereas the quadratic term could be obtained using an a fixed opening [157].

2.5.1 Comparison of Responses of Different Configurations of Add-on Absorbers

The crash responses of vehicle-occupant models employing different configurations of absorbers are evaluated over a wide range of frontal impact speeds (35 to 80 km/h). The resulting responses are expressed in terms of peak occupant HIC evaluated over 15 ms duration and peak vehicle deformation. The analyses are performed for two sets of parameters for the EIDV, EVIS and IV models. In the first set, the integrated elements are assumed to possess considerably lower stiffness compared to the extended element ($\lambda_1=0.3$; $\lambda_2=.01$) with nominal linear and cubic damping constants ($\mu_1=\mu_2=1$). In the second set, the damping constants of the integrated and extended elements are ($\mu_1=1.5\mu_2=1.7$), respectively. The responses of the models with add-on elements are compared with those of the baseline model, denoted as 'BL'. Figures 2.11 and 2.12 compare the occupant HIC and peak deformation responses of the models with add-on absorbers and the baseline model, as a function of impact speed using the two sets of parameters, respectively.



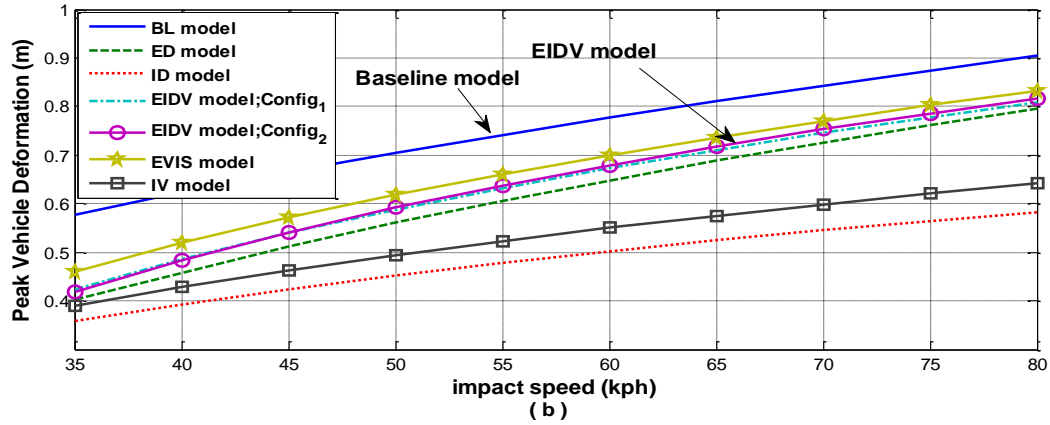


Figure 2.11: Comparison of occupant HIC and peak vehicle deformation responses with different arrangements of add-on absorbers at different impact speeds ($\lambda_2=0.1$; $\lambda_1=0.3$; $\mu_2=\mu_1=1.0$): (a) HIC; and (b) peak deformation.

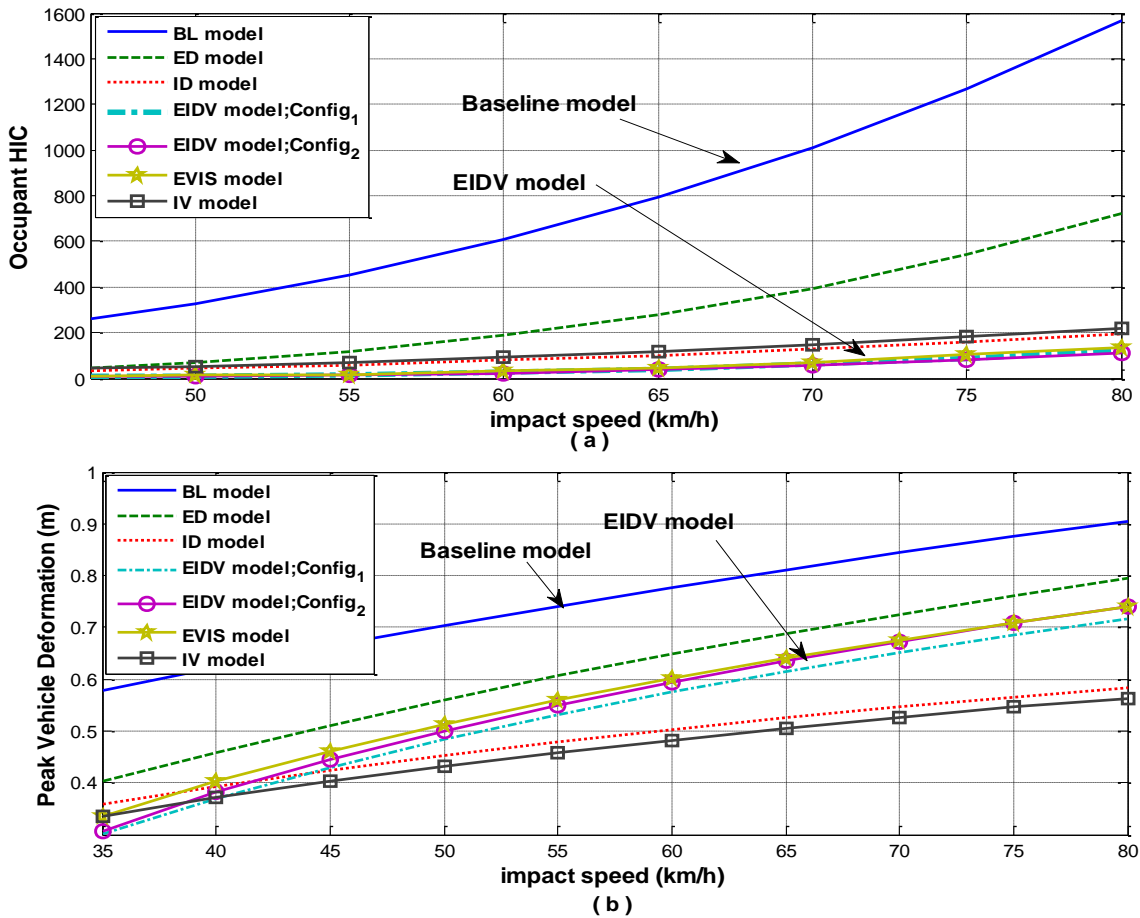


Figure 2.12: Comparison of occupant HIC and peak vehicle deformation responses with different arrangements of add-on absorbers at different impact speeds ($\lambda_2=0.1$; $\lambda_1=0.3$; $\mu_2=1.7$; $\mu_1=1.5$): (a) HIC; and (b) peak deformation.

The results clearly show that the add-on elements, irrespective of their configurations, yield lower values of HIC and peak deformation over the entire speed range. Furthermore, the model with extended dampers (ED) yields occupant HIC values that are considerably higher than those of the other configurations including the integrated dampers (ID), while the peak deflection tends to be lower than those of the EIDV and EVID models with nominal damping, as seen in Figure 2.12 (b). Furthermore the ID and IV models yield comparable HIC values, while the HIC response of the IV model is slightly higher and its peak deformation is lower in the entire speed range. This suggests that the stiffness property of the integrated absorber helps reducing the peak deformation by enhancing the structure stiffness, while the corresponding HIC values increases only slightly. The peak deflection responses of the models with damping factors ($\mu_1=1.5$ and $\mu_2=1.7$) tend to be lower than those attained with nominal damping, as seen in Figure 2.12 (b), suggesting that energy dissipation by the add-on elements also helps limiting intrusion during a frontal barrier impact, irrespective of the speed. Additionally, the EIDV model maintains lower HIC values over the entire range of impact speed in both configurations with a potential to achieve lower peak deformation by increasing the damping factor in the extended add-on part, as shown in Figures 2.11 (b) and 2.12 (b). This means that the EIDV model has the potential to reduce occupant HIC as well as peak vehicle deformation, since it combines the merits of extended model in lowering HIC value and for the integrated model in lowering the total deformation over the specified range of speed.

2.5.2 Sensitivity Analyses

Sensitivity analyses are performed to study the influences of variations in the design parameters of different configurations of the add-on elements on selected performance measures. These include the peak occupant HIC, peak vehicle deformation, peak occupant deceleration and deviation from the optimal deceleration pulse. The analyses are performed assuming that the entire impact energy is completely absorbed by the deformation of the crumple zone of the frontal substructure, add-on EA systems and by the occupant restraint system, and there is no rebound motion of the vehicle. Furthermore, the Voigt elements used in the extendable position are considered to be extended to 40 cm before the crash event. Table 2.2 presents the response measures of the baseline vehicle model in the 35 to 80 km/h impact speed range. The results clearly show that all the measures of the impact response increase most significantly with increase in the impact speed. The occupant HIC increases most significantly approaching nearly 1600 under the 80 km/h impact, while the corresponding peak deformation is in the order of 0.9 m. The sensitivity analyses are performed by varying the design parameters in specified range that are considered to be feasible in the context of design of dampers and Voigt elements. The ranges of parameters considered are: $0.1 \leq \lambda_1 \leq 0.3$; $0.1 \leq \lambda_2 \leq 0.3$; $0.1 \leq \mu_1 \leq 2.0$; and $0.1 \leq \mu_2 \leq 5.0$. The results attained are analyzed to identify the most desirable configuration of the add-on elements and the desirable parameters. For this purpose, the analyses are performed in three distinct sequences involving identifications of design parameters that yield minimal deformation, or minimal occupant HIC or minimal total deviation (Δ_{Err}) from the optimal deceleration pulse defined in section 2.4. The design variables are identified for each criterion at each speed, which could be

subsequently applied to identify design variables that yield a compromise solution over the entire speed range. Furthermore, the HIC and specific energy absorbed by the add-on components are also evaluated for each criterion and set of identified design variables.

As an example, Table 2.3 illustrates the identified design variables for the EIDV model that yield minimal deformation or minimal HIC or minimal total deviation at each impact speed. This particular model is selected on the basis of the results presented in Figures 2.11 and 2.12, which suggest that the EIDV configuration offers better potential in realizing lower occupant HIC and vehicle deformation. The results suggest that higher stiffness of the integrated absorber yields minimal vehicle deformation, irrespective of the impact speed. The lower stiffness due to integrated and extendable absorbers, however, is desirable to achieve minimal occupant HIC over the entire speed range, as seen in Table 2.3. Lower stiffness of the absorber also yields minimal total deviation from the optimal pulse up to impact speed of 55 km/h. At higher impact speeds, a higher stiffness of extendable absorber is desirable to achieve minimal deviation that is directly related to vehicle deceleration. These suggest contradictory stiffness requirements for preservations of occupant protection, particularly the occupant HIC and occupant compartment intrusion. The addition of damping, however, tends to provide a better compromise among the two measures. The results shown in Table 2.3 illustrate that minimal vehicle deformation is coupled with reasonable levels of occupant HIC, although the HIC values are higher than the minimal values shown in mid-section of the Table.

In a similar manner, the damped absorbers resulting in minimal HIC also yield peak deformations that are significantly lower than these of the baseline model over the entire speed range. Furthermore, the variation in minimal vehicle deformation is better

correlated with greater specific energy absorption by the absorbers, expressed as a percentage of the total impact energy. The portion of the absorbed energy corresponding to minimal HIC, however, is relatively smaller. This is attributed to relatively lower damping parameters identified from the sensitivity analyses targeting the minimal occupant HIC, as seen in Table 2.3. The results clearly emphasize the need for identification of optimal design variables that can yield an acceptable compromise in occupant HIC and peak deformation. The results confirmed that the peak vehicle deformation and HIC are mostly affected by damping coefficients of the extendable absorber, as seen in Table 2.3.

The results in Table 2.3 further show that damping factor μ_1 tends to converge towards its upper limit in most cases, irrespective of the criterion chosen. Consequently, additional sensitivity analyses are performed by relaxing the upper limit on μ_1 , while the upper limit on μ_2 was reduced, such that $0.1 \leq \mu_1 \leq 5.0$ and $0.1 \leq \mu_2 \leq 1.5$. The ranges of variations in λ_1 and λ_2 , however, were retained. This arrangement is denoted as (Config₂). The results, shown in Table A-1 (Appendix-A), were attained for desirable design variables that yield minimal deformation, minimal HIC and minimal total deviation (Δ_{Err}). The results confirmed that the peak vehicle deformation and HIC are mostly affected by damping coefficients of the extended absorber, while the reverse is happen for the second configuration. It can be concluded from both arrangements that the Voigt elements with the restrained upper limit converge towards the upper limit coupled with high stiffness in the entire speed range. On the other hand, the extended Voigt element with a relaxed upper limit, μ_2 saturate at the upper limit irrespective of the impact speed, as shown in Tables (2.3) and (A.1). However, the first configuration seems

to be more favorable than the second one, especially for realizing minimal vehicle deformation.

The sensitivity analyses were also performed for the vehicle-occupant model with extendable Voigt absorber and integrated dampers (EVID). The parameter values were permitted to vary in the ranges: $0.1 \leq \lambda_2 \leq 0.3$; $0.1 \leq \mu_1 \leq 2.0$; and $0.1 \leq \mu_2 \leq 5.0$. The results shown in Table A.2 (Appendix-A) confirmed that both the peak deformation and occupant HIC are most significantly affected by μ_2 . Furthermore, the sensitivity analyses of the IV model are conducted by varying the design variables in the ranges: $0.1 \leq \lambda_1 \leq 0.8$ and $0.1 \leq \mu_1 \leq 5.0$. The results, shown in Table A.3, suggest that minimal vehicle deformation is achieved when both stiffness and damping coefficients approach their upper limits, while the HIC values are higher than the baseline model over the entire speed range. On the other hand, design variables that achieve the optimal occupant HIC are noticed to have damping factors that linearly proportional with the impact speed, while the stiffness values converge towards the respective lower limits, irrespective of the impact speed. The design variables that yield optimal occupant HIC are thus selected to be the significant parameters of the IV model. This configuration, however, revealed that the minimal deformations are considerably higher than those of the EIDV model, over the entire range of speed, although significantly lower than the baseline vehicle model. The results attained for the model integrating Voigt absorber alone also revealed significantly higher peak deformations, while the damping was most effective in limiting both the HIC and the peak deformation.

From the results, it was concluded that the EIDV configuration is most promising in realizing a better compromise between the conflicting HIC and peak deformation

measures, and relatively lower values of the occupant HIC. Figure 2.13 and Table 2.4 illustrate comparisons of different measures of the baseline model (BL), with those of the models with integrated dampers (ID), extended dampers (ED) and integrated-extendable dual Voigt absorber (EIDV). The table presents the occupant HIC, deformation, vehicle deceleration, and specific energy absorption of the models. The results for the baseline, ID and ED models, are obtained using nominal parameters ($\mu_1=\mu_2=1$), while those for the EIDV model are obtained for parameters leading to minimal peak deformation at a speed of 48 km/h. The results clearly show that the EIDV arrangement can yield substantially lower measures of the barrier impact response. The integrated dampers configurations also yield substantial energy absorption, and reduction in HIC and peak deformation compared to the baseline model. The figure also illustrates the target deceleration pulse. The deceleration response of the EIDV configuration appears to be closest to the target pulse, followed by the ID configuration.

Table 2.2: Front barrier impact response of the baseline model at different impact speeds

Speed (km/h)	35	40	45	50	55	60	65	70	75	80
Vehicle Deformation, m	0.577	0.622	0.664	0.703	0.741	0.776	0.810	0.843	0.874	0.904
Occupant HIC	94.66	152.61	230.94	332.58	460.58	617.81	807.10	1,031.18	1,292.59	1,594.16
occupant deceleration, g	33.46	40.55	47.91	55.49	63.27	71.21	79.31	87.55	95.90	104.37
Total deviation error, Δ_{Err}	88.5	97.9	107.3	136.2	145.7	169.1	179.1	200.2	210.8	221.5

The performance measures attained from simulation results of different models, including the baseline model, are further compared in Table 2.4 and Figure 2.12. As it is clearly shown in the table, the EIDV model achieves better performance compared with the other proposed models.

Table 2.3: Identification of design variables of the EIDV model corresponding to minimal deformation, HIC, total deviation error at different impact speeds.

Speed (km/h)	35	40	45	50	55	60	65	70	75	80
Minimal peak vehicle deformation (m)										
	0.225	0.258	0.289	0.318	0.346	0.371	0.396	0.418	0.441	0.461
λ_2	0.1	0.1	0.1	0.1	0.1	0.1	0.1	0.1	0.1	0.1
μ_2	1.8	2.1	2.4	2.7	2.9	3.2	3.5	4.0	4.1	4.2
λ_1	0.3	0.3	0.3	0.3	0.3	0.3	0.3	0.3	0.3	0.3
μ_1	2.0	2.0	2.0	2.0	2.0	2.0	2.0	2.0	2.0	2.0
Occupant HIC	7.22	11.24	16.70	24.02	32.51	43.83	57.56	72.70	91.66	113.82
Specific absorbed energy	87.54%	88.28%	88.73%	89.02%	88.69%	87.09%	89.15%	89.99%	89.57%	89.12%
Total deviation, Δ_{Err}	73.0	78.9	85.1	111.1	117.5	137.5	144.6	157.5	165.1	172.6
Minimal occupant HIC										
	3.48	5.58	8.78	12.63	18.46	25.80	35.50	46.92	61.88	79.10
λ_2	0.1	0.1	0.1	0.1	0.1	0.1	0.1	0.1	0.1	0.1
μ_2	0.9	1.0	1.2	1.3	1.5	1.7	1.9	2.0	2.3	2.5
λ_1	0.1	0.1	0.1	0.1	0.1	0.1	0.1	0.1	0.1	0.1
μ_1	1.8	2.0	1.9	2.0	2.0	1.9	2.0	2.0	2.0	2.0
Vehicle deformation	0.402	0.440	0.465	0.497	0.516	0.539	0.553	0.580	0.588	0.604
Specific absorbed energy	68.55%	69.86%	71.67%	72.25%	74.09%	72.14%	76.74%	76.55%	78.65%	79.47%
Total deviation, Δ_{Err}	68.7	74.3	80.5	106.4	113.4	133.6	141.1	154.0	162.1	170.2
Minimal total deviation error										
	64.0	69.2	75.0	101.2	108.6	129.4	137.7	150.8	159.9	168.9
λ_2	0.1	0.1	0.1	0.1	0.1	0.1	0.1	0.1	0.1	0.1
μ_2	0.1	0.1	0.1	0.1	0.1	0.1	0.1	0.1	0.2	0.3
λ_1	0.1	0.1	0.1	0.1	0.1	0.3	0.3	0.3	0.3	0.3
μ_1	2.0	2.0	2.0	2.0	2.0	2.0	2.0	2.0	2.0	2.0
Vehicle deformation	0.25	0.34	0.40	0.33	0.37	0.39	0.41	0.43	0.44	0.46
Occupant HIC	38.4	44.6	65.9	104.9	129.2	165.1	207.5	256.8	313.6	378.6

Table 2.4: Comparison between HIC of the occupant for each model compared with the baseline model at 48 km/h impact speed

Models	Occupant HIC	Vehicle Deformation, m	Peak occupant deceleration, g	Specific energy absorbed by add-on	Total deviation (Δ_{Err})
BL- model	288.9	0.687 9	52.4	0%	54.5
ID-model	54.2	0.5057	26.6	68.7%	36.1
ED-model	107.4	0.5995	35.2	43.5%	52.7
EIDV model	19.1	0.3160	16.9	90.2%	35.5
EIDV model,Config_2	18.6	0.33324	17.5	89.9%	35.3
EVIS model	12.3	0.4324	13.7	86.4%	36.2
IV model	42.9	0.4328	31.0	39.8	36.9

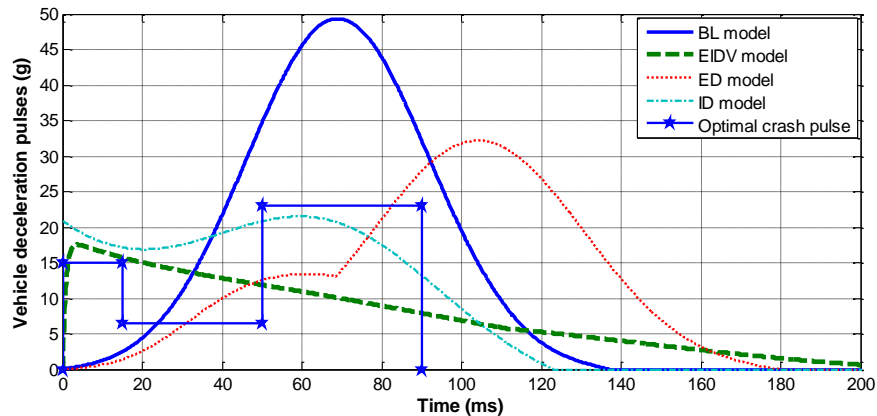


Figure 2.13: Comparison of vehicle deceleration responses of the baseline vehicle model with the three of models in the integrated (ID) and extended (ID) dampers, and integrated-extendable Voigt system (EIDV) and the target deceleration pulse ($v_0 = 48$ km/h).

Figures 2.14 illustrates comparisons of vehicle deformation and occupant deceleration response of the model under an impact speed of 48 km/h, as recommended in FMVSS 208 [73]. The figure also compares the responses of the ID and ED models, together with that of the BL model. The results show reasonably good agreements with

the results reported in [36], except for the ID model, while some deviations are evident in the deformation response. Such deviations are believed to be attributed to the approximate analysis method based on incremental harmonic balance method employed (IHBM) in [36]. The results also show that the proposed EIDV configuration can yield substantially lower occupant deceleration and vehicle deformation compared to the reported add-on energy absorption concepts. The results also show a reduction in occupant deceleration of the EIDV model compared to other models. The proposed model achieves 65.6% reduction in the occupant deceleration peak compared to the BL model.

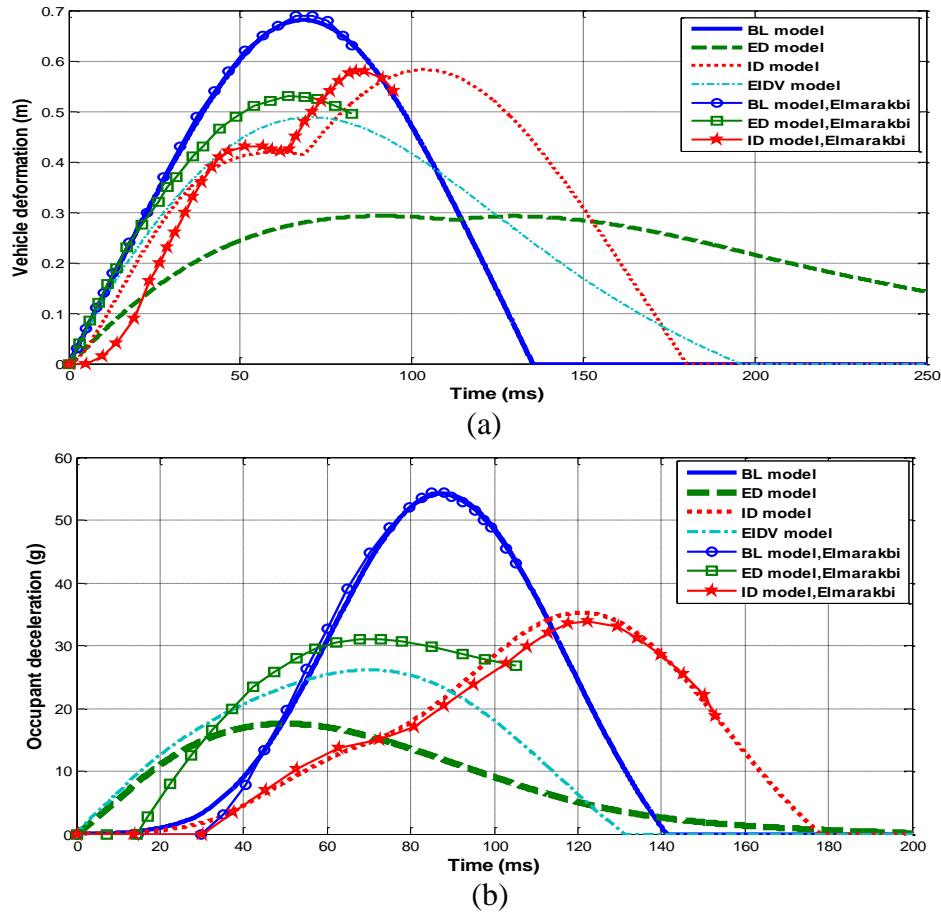


Figure 2.14: Comparison of response of different models subject to a 48 km/h frontal impact speed with the reported response [36]: (a) vehicle deformation and (b) occupant deceleration

The occupant HIC responses of different models over the 35 to 80 km/h impact speed range are further compared in Figure 2.15 (a). The results show that the HIC response of the EIDV model is below 150 in the entire speed range, which is well below the recommended threshold limit. The total vehicle deformation responses of different models are also compared in Figure 2.15 (b). The results suggest that the total vehicle deformation of the EIDV model is the lowest and does not exceed 50 cm.

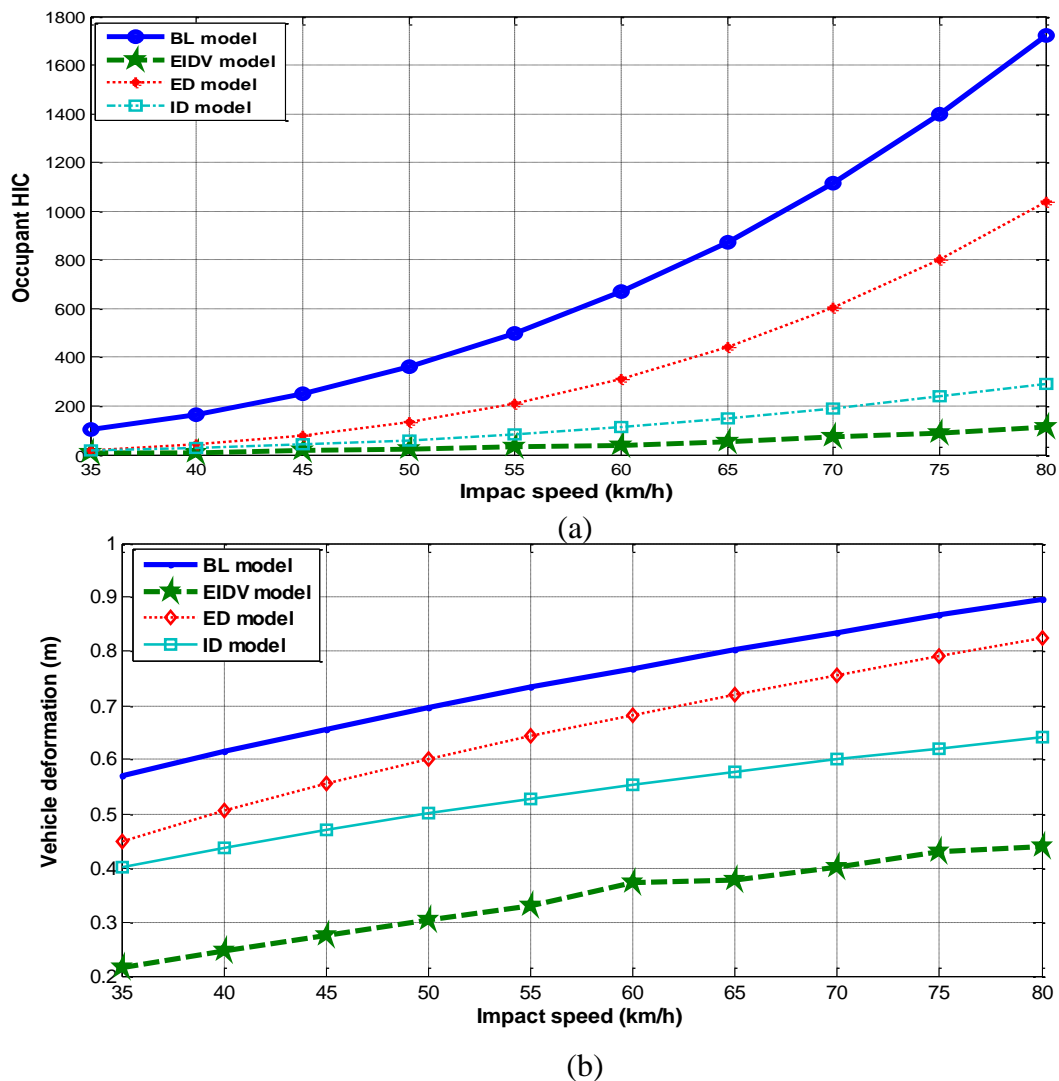
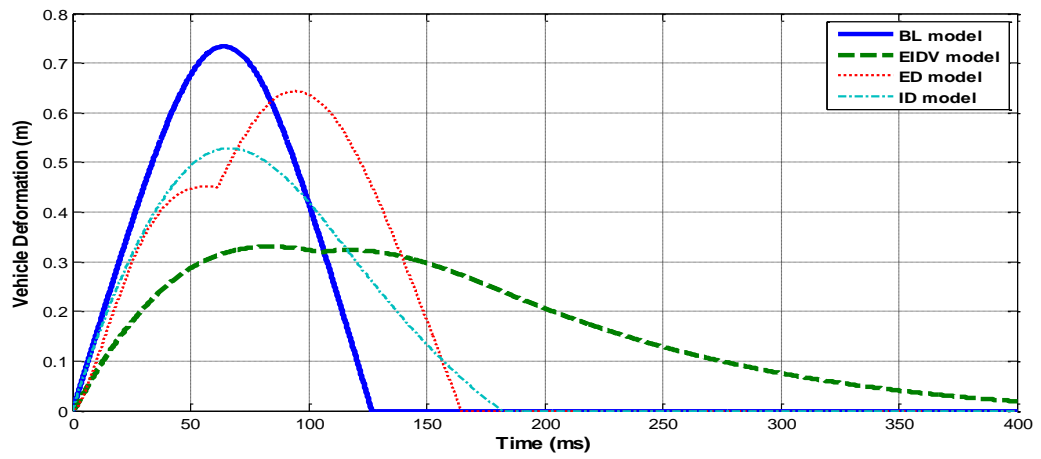
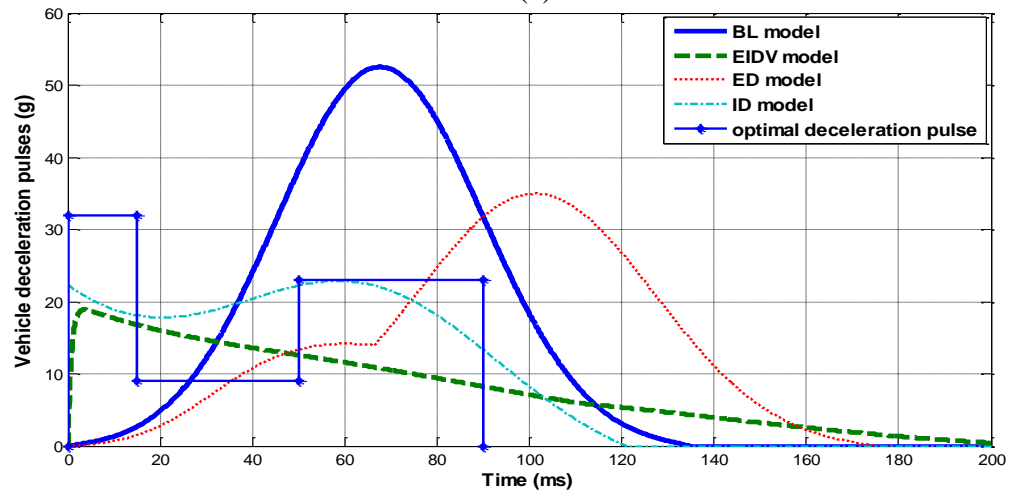


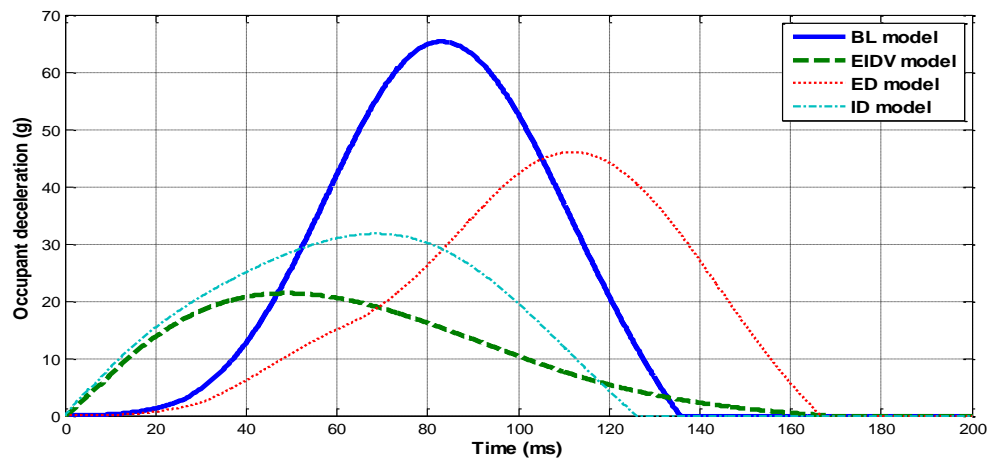
Figure 2.15: Comparison design responses of the EIDV model with different models at different impact speeds: (a) occupant HIC and (b) peak vehicle deformation



(a)



(b)



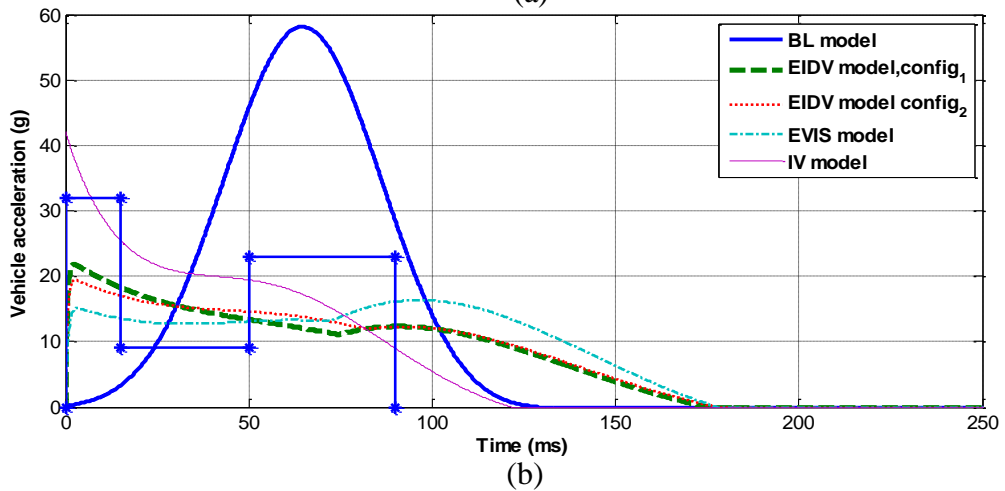
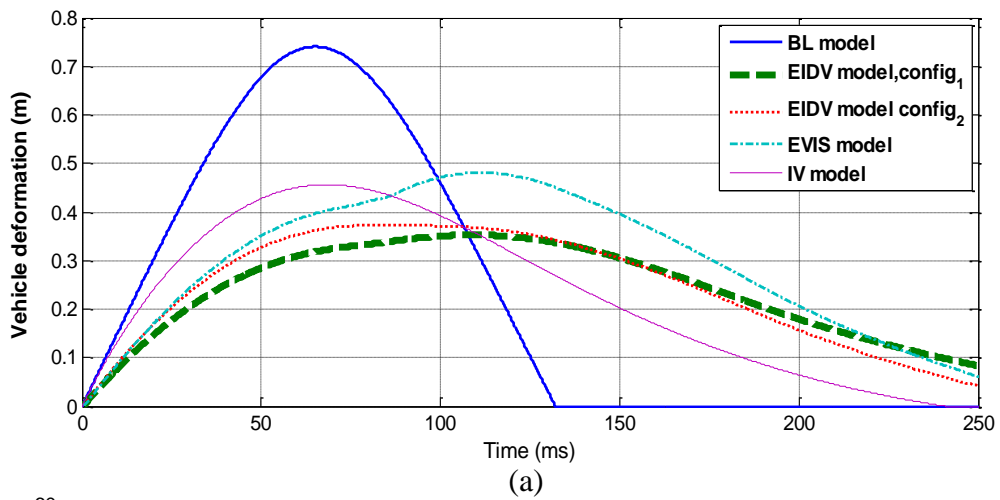
(c)

Figure 2.16: Comparison of response of different models subject to a 55 km/h frontal impact speed: (a) vehicle deformation and (b) vehicle deceleration and (c) occupant deceleration

The enhanced crash energy management potential of the proposed EIDV absorber is also illustrated at an impact speed of 55 km/h as recommended by UN-NCAP [74]. Figure 2.16 compares the vehicle deformation and vehicle and occupant deceleration responses of the BL, ED, ID and EIDV models, respectively. The results clearly show that the proposed EIDV configuration yields significantly lower peak deformation and decelerations of the vehicle and the occupant. The addition of the absorbers, however, yields continued gradual deformation of the structure over substantially longer periods compared to the baseline vehicle model. Figure 2.17 further compares the deformation and occupant and vehicle deceleration responses of the EIDV configuration with those of the models with IV and EVID configurations of the absorber under an impact speed of 55 km/h. The target optimal deceleration pulse is also illustrated in Figure 2.17 (b). The results again confirm that EIDV configuration yields lowest deformation and deceleration responses, while the vehicle deceleration is closer to the optimal pulse, followed by IV model. It is also noticed that both EIDV configurations (config₁ and config₂) have almost the same pattern with better enhancement shown by the first arrangement, while the other arrangement seems to be impractical since higher damping in integrated position may affect the compartment intrusion.

The configuration with integrated dampers and extendable Voigt elements (EVIS) also yields lower deceleration responses, although higher than the EIVD configuration. The EVIS model, however, yields considerably larger peak deformation. These results again confirm that the stiffness of the integrated absorber helps to reduce the vehicle deformation. Furthermore, the EIDV model that achieves minimal vehicle deformation is considered to be more practical than the other configurations that could result in lower

values of the performance measures. This agrees with the hypothesis that lower damping factor should be maintained in integrated position to reduce the risk of failure in the weakest points of the load paths. In order to demonstrate the degree of enhancement that can be achieved by the EIDV model, comparisons of the primary performance measures are further illustrated in Figure 2.17. The results show that the EIDV configuration yields vehicle deformation that is 53.3% lower compared to the BL model, while the corresponding vehicle and occupant decelerations are 61.5% and 65.6% lower, respectively. The comparison of occupant deceleration responses of the proposed models shows a noticeable enhancement for the EIDV model in Figure 2.17 (c).



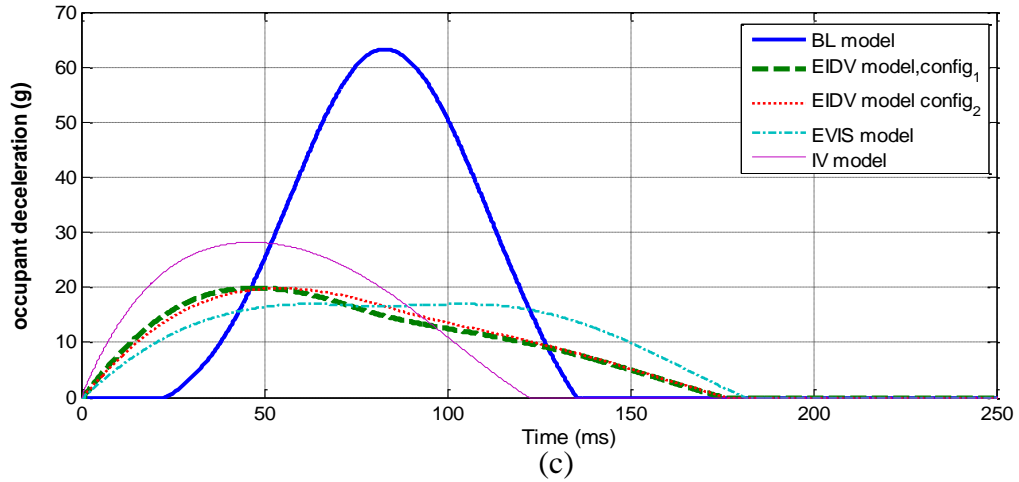


Figure 2.17: Comparison of response of different proposed models with the baseline model subject to a 55 km/h frontal impact speed: (a) vehicle deformation and (b) vehicle deceleration and (c) occupant deceleration

2.6 Summary

A new crash energy management technique is introduced to modify the energy absorption capability over a range of impact speeds. The new concept has the potential to modify the absorption properties during the crash event with only minimal alteration of the original structural stiffness. Sensitivity analyses are conducted over the specified ranges of different design variables for different configurations of add-on energy absorbers and the results are analyzed to select a desirable arrangement on the basis of selected optimal performance measures over the 35 to 80 km/h speed range. Comparisons of the models' responses with the baseline model revealed that the EIDV model can yield significantly improved performance compared with other configurations, followed by the IV model. The EIDV model yields 67.7%, 54.1% and 93.3% reductions in peak occupant deceleration, maximum vehicle deformation (or dynamic crush) and occupant HIC at an impact speed of 48km/h, respectively, compared to the baseline configuration.

Furthermore, the specific energy absorbed by the EIDV model is 90.2% of the impact energy at the same impact speed.

Considering the superior performance potential of EIDV configuration and conflicting requirements of HIC and vehicle deformation as a multiple objective optimization problem is formulated and solved to seek the optimal parameters of the absorbers in the next chapter.

CHAPTER 3

OPTIMAL ADD-ON ENERGY ABSORBERS CONFIGURATIONS

3.1 Introduction

In Chapter 2, a parametric study was conducted to identify the optimal parameters of energy absorber systems used in the proposed lumped parameter models (LMS). Design variables (DVs) were assumed to vary in a discrete manner within the assigned design range in order to be able to search the whole design space without formal optimal algorithm. In this chapter, the objective is to find true optimal configuration of the add-on systems for the proposed LMS models using the formal optimization techniques in which design variables can be considered as continuous variables in order to cover all the points in the design space. Before conducting any optimization, first the optimization problem should be well formulated. This requires properly identification of the design objective criteria to measure system performance through selection of the proper design variables and identifications of required constraints.

3.2 Formulation of the Optimization Process

There are many factors affecting the accuracy and successful termination of the optimization problems including proper formulation of the optimization problem, selection of the appropriate optimization techniques, and a full understanding of the system behavior [158,160]. Generally, optimization process may be categorized in two main types: single- and multi-objective optimization problems. Single objective optimization problems have been effectively addressed by both gradient-based and non-gradient based optimization algorithms. Among the gradient based optimization

algorithm, the Sequential Quadratic Programming (SQP) algorithm is a powerful algorithm that can easily tackle nonlinear constrained optimization problems [161,162]. The drawbacks of the gradient based optimization algorithms are that they can be easily trapped in local optimum points without any mechanism to climb up. On the other side non-gradient stochastic based algorithms such as Genetic Algorithms (GAs) [32,33] can approximately identify the location of the global optimal point. When designing vehicle structure for optimum crashworthiness configurations, there are different conflicting design performances, for which any further improvement in one objective must lead to worsening one or more other objectives to a certain extent.

There are different approaches to deal with these conflicting design performances as objective functions that can be summarized as: (i) conducting single objective optimization for each objective function separately in a sequential iterative manner, (ii) combining different objective functions using weighting factors to form single objective optimization problem, and (iii) implementing multiobjective optimization techniques. It has been concluded that the multiobjective optimization is an effective approach to identify optimal points within the whole range of design space since it involves the trade-off between the conflicting objective functions via optimal sets of design points that form what is known as Prato Frontier curves or surface [32,163].

As discussed before in Chapter 2, there are two important performance criteria that have to be minimized, namely: occupant HIC and peak vehicle deformation (*Def*) in order to assess vehicle crashworthiness enhancement since they directly affect the occupant safety. In this chapter different optimization algorithms and techniques are explored to implement design optimization for the add-on energy absorbers

configurations of the two proposed models, namely the EIDV and IV models which are formulated in sections 2.3.4 and 2.3.6, respectively. Advantages and disadvantages of each optimization technique are also discussed. In the following section, single objective optimization problem has been addressed and then the multi-objective optimization (MOO) problem is formulated. This is followed by discussion of the optimization results.

3.2.1 Single Objective Optimization

The mathematical formulation of a single objective optimization problem can be formally stated as follows:

$$\begin{aligned}
 & \text{Find } \mathbf{X} = \{x_1 \quad x_2 \quad \dots \quad x_n\} \text{ that:} \\
 & \text{Minimizes } F(\mathbf{X}) \\
 & \text{where, } \mathbf{X}_L \leq \mathbf{X} \leq \mathbf{X}_U \qquad \qquad \qquad (3.1) \\
 & \text{Subject to : } g_j(\mathbf{X}) \leq 0 \quad j=1,2, \dots, m \\
 & \qquad \qquad \qquad l_i(\mathbf{X}) \leq 0 \quad i=1,2, \dots, p
 \end{aligned}$$

where \mathbf{X} is an n -dimensional design variables bounded between the lower bound, \mathbf{X}_L , and the upper bound, \mathbf{X}_U , $F(\mathbf{X})$ is the objective function and $g_j(\mathbf{X})$ and $l_i(\mathbf{X})$ are the inequality and equality constraints functions, respectively. n is the number of design variables; and m and p are the number of inequality and equality constraints. The problem stated in Eqn. (3.1) is called a constrained single objective optimization problem [163]. Both SQP and GA are employed to solve different single objective optimization problems, defined in subsequent sections. Thus, a brief discussion about these optimization techniques and their considerations are provided in the following subsections.

3.2.1.1 Sequential Quadratic Programming (SQP)

The Sequential Quadratic Programming (SQP) algorithm is a gradient-based powerful technique that has been used to solve nonlinear constrained optimization problems in vehicle structural analysis [144,161,163]. SQP allows you to closely mimic Newton's method for constrained and unconstrained optimization problems. During each iteration process, an approximation is made by Jacobean and Hessian of the Lagrangian function using a quasi-Newton updating method. This is then used to generate a Quadratic sub-Problem (QP sub-problem) whose solution is used to form a search direction for a line search procedure.

The SQP optimization technique has been implemented in MATLAB environment and the following options from Matlab optimization environment toolbox [166] have been selected based on trial and error: (i) the maximum number of function evaluations to be allowed (*MaxFunEvals*) is 500; (ii) the maximum number of iterations to be allowed (*MaxIters*) is 40; and (iii) the termination tolerance used in case of a constraint violation (*TolCon*) is set to be 10^{-6} . In order to reduce the computational time, the *MaxFunEvals* and *MaxIters* are reduced below the default values.

The optimal results due to SQP may be local optimal points, different initial points are randomly selected to conduct optimization in an attempt to catch the global optima. It is observed that for all initial points at majority of the impact speeds, the objective function (F_{val}) are converged to approximately the same results and yields approximately the same DVs values. This implies that the optimal results obtained represent to a great extent the global minima.

3.2.1.2 Genetic Algorithm (GA)

Unlike the SQP technique that is based mainly on an incremental search using given starting points with the possibility of being trapped in local minima, the Genetic Algorithm (GA) is an evolutionary algorithms based on natural selection or survival of the fittest capable of catching the global minima. The genetic algorithm maintains a population of structures (usually randomly generated initially) that evolves according to rules of selection, recombination, mutation and survival which are referred to as genetic operators. A shared 'environment' determines the fitness or performance of each individual design point in the population. The fittest individuals are more likely to be selected for reproduction (retention or duplication), while both recombination and mutation modify those individuals, yielding potentially superior ones. Genetic algorithms have the capability to search complex spaces with a high probability of success in finding the minimum or maximum points in the search design space. In addition, GAs are derivative-free stochastic search algorithms since they require no derivative information about the fitness function and are less likely to be trapped by local minima, thus providing a nearly global optimal solution [167].

Each candidate solution within each iteration (string of character) is encoded as binary digits called chromosomes. The quantization level is a process that is responsible to convert a continuous range of values into a discrete binary value with an error between them known as a 'quantization error'. Each chromosome has a number of genes represented in a binary code. The population is a generation of a set of chromosomes at any iteration, and it usually consists of three types which are: (i) elite, (ii) crossover and (iii) mutation populations. This means that each created generation is composed of successive iterations, which in turn is composed of a set of chromosomes. The best

chromosomes (parents) with the highest fitness of the objective function are selected from the previous generation along with the best chromosomes from the offspring resulting from crossover and mutation based on natural selection. It should be mentioned that 'elitism' means that the best solution found thus far during the search always survives to the next generation. Crossover is a process of producing offspring from two parents (or chromosomes) by performing and combining the binary chromosomes at a cut-off point that is selected randomly. Mutation is a background operator which produces some random changes in various chromosomes to enable the genetic algorithm to search a broader space. The GA is also implemented in the MATLAB environment and the following options are used:

- Adaptive feasible option (@mutationadaptfeasible): This option is used for mutation to randomly generate directions, which are adaptive with respect to the last successful or unsuccessful generation.
- Heuristic option (@crossoverheuristic): This option is used for a crossover that returns a child (an offspring) that lies on the line containing the two parents close to the parent with the better fitness value in the direction away from the parent with the worse fitness value. The default parameter ratio ($\frac{1}{2}$) that determines how far the child is from the better parent is used.
- Pareto fraction option (set to 0.5): This option sets the fraction of individuals to keep on the Pareto Front (PF) from all the highest feasible points in the population within each iteration. Its value is scalar with a default value of 0.35.

- Crossover fraction option (set to 0.8): This option specifies the fraction of the next generation, other than elite children, that are produced by crossover. Its value is a fraction between zero and one, with a default value of 0.8 that is used.
- Termination criteria options: The following termination are used in this optimization:
 - Function tolerance (*TolFun*): Here the algorithm runs until the cumulative change in the fitness function value over stall generations (the number of generations since the last improvement of the fitness function) is less than or equal to the function tolerance value. The selected value is $1e^{-5}$.
 - Stall generations (*StallGenLimit*): The algorithm stops if the weighted average change in the fitness function value over stall generations is less than function tolerance. The selected value is 110 (the default value is 50).

It should also be noted that in order to reduce the run time, the GA accepts an initial guess of a DV range that lies within the DV bound limits, where the designer feels it should satisfy the global minima. In this study, the initial population is selected as the whole design range so as not to restrict the optimization conducted by the GA over a range of impact speeds.

3.2.1.3 Hybrid optimization Algorithm (HA)

This form of optimization is a combination of GA and SQP optimizations. It is based on genes and the natural selection of a GA to identify the nearly global optima, which is then used as the initial point for the SQP algorithm in order to catch the exact global optima. It is also a fairly recent research topic in the area of parallel evolutionary computation since it combines two optimization algorithms for refining the optimal result. Most of the hybrid parallel GAs are coarse-grained at the upper levels and fine-

grained at the lower levels [168]. Hybrid algorithms can be performed using one of the following forms: (i) running a GA until it slows down, and then letting a local optimizer take over, this is the method of approach used in this study; (ii) seeding the GA population with some local minima; and (iii) running the local optimizer (SQP) on the best set of solutions within each iteration and adding the resulting chromosomes to the population. For the options used in HA, in addition to the same GA options listed in the previous subsection, the (*fmincon*) option is used as the hybrid function (*HybridFcn*) to perform constrained minimization.

3.2.2 Combined Objective Optimization

Different studies have employed the combined objective function in car crashworthiness analysis [169,170]. This form of optimization combines normalized selected performance criteria into one single objective function using weighting factors. These weighting factors are selected based on the designer's decision concerning which of the design criteria should have more weightage. In order to form an objective function composed of different design criteria using a weighting factor, each term should be normalized, i.e. it should be unit-less and the summation of the weighting factor must be equal to unity. The normalizing factor is a matter of the designer's choice and there is no agreement over the value that should be used for normalization. It could be some reference number, the average, the maximum, or the difference between the maximum and minimum. The mathematical formulation of a general state single objective optimization problem obtained from combination of different performance criteria can be stated as follows:

Find $\mathbf{X} = \{x_1 \ x_2 \ \dots \ x_n\}$ that:

Minimizes $F(\mathbf{X}) = \varphi_1 * \mathbf{Obj}_1(\mathbf{X}) + \varphi_2 * \mathbf{Obj}_2(\mathbf{X}) + \dots + \varphi_k * \mathbf{Obj}_k(\mathbf{X}) + \dots + \varphi_r * \mathbf{Obj}_r(\mathbf{X})$,

where, $\mathbf{X}_L \leq \mathbf{X} \leq \mathbf{X}_U$ and $k = 1, 2, \dots, r$

Subject to : $\mathbf{g}_j(\mathbf{X}) \leq 0 \quad j = 1, 2, \dots, m$ (3.2)

$\mathbf{l}_i(\mathbf{X}) \leq 0 \quad i = 1, 2, \dots, p$

where: $\mathbf{Obj}_k(\mathbf{X})$ is the k^{th} normalized objective functions and φ_k is the k^{th} weighting factors. As mentioned, the main drawbacks for using the combined objective function are primarily related to its dependence on the weighting factors used and its applicability only in functions with a completely convex region.

3.2.3 Multi objective optimization

There are usually two or more contradicting performance criteria in any engineering system design, which necessitate conducting multi-objective optimization (MOO). This will enable the designer to obtain all the non-dominated optimal solutions spread across the Pareto-optimal front to choose the optimal design set based on trade-offs between different design criteria, depending on the designer's performance preference. In a MOO problem, one should bear in mind that the outcome is not just one optimum solution but that it, rather, contains a different set of optimum points locating on what is commonly known as the Pareto Frontier (PF) curve [163]. This means that the optimum solution is a trade-off between these objective functions. The mathematical formulation of a generic multi-objective optimization problem using two objective functions can be stated as follows:

$$\begin{aligned}
& \text{Find } \mathbf{X} = \{x_1 \ x_2 \ \dots \ x_n\} \text{ that:} \\
& \text{Minimizes } F(\mathbf{X}) \text{ and Minimizes } G(\mathbf{X}) \\
& \text{where, } \mathbf{X}_L \leq \mathbf{X} \leq \mathbf{X}_U, \ k = 1, 2, \dots, r \\
& \text{Subject to : } \mathbf{g}_j(\mathbf{X}) \leq 0 \ j = 1, 2, \dots, m
\end{aligned} \tag{3.3}$$

Evolutionary techniques such as Multi-objective Genetic Algorithms (MOGA) are currently gaining significant attention by researchers of various fields due to their effectiveness and robustness in searching for a set of global trade-off solutions [160]. Different studies have used the multi-objective function in crashworthiness of vehicle structure problems [32,33,146]. This research study uses MOO by conducting the MOGA technique to produce the best set of DVs that can optimally satisfy the two design criteria of occupant HIC and total vehicle deformation (*Def*). Besides the GA options discussed in section 3.2.1.2, the following options should also be considered when implementing the MOGA algorithm:

- Selection option: This option specifies how the genetic algorithm chooses parents for the next generation. You can specify the function that the algorithm uses in the selection function (*SelectionFcn*) field in the selection options pane. The only option that can work with MOGA is tournament (*@selectiontournament*). The default value of tournament size is 4, which is used in this simulation.
- Hybrid option: The '*gamultiobj*' option is used in place of the '*ga*' option when applying hybrid optimization. The '*gamultiobj*' offers only one hybrid function, the '*fgoalattain*', which runs after *gamultiobj* completes its run at each individual point in the calculated PF. The final population found by *gamultiobj* becomes the starting point for an optimization using *fgoalattain*.

In order to clarify the necessity of conducting MOO between occupant HIC (which depends mainly on the occupant deceleration and indirectly on vehicle deceleration) and peak vehicle deformation, a small experiment is conducted. Let us allow the stiffness of the baseline lumped model to be varied by $\pm 15\%$. The effect of this variation in the stiffness on the HIC and peak vehicle deformation is shown in Figure 3.1. As it can be realized by increasing the structural stiffness, the deformation decreases while the occupant HIC increases at each particular impact speed. Similarly, decreasing the stiffness causes the reverse effect to occur. It is also noticed that the effect of varying the structural stiffness on the HIC values become clearly noticeable as the impact speed increases because it is exponentially proportional to the peak occupant deceleration according to the HIC formula stated in Eqn. (2.24) in Chapter 2.

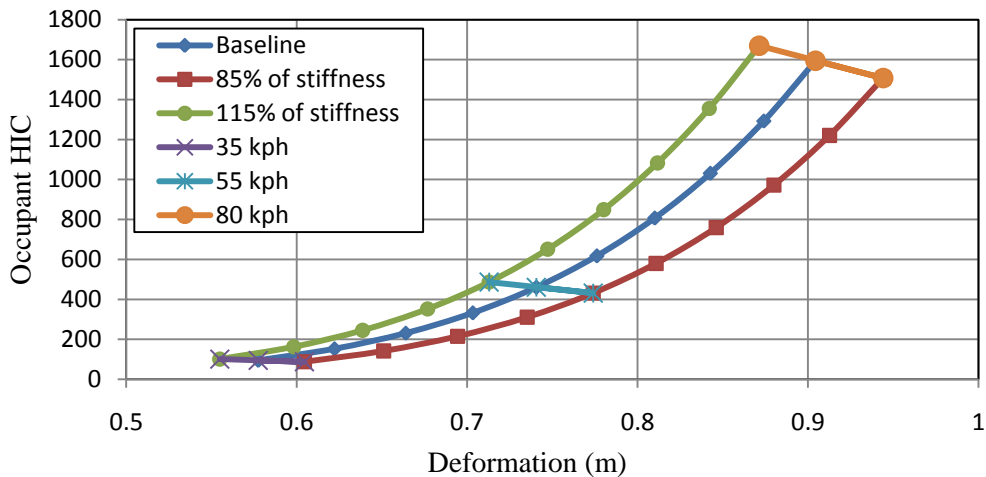


Figure 3.1: Effect of stiffness variation on both occupant HIC and peak vehicle deformation ‘Def’ at different impact speeds.

3.3 Illustrative Optimization Problems

Vehicle structures have nonlinear behavior when they are subjected to frontal crash events. The problem becomes even more complex when different add-on EA elements with nonlinear characteristics are implemented to enhance crashworthiness. The

objective here is to identify the optimal parameters of the add-on EA elements in order to have the optimal enhancement in the crashworthiness performance. In the previous chapter, optimal sets of DVs were identified through conducting a parametric study assuming DVs are discrete with a relatively coarse step size (0.1). In this chapter, single-objective optimization techniques are used to investigate the DVs required to achieve optimal solution for each design performance individually while constraining other design performances. Additionally, a combined objective function composed of different design criteria and using different weighting factors of discrete numbers will be optimized as a single objective function. This is followed by conducting MOO techniques to overcome the drawbacks of using single objective optimization.

Two LMS models, proposed in Chapter 2, are selected for conducting optimization in this study, namely: the extended-integrated dual Voigt (EIDV) and the integrated Voigt (IV) models formulated in sections 2.3.4 and 2.3.6, respectively. The design variables are the multiplication factors for both damping and stiffness coefficients assigned for the add-on EA elements, which are defined as:

$$X = [\lambda_2 \quad \mu_2 \quad \mu_1 \quad \lambda_1] \quad (3.4)$$

where μ_2 , λ_2 , μ_1 , and λ_1 : are damping and stiffness multiplication factors in extended and integrated positions for add-on energy absorbers used in the EIDV model, respectively.

The design vector of the IV model is simply obtained by omitting the first two terms of the vector assigned for the EIDV model. Design variables are allowed to be varied over a specified range assigned for each model where the upper and lower limits used for the EIDV and IV model are: $X_L = [0.1 \ 0.1 \ 0.1 \ 0.1]$, $X_U = [0.3 \ 5.0 \ 2.0 \ 0.3]$, $X_L = [0.1 \ 0.1]$, and $X_U = [5.0 \ 0.8]$, respectively. On the other hand, the performance

measures used are occupant HIC, peak vehicle deformation (Def) and the specific energy absorbed ($Sp.Eng.Abs$). These performances can be used separately, as in the case of the single objective criterion, or collectively, as in combined or multi-objective techniques. Single objective optimization method is conducted for different objective functions without imposing constraints except for optimizing the specific energy absorbed ($Sp.Eng.Abs$), where occupant HIC and vehicle deformation (Def) are constrained to 350 and 55 cm, respectively for both EIDV and IV models.

3.4 Optimization Results

Here the optimization results obtained for both the EIDV and IV models are discussed. For the sake of clarity, these models are again shown in Figures 3.2 and 3.3.

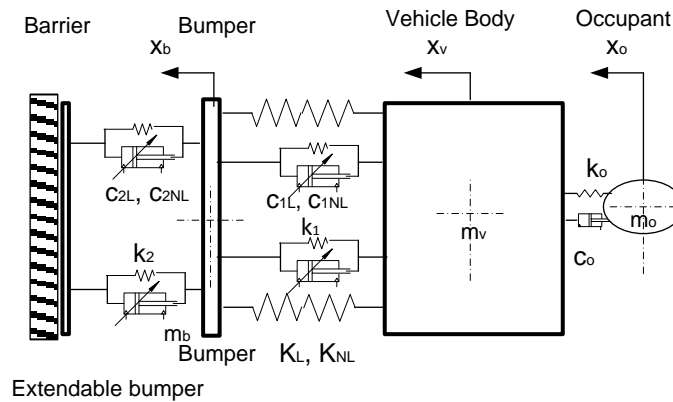


Figure 3.2: Three-DOF lumped-parameter EIDV model in a full frontal impact

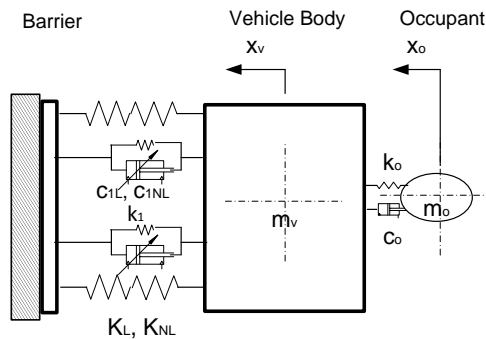


Figure 3.3: Two DOF lumped-parameter IV model with integrated Voigt element

3.4.1 Optimization Results for Extendable-Integrated Dual Voigt (EIDV) Model

Different optimization techniques are applied to the EIDV model. First, single unconstrained objective optimization using two different objective functions, namely HIC and *Def* are conducted. The SQP, GA and Hybrid algorithms have been employed as optimizers in all problems, in an attempt to catch the global optimal, SQP has been run through different randomly generated starting points. Finally, MOO is conducted using the MOGA technique with HIC and *Def* as objective functions.

3.4.1.1 Single Objective Optimization for Occupant HIC

Different starting points are used when conducting optimization using the SQP algorithm to ensure that the optimal values obtained are most likely to represent global minima. Figure 3.4 shows the iteration history of the optimization results using an SQP algorithm at an impact speed of 50 km/h in which HIC has been considered as the objective function. As it can be realized starting with different initial points, the optimizer has converged to the same optimal point.

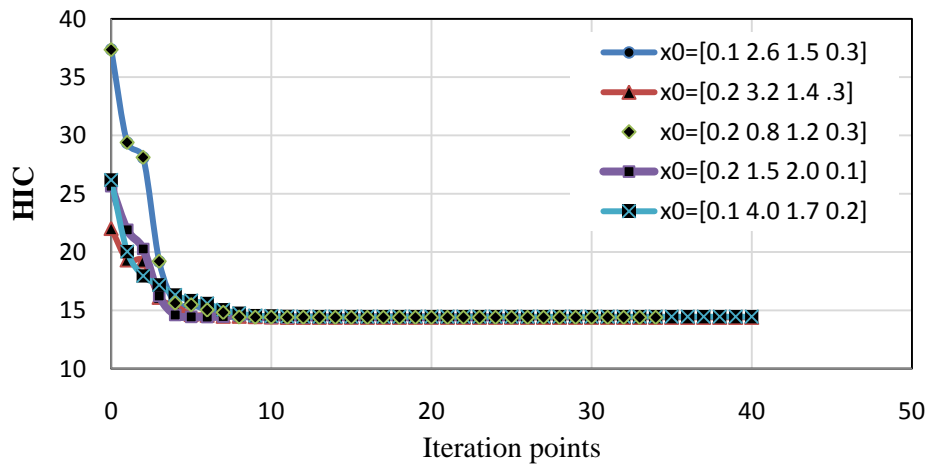


Figure 3.4: Convergence of optimization results using SQP technique for minimization of occupant HIC at an impact speed of 50 km/h using different initial starting points.

The variation of the optimal design parameters λ_2 , μ_2 , μ_1 and λ_1 with respect to impact speeds are shown in Figures 3.5 through 3.8, respectively. The optimal results are generated using SQP, GA and hybrid optimization and compared. As it can be realized, the optimal parameters μ_2 and μ_1 obtained from GA, Hybrid and SQP algorithms are in excellent agreement. This basically confirms that the accuracy of the obtained optimal results.

It is interesting to note that the optimal design variables λ_2 and λ_1 , which represent stiffness multiplication factors of Voigt elements in extended and integrated positions, are nearly constant (0.1) for different impact speeds as shown in Figures 3.5 and 3.8, respectively. On the other hand, the optimal design variables μ_2 and μ_1 , representing damping multiplication factors for Voigt elements in extended and integrated positions, are increasing nearly in linear fashion with respect to the impact speed. This observation reveals that the adaptivity would be needed for the damping coefficients μ_2 and μ_1 .

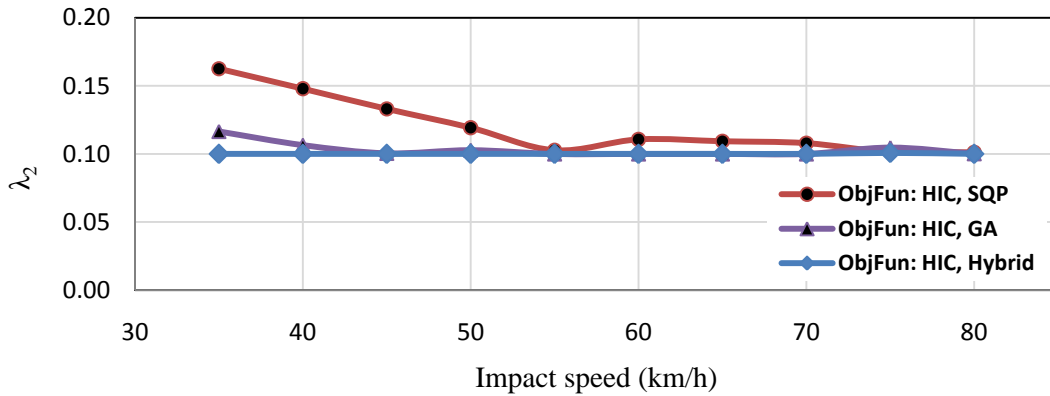


Figure 3.5: Comparison of DV (λ_2) values obtained from different optimization algorithms using HIC as an objective function for the EIDV model at different impact speeds

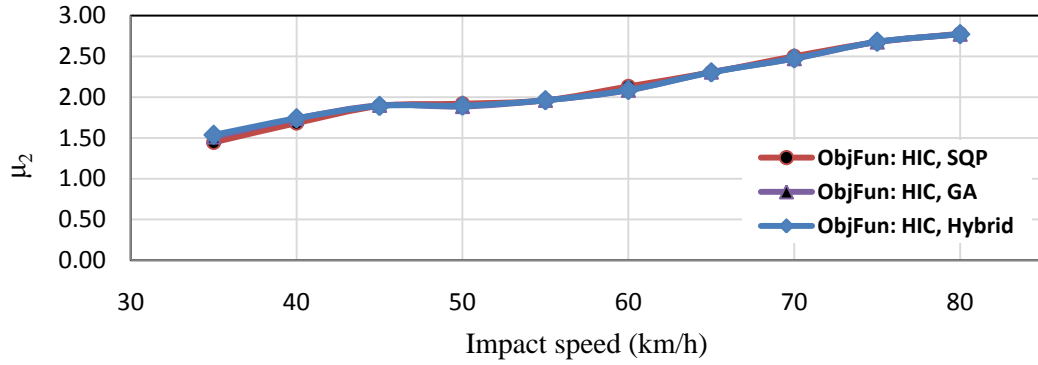


Figure 3.6: Comparison of DV (μ_2) values obtained from different optimization algorithms used in minimizing HIC for the EIDV model at different impact speeds.

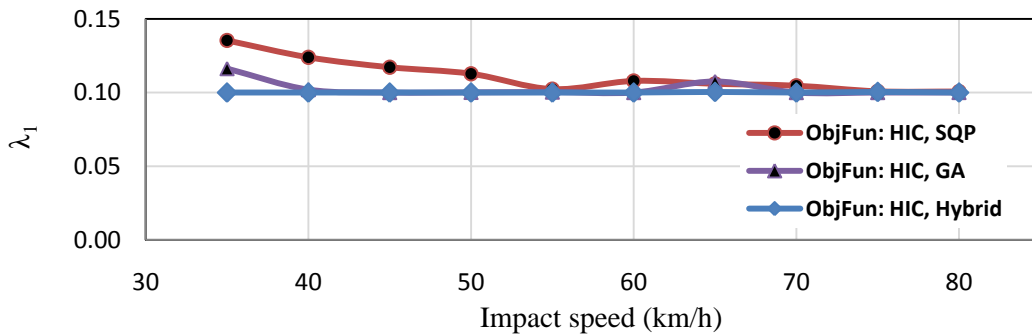


Figure 3.7: Comparison of DV (λ_1) values obtained from different optimization algorithms HIC as an objective function for the EIDV model at different impact speeds

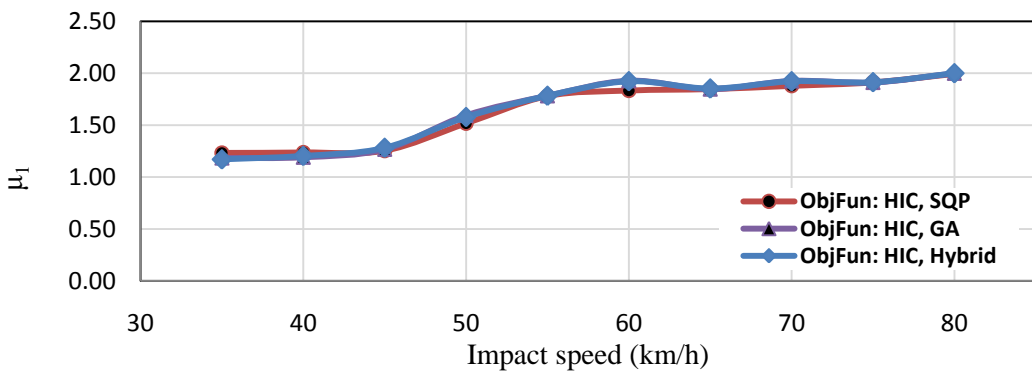


Figure 3.8: Comparison of DV (μ_1) values obtained from different optimization algorithms used in minimizing HIC for the EIDV model at different impact speeds.

The variations of the optimal HIC and the corresponding peak vehicle deformation (*Def*) with respect to impact speeds obtained from different optimization techniques are also shown in Figure 3.9 for the EIDV model.

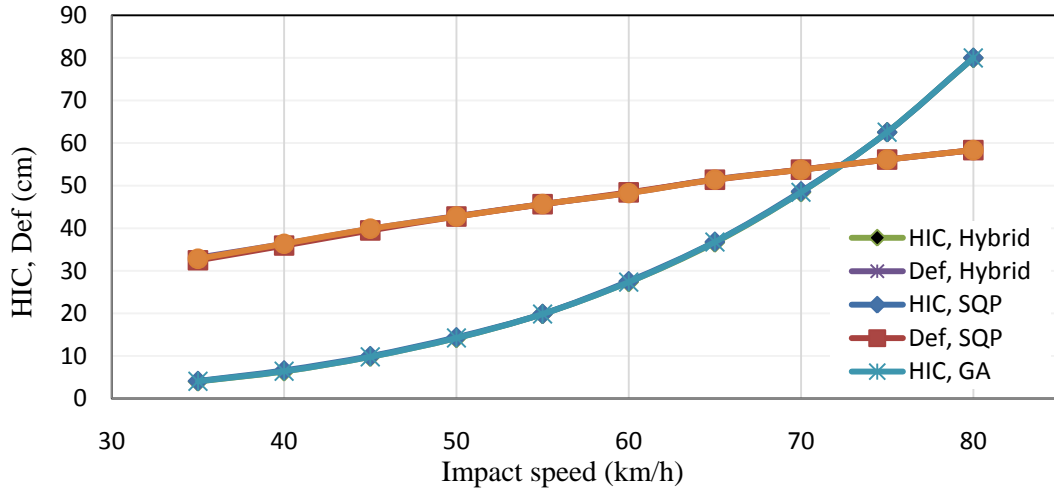


Figure 3.9: Comparison of optimal HIC values and corresponding Def values obtained from different optimization algorithms using different objective functions for the EIDV model

3.4.1.2 Single objective optimization for peak vehicle deformation ‘Def’

The same procedures conducted for occupant HIC as an objective function introduced in section 3.4.1.1, are repeated here using the peak vehicle deformation ‘Def’ as an objective function. Figure 3.10 shows the iteration history for the vehicle deformation at an impact speed of 80 km/h using the SQP optimization method. As it can be seen, optimization result has converged to the almost same optimal solution with different initial starting points.

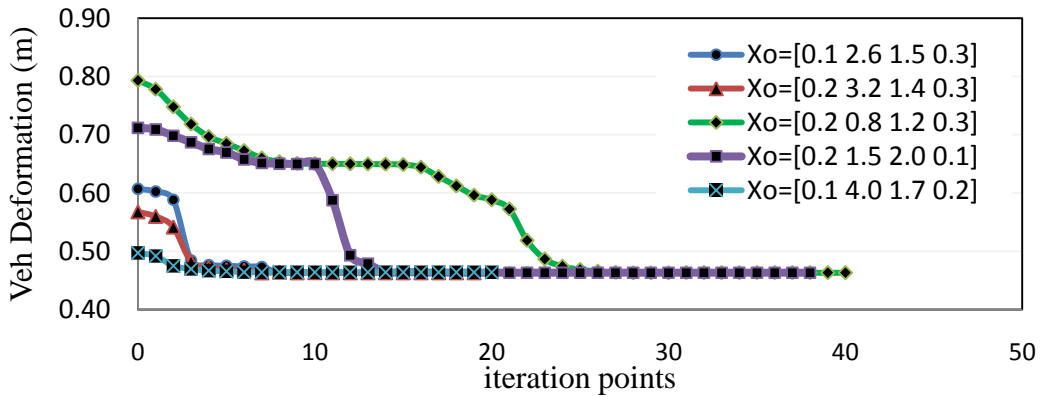


Figure 3.10: Convergence of optimization results using SQP technique for optimal peak vehicle deformation ‘Def’ of the EIDV model at 80 km/h with different starting point.

The variation of the optimal design variables with respect to impact speeds based on SQP, GA, and Hybrid optimization techniques are shown in Figures 3.11 to 3.14. As it can be seen that optimal results obtained by GA, hybrid and SQP optimization techniques are almost similar over the specified range of impact speeds, as in the previous section. However, there is a noticeable difference between optimal results obtained using SQP algorithm and those of GA and Hybrid optimization methods. This confirms that SQP, although simulated from different initial points, was not able to catch the global optimal points at some impact speeds. It is also interesting to note that only optimal design parameter μ_2 associated with the damping coefficient for extended Voigt element varies linearly with respect to impact speeds, as shown in Figure 3.11. The optimal design parameters λ_2 , λ_1 and μ_1 are nearly constants over the specified impact speed range, while the damping parameter in extended add-on EA element μ_1 varies linearly with impact speed, as shown in Figures 3.10 to 3.13.

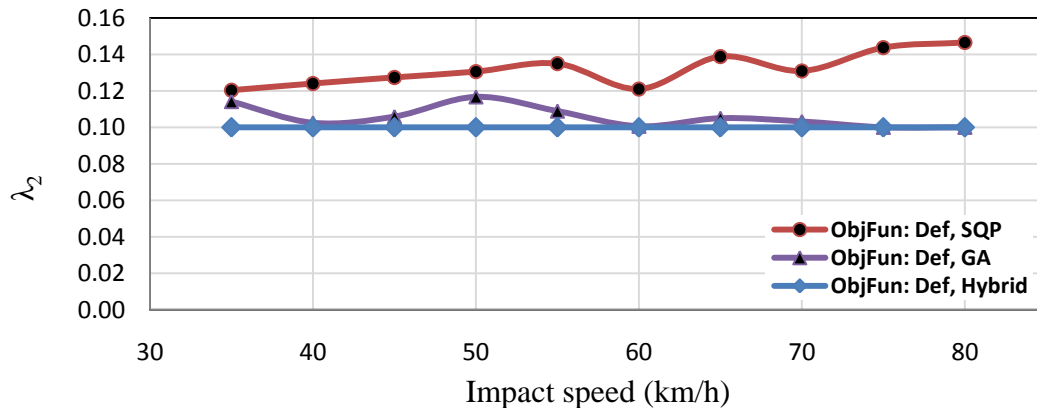


Figure 3.11: Comparison of DV (λ_2) values obtained from different optimization algorithms used in minimizing peak deformation for the EIDV model at different impact speeds

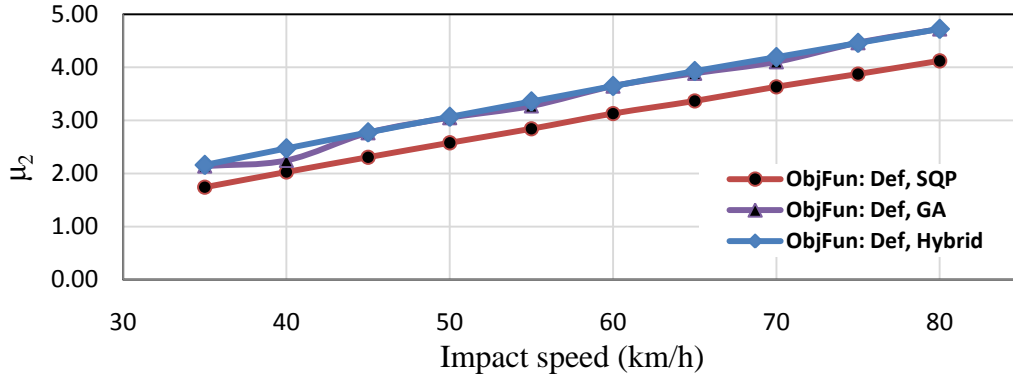


Figure 3.12: Comparison of DV (μ_2) values obtained from different optimization algorithms used in minimizing peak deformation for the EIDV model at different impact speeds

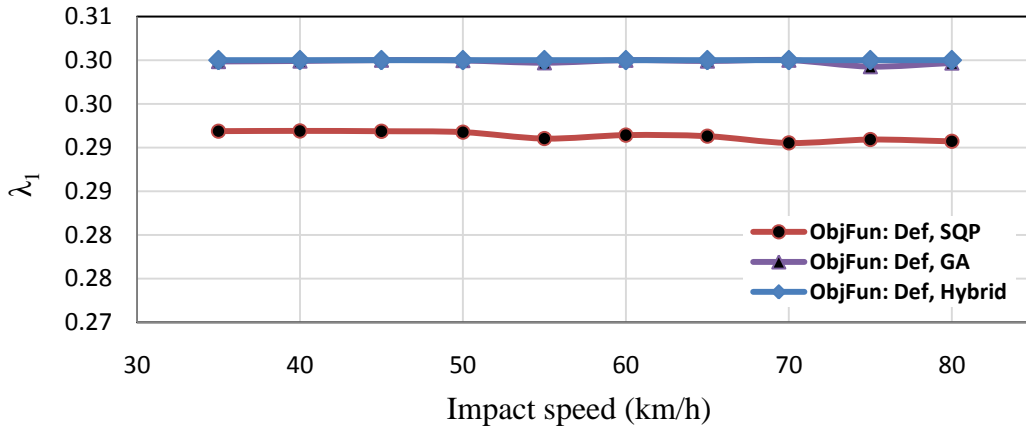


Figure 3.13: Comparison of DV (λ_1) values obtained from different optimization algorithms used in minimizing peak deformation for the EIDV model at different impact speeds

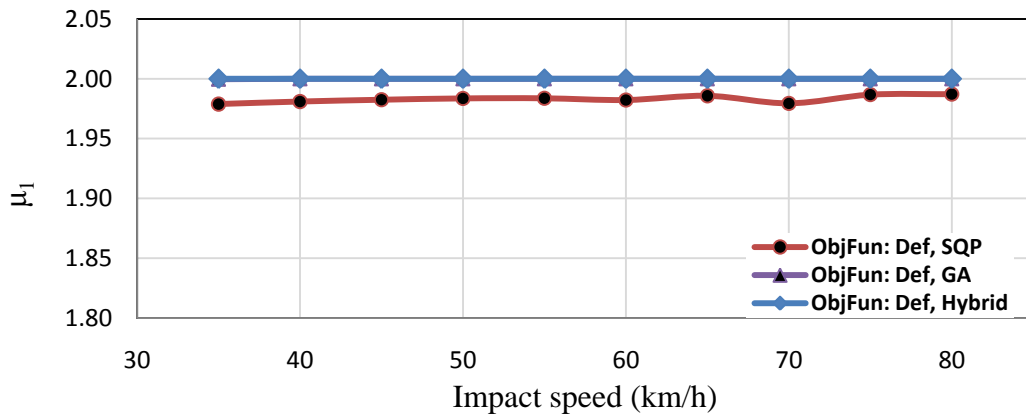


Figure 3.14: Comparison of DV (μ_1) values obtained from different optimization algorithms used in minimizing *Def.* for the EIDV model at different impact speeds

The optimal peak vehicle deformation (*Def*) obtained from different optimization results and the corresponding occupant HIC for different impact speeds are also shown in Figure 3.15. The obtained results agree, to a great extent, with the results obtained from the parametric study conducted in section 2.5.2.

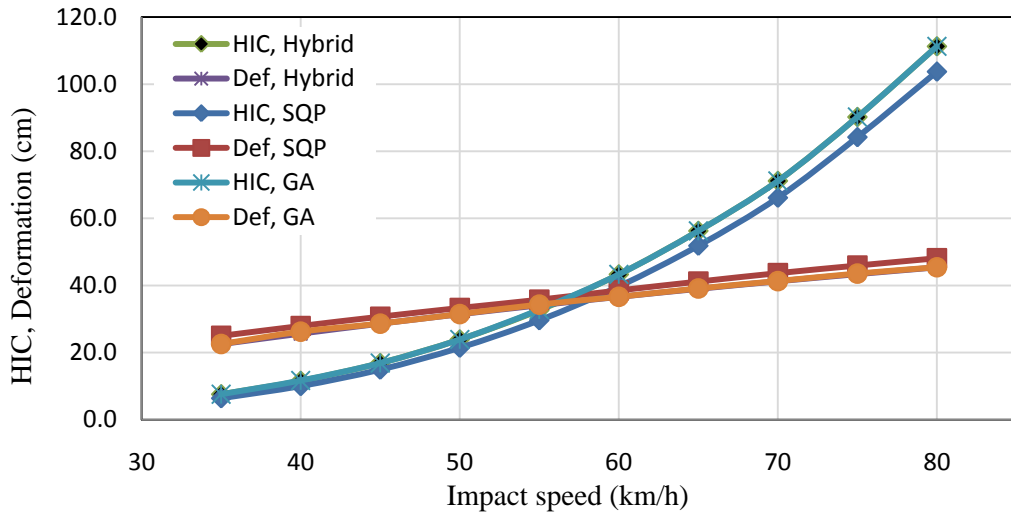


Figure 3.15: Comparison of optimal peak deformation values and the corresponding values of HIC using different optimization algorithms for the EIDV model at different impact speeds.

Figures 3.16 and 3.17 show the variation of occupant HIC and peak vehicle deformation with respect to impact speeds considering HIC, peak deformation (*Def*) and impact energy absorption ratio (IEA-ratio) as a single objective functions for optimizations, respectively and their associated optimal set of DVs at different impact speeds are also tabulated in Table 3.1. As it can be seen from Figure 3.16, the values of occupant HIC corresponding to the optimal specific absorbed energy is slightly higher than those corresponding to the HIC and *Def* as objective functions. This can be interpreted due to the fact that vehicle structure is represented as non-deformable nonlinear spring. Additionally, using specific absorbed energy as an objective generates relatively higher vehicle deformation (*Def*) compared with that considering vehicle

deformation as objective function, while that corresponding to occupant HIC is higher compared with the other values, as shown in Figure 3.17.

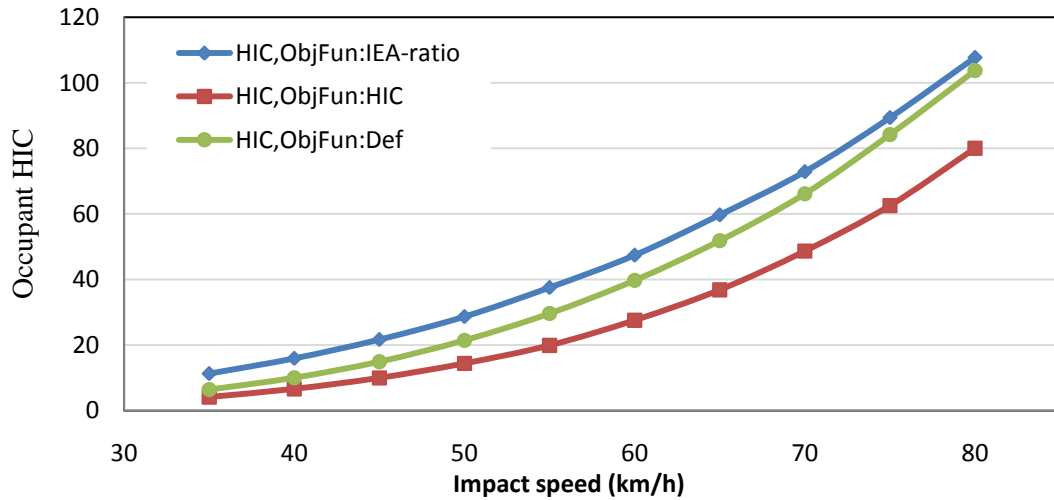


Figure 3.16: Comparison between values of occupant HIC obtained from different optimization algorithms using different optimal targets for the EIDV model

It should also be noted that different single performance criteria exhibit nearly the same trend. The only noticeable difference is the resulting optimal DVs and their variation with respect to the impact speed. As it can be realized that the proposed CEM model will provide variable energy absorption characteristics with respect to impact speed. This means that the add-on EA systems with fixed design parameters over the specified range of impact speeds would not optimally dissipate energy.

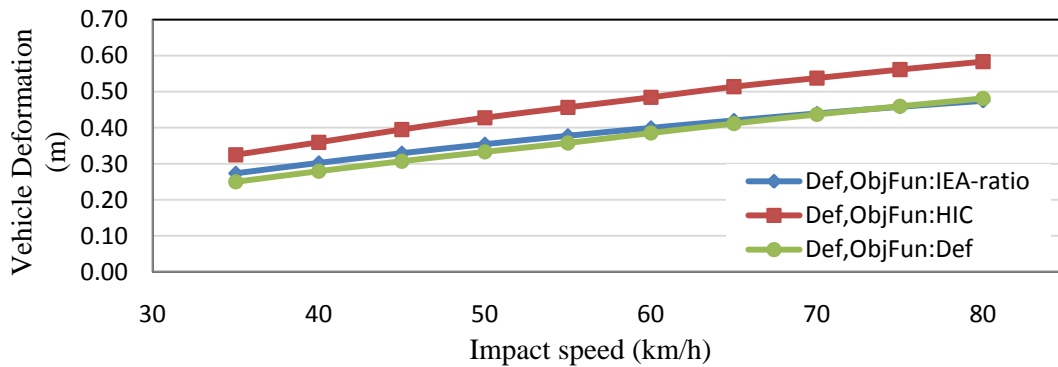


Figure 3.17: Comparison between values of *Def* obtained from different optimization algorithms using different optimal targets for the EIDV Model

The result shows that in order to obtain maximum specific impact energy absorbent (*Sp.Eng.Abs.*), the maximum amount of damping coefficients μ_1 and μ_2 should be utilized while minimizing the add-on stiffness coefficients λ_1 and λ_2 as provided in Table 3.1. However, keeping design variable values at their maximum could lead to crack initiations in the weakest points throughout the load path. It should be noted that the optimal values of specific energy absorbed by the add-on system could not really represent reliable values since there is no permanently deformable vehicle structure, as previously explained in section 2.5.2. As previously discussed, DVs that achieve optimal vehicle deformation are the most preferable and applicable system characteristics since they only need a variation of one damping coefficient and the corresponding HIC values are very low compared to HIC threshold value.

Table 3.1: Comparison of optimal DVs for different single objective functions for *EIDV* model at different impact speeds:

a) Variation of damping multiplication factor μ_2 :

speed (km/h)	35	40	45	50	55	60	65	70	75	80
μ_2 -Def	2.161	2.473	2.774	3.067	3.357	3.648	3.929	4.192	4.459	4.723
μ_2 -HIC	1.537	1.740	1.892	1.895	1.962	2.087	2.303	2.475	2.678	2.772
μ_2 -Sp.Eng.Ab.	5.000	5.000	5.000	5.000	5.000	5.000	5.000	5.000	5.000	4.941

b) Variation of damping multiplication factor μ_1 :

speed (km/h)	35	40	45	50	55	60	65	70	75	80
μ_1 -Def	2.000	2.000	2.000	2.000	2.000	2.000	2.000	2.000	2.000	2.000
μ_1 -HIC	1.170	1.203	1.281	1.578	1.783	1.923	1.853	1.923	1.914	2.000
μ_1 -Sp.Eng.Ab.	2.000	2.000	2.000	2.000	2.000	2.000	2.000	2.000	2.000	1.998

c) Variation of stiffness multiplication factor λ_2 :

speed (km/h)	35	40	45	50	55	60	65	70	75	80
λ_2 -Def	0.100	0.100	0.100	0.100	0.100	0.100	0.100	0.100	0.100	0.100
λ_2 -HIC	0.100	0.100	0.100	0.100	0.100	0.100	0.100	0.100	0.101	0.100
λ_2 -Sp.Eng.Ab.	0.100	0.100	0.100	0.100	0.100	0.100	0.100	0.100	0.100	0.102

d) Variation of stiffness multiplication factor λ_1 :

speed (km/h)	35	40	45	50	55	60	65	70	75	80
λ_1 -Def	0.300	0.300	0.300	0.300	0.300	0.300	0.300	0.300	0.300	0.300
λ_1 -HIC	0.100	0.100	0.100	0.100	0.100	0.100	0.100	0.100	0.100	0.100
λ_1 - Sp.Eng.Ab.	0.100	0.100	0.100	0.100	0.100	0.100	0.100	0.100	0.100	0.105

3.4.1.3 Multi-Objective Optimization using Genetic Algorithm (MOGA)

Two objective functions are assigned for conducting MOO namely: vehicle deformation (*Def*) and the occupant HIC. GA has been used as optimization algorithms that produce a group of non-dominated optimal points in the design space obtained using MOGA technique is shown in Figure 3.18. Figure 3.19 and 3.20 also show Pareto Front (PF) and Anti Pareto Front (APF) curves for different impact speeds respectively. It should be mentioned that the Pareto Frontier (PF) terminology is used to analyze and describe tradeoffs between optimal set of design points between conflicting objectives functions based on evaluation techniques and general selection of DVs [171]. On the other hand, the terminology Anti Pareto Frontier (APF) is used to define the worst sets of design variables and associated objective functions that can be simply obtained by reversing the objectives in the multiobjective optimization problem [33].

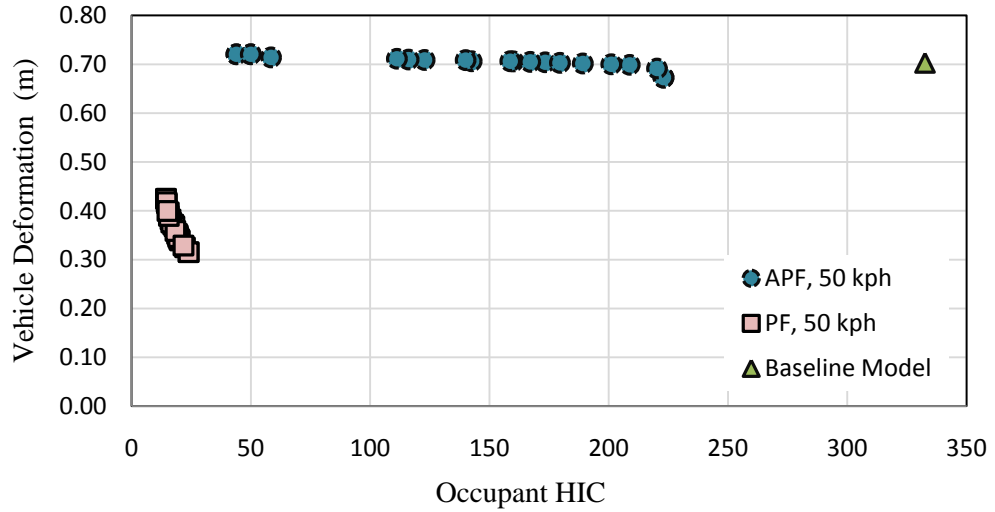


Figure 3.18: Comparisons of Pareto Front (PF) and Anti Pareto Front (APF) curves at a 50 km/h impact speed for the EIDV Model using four DVs

As mentioned before, it is observed that stiffness multiplication factors λ_1 and λ_2 do not vary by changing impact speeds. This is fortunate as direct stiffness variation is very hard to attain as previously described in section 2.3.3. Thus, here it is decided to assume λ_1 and λ_2 to be fixed values of 0.1 and 0.3, respectively, while maintaining the damping factors μ_1 and μ_2 as design variables for the EIDV model.

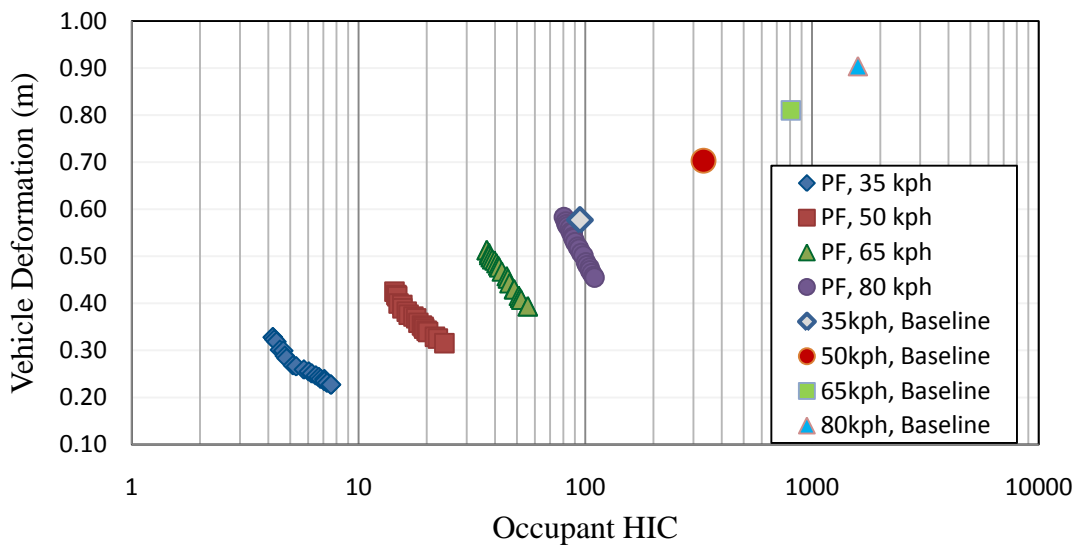


Figure 3.19: Comparison of Pareto Frontier 'PF' curve between the EIDV Model (DV: μ_1 and μ_2) and baseline model at different impact speeds using x-axis logarithmic scale

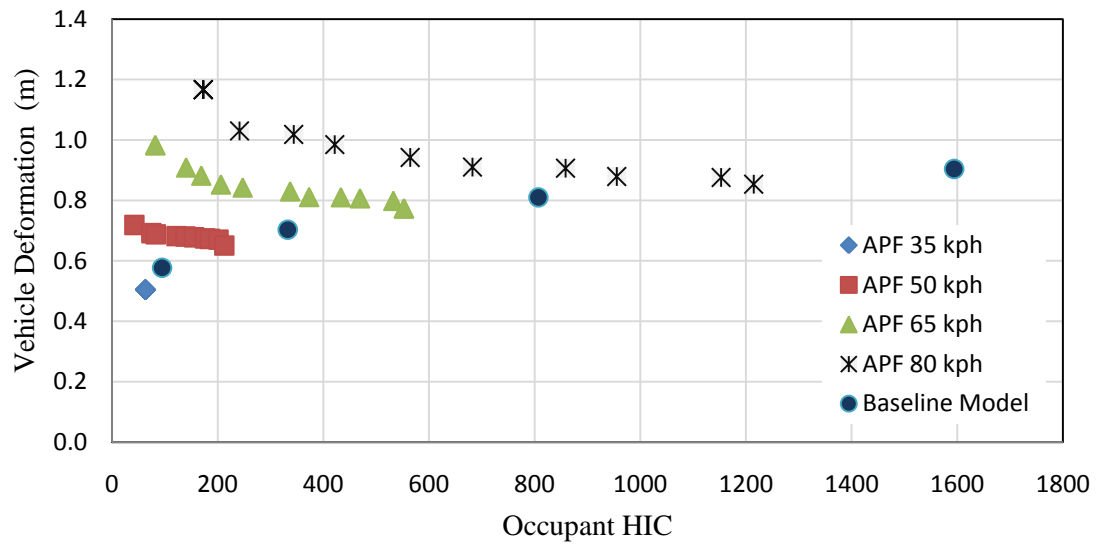


Figure 3.20: Comparison of the Anti-Pareto Frontier (APF) curves between for the EIDV Model (DVs: μ_1 and μ_2) and the baseline model at different impact speeds

3.4.2 Optimization Results for Integrated Voigt (IV) Model

Here, different optimization-techniques that are applied for the IV model, formulated previously in section 2.3.6 and shown in Figure 3.3, are discussed in this section. As mentioned before, for the IV model the design variables (DVs) include only μ_1 and λ_1 .

3.4.2.1 Single Objective Optimization for Occupant HIC

The same procedures conducted for occupant HIC as an objective function in the EIDV model are performed here. The iteration history of HIC based on the SQP algorithm is shown in Figure 3.21. As it can be seen, SQP optimizer has converged to the same optimal solution from different initial design points are shown in Figure 3.21.

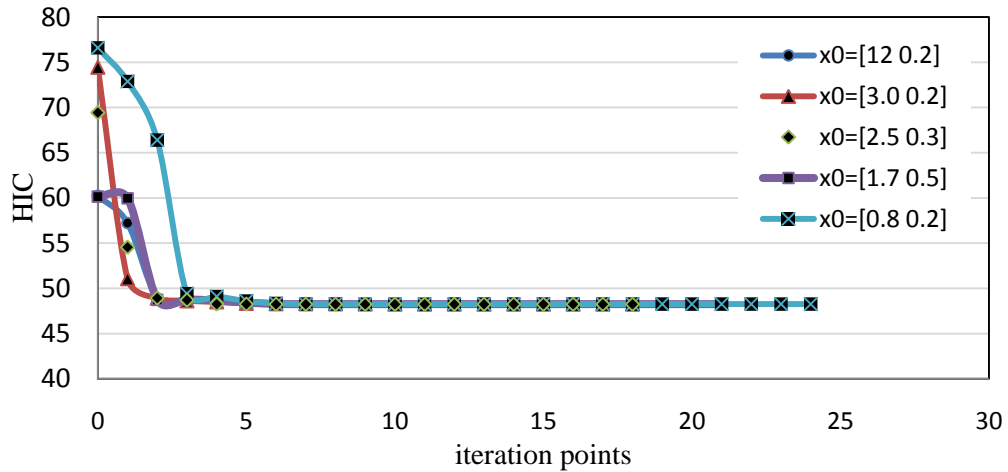


Figure 3.21: Convergence of optimization results using *SQP* technique with optimal occupant HIC using different initial starting points for IV model at 50 km/h impact speed.

Figures 3.22 and 3.23 show the values of the optimal design variables (λ_1 and μ_1) associated with the integrated stiffness and damping elements at different impact speed, respectively. As it can be realized, the optimal results obtained from GA and hybrid optimization algorithms are in very good agreements, while optimal results for λ_1 obtained using SQP have considerable difference with those obtained by GA and hybrid algorithms. On the other hand as shown in Figure 3.23, optimal results for μ_1 obtained from SQP, GA and Hybrid algorithms are in good agreements and almost the same.

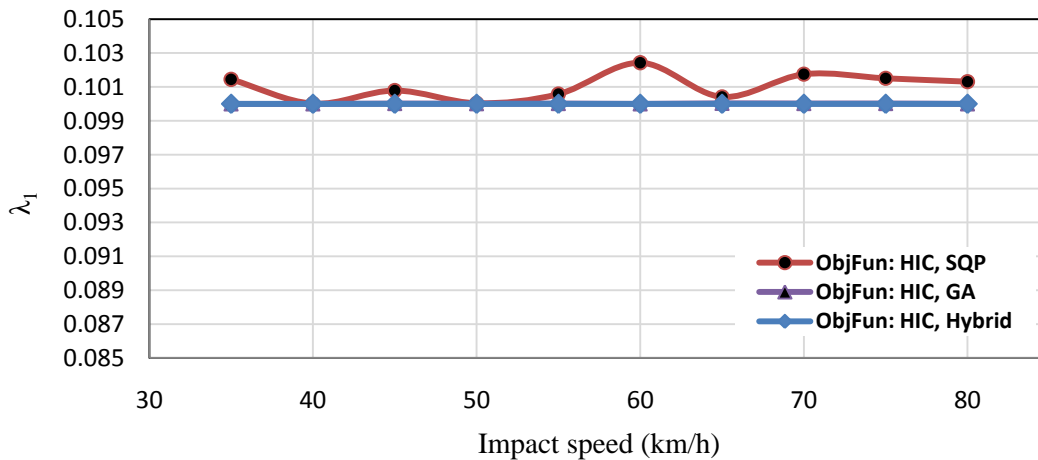


Figure 3.22: Comparison of DV (λ_1) values obtained from different optimization algorithms used in minimizing HIC for IV model at different impact speeds

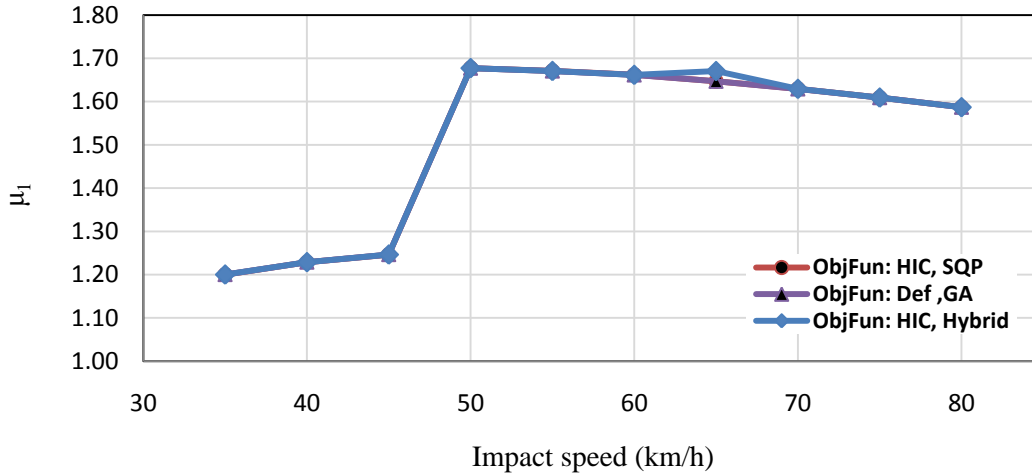


Figure 3.23: Comparison of DV (μ_1) values obtained from different optimization algorithms used in minimizing HIC for the IV model at different impact speeds

Considering Figure 3.22, it is also interesting to note that the optimal stiffness factor λ_1 is nearly constant at 0.1 for all impact speeds. Furthermore, from Figure 3.23 one can realize that the optimal damping factor μ_1 starts at the lower bound of the design range with a gradual increase as the impact speed increases up to 45 km/h speed. This is followed by a relatively sudden increase of μ_2 at an impact speed of 50 km/h. After the impact speed of 50 km/h, μ_1 gradually decreases as the impact speed increase. This can be explained due to the nonlinear behavior of both the add-on damping force and the structural properties as well. It should also be noted that the HIC value should be lower than the assigned threshold limit in this study, which is 350. The objective function HIC obtained from different optimization results and the corresponding peak vehicle deformation (Def) is shown in Figure 3.24. The obtained results agree well with those obtained from the parametric study conducted in section 2.5.2.

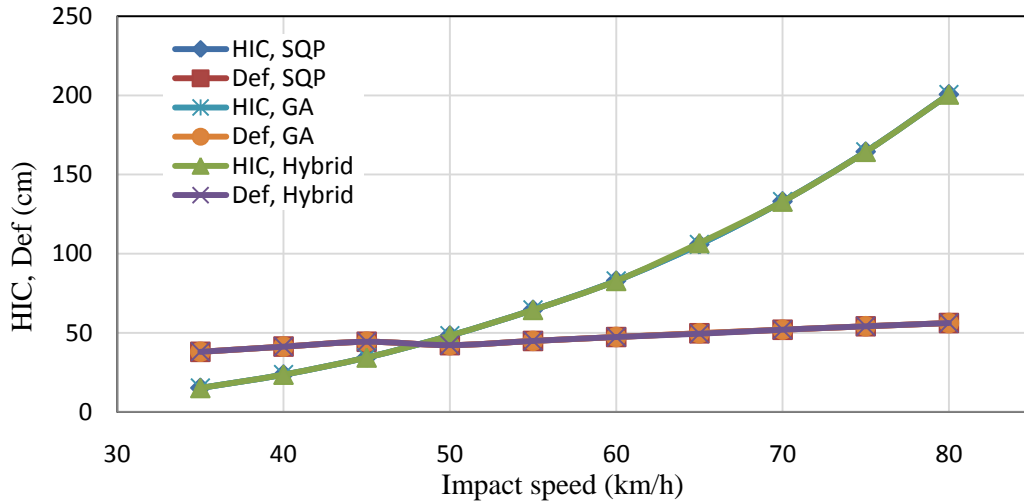


Figure 3.24: Comparison of optimal HIC values and corresponding peak deformation obtained from different optimization algorithms for the IV model

3.4.2.2 Single objective optimization for peak vehicle deformation ‘Def’

The same procedures conducted for occupant HIC as an objective function are repeated here using peak vehicle deformation ‘Def’ as an objective function. The iteration history for vehicle deformation (Def) using the SQP algorithm. Again, it can be realized that the objective function converges to the same optimal solution from all randomly selected initial points, as shown in Figure 3.25.

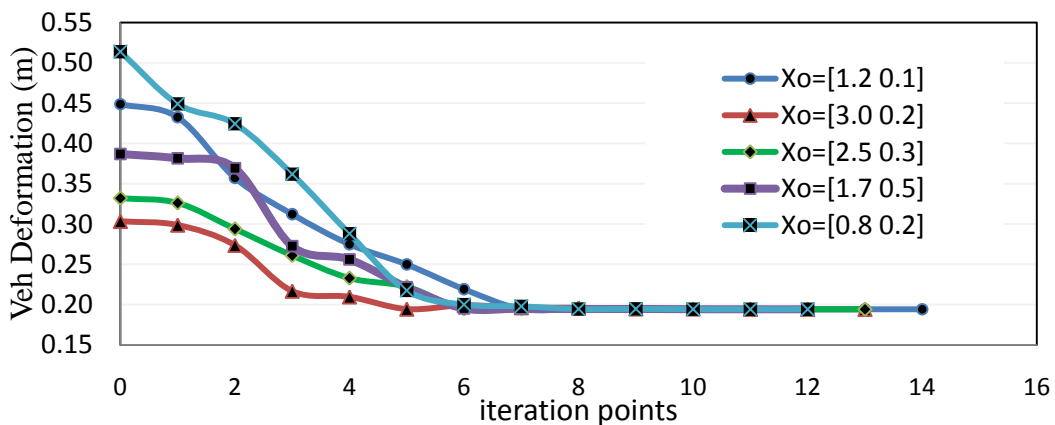


Figure 3.25: Convergence of optimization results using SQP technique with optimal vehicle deformation using different initial starting points for the IV model at 50 km/h.

The variation of optimal DVs μ_I and λ_I with respect to impact speed from different optimization algorithms are also shown in Figures 3.26 and 3.27, respectively.

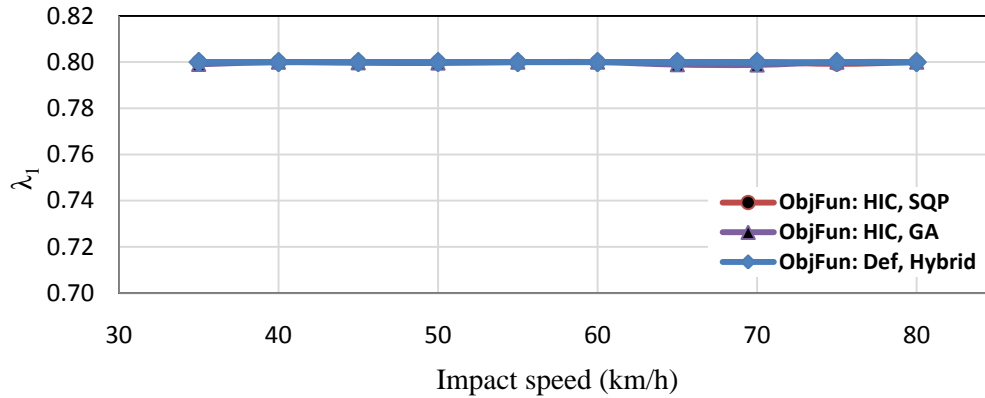


Figure 3.26: Comparison of DV (λ_I) values obtained from different optimization algorithms used in minimizing deformation for the IV model at different impact speeds

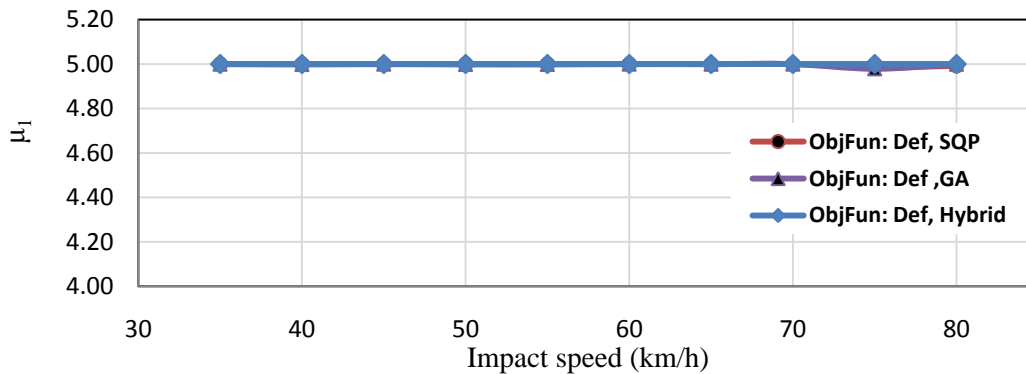


Figure 3.27: Comparison of DV (μ_I) values obtained from different optimization algorithms used in minimizing deformation for the IV model at different impact speeds

As it can be realized the optimal design variables λ_I and μ_I are almost constant on the defined impact speed range. Furthermore, optimal results generated by SQP, GA and Hybrid algorithms are all in excellent agreements. The objective function Def^o obtained from different optimization results and the corresponding peak occupant HIC values are also shown in Figure 3.28. The obtained results are also in agreement with those obtained from parametric study conducted in section 2.5.2.

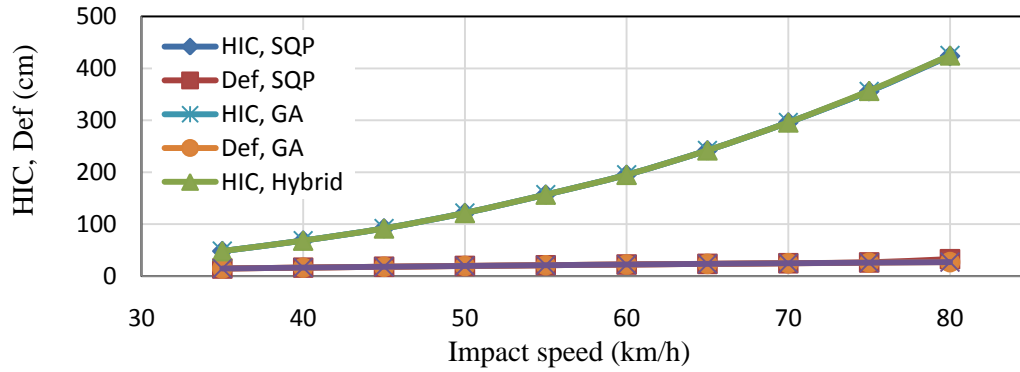


Figure 3.28: Comparison of optimal value of Def and corresponding value of HIC obtained from different optimization algorithms for IV model at different impact speeds

The summary of single objective optimization techniques using different objective functions are tabulated in Table 3.2. As it can be realized in order to obtain maximum specific absorbed energy, the maximum amount of damping coefficient μ_l should be utilized while minimizing the add-on stiffness coefficients λ_l , as shown in Table 3.2.

Table 3.2: Comparison of DVs for different single objective functions for IV model at different impact speeds:

a) Variation of damping multiplication factor μ_l

speed (km/h)	35	40	45	50	55	60	65	70	75	80
μ_l-Def	5.000	5.000	5.000	5.000	5.000	5.000	5.000	5.000	4.855	3.768
μ_l-HIC	1.200	1.229	1.246	1.677	1.671	1.662	1.647	1.630	1.609	1.587
$\mu_l-Sp.Eng.Ab$	5.000	5.000	5.000	5.000	5.000	5.000	5.000	5.000	5.000	4.152

b) Variation of stiffness multiplication factor λ_l

speed (km/h)	35	40	45	50	55	60	65	70	75	80
λ_l-Def	0.800	0.800	0.800	0.800	0.800	0.800	0.800	0.800	0.799	0.800
λ_l-HIC	0.101	0.100	0.101	0.100	0.101	0.102	0.100	0.102	0.102	0.101
$\lambda_l-Sp.Eng.Ab$	0.100	0.100	0.100	0.100	0.100	0.100	0.100	0.100	0.100	0.100

3.4.2.3 Multi-Objective Optimization using the Genetic Algorithm (MOGA)

Again the two contradicting objective functions are assigned for multiobjective optimization method, are peak vehicle deformation ' Def ' and occupant HIC. As shown in Figure 3.29, MOGA yields a group of optimal points forming Pareto Frontier curve in the design space that contains all optimal design points. Clearly MOGA enable the designer, the chance to choose the optimal configuration based on preference of the most affecting design performance. Additionally, the worst design configurations of the IV model (APF) falls below or nearby the baseline model, which clearly indicates the degree of enhancement achieved by the proposed IV model.

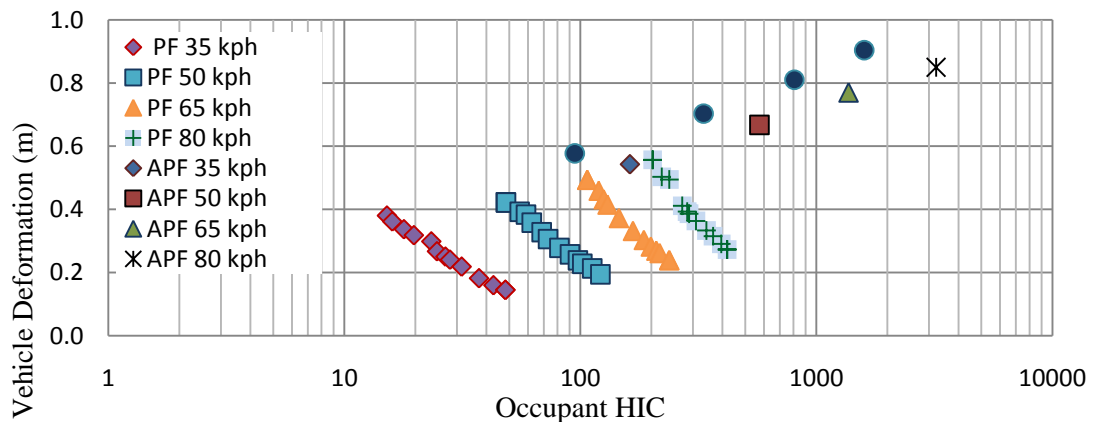


Figure 3.29: Comparison between PF and APF curves at different impact speed for the IV model using MOGA technique and baseline model.

3.5 Performance Analysis and Comparison of the Results

In this section, optimization results obtained from multiobjective optimization (MOO) techniques for both EIDV and IV models are discussed and the results are compared with the baseline model performance. For convenience and ease of comparison, the two anchor points, which are the outmost point on the curve, obtained

from PF and APF curves for each model are compared with respect to the design performance of the baseline model.

It was concluded before that using only the two DVs corresponding to the damping factors (μ_1 and μ_2) for the EIDV model while fixing the stiffness factors (λ_1 and λ_2) provide more or less the same optimal results as if four DVs (μ_1, μ_2, λ_1 and λ_2) is considered. As it is clearly shown from Table 3.3, and Figures (3.30 and 3.32), the values of design variables and objective functions obtained from four and two design variables for the EIDV model are in good agreements. From comparing the behavior of EIDV and IV models, it was also shown that the EIDV model achieves a better degree of enhancements than those achieved by the IV model. Furthermore, the design performance of both HIC and *Def* of the baseline model is located near the worst design performance represented by the APF curves in both models.

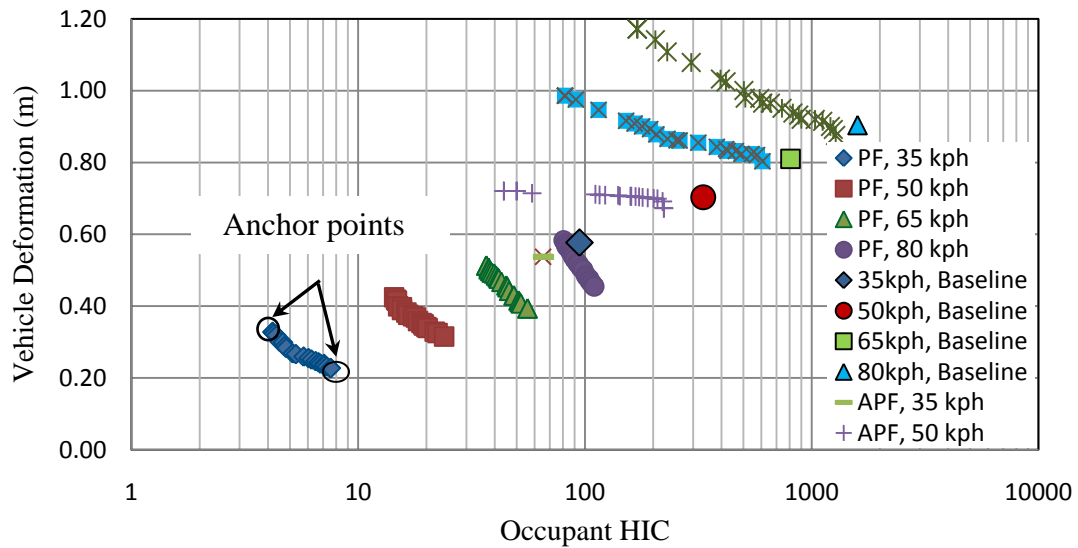


Figure 3.30: Comparison between the PF and APF for EIDV model with the baseline model at different impact speeds using x-axis in logarithmic scale

It is very interesting to note that measuring the variations of design variables of the upper and lower anchor points of PF curve at different impact speeds are consistent with the results obtained from single objective optimization using HIC or *Def* as objective functions respectively. The variation of DVs at the upper (UPR) and lower (LWR) anchor points of PF curves for the EIDV model at different impact speeds is shown in Figure 3.31.

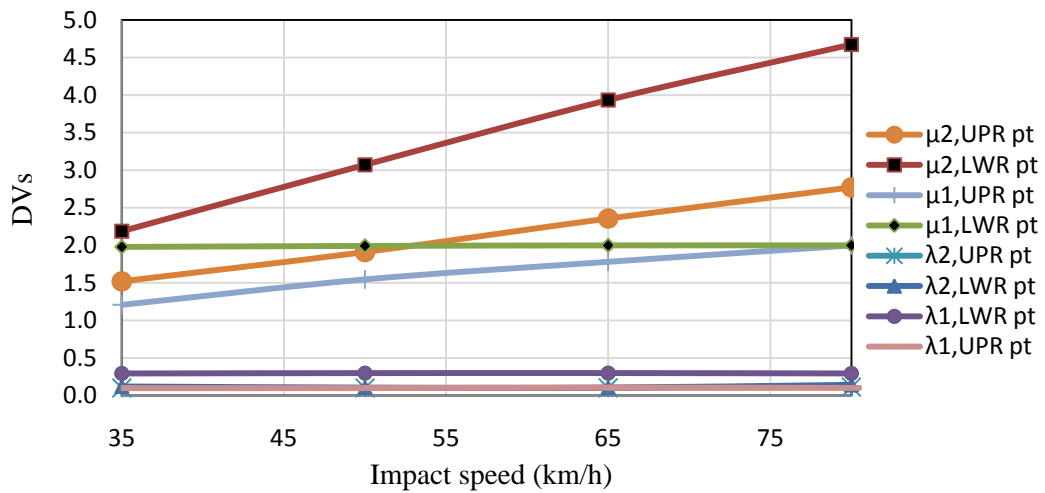


Figure 3.31: Variations of design variables for the EIDV model at anchor points of PF curves at different impact speeds for EIDV model

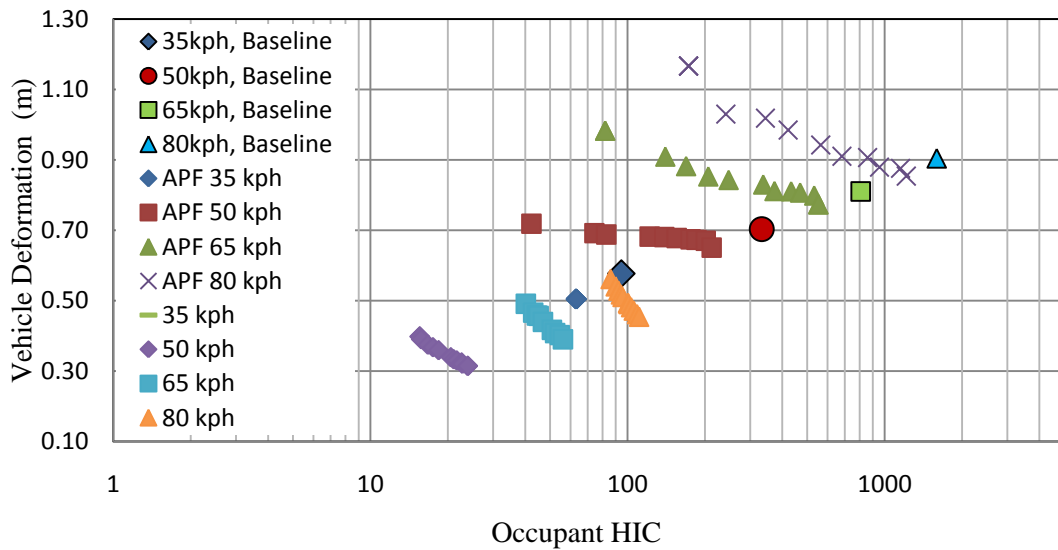


Figure 3.32: Comparison between the PF and APF for EIDV model with the baseline model at different impact speed using two design variables: μ_1 , μ_2

Comparing the results with those previously obtained based on two DVs, it can be concluded that using only two design variables in conducting multiobjective optimization for the EIDV model provides optimal results comparable with those obtained using four design variables, as demonstrated in Table 3.3.

Table 3.3: Comparisons of system performance at anchor points of PF and APF curves of the EIDV model with baseline model performance measures at different impact speeds using four design variables (μ_1, μ_2, λ_1 and λ_2) and two design variables (μ_1, μ_2)

Models	35 (km/h)		50 (km/h)		65 (km/h)		80 (km/h)	
	HIC	Def	HIC	Def	HIC	Def	HIC	Def
Baseline Model	94.66	0.577	332.58	0.703	807.1	0.81	1,594.16	0.904
4DVs, UPR AP, PF	4.19	0.3280	14.40	0.4247	36.77	0.5131	80.50	0.5832
4DVs, LWR AP, PF	7.56	0.2273	23.93	0.3152	55.81	0.3938	109.92	0.4547
4DVs, UPR AP, APF	65.43	0.5375	43.92	0.7205	81.70	0.9861	170.18	1.1715
4DVs, LWR AP, APF	65.89	0.5370	222.96	0.6729	606.50	0.8033	1275.83	0.8754
2DVs, UPR AP, PF	4.47	0.3015	15.56	0.3980	40.22	0.4910	85.92	0.5614
2DVs, LWR AP, PF	7.60	0.2250	23.92	0.3143	56.07	0.3900	110.90	0.4543
2DVs, UPR AP, APF	62.97	0.5046	42.28	0.7185	81.87	0.9829	172.70	1.1665
2DVs, LWR AP, APF	63.31	0.5040	212.48	0.6505	552.62	0.7734	1214.74	0.8538

Figure 3.33 also shows the PF and APF obtained for IV model using MOGA technique and its comparison with the baseline model. The value of Anchor Points of PF and APF curves in Figure 3.33 at different impact speed is provided in Table 3.4.

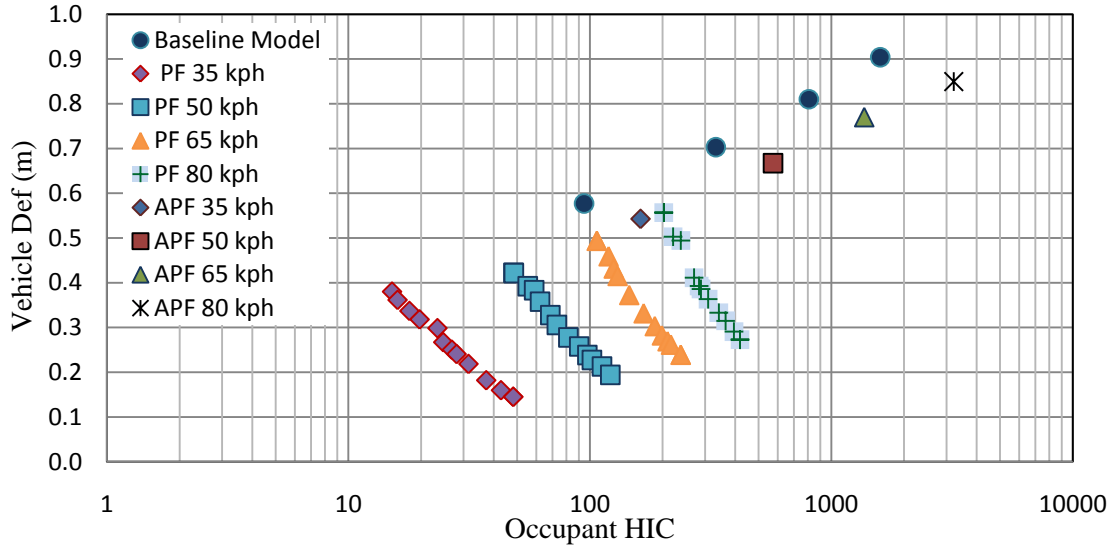


Figure 3.33: Comparison between the PF and APF of the IV model with the baseline model at different impact speeds using x-axis logarithmic scale.

Table 3.4: Comparison of the system performance at anchor points of PF and APF curves of the IV Model with baseline model at different impact speeds

Obj. Fn	35 (km/h)		50 (km/h)		65 (km/h)		80 (km/h)	
Models	HIC	Def	HIC	Def	HIC	Def	HIC	Def
Baseline Model	94.66	0.577	332.58	0.703	807.1	0.81	1,594.16	0.904
UPR AP, PF	15.16	0.3801	48.28	0.4223	106.90	0.4939	202.37	0.5568
LWR AP, PF	48.13	0.1449	121.55	0.1942	237.95	0.2393	418.64	0.2728
UPR AP, APF	162.15	0.5426	573.65	0.6672	1368.83	0.7702	3214.98	0.8496

The variation of design variables at upper and lower anchor points of the IV model is also shown in Figure 3.34. The lower anchor point needs the maximum utilization of the damping and stiffness which varies slightly at different impact speeds. On the other hand, the optimal design performance at the upper anchor points provides stiffness factor much lower than those at lower anchor points, while keeping damping factors at reasonable range. Thus optimal design values at the upper anchor points are particularly more desirable.

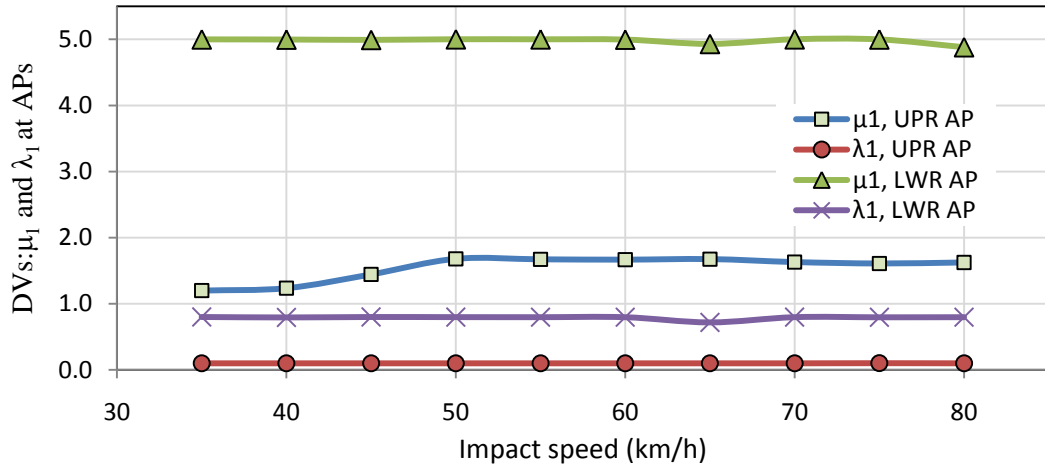


Figure 3.34: Variations of design variables at anchor points of PF curves at different impact speeds for the IV model

It should be noticed that the variation of design variables at the anchor points of PF curve have the same trend and are closely matched to the single objective optimization of both HIC and vehicle deformation. Figure 3.35 compares the EIDV and IV model at anchor points of PF curves at different impact speeds. The values at anchor points are also tabulated in Table 3.5. As it can be observed, EIDV model provides more crashworthiness enhancement compared with the IV model.

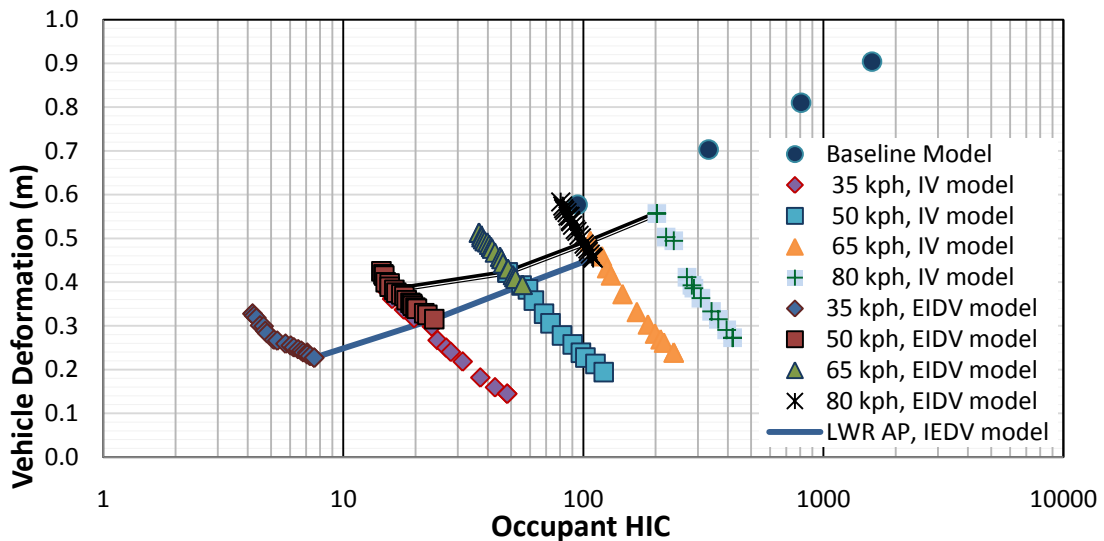


Figure 3.35: Comparison between the Pareto Frontier (PF) curves of the EIDV and IV models with baseline model at different impact speeds in x-axis logarithmic scale

Table 3.5: Comparison between EIDV and IV models at both anchor points of Pareto Frontier curves with the baseline model and at different impact speeds

Models	35 (km/h)		50 (km/h)		65 (km/h)		80 (km/h)	
	HIC	Def	HIC	Def	HIC	Def	HIC	Def
Baseline Model	94.66	0.577	332.58	0.703	807.1	0.81	1,594.16	0.904
UPR AP, EIDV model	4.47	0.3015	15.56	0.3980	40.22	0.4910	85.92	0.5614
LWR AP, EIDV model	7.60	0.2250	23.92	0.3143	56.07	0.3900	110.90	0.4543
UPR AP, IV model	15.16	0.3801	48.28	0.4223	106.90	0.4939	202.37	0.5568
LWR AP, IV model	48.13	0.1449	121.55	0.1942	237.95	0.2393	418.64	0.2728

3.6 Summary

Both single and multiobjective optimization problems have addressed in this chapter. Different optimization techniques based on SQP, GA and Hybrid optimization techniques have been applied to find optimal solution for single objective function HIC and peak deformation (Def). Initial points are selected randomly for SQP algorithm, and it has been shown that the result generally converge to the same optimal solutions. Moreover, optimal results based on SQP, GA and Hybrid optimization algorithms are generally in good agreements, although some deviation exists between optimal results obtained from SQP and those based on GA and Hybrid optimization algorithms for some design parameters at different impact speeds. This may be attributed to the local optimum points which may have been caught by SQP. Multiobjective optimization between conflicting design performance has been done using GA and PF and APF curves have been generated and optimal design points have been compared with those of baseline model. It has been demonstrated that the EIDV model provides better crashworthiness

performance compared with the IV model. This can be attributed to the fact that the EIDV model has an extended distance, which allows the reduction of the impact velocity and absorption of impact energy without affecting the peak value of vehicle crash pulse.

CHAPTER 4

CRASH ENERGY MANAGEMENT ANALYSES OF VEHICLES WITH ADD-ON ENERGY ABSORBES

4.1 Introduction

The two- and three-DOF lumped-parameter models of the vehicle-occupant system, presented in chapter 2, permit analyses of energy dissipation potentials of the add-on passive and adaptive absorbers in a highly convenient and efficient manner. The crash energy management of a vehicle, however, strongly relies on energy absorption of the structural members attributed to their plastic deformations. Such analyses are performed via large scale FE models [172-176], which would be computationally demanding for design and analyses of the add-on energy absorbers.

Considering the greater computationally efficiency of the lumped-parameter models, Kamal [43], Kamal and Wolf [177] and Lin et al. [37] proposed lumped-parameter representations of various structural members considering their elastic and plastic deformation behaviors so as to study the crash behavior of the total vehicle. The studies have characterized the force-deflection properties of various components under increasing and decreasing loads leading to crush of the component. These were measured for the torque box, front frame, firewall, sheet metal, radiator, etc. A lumped-parameter model of a vehicle was subsequently formulated and validated by Kamal [43], Kamal and Wolf [177] and Lin et al. [37]. The model has also been applied to study the effectiveness of a damped under-ride guard and crash energy management of the total vehicle [48].

The lumped-parameter model considering the elastic-plastic deformation behaviors of various substructures could be efficiently applied to study the performance

potentials of add-on energy absorbers and crash energy management of the total vehicle. The development of such a model, however, requires characterizations of force-deformation characteristics of structural components under high loads leading to crush. For the purpose of design and analysis of add-on energy absorbers and their contributions to the total crash energy management, the lumped parameter model proposed by Kamal [43], Kamal and Wolf [177] and Lin et al. [37] may be applied. This would also permit relative analyses of different configurations of add-on devices in an efficient manner considering the energy absorption of the structural components. The proposed model, however, was developed for a relatively heavier automobile with total mass of 1945 kg [38,157]. Considering that the masses of modern vehicles are generally smaller and the crash energy management and distribution strongly depends on the component and vehicle masses, it would be desirable to develop a model for a lighter vehicle. Owing to the lack of force-deflection data of various components, the reported model may be appropriately scaled for relative analyses of add-on absorbers. It should be mentioned that scaling techniques have been extensively used in vehicle structure designs under crash analyses [172-176].

In this chapter, the lumped-parameter model of the baseline vehicle, proposed by Kamal [43], Kamal and Wolf [177] and Lin et al. [37], is formulated and enhanced to incorporate occupant, seat and restraint system. A scaling technique is proposed to drive a model of vehicle mass similar to that considered for the simplified lumped-parameter models (1500 kg). The integrated and extendable energy absorbers, proposed in Chapter 2, are subsequently introduced in the model to study their performance potentials in crash energy management using optimal set of design variables obtained in Chapter 3.

4.2 Baseline Model Formulation and Validation

The baseline vehicle model is represented as a three-DOF lumped-parameter model with eight nonlinear springs representing force-deflection properties of different structural components, as shown in Figure 4.1. This model was proposed to describe the crash behavior of a sedan with front-engine and rear-axle drive. The model comprises three rigid bodies representing the main body, engine and suspension. The vehicle frontal sub-structure designed to absorb impact energy in the form of potential energy except for a small portion in rebound movement, is represented by eight nonlinear springs, some of which exhibit considerable clearance. The equations of motion of the baseline vehicle model are formulated as:

$$m_1 \ddot{x}_1 = -F_1 - F_3 - F_4 - F_5 + F_8 \quad (4.1)$$

$$m_2 \ddot{x}_2 = -F_6 - F_7 - F_8 + F_3 + F_5 \quad (4.2)$$

$$m_3 \ddot{x}_3 = -F_2 + F_1 + F_7 \quad (4.3)$$

where m_1 , m_2 and m_3 are vehicle body, engine and suspension masses, respectively. x_1 , x_2 and x_3 are longitudinal deflections of these masses, respectively. The notations F_1 to F_8 represent the nonlinear dynamic forces of the torque box, front frame, driveline, sheet metal, firewall, radiator, engine mounts and transmission mount, respectively, and C_4 , C_5 and C_6 are the clearances associated with sheet metal, firewall and radiator structures, respectively.

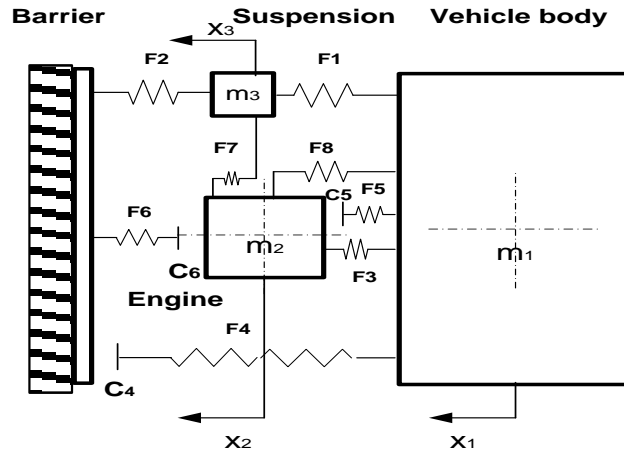


Figure 4.1: Three-DOF lumped-parameter model of the vehicle subject to an impact with a rigid barrier [37,43,157]

The initial clearances C_4 and C_5 of the sheet metal and firewall structure were specified as 7.62 and 10.16 cm, respectively. The clearance C_6 , however, describes the dynamic radiator clearance, the difference between allowable engine displacement and the radiator effective thickness prior to the loading [157]. The dynamic radiator clearance C_6 was reported as 20.32 cm, which was validated using the dynamic crash data. The values of lumped masses were taken as 1451, 340 and 154 kg for m_1 , m_2 and m_3 , respectively, while the bumper mass was taken as 50 kg. The total mass that contributed to kinetic energy during the impact was thus considered as 1945 kg.

4.2.1 Method of Analysis

The responses of the structural components under an impact load could be evaluated by considering different load paths, coupling the rigid barrier to the primary masses, namely the body and engine masses, as shown in Figure 4.2. There exist two primary load paths transferring the load to the body mass, the upper and lower load paths. The upper load path concerns the resisting force due to the sheet metal (F_4), which includes the power-plant, wheels and suspension. Whereas the lower path that concerns

with the longitudinal members that are separated into two parts at the engine cross-member, namely the front frame (F_2) and the torque box (F_1), as shown in Figure 4.2. On the other hand, the load path for the engine mass is represented by the radiator assembly denoted by F_6 . The inertia force due to the engine mass is subsequently transferred to the body mass indirectly through the engine and transmission rubber mounts, (F_7 and F_8), and directly through the deformation to driveline (F_3) and the firewall (F_5). It should be mentioned that the engine mass is assumed to be mounted at its front end on the engine cross-member via the rubber mounts (F_7), where the cross-member is fixed in the mid-span of longitudinal members. In addition, the rear end of the engine, coupled with the transmission, is mounted on the rubber mount (F_8) to the underbody (vehicle mass, m_1).

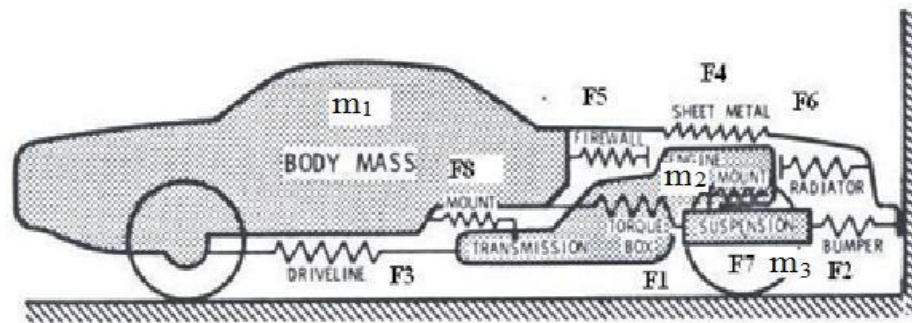


Figure 4.2: Schematic of vehicle components illustrating different load paths in frontal car impact [157]

During a frontal impact, the impact load is transmitted from the rigid barrier to the vehicle body through both upper and lower load paths by crushing sheet metal and the longitudinal members. At the same time, the engine mass continues to move forward and its inertia force is transmitted to the rest of the load carrying members through engine rubber mounts and to the underbody mass via transmission mounts. During the initial stage of the impact, the engine mass inertia force imposes increasing load on the front frame (F_2) and decreasing load on the torque box (F_1). This state would continue until the

engine crushes the radiator (F_6) and comes to a stop against the barrier. Henceforth, the body mass and the frontal substructure crush the driveline (F_3) and the transmissions mount (F_8) against the engine until the latter comes in contact with the firewall (F_5). Meanwhile, the vehicle body approaches to a rest position reducing the frontal substructure to approximately the engine length.

In order to briefly illustrate how load paths concepts are applied during the simulation process, the structural deformation at the beginning of an impact is visualized. At the instant of a crash event, the three lumped masses move with the same initial velocity ($\dot{x}_1(0) = \dot{x}_2(0) = \dot{x}_3(0) = V_0$) that causes the front frame (F_2) member to resist the impact force and undergoes deformation, as it lies between the bumper/rigid barrier and the suspension mass. This is followed by deformation of the torque box (F_1), where deformation and deformation rate may be small, as it couples two moving lumped masses, m_1 and m_3 . In this initial stage, the remaining structural members, except for the elastic deformations of the rubber mounts, do not incur notable deformation. This is mostly attributed to the clearances among different members, especially the large radiator clearance (C_6). The resisting forces due to the structural members are subsequently computed based on the deformation and deformation rate responses together with the force-deflection data of each structure. This permits to determine if a structure member is engaged in the crash energy management at a particular time step of the simulation process. A structural member may also undergo repetitive partial relaxation or unloading phase followed by reloading as it approaches the loading zone (Z_I), as seen in the dynamic load-deflection curve of Figure 4.3. It should be noted that a structural member under impact load is subjected to continuous compression until the maximum

compression utilization is attained or member fracture is reached. The figure shows that the dynamic resisting force of a component is a function of its deformation and deformation rate. Figure 4.3 illustrates generic behavior of structural components subject to impact load [178]. The generic form of the nonlinear dynamic force developed is represented by F_i , and is related to the deflection δ_i and the rate of deflection $\dot{\delta}_i$ and is defined in seven different loading/unloading zones in the following manner:

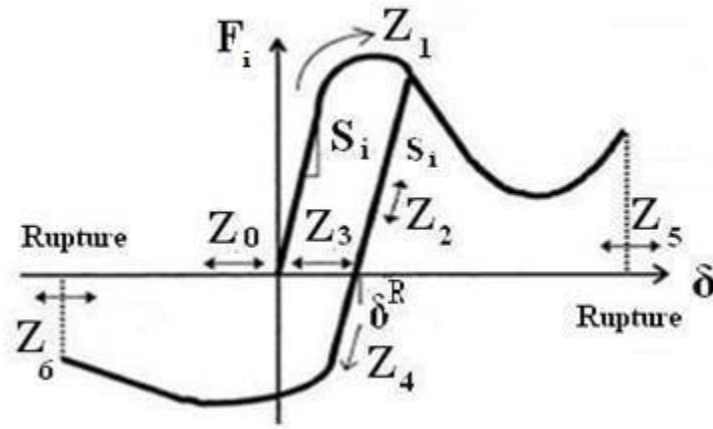


Figure 4.3: Generic dynamic load deflection characteristics [157]

$$F_i = (1 + K \dot{\delta}_i) f(\delta_i) \quad \text{loading in the forward direction} \quad (\text{zone } Z_1) \quad (4.5)$$

$$F_i = S_i (\delta_i - \delta_i^R) \quad \text{the unloading/reloading case} \quad (\text{zone } Z_2) \quad (4.6)$$

$$F_i = (1 - K \dot{\delta}_i) f_{RWD}(\delta_i^R - \delta_i) \quad \text{loading in the backward direction} \quad (\text{zone } Z_4) \quad (4.7)$$

$$F_i = 0 \quad \text{loading zones:} \quad (\text{zone } Z_0, Z_3, Z_5 \text{ and } Z_6) \quad (4.8)$$

where $f(\delta_i)$ and $f_{RWD}(\delta_i)$ define the static load-deflective curves under forward and reverse loadings, respectively, obtained through experimental tests; K is a Dynamic Load Factor (DLF) and S_i is the slope of the elastic loading or unloading curve, δ_i^R is the permanent plastic deformation and i is the i^{th} structural member ($i=1, \dots, 8$).

Each structural member undergoes the loading and unloading zones indicated in Figure 4.3, while the loading in the rearward direction is applicable only to the rubber mounts, F_7 and F_8 . The dynamic load factor (K) assumes a value of 0.621% per km/h of impact speed for all structural members. Furthermore, the deflections δ_i and the rate of deflection $\dot{\delta}_i$ represent the relative longitudinal displacement and velocity across the component, respectively. In addition, the slopes S_i of unloading/reloading phase may not be identical to that in the elastic loading zone. The deflections δ_i , where $i=1,\dots,8$, of various structural members are related to the generalized coordinates in the following manner:

$$\begin{aligned}
 \delta_1 &= x_1 - x_3; & \delta_2 &= x_3; & \delta_3 &= x_1 - x_2; \\
 \delta_4 &= x_1 - C_4; & \delta_5 &= x_1 - x_2 - C_5; & \delta_6 &= x_2 - C_6; \\
 \delta_7 &= x_2 - x_3; & \text{and} & & \delta_8 &= x_2 - x_1
 \end{aligned}
 \tag{4.9}$$

It should be noted that for an accurate analyses of the frontal crash response would require thorough characterizations of crash test data of main load carrying members in the simulation process. Furthermore, the static load-deflection data would also be necessary to predict collapse modes of different components that would permit design targets based on identification of optimum distribution of component collapse modes [157,178]. It has been shown that crashworthiness of vehicle structures depends largely on the collapse behavior of its structural components and their connectivity [178]. Failure modes are important for accurate crash simulation since the measured force-deflection curves should have the same patterns and sequences of collapse mechanisms that would take place in the real crash test. The static load-deflection curves for different structural members considered in the model are illustrated in Figure 4.4 through Figure

4.11. These have been measured under loading/unloading of a structural member in structural assembly, while constraining the adjoining members appropriately [177].

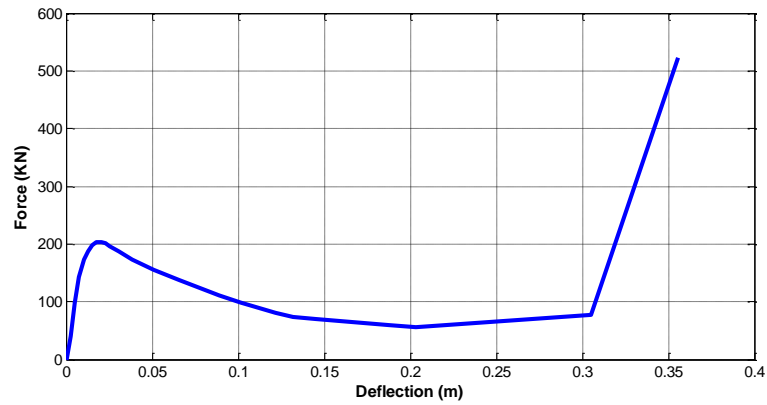


Figure 4.4: Static load-deflection curve for the torque box structure (F_1) [37].

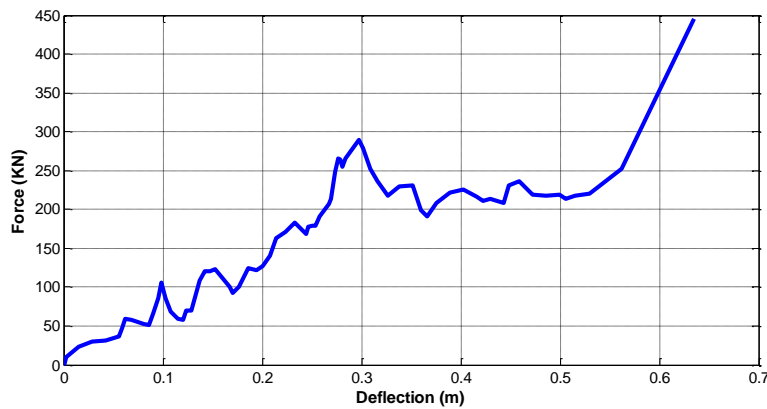


Figure 4.5: Static load-deflection curve for the front frame structure (F_2) [37].

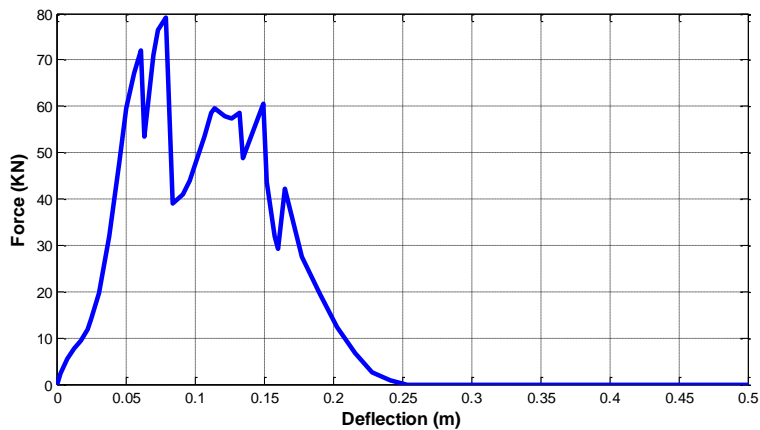


Figure 4.6: Static load-deflection curve for the driveline structure (F_3) [37].

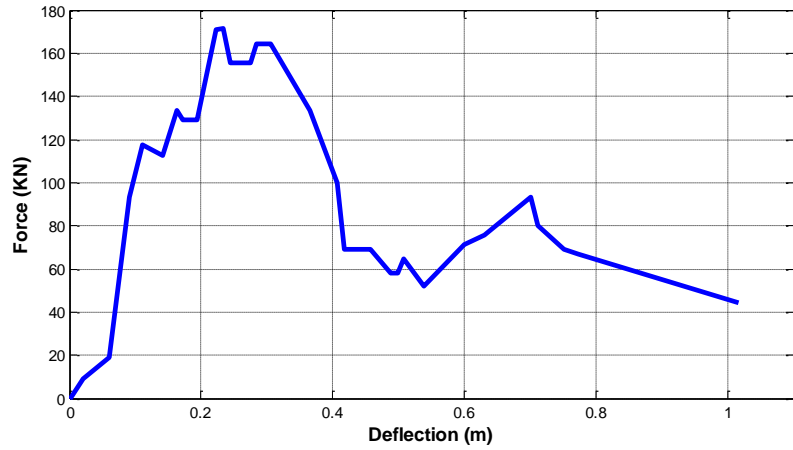


Figure 4.7: Static load-deflection curve for the sheet metal structure (F_4) [37].

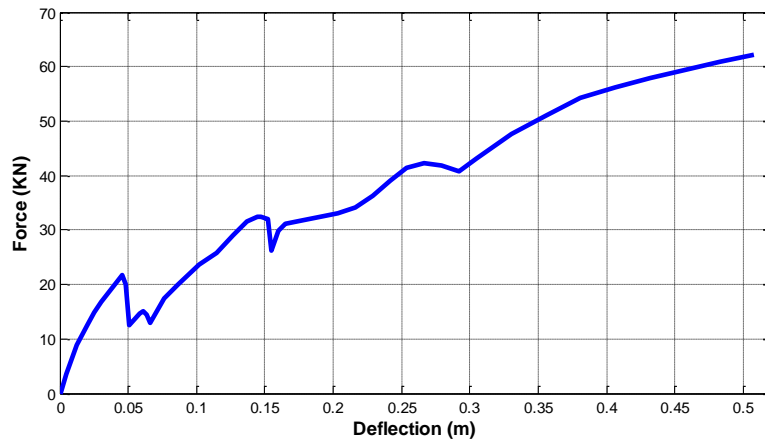


Figure 4.8: Static load-deflection curve for the firewall structure (F_5) [37].

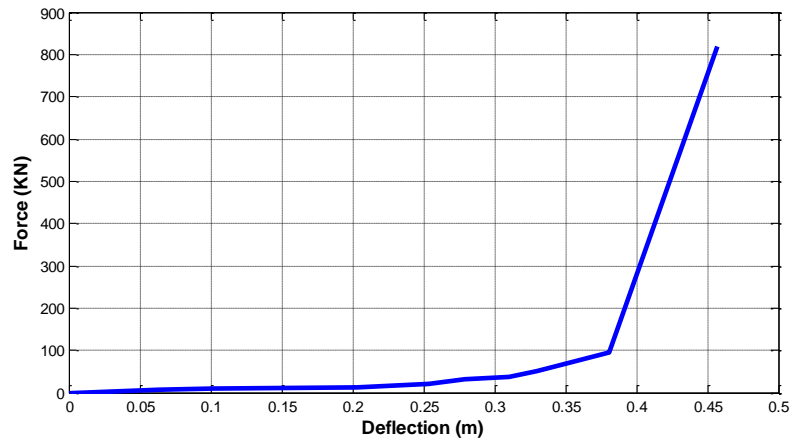


Figure 4.9: Static load-deflection curve for the radiator structure (F_6) [37].

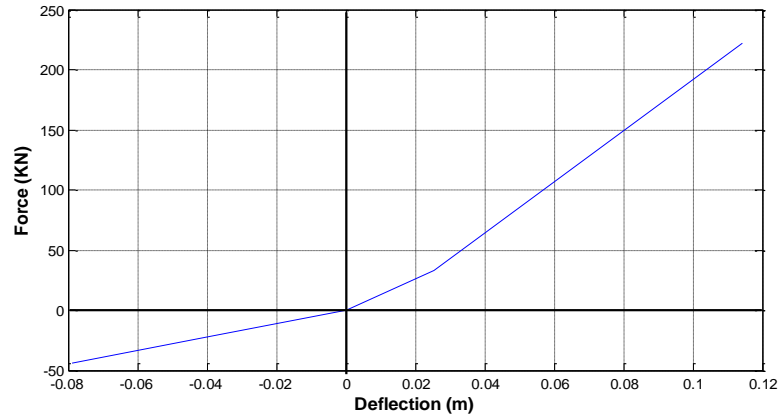


Figure 4.10: Static load-deflection curve for the engine mounts structure (F_7) in forward and rearward directions [37].

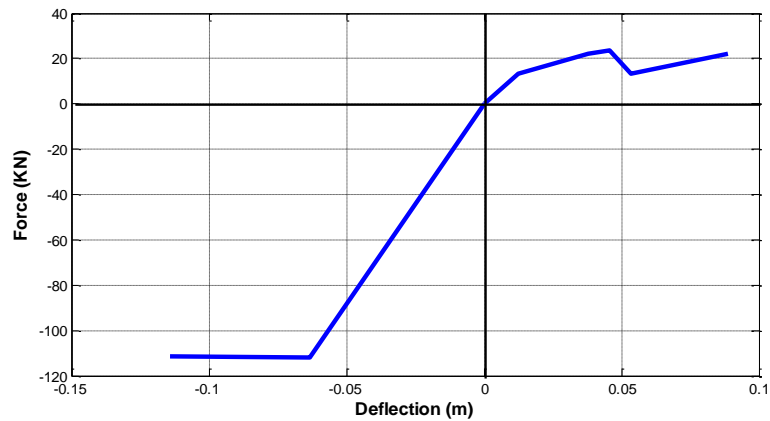


Figure 4.11: Static load-deflection curve for the transmission mount (F_8) in forward and rearward directions [37].

The crash responses of the vehicle model are evaluated using the force-deflection properties of various structural members shown in Figures 4.4 to 4.11 through solutions of the equations of motion. The analyses are conducted subject to the following simplifying assumptions [37,177]:

- Structural integrity of the passenger compartment is maintained throughout the impact.
- The inertia force of each component is significantly smaller than the relative collapse strength and the failure modes of structural components under static and

dynamic loads are similar. Consequently, the static load-deflection data is considered sufficient for estimating dynamic crash force by employing dynamic load factor [177].

- The barrier is assumed to be perfectly vertical, fixed and non-deformable.
- The resistance force of each structural component is a function of the crush distance and rate of deformation (crush rate). The effect of impact speed (crush rate) is added to the dynamic load.
- The vehicle is symmetric about its vertical central plane with negligible pitch, roll and yaw motions.
- Each structural element is represented by its inelastic deflection behavior, except during unloading/reloading conditions, where the structure is assumed to undergo elastic deflection.

4.2.2 Validation of the Baseline Model

The baseline model is analyzed under an initial velocity of 56 km/h and the dynamic responses of different masses and structural members are compared with those reported in [38] to demonstrate the validity of the modeling process. Figure 4.12 illustrates comparison of displacements, velocity, deceleration responses of the masses m_1 , m_2 and m_3 with those reported in [37]. The comparisons show reasonably good agreements in the displacement and velocity response with only small deviations, which are attributed to estimations of some of the model properties. The deceleration responses of the vehicle body and the engine mass also compare well with the reported responses, as seen in Figure 4.12 (c), while the deceleration response of the suspension mass was not reported in [37].

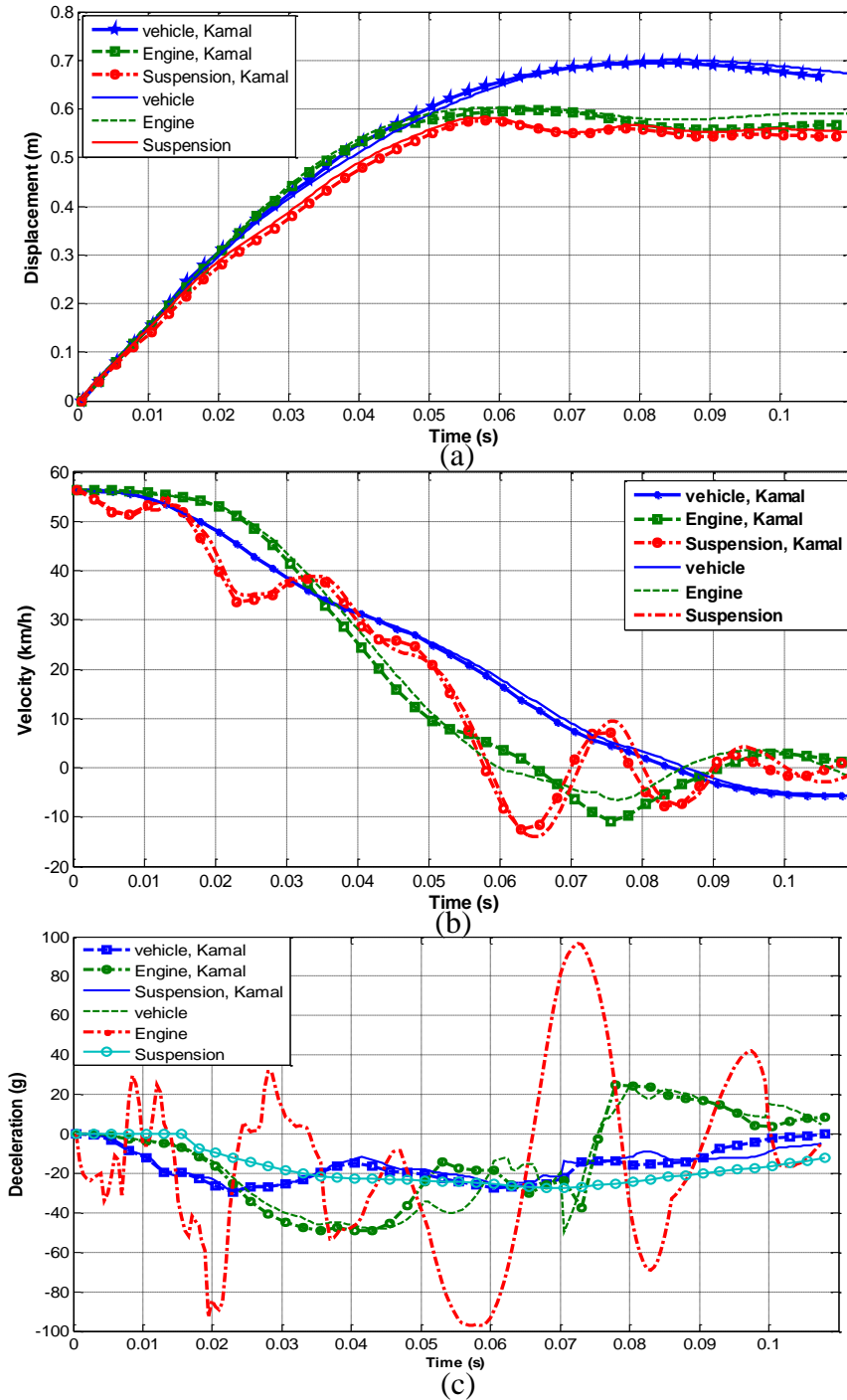


Figure 4.12: Comparison of dynamic responses of different bodies of the model with reported responses [37]: (a) displacement; (b) velocity; and (c) deceleration

It also needs to be noted that the results presented in Figure 4.12 were attained over a simulation period of 110 ms for the purpose of comparisons with reported results.

Figure 4.13 illustrates the simulation results for the three masses over a duration of 200

ms. The results show that the accelerations approach their respective steady values near 0 g, while the rebound velocity approaches 5.65 km/h. The maximum deformation or dynamic crush distance approaches approximately 0.7 m, as shown in Figure 4.13 (a).

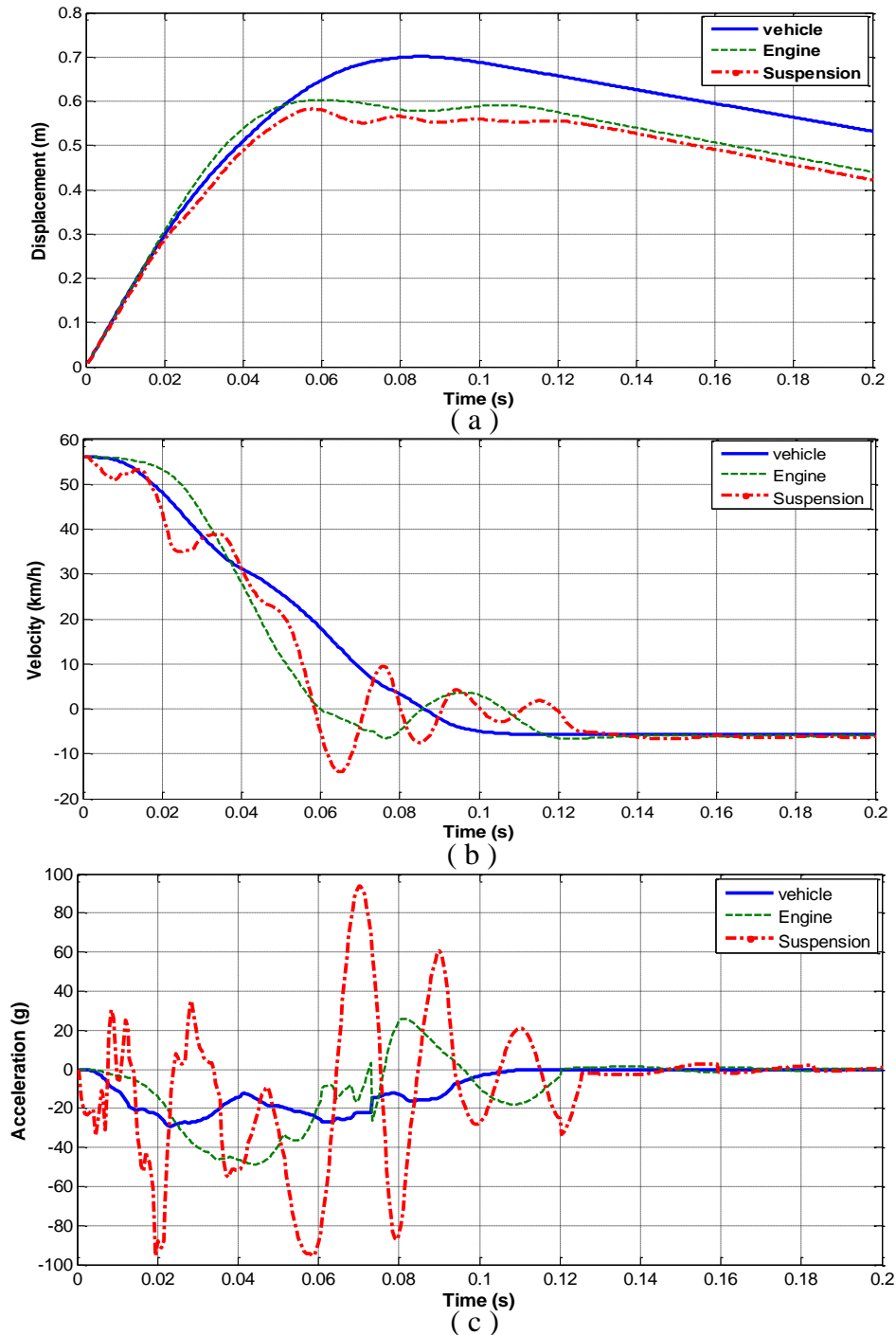


Figure 4.13: Dynamic responses of different bodies of the model in a 56 km/h frontal impact with a rigid barrier: (a) displacement; (b) velocity; and (c) acceleration.

The results in Figure 4.12 and 4.13 show that the deceleration response of the suspension or cross member mass oscillates significantly at a relatively low frequency, and the peak magnitude approaches near 90 g. This deceleration magnitude is significantly higher than those of the engine and vehicle body masses, which approach approximately 50 g and 30 g, respectively. This is in-part attributed to relatively low mass of the suspension compared with the engine and vehicle masses and in-part to relatively lower stiffness of the engine mounts that couple the suspension mass with high inertia of the engine.

The simulations were also performed to derive variations in forces and dynamic force-deflection responses of different structural components, as shown in Figures 4.14 and 4.15, respectively. The torque box F_1 and front frame F_2 structures undergo loading, unloading and reloading over the simulation period of 150 ms, as seen in Figure 4.14. The front frame yields the highest force in the order of 360 kN in the early impact stage, near 22 ms. The torque and the sheet metal also yield peak forces during the early impact stage (~22 ms). All of the components yield forces in the positive direction, except for the engine mounts, which yield negative force over $50 < t < 75$ ms. The dynamic force-deflection responses, shown in Figure 4.15, can be applied to obtain the energy absorbed by each structural member and thereby the crash energy distribution property of the vehicle model. The results suggest that the front frame yields greatest energy absorption followed by the sheet metal and the torque box members. It should be noted that the majority of the impact energy of 1945 kg vehicle (kinetic energy = 235.3 kJ) is absorbed by different structural members during crash, while the residual energy causes rebound motions of the vehicle masses.

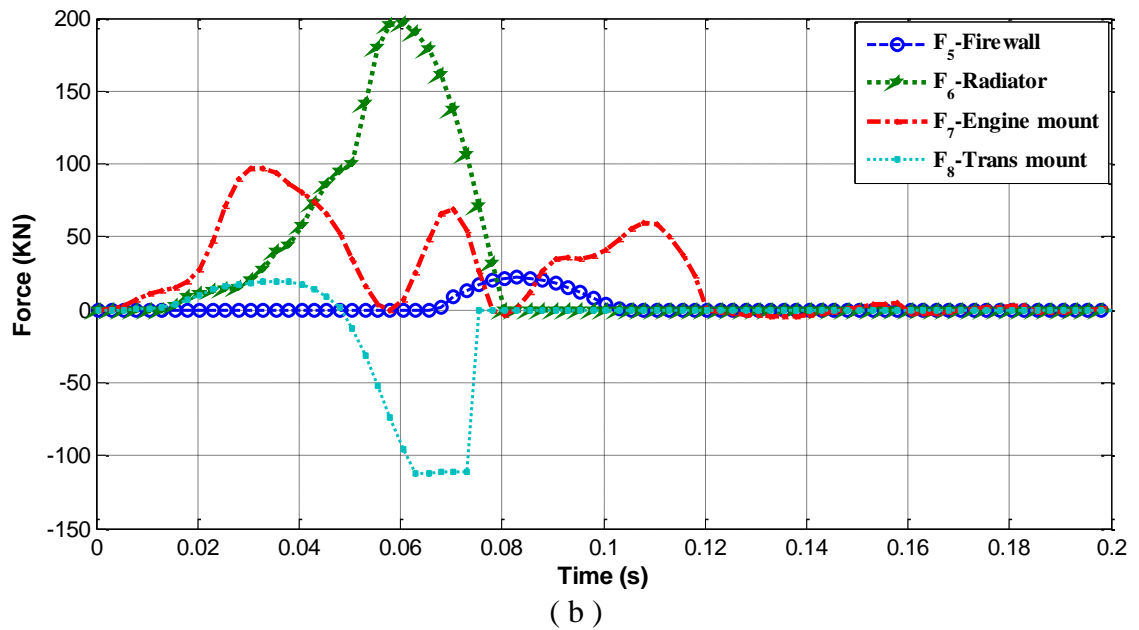
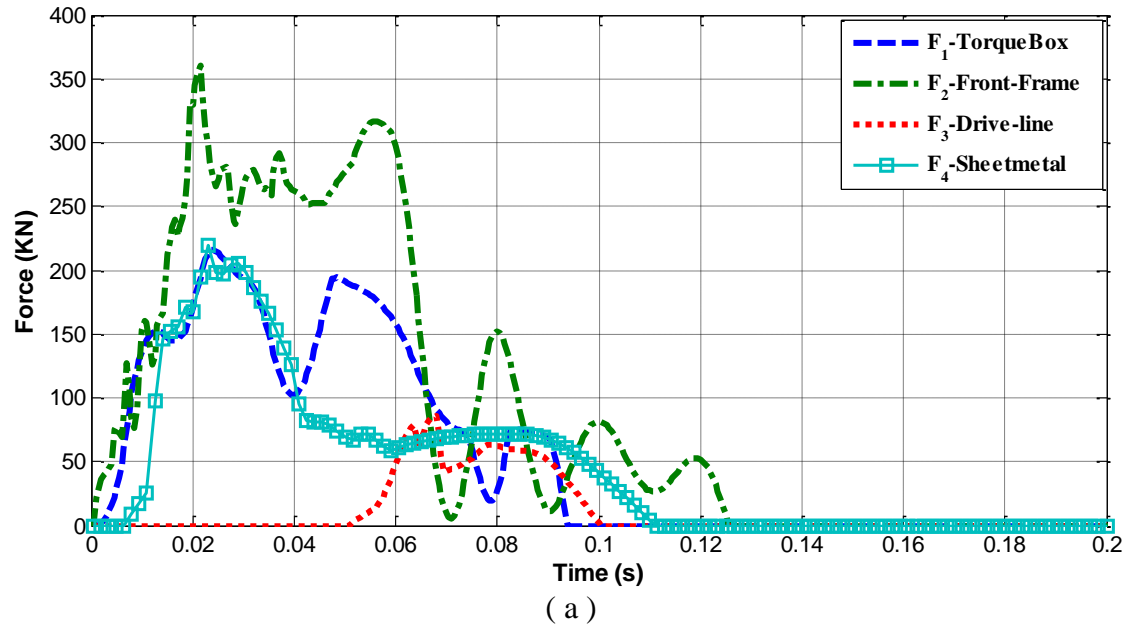
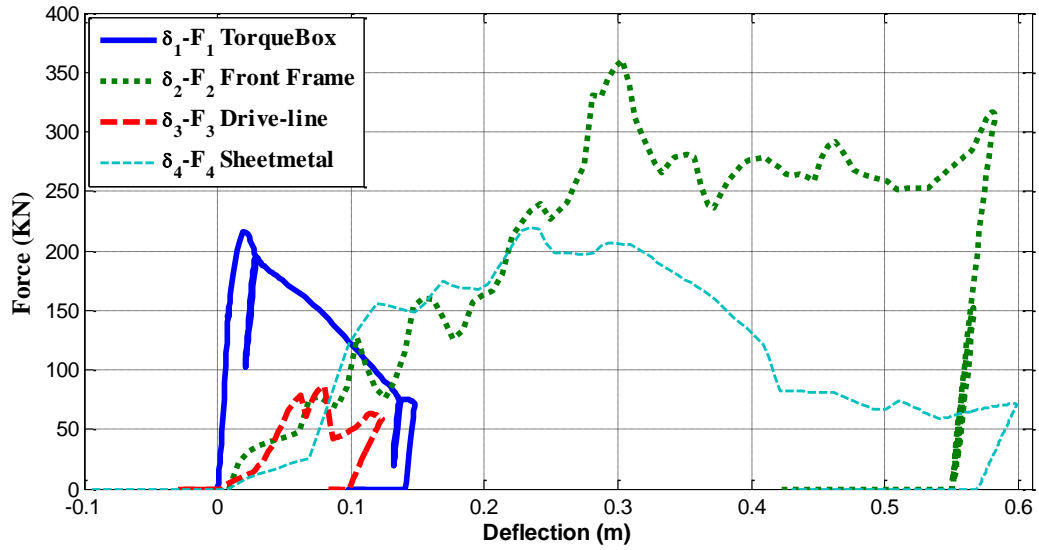
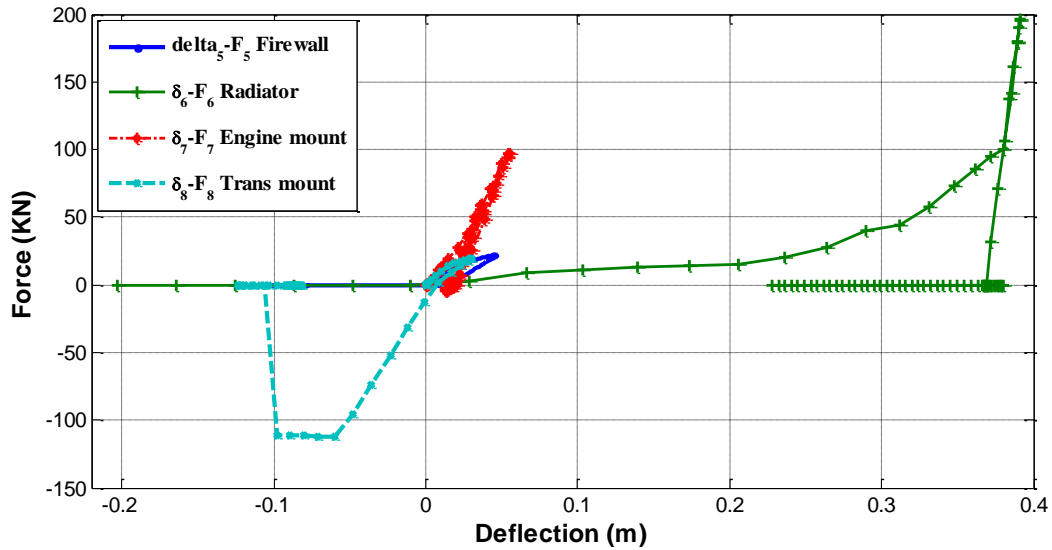


Figure 4.14: Variation in dynamic force developed by various structural components in a 56 km/h frontal impact with a rigid barrier for structural members: (a) F₁-F₄, (b) F₅-F₈



(a)



(b)

Figure 4.15: Dynamic force-deflection curves for different lumped masses of the baseline model at an impact speed of 56 km/h with a rigid barrier for structural members: (a) F_1 - F_4 , (b) F_5 - F_8 .

From the results shown in the above figure, it can be concluded that the front frame, sheet metal and torque box members are the main load carrying members and absorb a significant portion of the impact energy. It should be noted that the majority of impact energy, which is calculated using total mass of 1945 kg with an initial impact speed of 56 km/h (23.53 kJ) is transferred as a potential energy absorbed by different

structural members. The rest of impact energy is used in creating rebound motion for different lumped masses with a speed of 5.6 km/h.

4.3 Baseline Vehicle Model with Occupant and Passive Restraint System

The vehicle model with elasto-plastic structural properties could be used to obtain the impact loads transmitted to the occupant and thus the potential injury risks of a crash. For this purpose, the occupant-restraint system, represented as a single-DOF dynamic system, is introduced within the vehicle body mass, as shown in Figure 4.16.

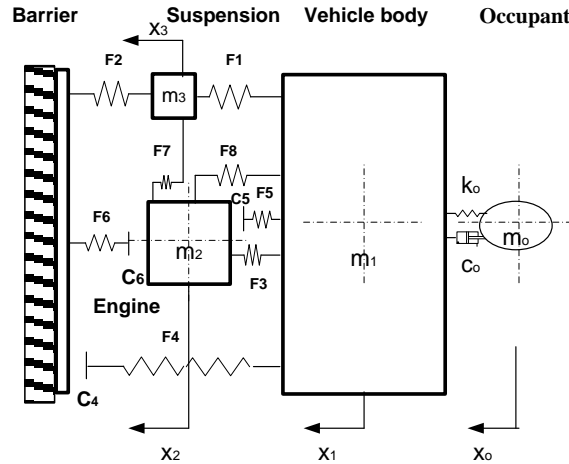


Figure 4.16: Four-DOF lumped mass model for baseline model equipped with a restrained occupant in full frontal impact

The restraint system is represented by a parallel combination of a linear spring and linear viscous damper with a clearance δ_{oc} , as described in Chapter 2. The equations of motion of the model are presented below:

$$m_o \ddot{x}_o = -F_{rest} - F_{seat} \quad (4.10)$$

$$m_1 \ddot{x}_1 = -F_1 - F_3 - F_4 - F_5 + F_8 + F_{rest}$$

$$m_2 \ddot{x}_2 = -F_6 - F_7 - F_8 + F_3 + F_5$$

$$m_3 \ddot{x}_3 = -F_2 + F_1 + F_7$$

$$F_{rest} = \begin{cases} k_o(x_o - x_v - \delta_{oc}) + c_o(\dot{x}_o - \dot{x}_v) & \text{for } (x_o - x_v) \geq \delta_{oc} \\ 0 & \text{for } (x_o - x_v) < \delta_{oc} \end{cases} \quad (4.11)$$

where F_{rest} is the amount of force due to the restraint systems, and c_o and k_o are linear damping and stiffness factors for the restraint system, respectively.

4.3.1 Occupant Responses to Frontal Barrier Impact

The above equations of motion are solved assuming an initial velocity of 56 km/h to study the responses of the occupant mass to a frontal barrier impact. Figure 4.17 illustrates comparisons of displacement, velocity and acceleration response histories of the occupant mass with those of the vehicle body, engine and suspension masses. The results suggest that the peak relative occupant displacement, the difference between the occupant and vehicle displacement, approaches 14.77 cm at 83 ms which is acceptable compared with the average available interior space (more than 40 cm) in most of passenger cars. The initial slack is overcome near 15.5 ms, as shown in Figure 4.17 (a), where the restraint coupling phase starts with relatively contact velocity of 4.37 km/h (Figure 4.17 (b)). The maximum occupant deceleration is 27.35 g at 70.5 ms whereas the maximum body mass deceleration is 29.39 g at 23.5 ms, as shown in Figure 4.17 (c). Furthermore, the occupant HIC value was computed as 55.18, which is very low compared with the occupant HIC value obtained from the baseline model introduced in Chapter 2 with a value of 465. This can be attributed to the energy absorption of the frontal substructure considered in the model. Furthermore, the peak absorbed energy of the occupant restraint system reaches a value of 17.63 kJ at 70.5 ms.

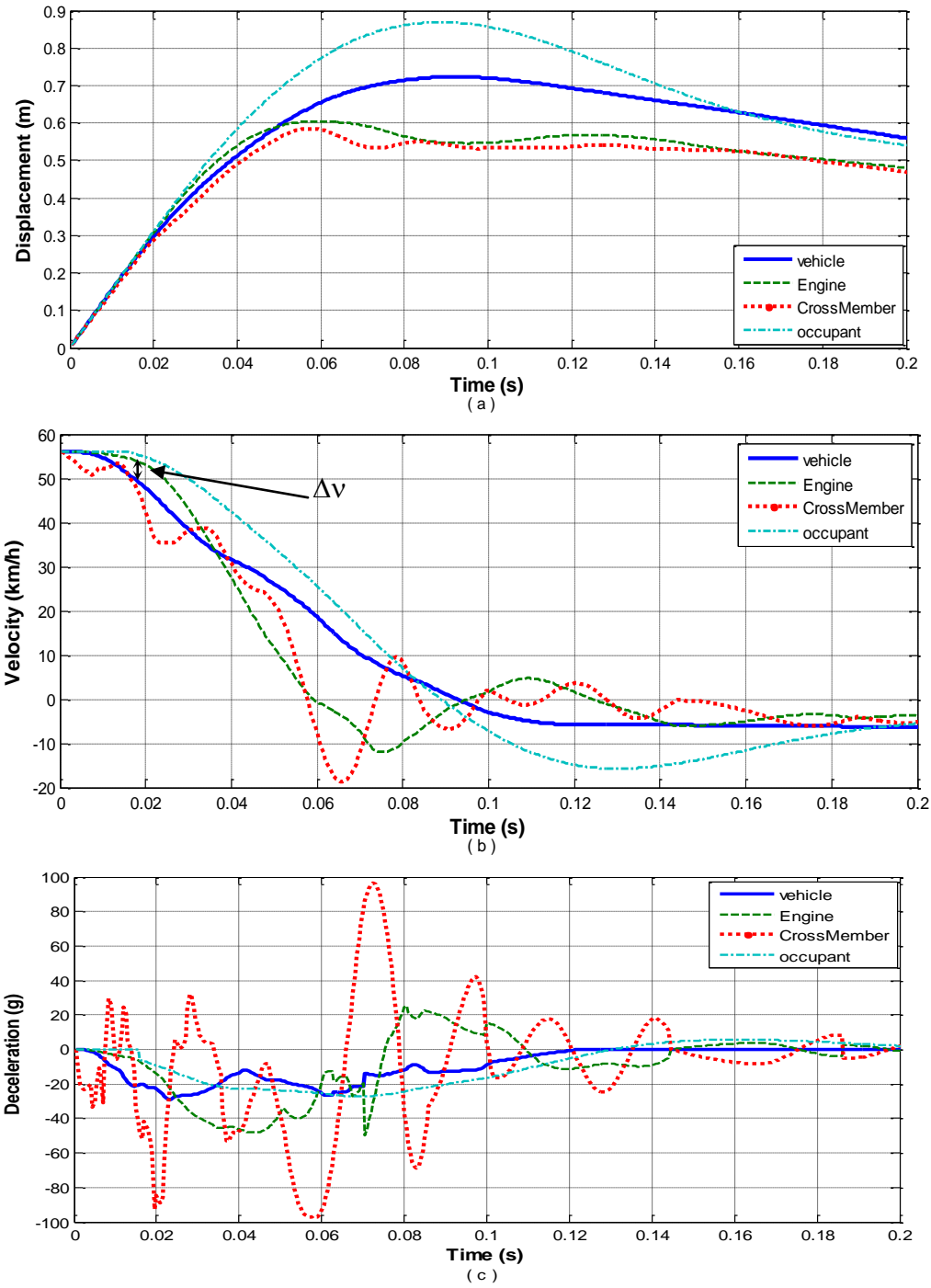


Figure 4.17: Dynamic responses of different bodies of the baseline model equipped with occupant in a 56 km/h frontal impact with a rigid barrier: (a) displacement; (b) velocity; and (c) acceleration.

4.3.2 Vehicle Model with Occupant Seat Interactions

In the event of a crash, the occupant seat tends to absorb a portion of the crash energy attributed to dynamic occupant-seat interaction. A number of studies have proposed widely different models of the occupant seat system models for analyses of energy absorption and ride comfort characteristics [180-183]. Few of these studies have clearly considered multi-DOF occupant models for analyses of energy absorption characteristics of car seat and the occupant. A proven multi-DOF biomechanical model of the human occupant, however, has not yet been reported. It is reported that the seat back frame exhibits only little effect on the occupant response during frontal impacts [56]. In this study, the properties of the car seat are represented by combination of a piecewise linear stiffness and a nonlinear damping element attributed to the cushioning effect and seat frame. The occupant is represented by a rigid mass resulting in a four-DOF vehicle model, as shown in Figure 4.18. The equations of motion of the model are formulated as:

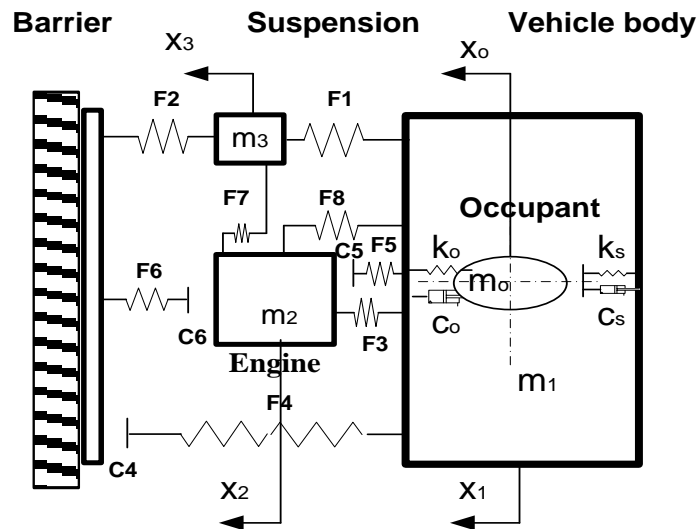


Figure 4.18: Four-DOF lumped-parameter model of the vehicle with occupant-seat-restrained under full frontal impact

$$\begin{aligned}
m_o \ddot{x}_o &= -F_{rest} - F_{seat} \\
m_1 \ddot{x}_1 &= -F_1 - F_3 - F_4 - F_5 + F_8 + F_{rest} + F_{seat} \\
m_2 \ddot{x}_2 &= -F_6 - F_7 - F_8 + F_3 + F_5 \\
m_3 \ddot{x}_3 &= -F_2 + F_1 + F_7
\end{aligned} \tag{4.12}$$

where F_{seat} is the force due to occupant-seat interaction, given by:

$$F_{seat} = \begin{cases} 0 & \text{for } \delta_o \geq \delta_s \\ k_s(\delta_o) + c_{sL}(\dot{x}_o - \dot{x}_1) + c_{sNL}(\dot{x}_o - \dot{x}_1)^3 & \text{for } |\delta_o| \leq |\Delta_{cush} - \delta_s| \\ k_s(\delta_o) + k_{s1}(\delta_o - |\Delta_{cush} - \delta_s|) + c_{sL}(\dot{x}_o - \dot{x}_1) + c_{sNL}(\dot{x}_o - \dot{x}_1)^3 & \text{for } |\delta_o| > |\Delta_{cush} - \delta_s| \end{cases} \tag{4.13}$$

where δ_s is the static deflection in the seat cushion and Δ_{cush} is the seat cushion thickness, C_{sL} and C_{sNL} are linear and cubic damping coefficients, respectively, and k_s is linear seat stiffness under low level deformations $|\delta_o| \leq |\Delta_{cush} - \delta_s|$ and k_{s1} is the higher linear stiffness when $|\delta_o| > |\Delta_{cush} - \delta_s|$, Figure 4.19 shows the force-deflection curve for the car seat.

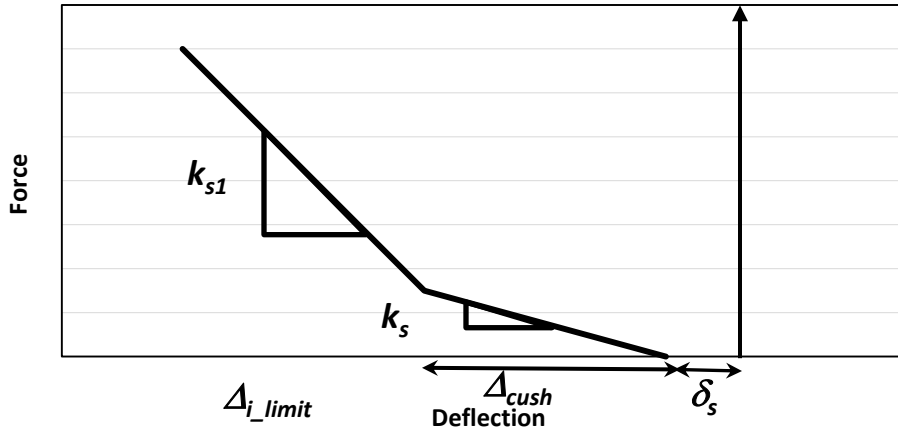


Figure 4.19: Piecewise-linear representation of the car seat cushion-metal spring

4.3.3 Response analysis of the Occupant-Seat System

The equations of motion, presented in Eqns. (4.12) and (4.13), are solved under a frontal impact at a speed of 56 km/h to obtain the occupant mass responses. The seat-

occupant model parameters were taken as $k_s=30.12$ kN/m; $k_{sI}=79.9$ kN/m and $\Delta_s = 0.01$ m, $C_{sL}=92.06$ Ns/m $C_{sNL}=243.96$ Ns³/m³. Figure 4.20 (a) illustrates the occupant mass acceleration response when the occupant interacts with the vehicle considering restraint system alone, and restraint with the seat and the restraint. The force-deflection response of the occupant mass is shown in Figure 4.20 (b) at a speed of 56 km/h.

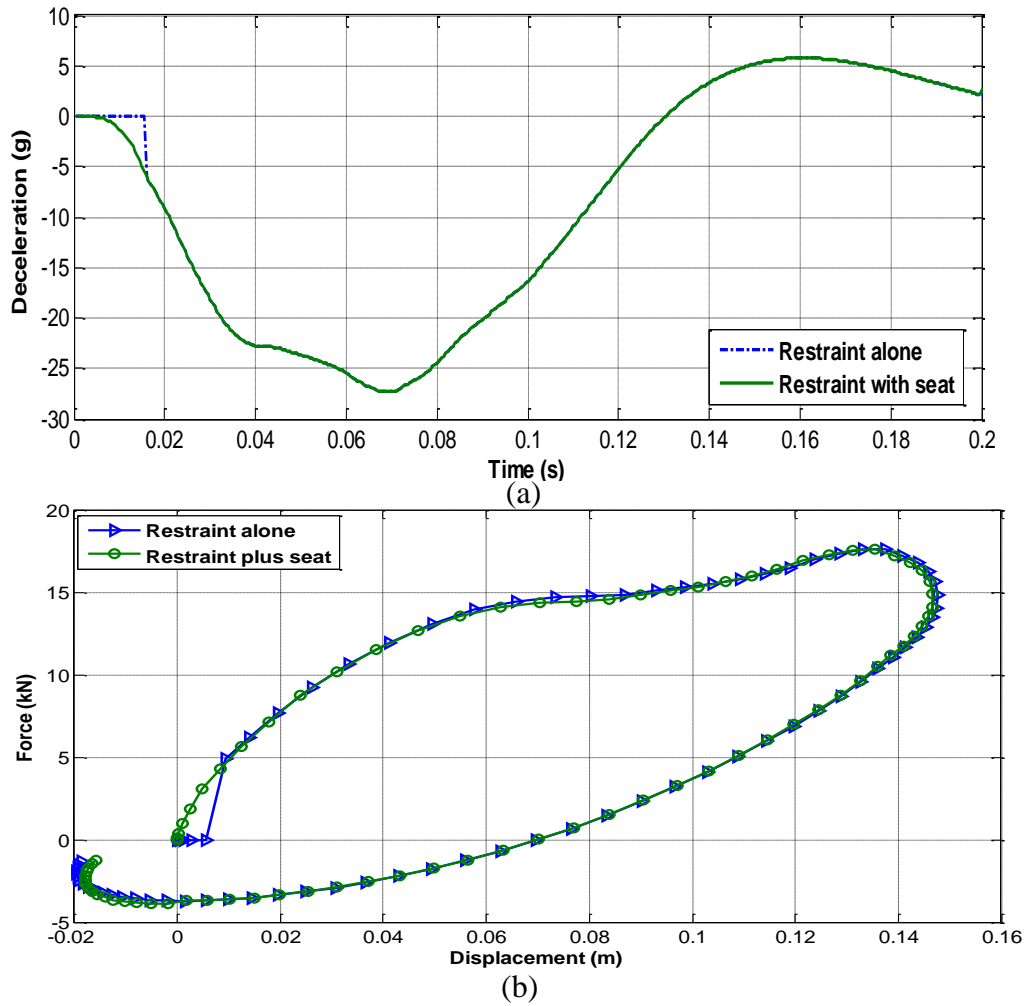


Figure 4.20: Comparison of the occupant mass response of the vehicle-occupant system model with restraint alone and with restraint and the seat system: (a) deceleration, (b) force-displacement.

The results show only very little contribution due to occupant-seat-interaction to the deceleration and energy distribution responses. Table 4.1 summarizes the peak

responses of the occupant restraint system with or without the seat. The Table also presents the peak relative velocity and the occupant HIC. The results further confirm negligible contribution due to the seat, as reported in [56]. The vehicle model with occupant restraint-seat-interaction is applied for further analyses of different configurations of add-on energy absorbers to assess their performance potentials.

Table 4.1: Comparison of occupant restraint system responses subjected to frontal barrier impact at 48 km/h impact speed.

Comparison		VOR with seat	VOR without seat
EA of restraint system	(J)	1714.5	1726.0
Peak occupant deceleration	(g)	27.30 at 70.5 ms	27.35 at 70.5 ms
Peak occupant relative displacement	(m)	0.1467 at 83.5 ms	0.1477 at 83 ms
Peak occupant relative velocity	(m/s)	3.278 at 34.5 ms	3.278 at 34.5 ms
Estimated HIC		54.95	55.18

4.4 Scaling of the Vehicle model

The results presented in sections 4.2 and 4.3 demonstrate that the lumped-parameter models could be effectively applied to determine the energy absorption of various structural components and thus the crash energy management system. The mass of the vehicle considered in the model, however, is considerably higher than the modern light-weight vehicles. The vehicle model, in this study, is selected in order to explore the performance potentials of optimal add-on energy absorbers identified in section 3.5.2 for both EIDV and IV models. An appropriate scaling law is explored and applied to the baseline model to achieve a vehicle mass of 1500 kg, identical to that considered in the simplified models.

Different scaling techniques have been applied in car crash simulations at both the component and the total vehicle level [173-176]. These have been applied to develop scale model prototypes for crash testing prior to the full-scale model development. The scaled models are derived to yield structural behavior comparable to that of the full vehicle so as to relate the test results of small-scale model to that of the full-scale vehicle [172,173]. Various studies involving scale model tests have suggested that the application of normalized impact responses could yield satisfactory scaling of the prototype models [174,175]. This normalization is based on a simple characteristic length ratio of the prototype and full vehicle designs, which is applied to determine the stiffness and mass ratios that further define a scale factor for normalizing dynamic force and simulation time. This scaling method was based mainly on particular experimental data acquired in the study, while its general validity has not been demonstrated. Alternate scaling techniques involving the strain rate effects of different structural members apart from the inertial and geometric properties, have been proposed [172,173]. In order to satisfy the requirements of geometrically similar scaling, the method involves following simplifying assumptions:

- The structural members of both the scaled and full-size models possess identical material properties, especially the Young's modulus (E) and mass density (ρ).
- The external loads are assumed to occur at geometrically homogenous locations.
- The structural components of both models exhibit identical stress-strain and normalized pressure characteristics.
- The compression wave propagates with the same speed in both models and the time duration is proportional to the scaling factor.

In this study a geometric scale factor B is defined as:

$$B = \frac{l}{L} \quad (4.14)$$

where l and L are the lengths of the scaled and full vehicle models, respectively. This scaling factor is applied to determine the factor to be applied to various properties of the full vehicle model [172,173]. The factors thus derived are summarized in Table 4.2.

Table 4.2: Scaling factors for different model properties

Parameters	Scaled Model	Full model	Scale factor	Parameters	Scaled Model	Full model	Scale factor
Length	l	L	B	velocity	v	V	-
Strain	ε	ε	-	Deceleration	a	A	$1/B$
Stress	σ	ς	-	Time	t	T	B
pressure	p	P	-	Stiffness	k	K	B
Mass	m	M	B^3	Damping	c_d	C_d	B^2
Dynamic force	f_d	F_d	B^2	Strain rate $\dot{\varepsilon}$	$\dot{\varepsilon}$	ε	$1/B$

It should be mentioned that the strain rate $\dot{\varepsilon}$ was added to the properties in order to compensate for the distortion that was observed upon application of the geometrical scaling. It was observed that the strain rate does not follow the geometric scaling and can considerably distort some of the response properties. A need to adjust the strain rate was thus identified. Both the strain and stress are not dependant on scale factor as seen in Table 4.2, while the time is dependent on the scale factor. This suggests a scale factor of $1/B$ for the strain rate. The Cowper-Symond relation has been employed in the structural impact problems to predict the dynamic stress in elasto-plastic materials [172]. This relation employs static yield stress to predict dynamic yield or flow stress σ_d , which depends on the strain-rate, such that:

$$\frac{\sigma_d}{\sigma} = I + \left(\frac{\dot{\epsilon}}{M} \right)^{\frac{1}{q}} \quad (4.14)$$

where, q and M are the material constants. The dynamic stress of a scaled model ζ_d may thus be expressed as:

$$\frac{\zeta_d}{\zeta} = I + \left(\frac{\dot{\epsilon}}{BM} \right)^{\frac{1}{q}} \quad (4.15)$$

This yields a dynamic stress ratio for models with different scales denoted by:

$$\frac{\sigma_y^{dyn}}{\zeta_y^{dyn}} = \frac{I + \left(\frac{\dot{\epsilon}/BM}{M} \right)^{\frac{1}{q}}}{I + \left(\frac{\dot{\epsilon}}{M} \right)^{\frac{1}{q}}} \quad (4.16)$$

This reveals that the dynamic flow stress in a small-scale model σ_d is larger than that of a large-scale model ζ_d and, therefore it violates, the stress invariance in Table 4.2. In order to compensate for this, the strain rate of the small scaled model should be multiplied by the scale factor of $1/B$, as shown in Table 4.2. In the absence of knowledge of characteristic lengths of the full and scaled models, the mass ratio may be applied to determine the scale factor, such that:

$$B = \sqrt[3]{\frac{m}{M}} \quad (4.17)$$

where $m=1500$ kg and $M=1945$ kg, are the masses of the scaled and full vehicle, respectively, which yields the scale factor, $B=0.917$. The lumped-parameters model, proposed by Kamal [37,157], is subsequently scaled to realize a total vehicle mass of 1500 kg. Subsequently, the simulations are performed at a speed of 56 km/h to determine frontal impact response of the scaled model.

Figure 4.21 illustrates the acceleration responses of the vehicle, engine and suspension masses of the scaled vehicle model. The results show peak vehicle mass acceleration of 35.51 g occurring at $t = 21$ ms. The validity of the scaling technique is

further examined by expressing the scaled model responses in term of the full vehicle model and comparing the resulting responses with those presented in section 4.2. The application of $B=0.917$ reduces this peak acceleration to 32.56 g and the corresponding time increases slightly to 22.9 ms. These are quite comparable with those attained for baseline model and illustrated in Figure 4.13 (c). The baseline vehicle model revealed peak vehicle mass acceleration of 29.39 g occurring at 23.5 ms. The comparison suggests a deviation of approximately 10% and less than 0.1% in peak accelerations and the corresponding time. The peak vehicle deformation of the scaled vehicle model was obtained as 63.38 cm occurring at 76.1 ms. This is equivalent to 69.12 cm deformation of the baseline vehicle model occurring at 83.5 ms. The peak deformation response compares very well with the baseline model responses: 70.1 cm at 85.0 ms. The results confirm validity of the scaling methods and the scaled model. The scaled model is subsequently applied to determine the performance potential of the optimal add-on absorbers together with energy absorptions properties of the vehicle components.

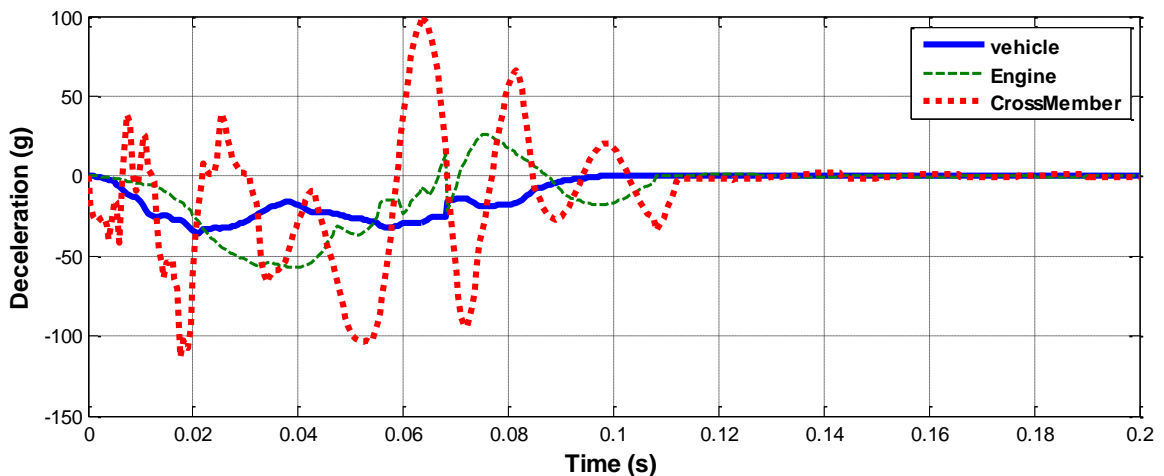


Figure 4.21: acceleration responses of vehicle, engine and suspension to a 56 km/h impact with a rigid barrier

4.5 Analysis of Crash Energy Distribution of Vehicle-Occupant Model with Add-on Absorbers

In this section, the two proposed models, introduced in section 2.3.4 and 2.3.6 with their optimal design variables obtained using multiobjective optimization (section 3.4.1), are implemented to the scaled baseline vehicle model.

4.5.1 Model Developments

The distribution of impact energy in the vehicle components and add-on absorbers are evaluated by introducing the absorber models to the vehicle model. Two configurations of optimal add-on absorbers are considered: (i) Extendable and integrated dual Voigt system (EIDV); and (ii) integrated Voigt absorbers systems (IV). Figures 4.22 (a) and (b) illustrate the four- and five-DOF models of the vehicles with IV and EIDV add-on absorbers, respectively. The equations of motion of the vehicle model with integrated Voigt (IV) absorbers are formulated as:

$$\begin{aligned}
 m_o \ddot{x}_o &= -F_{rest} - F_{seat} \\
 m_1 \ddot{x}_1 &= -F_1 - F_3 - F_4 - F_5 + F_8 + F_{rest} + F_{seat} - F_{v_i} \\
 m_2 \ddot{x}_2 &= -F_6 - F_7 - F_8 + F_3 + F_5 \\
 m_3 \ddot{x}_3 &= -F_2 + F_1 + F_7
 \end{aligned} \tag{4.20}$$

where the forces developed by various structural components ($F_i, i=1, \dots, 8$) are computed from their respective deflections ($\delta_i, i=1, \dots, 8$) given by:

$$\begin{aligned}
 \delta_1 &= x_1 - x_3; \quad \delta_2 = x_3; \quad \delta_3 = x_1 - x_2; \\
 \delta_4 &= x_1 - C4; \quad \delta_5 = x_1 - x_2 - C5; \quad \delta_6 = x_2 - C6; \\
 \delta_7 &= x_2 - x_3; \quad \text{and} \quad \delta_8 = x_2 - x_1
 \end{aligned} \tag{4.21}$$

In a similar manner, the equations of motion for the vehicle-occupant model with extendable and integrated Voigt systems (EIDV) are formulated as:

$$\begin{aligned}
m_o \ddot{x}_o &= -F_{rest} \\
m_1 \ddot{x}_1 &= -F_1 - F_3 - F_4 - F_5 + F_8 + F_{rest} + F_{seat} - F_{v_i} \\
m_2 \ddot{x}_2 &= -F_6 - F_7 - F_8 + F_3 + F_5 \\
m_3 \ddot{x}_3 &= -F_2 + F_1 + F_7 \\
m_b \ddot{x}_b &= F_2 + F_4 + F_6 + F_{v_i} - F_{v_e}
\end{aligned} \tag{4.22}$$

where structural members' deflection are defined according to the following set of Equation.

$$\begin{aligned}
\delta_1 &= x_1 - x_3; \quad \delta_2 = x_3 - x_b; \quad \delta_3 = x_1 - x_2; \\
\delta_4 &= x_1 - x_b - C_4; \quad \delta_5 = x_1 - x_2 - C_5; \quad \delta_6 = x_2 - x_b - C_6; \\
\delta_7 &= x_2 - x_3; \quad \text{and} \quad \delta_8 = x_2 - x_1
\end{aligned} \tag{4.23}$$

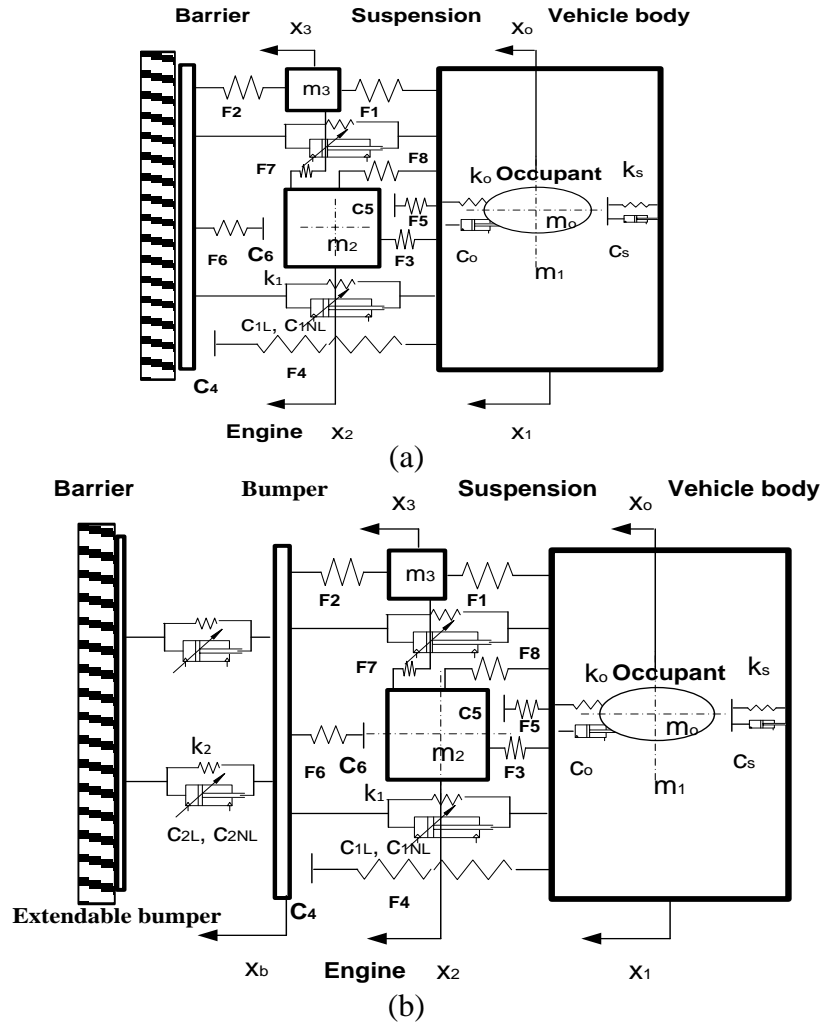


Figure 4.22: Mutli-DOF lumped-parameters representation of vehicle-occupant models with add-on absorber systems: (a) IV model, (b) EIDV model.

4.5.2 Crash Dynamic Responses of the Integrated Voigt (IV) Model

The equations of motion of the vehicle model with integrated add-on Voigt energy absorbers (IV) are solved at three different impact speeds for frontal barrier impact to determine the model responses. The simulations are performed at different impact speeds to validate the applicability of the proposed model over a range of impact speeds. The model implements the optimal sets of design variables, obtained from section 3.4.2, listed in Table 4.3. Figure 4.23 shows the simulation results for the three masses of the IV model over a 200 ms time duration at a 56 km/h impact speed. The results show that the accelerations approach steady value near 0 g, while the rebound velocity approaches 3.6 km/h. The maximum deformation or dynamic crush distance reaches approximately 0.31 m, as shown in Figure 4.23 (a). The peak occupant deceleration is increased from 27.1 g to 42.92 g, which subsequently increases the occupant HIC from 55.18 to 148.8 for the baseline and IV models respectively, as shown in Figure 4.23 (c). On the other hand, the peak vehicle deformation is reduced from 0.701 m to 0.3193 m, as shown in Figure 4.23 (a).

Table 4.3: design variables corresponding to three chosen impact speeds for IV model

Impact speed (km/h)	λ_1	μ_1
56	0.1	1.65
48	0.1	1.25
35	0.1	1.2

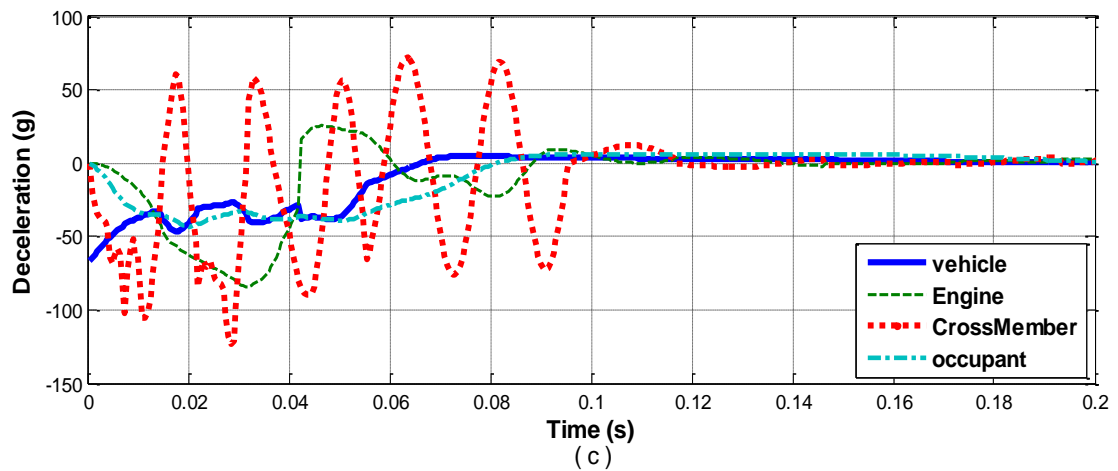
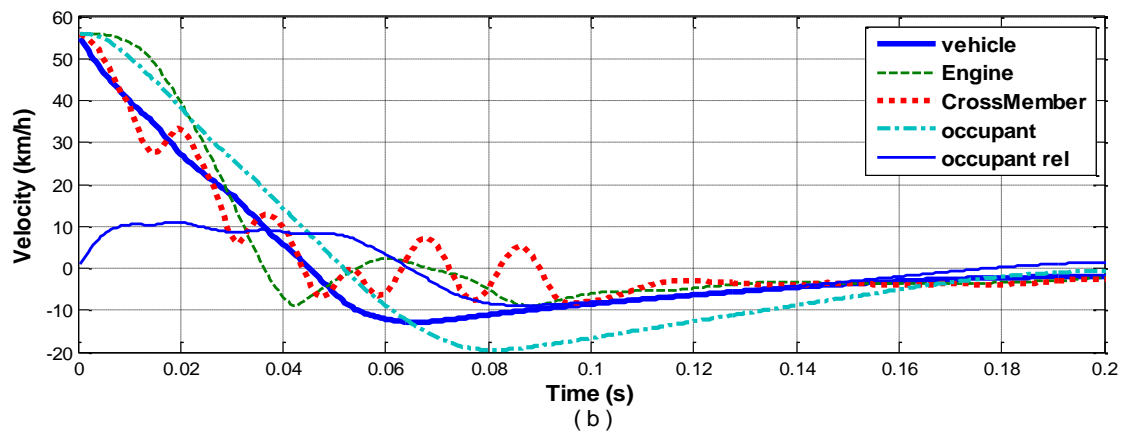
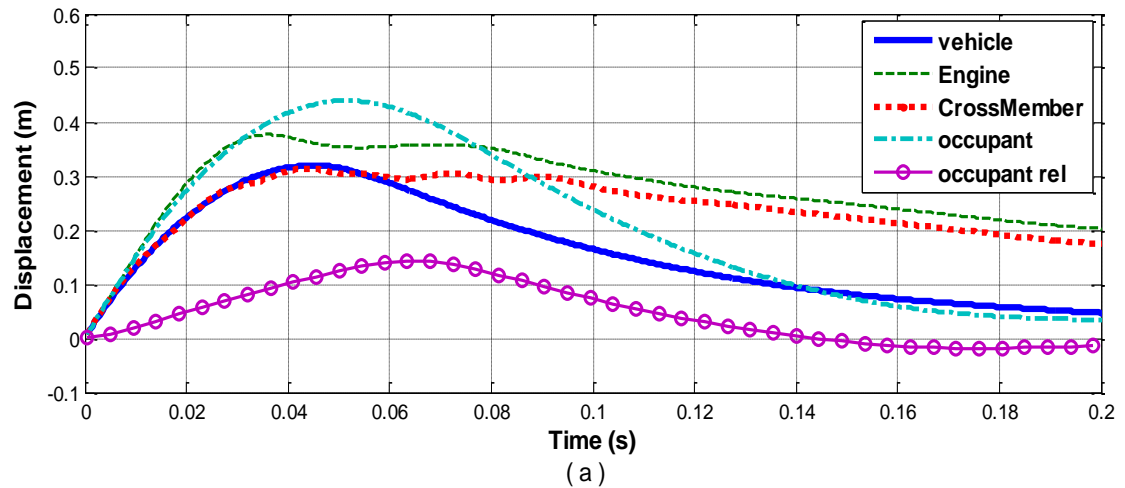


Figure 4.23: Comparison of frontal barrier impact responses of the occupant mass with those of the vehicle, engine and suspension masses for the IV model at a 56 km/h impact speed: (a) displacement; (b) velocity; and (c) acceleration

4.5.3 Crash Dynamic Responses of the Extended Integrated Dual Voigt (EIDV) Model

The equations of motion of the vehicle model with extendable and integrated dual add-on Voigt energy absorbers model (EIDV) are solved at three impact speeds under frontal barrier impact to determine the model responses. The simulation results are obtained using the optimal sets of design variables obtained from section 3.4.1, which are tabulated in Table 4.4. Figure 4.24 shows the simulation results at a 56 km/h impact speed for the three masses of the EIDV model over a 200 ms duration. The results show that the accelerations approach steady value near 0 g, while the rebound velocity approaches 3.6 km/h. The maximum deformation or dynamic crush distance approaches approximately 0.31 m as shown in Figure 4.24 (a). The results show that the peak occupant relative displacement is reduced from 12.32 cm to 11.61 m, which is 5.8 % lower than that obtained with the baseline model. Additionally, the maximum relative occupant velocity is reduced from 9.19 km/h to 7.967 km/h, as shown in Figure 4.24 (b), a percent reduction of 13.31%. Simulation results of the EIDV model show considerable reduction in peak vehicle deformation from 0.701 m to 0.2188 m, a percent reduction of 68.79%. Additionally, the maximum occupant deceleration is reduced from 27.1 g to 22.9 g (15.5% reduction).

Table 4.4: Design variables at the three chosen impact speeds for IDEV model

Impact speed, km/h	λ_2	μ_2	λ_1	μ_1
56	0.1	3.33	0.3	2.0
48	0.1	2.95	0.3	2.0
35	0.1	2.19	0.3	2.0

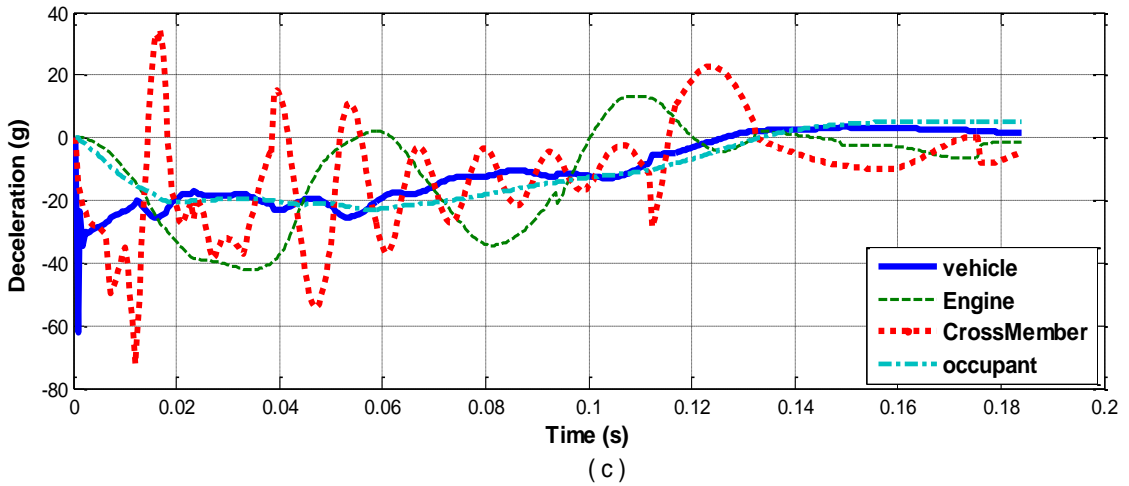
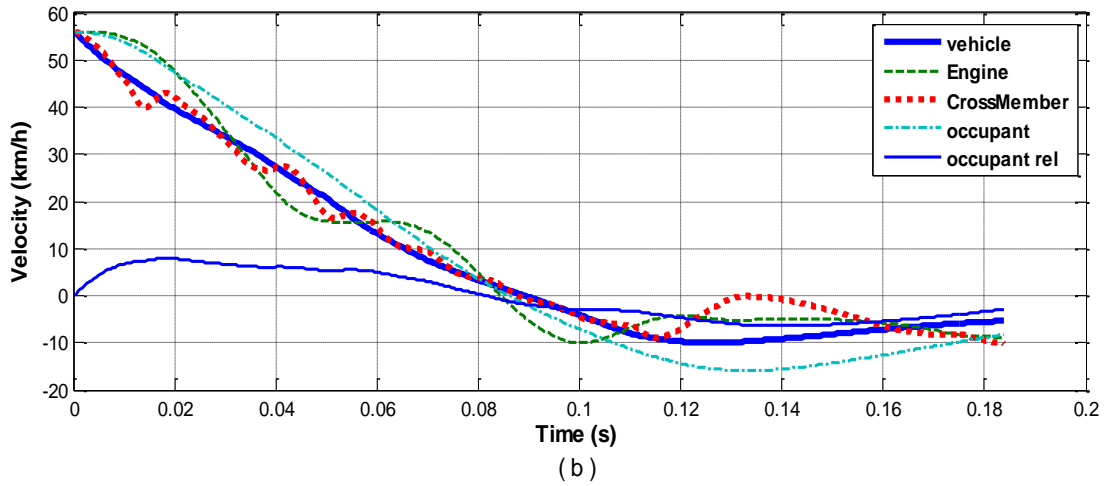
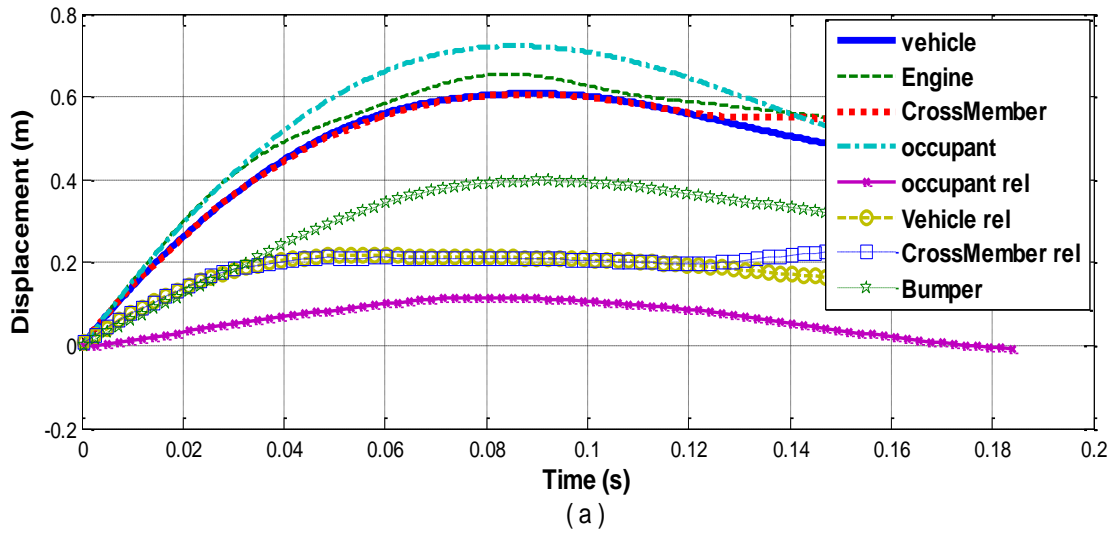


Figure 4.24: Comparison of frontal barrier impact responses of the occupant mass with those of the vehicle, engine and suspension masses for the EIDV model at a 56 km/h impact speed: (a) displacement; (b) velocity; and (c) acceleration.

The amounts of energy absorbed by Voigt elements in extended and integrated positions with vehicle structure are 59.21 kJ and 22.79 kJ, respectively, which are derived from the force-deflection responses, as shown in Figure 4.25. The percentages of specific energy absorbed by the extendable and integrated Voigt elements are obtained as 65.25% and 25.12%, respectively. The amount of energy transferred to occupant through VOR system is reduced from 1714.5 J to 1350.9 J, percent reduction of 21.21%, which were obtained from Figure 4.26.

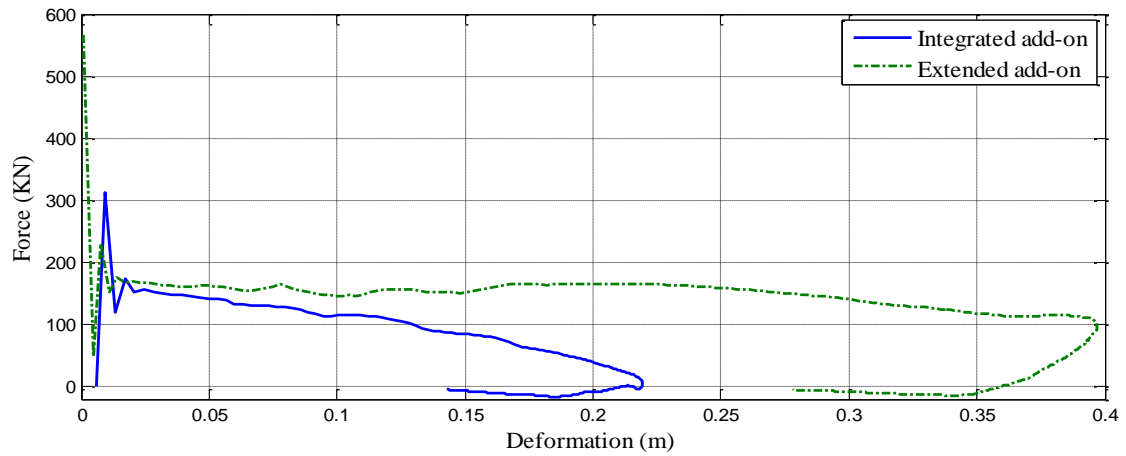


Figure 4.25: Dynamic force-deflection curves for the add-on in extendable and integrated positions with vehicle structure for the EIDV model at 56 km/h impact speed

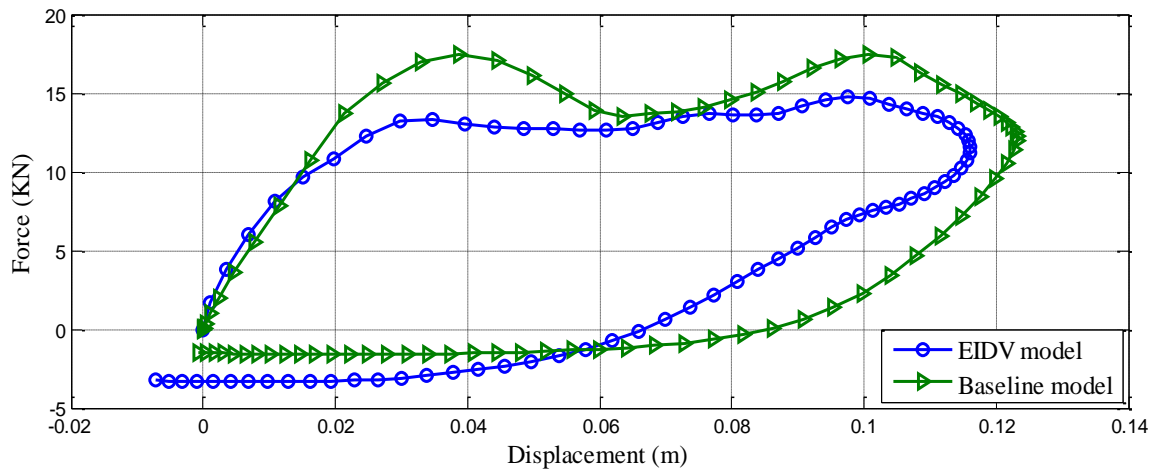


Figure 4.26: Comparison of occupant mass responses between the baseline and the EIDV models at an impact speed of 56 km/h with a rigid barrier

4.5.4 Compassion of Responses of the Proposed Models

From the simulation results obtained in previous subsections, the structural responses of both the EIDV and IV models are compared with the baseline model at three different impact speeds, as shown in Table 4.5. The simulation results listed in Table 4.5 show that the EIDV model achieves reductions in the peak values of both occupant deceleration and vehicle deformation at the three impact speeds. It also reduces the percentage of energy absorbed by structural members during frontal impact by maximizing the absorbed energy of the add-on EA system. These observations suggest that the EIDV configuration is desirable compared to the IV configuration for better structural crashworthiness enhancement.

Table 4.5: Comparison of simulation results of both EIDV and IV models with a baseline model at three impact speeds

Model	Peak vehicle deceleration (g)	Peak vehicle deformation (cm)	Peak occupant deceleration.(g)	Occupant HIC	Specific absorbed energy by add-on
56 (km/h)					
Baseline model	35.51	69.05	27.1	55.18	
EIDV model	34.54	21.88	22.9	35.8	90.4%
IV model	66.26	31.93	42.9	148.8	69.2%
48 (km/h)					
Baseline model	33.37	52.23	26.6	46.8	
EIDV model	24.94	19.11	19.1	21.8	91.0%
IV model	39.19	31.13	36.3	120.9	60.8%
35 (km/h)					
Baseline model	30.10	37.26	26.1	44.2	
EIDV model	14.14	14.53	12.2	7.3	91.7%
IV model	24.03	24.47	23.0	37.2	27.8%

Distribution of impact energy through different structural members of the baseline model indicates that the frontal part of longitudinal member; front frame F_2 followed by sheet metal F_4 are the major contributing load carrying members. Figure 4.27 shows the

energy distribution of load carrying structural members of the baseline model at different impact speeds. Simulation results clearly indicate that higher reductions in the absorbed energy by different load carrying members are achieved by the EIDV model compared with the IV model, as shown in Figure 4.28 and Table 4.6. This can be inferred due to the fact that the percentage of impact energy absorbed by the add-on energy absorbers in the EIDV model is very high compared to those absorbed in the IV model, as shown in Table 4.5. Figure 4.29 shows the comparisons of different performance measures of the EIDV and IV models together with those of the baseline model.

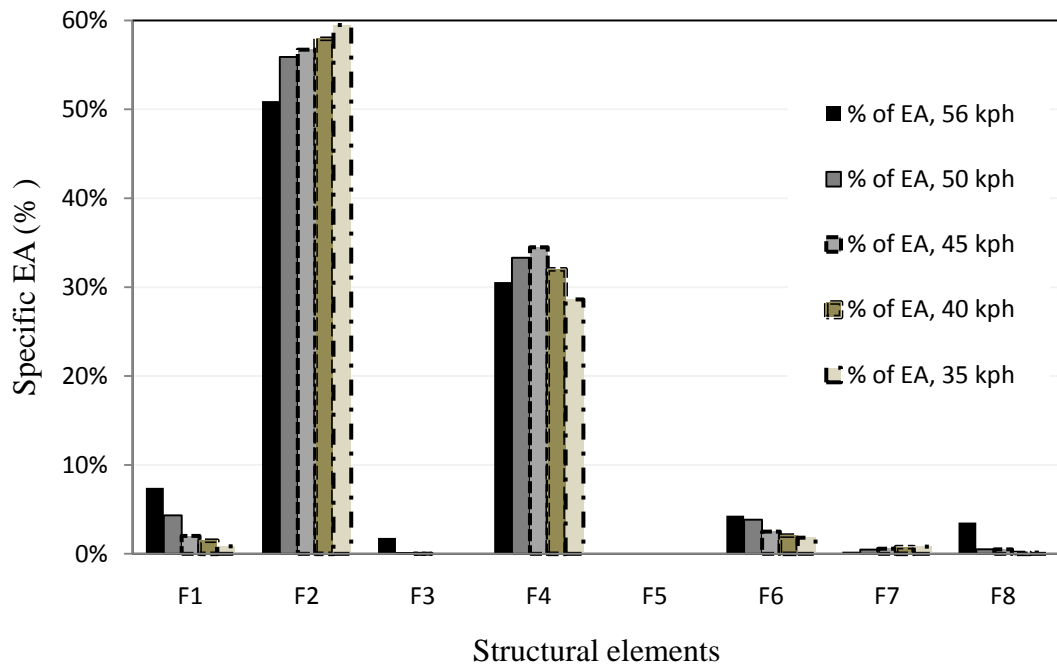


Figure 4.27: Distribution of percentage of absorbed energy by the structural members of the baseline model at different impact speeds

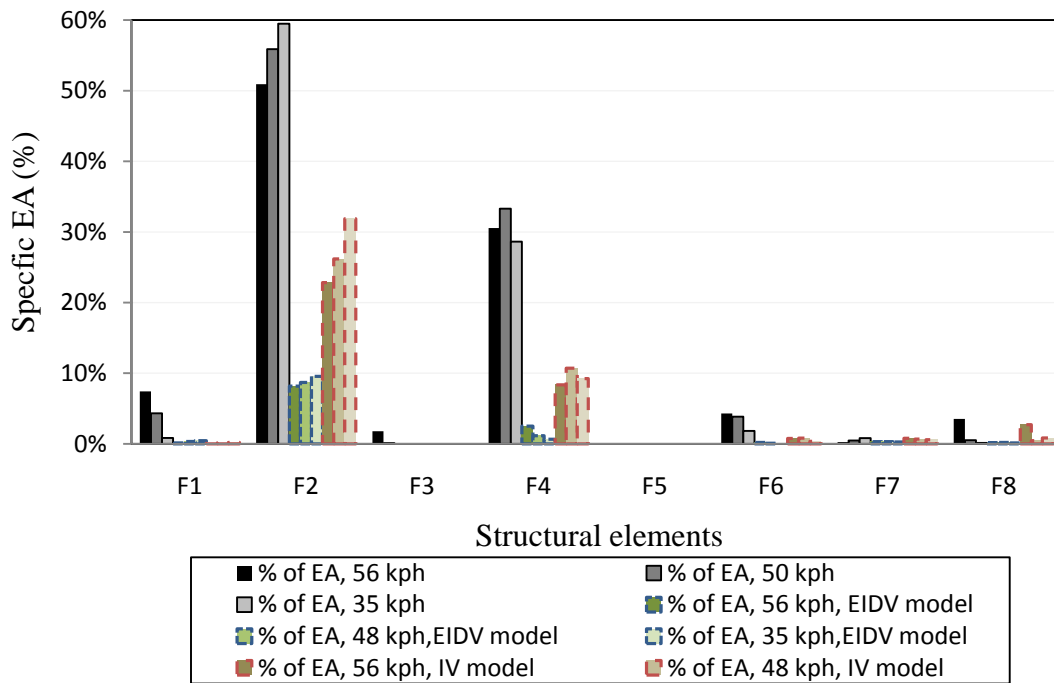


Figure 4.28: Comparison the percentage of absorbed energy over structural members between baseline and both the EIDV and IV models at different impact

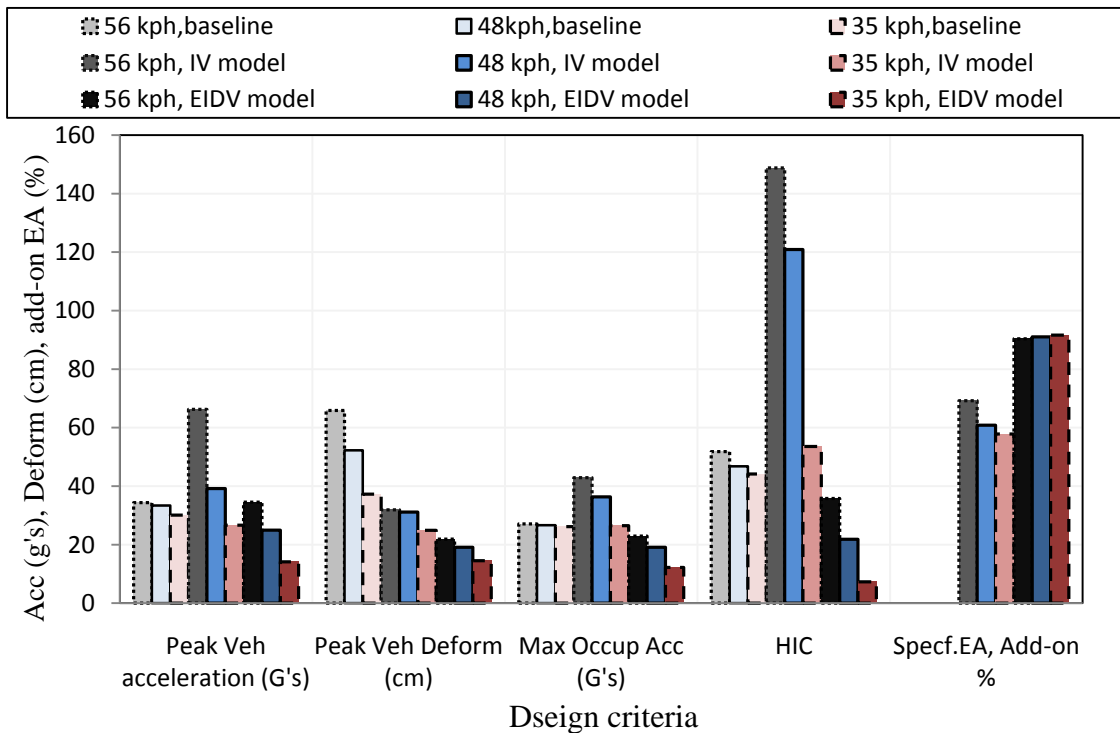


Figure 4.29: Comparison of system performance between both EIDV and IV detailed model with the baseline model at different impact speeds.

Table 4.6: Comparison of the percentage of energy absorption for each structural member between different models at different impact speeds EIDV model

speed	Model	F1	F2	F3	F4	F5	F6	F7	F8	Sum Σ
56 (km/h)	Baseline	7.4%	50.9%	1.8%	30.6%	0.1%	4.3%	0.2%	3.5%	98.8%
	EIDV model	0.1%	8.2%	0.0%	2.5%	0.0%	0.2%	0.3%	0.2%	11.5%
	IV model	0.1%	22.8%	0.0%	8.4%	0.0%	0.8%	0.8%	2.7%	35.5%
48 (km/h)	Baseline	4.3%	55.9%	0.1%	33.3%	0.0%	3.8%	0.5%	0.5%	98.4%
	EIDV model	0.3%	8.7%	0.0%	1.1%	0.0%	0.1%	0.3%	0.2%	10.8%
	IV model	0.1%	26.2%	0.0%	10.7%	0.0%	0.8%	0.7%	0.4%	38.9%
35 (km/h)	Baseline	0.8%	59.5%	0.0%	28.6%	0.0%	1.8%	0.8%	0.1%	91.7%
	EIDV model	0.5%	9.6%	0.0%	0.6%	0.0%	0.0%	0.3%	0.1%	11.0%
	IV model	0.2%	31.9%	0.0%	9.2%	0.0%	0.4%	0.6%	0.8%	43.1%

4.6 Sensitivity analysis

The effectiveness of the proposed CEM systems are evaluated with the elasto-plastic vehicle model using optimal design variables identified for the simplified LMS model through a sensitivity analysis. Sensitivity analysis is performed by allowing each of the identified design variables to be individually varied over a range of $\pm 15\%$ with a uniform step of 5%, while keeping the other design variables unchanged. The results are analyzed in terms of the performance measures namely: the peak vehicle deformation (*Def*), the peak occupant deceleration, and the amount of specific energy absorbed by the add-on system (*SpEngAbs*). The sensitivity analysis results are shown in Figures 4.30 to 4.35 and tabulated in Table 4.7, where the highlighted rows correspond to design variables identified from the simplified LMS models in Chapter 3.

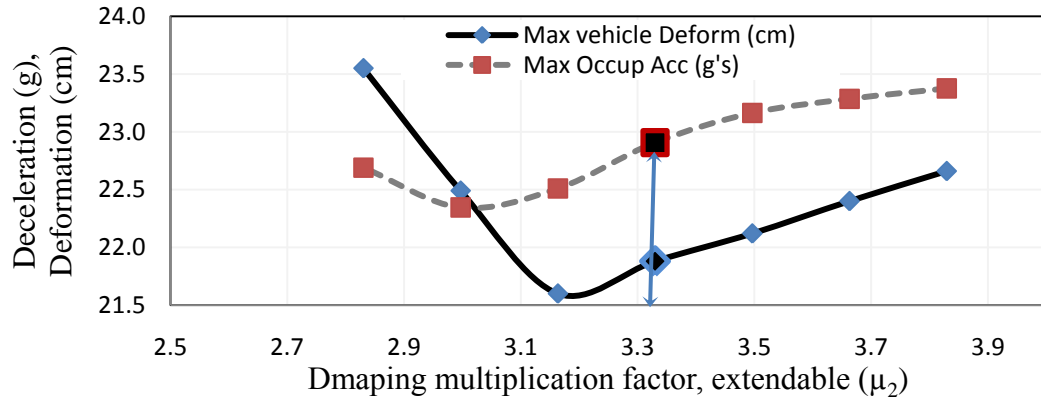


Figure 4.30: Sensitivity of the peak vehicle deformation and maximum occupant deceleration to variations in μ_2 (EIDV model at 56 km/h)

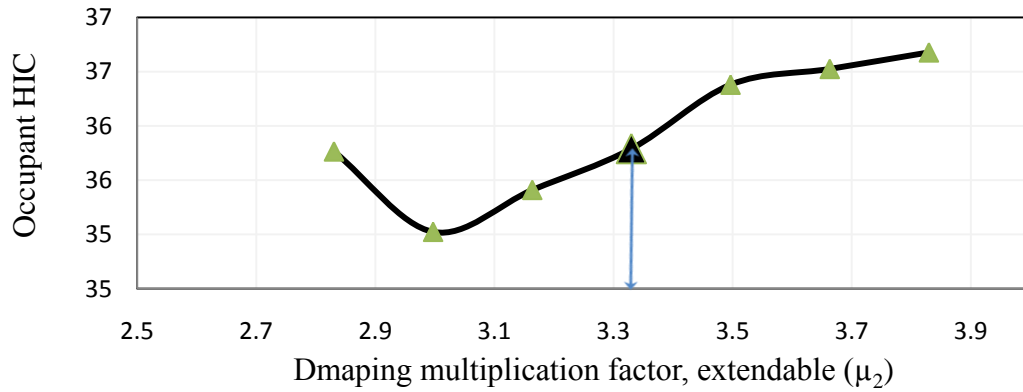


Figure 4.31: Sensitivity of the occupant HIC to variations in μ_2 (EIDV model at 56 km/h).

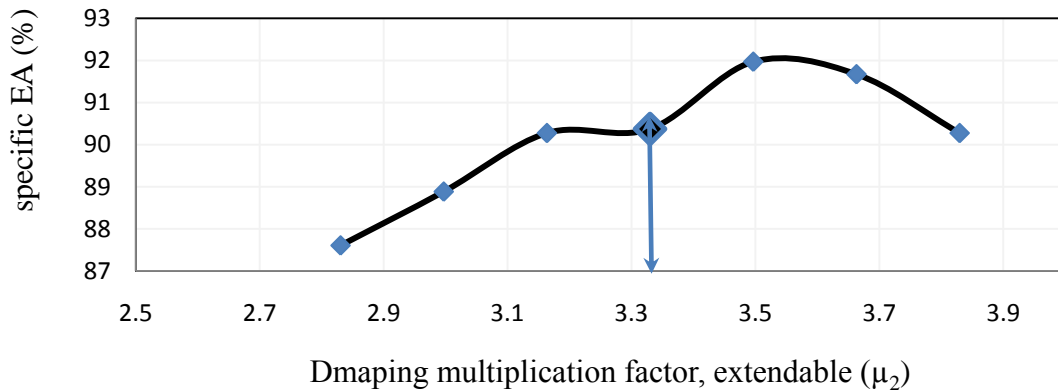


Figure 4.32: Sensitivity of the specific energy absorption by the add-on to variations in μ_2 (EIDV model at 56 km/h).

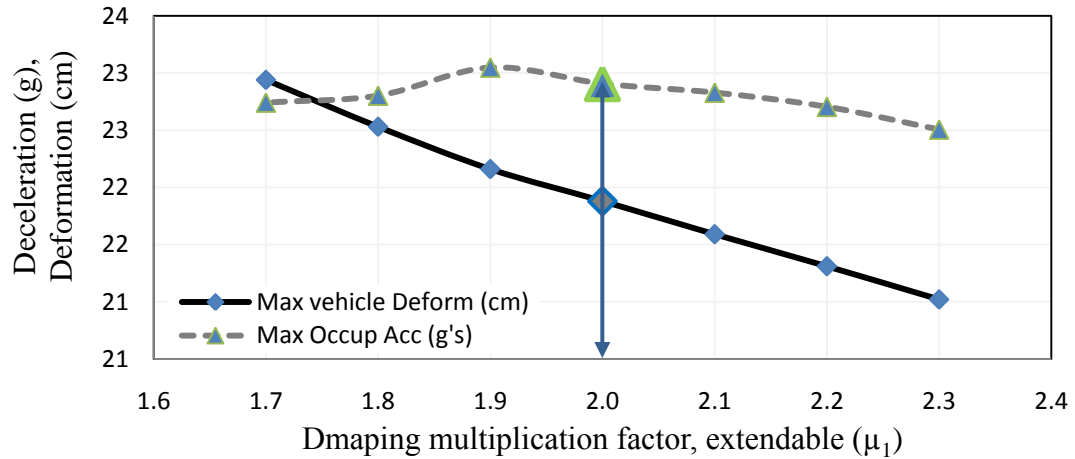


Figure 4.33: Sensitivity of the peak vehicle deformation and maximum occupant deceleration to variations in μ_1 (EIDV model at 56 km/h)

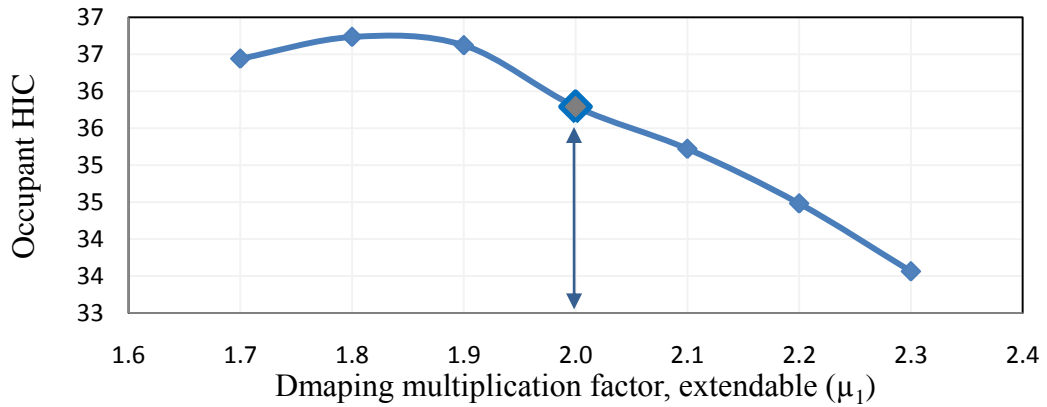


Figure 4.34: Sensitivity of the occupant HIC to variations in μ_1 (EIDV model at 56 km/h)

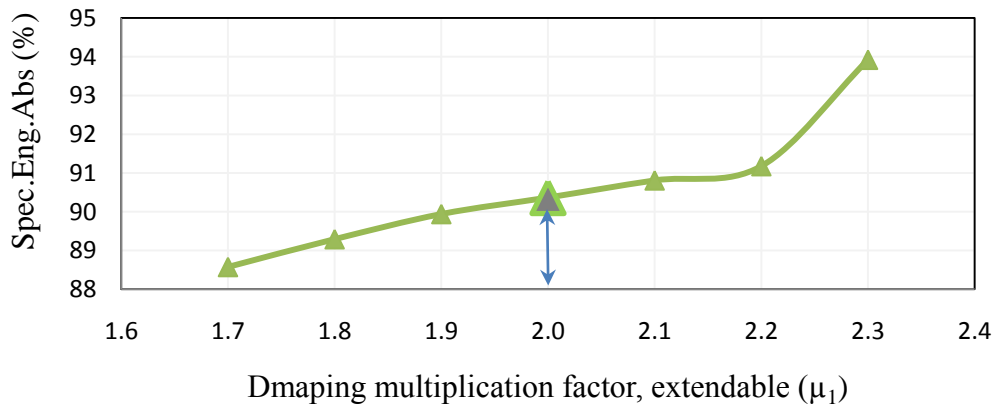


Figure 4.35: Sensitivity of the specific absorbed energy by the add-on to variations in μ_1 (EIDV model at 56 km/h).

The analyses of the results clearly show relatively small changes in the performance measures over the range of variations considered for μ_1 and μ_2 . This suggests that the optimal design variables identified from the simple LMS model may be considered valid for the elasto-plastic vehicle model. Furthermore, small changes in the values of damping design variables (μ_2 and μ_1) exhibit relatively small effects on the variations in the performance values, as shown in Figures 4.30 to 4.35. However, the variations in the peak vehicle deformation and the maximum occupant deceleration with changes in μ_2 (Figure 4.30) exhibit an interested pattern. Both the measures decrease with decrease in μ_2 values. Consequently, the corresponding HIC value also decreases. This may be attributed to nonlinear behaviors of different structural components and elastic mounts that cause oscillatory motions of the masses. Considering, only small variations in the measures with to $\pm 15\%$ variations in the identified damping variables, the optimal parameters presented in section 3.4.1 are considered applicable for the detailed elasto-plastic vehicle model. Table 4.7 shows the sensitivity of the measures to design variables, variations in damping (μ_2 and μ_1) and stiffness (λ_2 and λ_1), respectively. The nominal design variables refer to the optimal variables identified from the simplified LMS models.

Table 4.7: Sensitivity analysis of system performance measures to variation in the, damping, variables at 56 km/h impact speed for EIDV model

Variation	Vehicle deceleration		Vehicle deformation		Occupant Deceleration		HIC	Spf. EA
	Value(g)	Time (ms)	Value(cm)	Time(ms)	Value (g)	Time(ms)		
μ_2 variation								
+15%	33.6	2.0	22.66	56.4	23.38	58.2	36.7	90.8%
+10%	32.5	2.0	22.40	55.9	23.29	57.8	36.5	91.7%
+5%	31.6	2.0	22.12	55.5	23.16	57.8	36.4	92.0%
Nominal	34.5	1.9	21.88	55.4	22.91	57.8	35.8	90.4%
-5%	32.9	2.0	21.60	55.5	22.51	59.1	35.4	90.3%
-10%	31.4	2.0	22.49	88.0	22.35	62.4	35.0	88.9%
-15%	30.1	2.0	23.55	88.5	22.69	65.1	35.8	87.6%
μ_1 variation								
+15%	33.7	2.0	21.02	58.7	22.51	61.0	33.6	93.9%
+10%	33.5	2.0	21.31	57.8	22.70	59.6	34.5	91.2%
+5%	33.3	2.0	21.59	56.4	22.83	58.7	35.2	90.8%
Nominal	34.5	1.9	21.88	55.4	22.91	57.8	35.8	90.4%
-5%	32.9	2.0	22.16	55.5	23.04	57.3	36.6	89.9%
-10%	31.4	2.0	22.53	55.7	22.80	58.2	36.7	79.7%
-15%	30.0	2.0	22.94	55.9	22.74	59.6	36.4	91.4%
λ_2 variation								
+15%	30.75	2.0	21.97	55.5	23.05	57.8	36.4	90.18
+10%	30.75	2.0	21.94	55.5	23.00	57.8	36.2	90.25
+5%	30.75	2.0	21.91	55.5	22.96	57.8	36.0	90.31
Nominal	34.54	1.9	21.88	55.5	22.92	57.8	35.8	90.36
-5%	30.74	0.2	21.84	55.5	22.86	57.8	35.7	90.45
-10%	30.74	2.0	21.81	55.0	22.82	57.8	35.5	90.52
-15%	30.73	2.0	21.78	55.0	22.78	57.8	35.4	90.59
λ_1 variation								
+15%	30.8	2.0	21.82	55.5	22.91	57.8	33.9	90.43
+10%	30.8	2.0	21.84	55.5	22.91	57.8	35.9	90.42
+5%	30.7	2.0	21.86	55.5	22.91	57.8	35.9	90.39
Nominal	34.5	1.9	21.88	55.5	22.92	57.8	35.8	90.36
-5%	30.7	2.0	21.90	55.5	22.91	57.8	35.8	90.36
-10%	30.7	2.0	21.91	55.5	22.90	57.8	35.8	90.35
-15%	30.7	2.0	21.93	55.5	22.91	57.8	33.9	90.33

4.7 Summary

The proposed EIDV and IV models introduced in Chapter 2 are applied to a large-scale elasto-plastic LMS model of a vehicle to evaluate their effectiveness. A scaling technique is applied to realize an elasto-plastic model of the vehicle representative of the current vehicle designs. The optimal design parameters of the add-on absorbers, identified from the simplified LMS models, are also applied for the detailed vehicle model. The elasto-plastic vehicle model with EIDV model of the absorbers revealed significant improvements in the selected performance measures over a wide range of speed. The finding concurs with those observed for the simplified model. Furthermore, the selected performance measures varied only slightly with $\pm 15\%$ variations in the optimal parameters identified from the simplified model. These optimal design parameters are thus considered valid for the detailed elasto-plastic model of the vehicle. The validity of the proposed add-on energy absorber and the optimal design parameters is further investigated for an elaborate finite-element model of a vehicle in the subsequent chapter.

CHAPTER 5

CRASH ENERGY MANAGEMENT IMPLEMENTATION ON A FINITE ELEMENT MODEL USING LS-DYNA

5.1 Introduction

The manufacture of automobile structures has recently evolved to satisfy both car manufacturers' interests and consumer demand. However, the evolution process has been subjected to several potentially conflicting constraints such as: minimum structural weight, sufficient occupant protection according to safety regulations, and efficient power and the corresponding vehicle acceleration. This has led to many necessary vehicle structural modifications that are designed to apply to different car models pending minimum changes, and to cope with engineering technology and manufacturing capabilities. Current vehicle body structures are classified into two main categories: the body-over-frame structure (or ladder frame) and the unitary-body (or integral) structure. The second category, known as a '*monocoque*' structure, is widely used in manufacturing all passenger, SUV, minibus, and bus vehicles.

Experimental crashworthiness investigations of vehicle structures through crash tests are extremely costly; it costs more than \$25,000 per crash test and could reach to \$200,000 for a full crash test. In addition to the high costs involved, they are time consuming process that does not always provide definitive information [30,30]. However, with improvements in the computational power and the accuracy of simulation models, virtual testing can be extensively used as an alternative to the time consuming and costly full-scale tests, especially when testing severe maneuvers. As a result, different types of computational models, especially Finite Element (FE) model, have emerged to simulate

the response of vehicle structures under crash events. Calibrating the degree of crashworthiness enhancement via conducting virtual testing of FE model simulations is extensively used as an alternative of crash tests. Additionally, the designers can conduct necessary modifications by modifying and strengthening load carrying members via parametric studies. These studies are carried out through controlling design factors that have noticeable influences in enhancing crashworthiness [49,54,59]. Crash simulation of vehicle's structure is a highly nonlinear and short event duration problem and generally includes the following nonlinearities: (i) geometric (concerned with changes in configuration of each structural member's shape); (ii) material (concerned with changes in material properties such as plasticity); and (iii) boundary or contact (concerned with changes in contact area due to frictional or applied force) [184]. This implies that specialized software is required for simulating crash events. Among the available FE software packages, the LS-DYNA is one of the most widely used programs and is well suited for conducting crash analysis.

Crash simulation of vehicle's structure is computationally very expensive due to inherent nonlinearity and thus has an iterative nature of analysis. A simple crash simulation may take several hours to several days depending on the number of elements used to model the vehicle structure. Design optimization of vehicle structure for crashworthiness improvement may be achieved by combining a full nonlinear FE model of the vehicle structure with optimization algorithms. However, this is extremely expensive since both analysis and optimization models are iterative in nature. In case of conducting optimization directly to a FE model, the analysis module need to be executed several times in each optimization iterations and as mentioned before each analysis is

computationally expensive by itself. Therefore, a successful formal design optimization for crashworthiness improvement using a full scale nonlinear model is quite impossible. Different studies have used a surrogate model based on metamodeling technique to enable conducting optimization of vehicle structure under impact loads via a simplified models [32,33].

In this chapter, a multi-purpose FE model of a light-weight passenger car with a monocoque structure-type is used to investigate crashworthiness enhancement by implementing the proposed crash energy management (CEM) concept. This will be done by replicating the EIDV model, introduced in section 2.3.4, using a high fidelity FE model. Necessary modifications for the baseline model are conducted to validate the model's performance behaviors with crash test results. Add-on Voigt element energy absorbers are then created using the proper nonlinear discrete elements and their performance behaviors under impact loads are investigated. Different Voigt elements in extendable and integrated positions with vehicle structure are then added to the validated FE baseline model using the appropriate fixation types and the created bracket supports. The optimal damping and stiffness values obtained in section 3.4.1 are used (after conducting the proper scaling) as the initial design variables for the add-on elements in FE model. Finally, a surrogate metamodel of the nonlinear FE model is developed using design-of-experiments (DoE) and response surface method (RSM). This will allow optimization to be directly conducted on the developed surrogate model instead of a computationally expensive optimization on the full detailed nonlinear FE model. Different optimization techniques are then applied to the developed response function

obtained from the metamodel technique to fine tune the optimal design values of the add-on components.

5.1.1 Nonlinear Finite Element Modeling for Crashworthiness

The FE methods have been extensively used in simulating different dynamic problems through the discretization of the whole structure into finite elements, development of the equations of motion (EOM) for each element, assembly of all EOMs based on continuity, applying boundary conditions, and solving the set of governing equations of motion using the appropriate technique [184]. The generalized dynamic equations of motion of a structure in the finite element form can be represented as:

$$[M]\{\ddot{X}\} + [C]\{\dot{X}\} + [K]\{X\} = \{F^{ext}\} \quad (5.1)$$

where $[M]$, $[K]$ and $[C]$ are the system structural mass, stiffness and damping matrices respectively, $[K]\{X\}$, which equals $\{F^{int}\}$, represents the internal forces resulting from the plastic deformation of a structural part, $\{X\}$, $\{\dot{X}\}$ and $\{\ddot{X}\}$ are the nodal displacement, velocity and deceleration vectors, respectively, and $\{F^{ext}\}$ is the external nodal load vector. It should also be noted that for problems that involve material and geometrical nonlinearity, such as crash simulation problems, the stiffness matrix $[K]$ is not constant; instead, it is a function of displacement and time [197]. There are two methods of analysis that can be used in solving Eqn. (5.1), namely: implicit and explicit methods. An explicit method is more appropriate for impact problem or nonlinear transient dynamic problems with very short time durations as in the case of a crash simulation event. On the other hand, the implicit method is more suitable for dynamic problems in which the duration of the applied load is relatively large compared with the fundamental period of

structure [186,187]. Additionally, due to the usage of fixed and small time step in order to meet conditional stability and a high computation cost, the implicit method is unconditionally stable under some conditions and is not suitable for crash analysis simulation [33,188].

Because of the fact that vehicle structure is composed of different structural members that are totally deformed under impact loads, an algorithm is required to manage the transmission of the internal forces between different structural mating members, which is known as contact algorithm. Among three types of contact algorithms available in LS-DYNA, the penalty-based contact algorithm is the most widely used in crash simulation [189]. The method consists of placing normal interface springs between all penetrating nodes and the contact surface to be used in calculating contact forces. For more information on the subject, one can refer to Refs. [188, 189]. In the same trend, LS-DYNA handles friction forces between the moving parts using the Coulomb formulation with the possibility of defining an unlimited number of interacting part pairs and their corresponding friction parameters [189].

5.1.2 Method of Analysis and Performance Criteria

A small-size passenger car is selected to demonstrate that the proposed crash energy management (CEM) concept with the optimal configuration obtained in section 3.4.1 can be applied to a variety of vehicles of different mass and size using scaling techniques. It should be mentioned that the CEM concept was applied on a large-scale passenger car (represented by lumped mass model) introduced in section 4.4 by scaling down the whole model to the same mass of the model introduced in section 2.3.4.

In this chapter, the nominal values of the add-on EA system are scaled down to meet the lower mass of the vehicle and are then implemented to the finite element model, provided that the add-on locations are well selected. Explicit double precision analysis is used to make sure that the FE model is suitable for vehicle crash simulation. The assigned performance measures for measuring the crashworthiness enhancement used in FE models are the peak car deformation (*Def*), the maximum longitudinal deceleration at the rear seat location, the conceptual HIC value measured at the firewall accelerometer location and the peak normalized rigid wall force. It is important to note that the change in the total energy absorbed by the car structure will be recorded to investigate the degree of crashworthiness enhancement that is achieved in the modified FE model.

5.2 Validation of the Baseline FE Model

Performance testing is an important step in the development of any vehicle model. Normally, full-scale field tests are conducted to collect the dynamic response behaviors for evaluating vehicle model performance. Validation of the simulation results is critical for the acceptance of such simulation models.

The Geo-Metro FE-detailed model is selected for this study which was originally developed by the National Crash Analysis Center (NCAC) and is available online [190]. It should be mentioned that the NCAC group is a cooperation sponsored and funded by the Federal Highway Administration (FHWA), National Highway Traffic Safety Administration (NHTSA) and the George Washington University. It should be mentioned that the NCAC posted these FE models on their website to encourage users to contribute towards their validation and further development. This model is one of the earliest models developed by the NCAC, where the software packages used for simulation were

not so advanced. Accordingly, it should undergo some modifications in order to obtain a validated FE model for frontal crash impacts. In few studies, different modifications needed to update this particular model have been investigated [58,191]. Hence, frontal crash simulation is conducted in parallel with performing the necessary model modifications followed by validation of the obtained results using the real crash test results [192].

LS-DYNA is used to modify and simulate a full frontal vehicle impact test with a rigid barrier by assigning an initial velocity of 56.6 km/h to the whole model according to the New Car Assessment Program (NCAP) regulations for frontal impact. The FE model of the Geo-Metro car is shown in Figure 5.1, while the model parameters and platform information or benchmark data are summarized in Table 5.1.

Geo-Metro Detailed (NCAC V01)

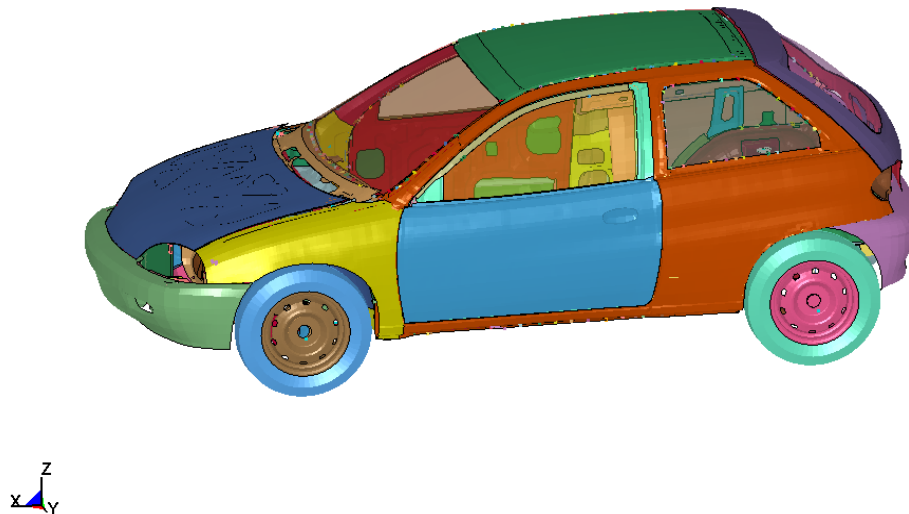


Figure 5.1: Isometric view of Geo-Metro FM model

Table 5.1: Comparison between FE model and test vehicle parameters of the vehicle model and benchmark data

Parameter	FE model	Test vehicle
Weight (Kg)	865	1125
Wheel track , F (mm)	640	646
Wheel track, R (mm)	655	661
Wheelbase (mm)	2325	2375
CG Rearward of front wheel C.L. (mm)	884	1117

LS-DYNA is run using this benchmark:

Parameter	Specifications
Model#:	mpp971d R2
Platform :	Linux Workstation AMD-Opteron
Precision :	Double precision, I8R8
Total CPU time:	7 hrs 14 min 4 sec (for 150 ms)
Number of Processors	42

Different modifications are applied to the detailed baseline FE model available on the NCAC website to improve simulation results and to obtain good agreements between the simulations results and the experimental crash test, which can be summarized as follows:

- The rims of the tires were simulated as one part to prevent the wheels to rotate, which yield lower impact energy due to increased friction between the sliding tires and the road surface. In order to remedy the problematic assembly of the tires' rim parts into one part which prevents tires from rotation, they are separated into four rims. Additionally, each rim is separated into two parts: the inner and the outer rims. The inner rim is modeled as a rigid material definition to be used in fixing the rotating tire assembly to the rest of the vehicle structure. The material of the outer

rim is kept as a deformable material for nearly accurate representation of real vehicle structure. In order to enable the tire assemblies to rotate, four rotating axles are defined (one axle per each tire).

- The local coordinate systems of the seat belt accelerometers are modified to get the correct readings of the deceleration components by reordering the nodes that direct the local x-axis to coincide with the longitudinal axis of the generalized coordinate system.
- The rigid body constraints used to unite the structural components of the front disc brake systems are modified by simply using the rotating disc brake as the master part while the uprights and brake calipers are set to be slaved parts.
- The material properties of different structural components are properly modified, especially those concerning the engine block mass.
- The front wheel alignments are adjusted to prevent rear outward motion during the impact event. It is noticed that during the frontal impact, the wheels' assemblies contribute in transferring part of the impact energy to the side-frames. Thus, if the wheels do not maintain their forward direction, the frontal substructure deforms more rapidly, which yields improper simulation results and consequently increases the probability of passenger compartment penetration.
- The wheel track of the front axle is modified to be smaller than the rear one by the same amount of the simplified Geo-Metro model posted on the website. This comes in agreement with two facts namely: (i) the torsion loading case induced during negotiating a bump yields equal moments on the front and rear axles, where the normal force applied on the rear axle is usually less than that of the front, which

implies that the wheel track of the rear axle should be greater than that of front [193]; and (ii) the car roll axle; that connects the rear and front axles roll centers; should incline towards the front which will be violated if the front wheel track is greater than the rear one since the front axle roll center's height is increased, especially in the case of independent wheel suspension [194].

- Steering rods are added to the front wheels to ensure that both wheels are generally correlated and to prevent their relative movement and rear outward opening.
- The stiffness properties of the front and rear suspension springs are represented as elasto-plastic stiffness with rebound behavior. It is important to note that proper suspension system performance permits the right kinematical behavior of the system tire-limb since the vehicle weight acts on the wheels through suspension.

The crash test results that conducted by the NHTSA of the Geo-Metro are obtained from NHTSA website [192]. The results are filtered using the signal analysis software 'BW filter' offered by the NHTSA, which stands for the Butterworth filtering program that is in compliance with SAE filtering requirements J211. This software enables researchers to open and deal with the encoded data of the crash test results, where filtering of the data can be executed using different the Channel Frequency Class (CFC) that range from 60 to 1000 Hz. During crash tests, the maximum amount of data should be extracted, which requires the following: high-speed data-acquisition and one or more tri-axial accelerometer at different locations such as the B-pillar of the driver's side to record vehicle dynamic responses. Different kinematical behaviors of both car structure and occupant dummies at specified locations of the experimental crash test are available on NHTSA website. Seven accelerometers at different locations were used to record the

dynamic performance of the vehicle structure, as shown in Figure 5.2. They are located at the following places: engine (upper and lower), firewall, rear seat (left, right, and middle) and luggage, for more information, one can refer to Ref [192].

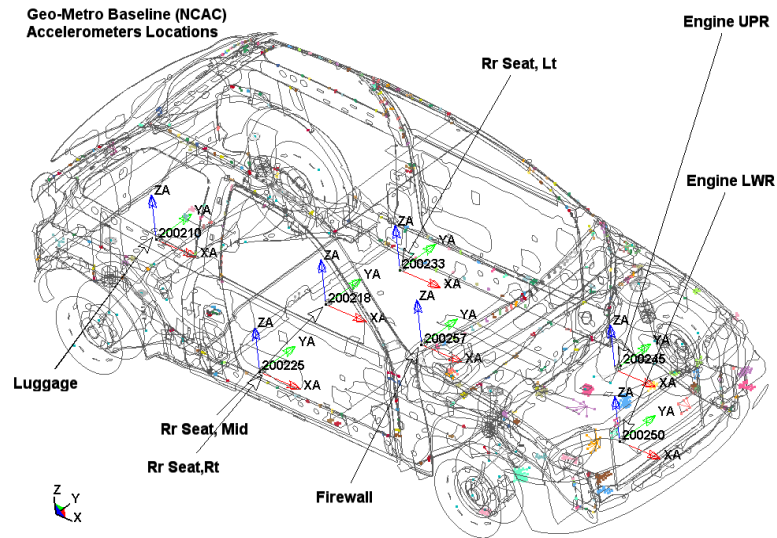


Figure 5.2: Accelerometer locations

A thorough familiarity with the FE model and crash test conditions is needed to ensure that the FE model is applied correctly to a specific test. Comparisons between the crash test and the simulation results are shown in Figures 5.3 to 5.6, where the simulation sampling frequency is 10 MHz. It should be mentioned that both crash tests and simulation results are filtered with SAE 1000 Hz filter. The proposed enhancements made on the baseline FE model allows us to obtain a well refined model that is in good agreement with the crash tests. The general agreement between the simulated full scale FE model and the real crash test results is clearly shown in the figures. The differences between the simulation and test results can be attributed to many factors such as computer model limitations, model development, test data quality, and test and manufacturing variances, among others. Human error and randomness can play a large part in the errors that occur during test data acquisition. Figures 5.3 and 5.4 show the

comparisons between the simulated and crash test results for the left and right rear car seats, respectively. Similarly, Figures 5.5 and 5.6 show the simulated results for the accelerometers mounted on the upper and lower parts of the engine.

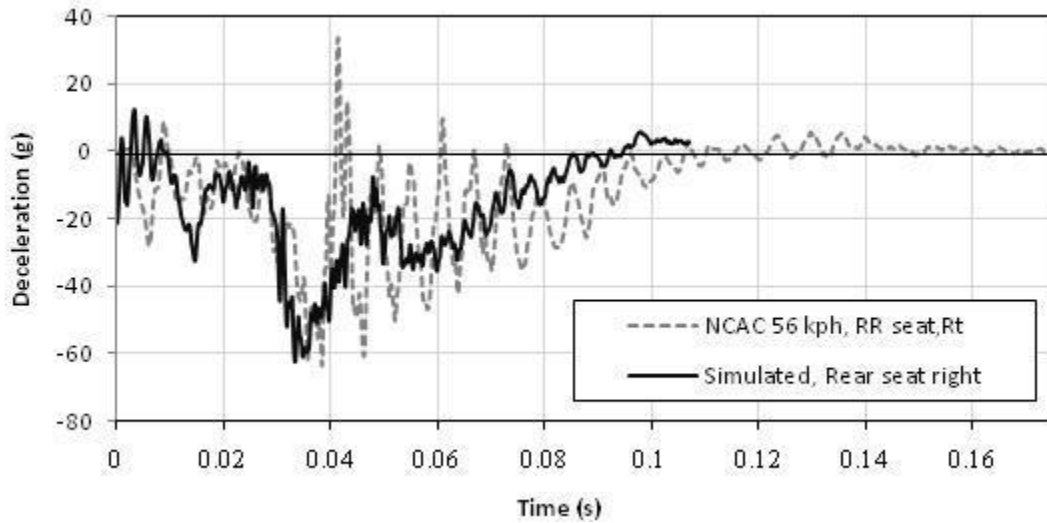


Figure 5.3: Comparison between the right rear seat deceleration of the Geo-Metro FE model with NCAC crash test results at 56.6 km/h

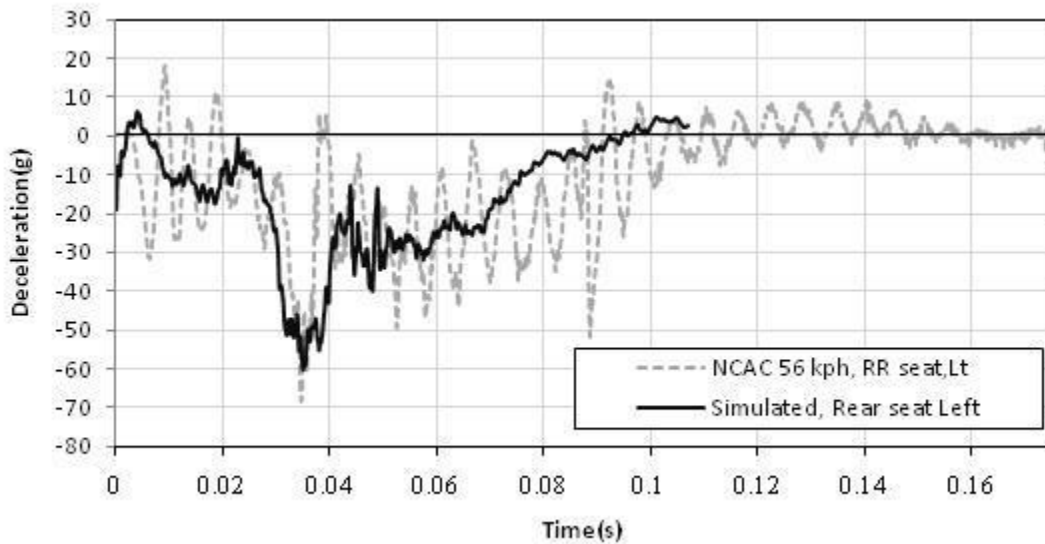


Figure 5.4: Comparison between the left rear seat deceleration of the Geo-Metro FE model with NCAC crash test results at 56.6 km/h

As shown from the above figures, both the simulated and crash test results are in good agreements since they almost have the same peak value and follow the same

pattern. Considerable oscillations in the measured acceleration of the crash test could be observed before it approaches steady state value of 0 g deceleration, which could be inferred due to improper fixation of the accelerometers or the sampling frequency of the data acquisition system used. Comparisons of the deceleration response measured at the engine upper accelerometers between the simulation and crash test results show good match of the peak values and the pattern, as shown in Figure 5.5. However, the deceleration of the crash test seems to saturate at nearly 220 g, which could be attributed to: improper electric connections, or reaching the frequency saturation level, or the effect of temperature on the accelerometer output.

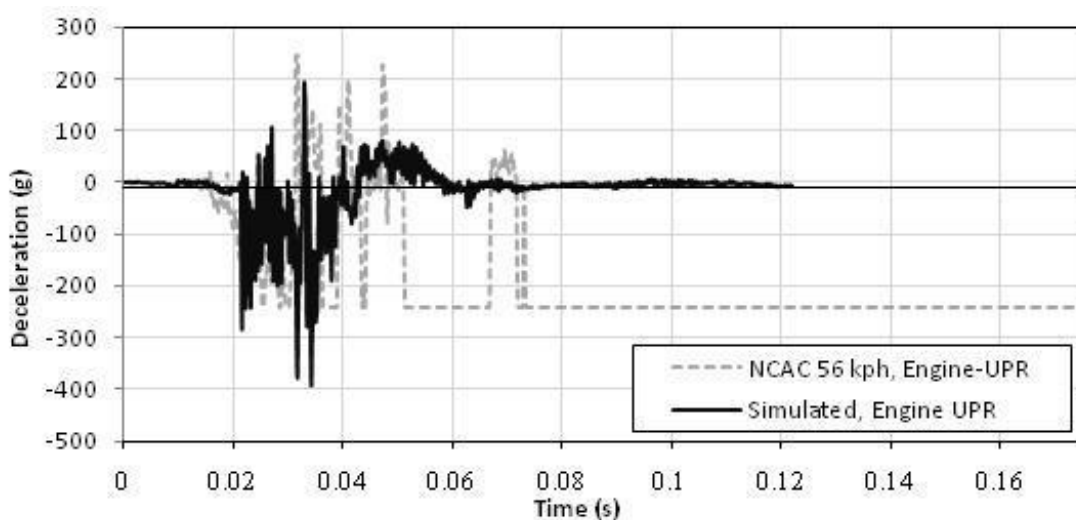


Figure 5.5: Comparison between top engine deceleration measured of the Geo-Metro FE model with NCAC crash test results at 56.6 km/h

Additionally, there is a considerably high peak for the simulated longitudinal deceleration signal measured at the engine's lower location (shown in Figure 5.6), which could be due to the type of fixation used for the engine or the type of filter used or the difference between the sampling rates with the crash test results.

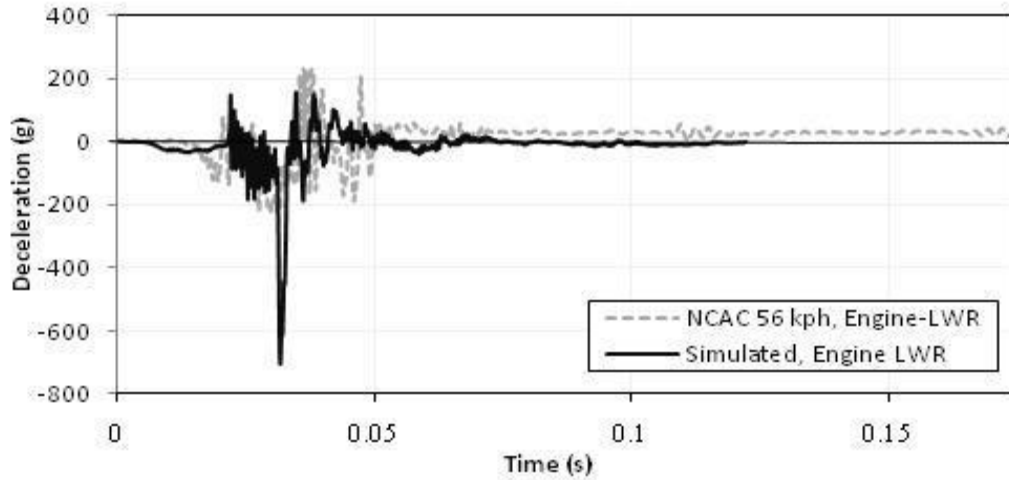


Figure 5.6: Comparison between bottom engine deceleration of Geo-Metro FE model with NCAC crash test results at 56.6 km/h

It should be noted that there are reading inaccuracies and abnormal behaviors of the crash test results at the accelerometers mounted on the engine's upper and lower locations, as shown in Figures 5.5 and 5.6. These could be attributed to some of the possible reasons namely: inefficient data acquisition or accelerometers with low saturation points or improper electric connections. The comparison of the normal rigid wall force obtained from the simulated Geo baseline model and those obtained from both the NCAP crash test and simulated NCAC, are shown in Figure 5.7.

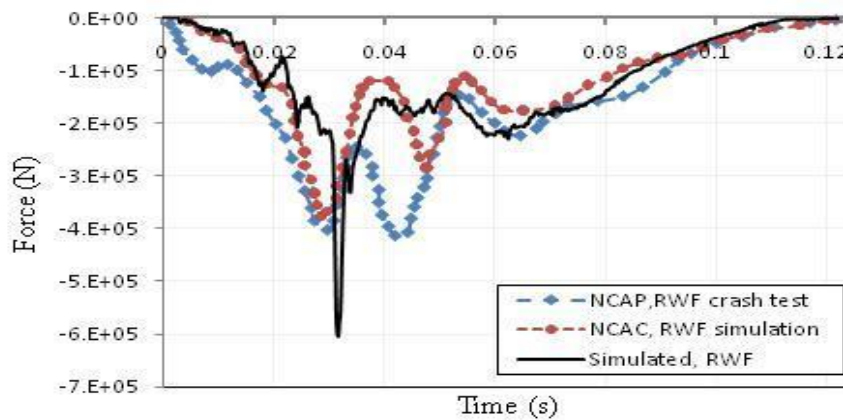


Figure 5.7: Comparison between longitudinal rigid wall force of the baseline Geo-Metro FE model and both NCAC simulation and NCAP crash test results [195] at 56.6 km/h

As it is shown in Figure 5.7, there is a good agreement between the simulation results with those simulated by NCAC group except for a high peak at around 326 ms, which could be due to the type of filter used or the difference in sampling rates. To confirm this, the normalized force of the modified baseline model is filtered using different types of filters, namely the SAE and Fir100 types, and the results are shown in Figure 5.8. It is clearly shown that the value of the peak value is dropped from 605 KN to 397.9 KN, which is very close to that of both NCAP-crash test and NCAC simulation shown in Figure 5.7.

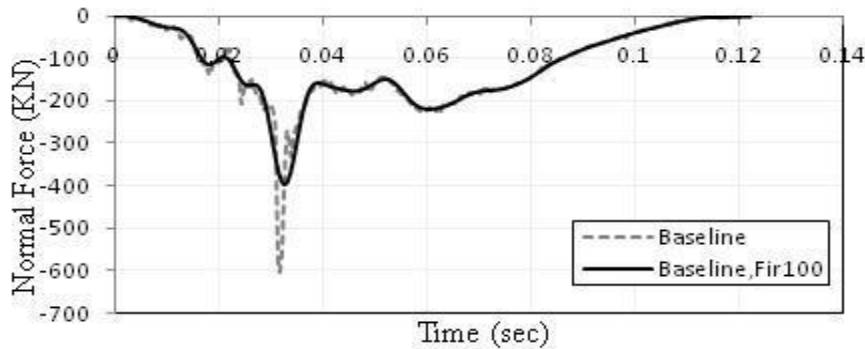


Figure 5.8: Rigid-wall force of the baseline Geo-metro FE model at 56.6 km/h impact speed using two types of filters

The comparison of the energy balance response between the baseline Geo-metro model and the NCAC simulation results [195] are shown in Figure 5.9. It is clearly shown that there is a good agreement of both total energy (TE), kinetic energy (KE) and hourglass energy (HE) obtained from the simulation with those of the NCAC simulation. However, there is 10% deviation in the potential energy (PE) components between the simulation and NCAP simulation. This may be due to the fact that there is no sliding energy (SE) component in NCAC simulation or they might add up this component to the potential energy.

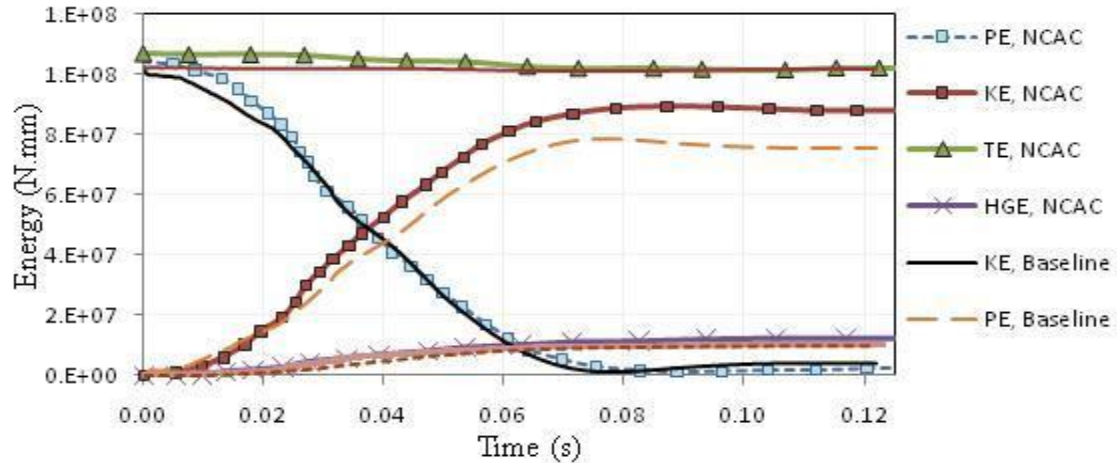


Figure 5.9: Comparison of energy balance response between the baseline and NCAC simulation results, for Geo-Metro FE model at 56.6 km/h [195]

5.3 Modeling and Analysis of the proposed Extended-Integrated Dual Voigt (EIDV) Model

In order to develop the same crash energy management (CEM) concept applied before to the lumped-parameter models (presented in Chapter 2 through 4) on the finite element model, different steps have to be undertaken. This includes modeling of the shock absorber (Voigt element) under impact load using a simplified FE model to validate its action and the proper fixation of the Voigt elements to the rest of car structure in the extended and integrated locations. Simulation of the hydraulic dampers under impact load in LS-DYNA requires certain procedures in order to correctly select the proper elements [197].

The integrated set of add-on energy absorbers is fixed to brackets that are modeled using the Hypermesh software as solid elements and are then imported in LS-DYNA. The proper concatenations for the component coordinate systems of the brackets are then accurately calculated to define the transformation matrixes that enable these

brackets to coincide with the parts of the longitudinal members, which will be attached to them, as shown in Figure 5.10.

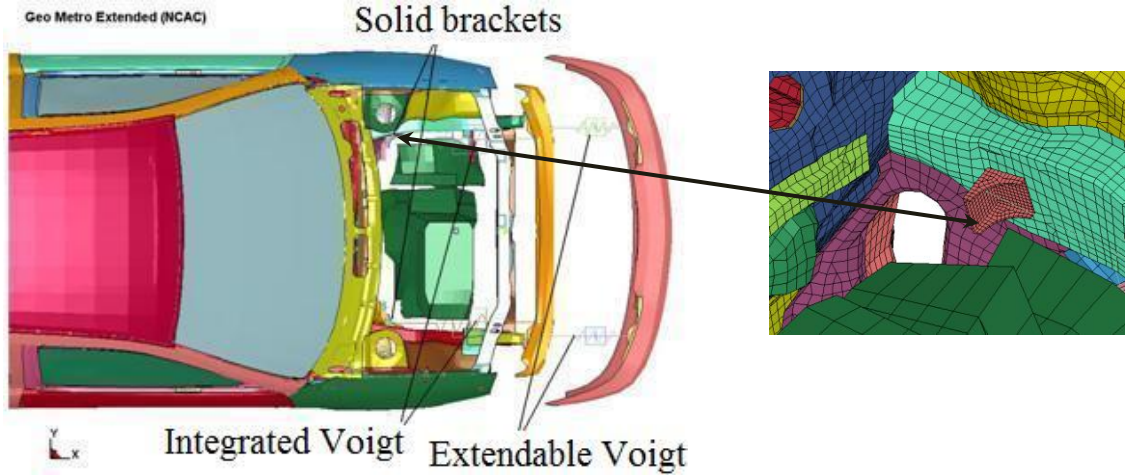


Figure 5.10: Modified Geo-metro model

The total mass of the extended FE model ' m_{FE} ' after incorporating the proposed add-on EA system is 845 kg, while the simplified lumped-parameter model (m_v) is 1500 kg. As explained in section 4.4, the scaling factor should be implemented to adjust the damping and stiffness properties of the add-on EA elements. For this case, the scaling ratio (B) defined before will be:

$$B = \sqrt[3]{m_{FE}/m_v} = \sqrt[3]{845/1500} = 0.8262 \quad (5.2)$$

Scaling law is implemented on the nominal values of the look up tables of the stiffness and damping properties of the add-on EA elements in order to use the same values of the optimal design variables (DVs). The optimal set of design variables, obtained by interpolation, is the same as those used in section 4.5.3 which is presented in Table 5.2. As it can be noted there is a slight increase in the value of μ_2 from 3.3 to 3.345 because the simulation is conducted at a 56.6 km/h to resemble the crash test speed [185].

Table 5.2: Design variables at the assigned impact speed for modified Geo-Metro model

Impact speed (km/h)	λ_2	μ_2	λ_1	μ_1
56.6	0.1	3.345	0.3	2.0

The front bumper is extended to a distance of 0.45 m in front of the car, and the inner part of the bumper is duplicated to remain in the ordinary position as shown in Figure 5.10. The positions of the extended Voigt elements are carefully selected to maintain continuity of the load path to the main longitudinal members. They are fixed between the inner part of the extended bumper and the original bumper using rigid patched shells to ensure proper distribution of the impact force through these structural members. On the other hand, the integrated Voigt elements are attached to the structural members in such a way to reduce the bending moment on the longitudinal members and to sustain the extended Voigt elements. The integrated add-on EA systems are attached using rigid patches and a pair of brackets at the forward and rearward ends, respectively. These brackets are rigidly connected to the longitudinal rails using two pairs of rigid patched shells as shown in Figure 5.10.

It is important to note that there are different types of contact method that can be used to join any two mating surfaces. The appropriate method is to create rigid patches since both the rigid brackets and longitudinal members have different mesh sizes and thus nodes at the interface surfaces are not matched. This can be done by creating two rigid patched surfaces on the longitudinal members and constrain these rigid brackets as slaves to these surfaces, for more information regarding contact modeling one may refer to Refs [189,197]. It should be noted that in order to avoid penetration between different structural parts and the extended bumper, an additional automatic surface-to-surface

contact is assigned in the model. A comparison between the baseline and modified Geo-Metro model simulation results illustrates a remarkable reduction in the peak values of different performance measures, as shown in Figures 5.11 through 5.16. Close examination of Figures 5.11 and 5.12 shows that the decelerations at the rear seat left and right locations have been reduced by almost 43 % and 32 %, respectively in the proposed extended Geo-Metro model. The results for the peak rear seat decelerations in the baseline and extended Geo-Metro models are provided in Table 5.3.

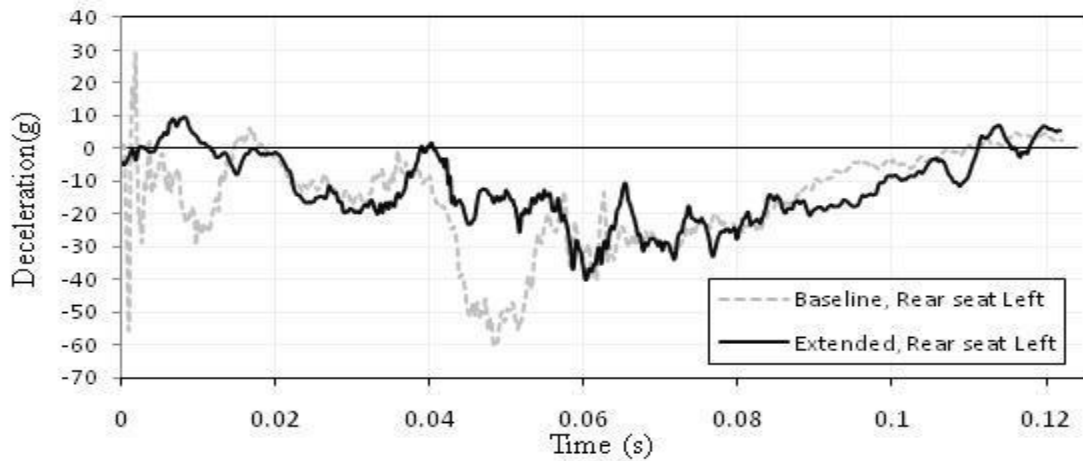


Figure 5.11: Comparison between left rear seat deceleration signal of baseline model and modified Geo-Metro FE model at 56.6 km/h

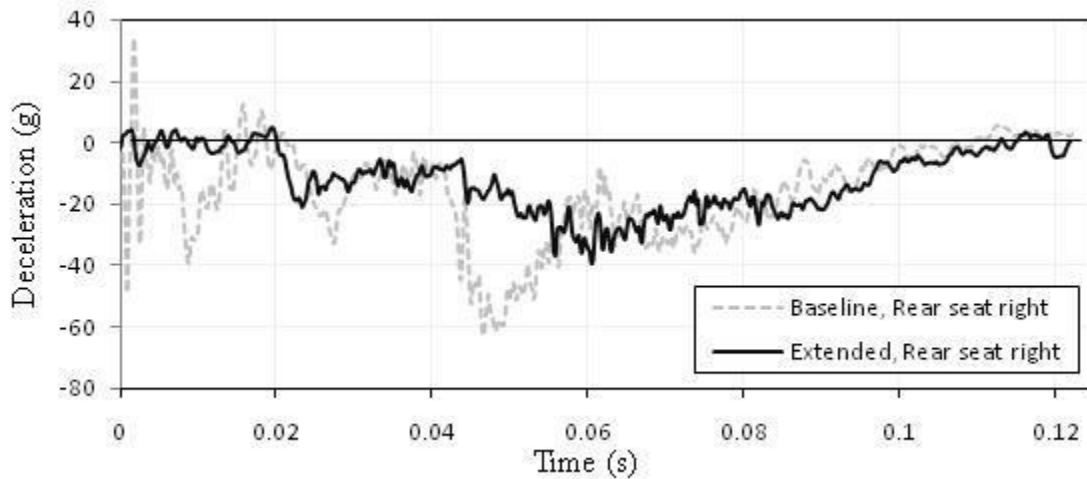


Figure 5.12: Comparison between right rear seat deceleration signal of the baseline model and modified Geo-Metro FE model at 56.6 km/h.

Table 5.3: Percentage of enhancement of rear seat peak deceleration at 56.6 km/h

Model	Rear seat Rt.	Rear seat Lt.
Baseline	62.75 g	60.38 g
Extended	35.97 g	40.91 g
% reduction	42.68 %	32.25 %

Figures 5.13 and 5.14 show clearly the degree of enhancement of deceleration responses measured at upper and lower engine position, where their peak values are also tabulated in Table 5.3. As it can be seen, significant reductions (about 62% and 65 %) are achieved in the engine peak deceleration of the upper/lower accelerometers respectively using the proposed extended FE model.

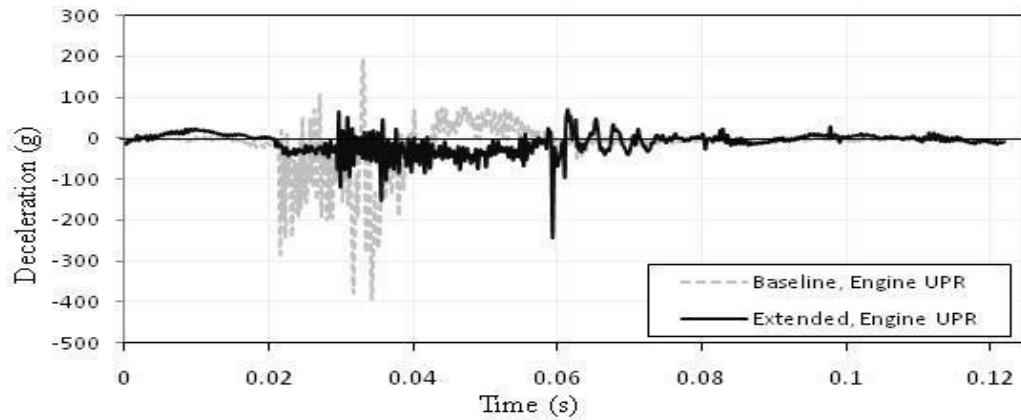


Figure 5.13: Comparison of upper engine deceleration signal between the baseline model and the modified Geo-Metro FE model at 56.6 km/h.

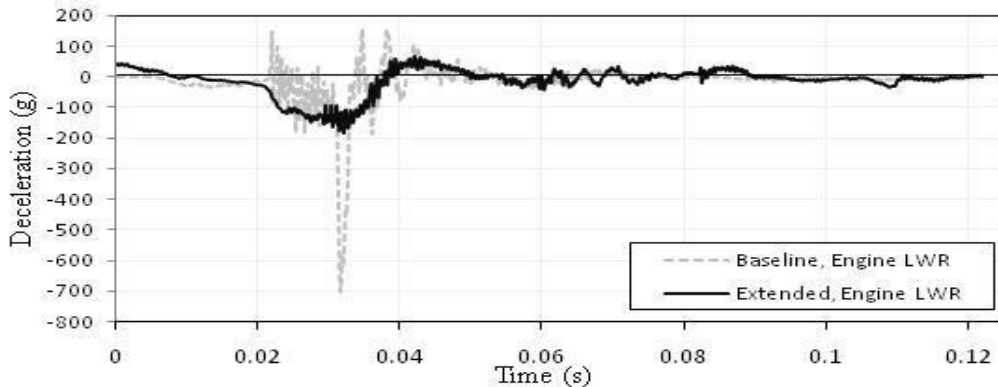


Figure 5.14: Comparison of lower engine deceleration signal between the baseline model and the modified Geo-Metro FE model at 56.6 km/h.

Table 5.4: Percentage of enhancement of the engine peak decelerations at a 56.6 km/h impact speed

Model	Engine UPR	Engine LWR
Baseline	392.01 g	704.91 g
Extended	150.55 g	247.94 g
% reduction	61.59 %	64.83 %

Similarly, remarkable reductions are achieved for both the normal rigid wall force and the peak vehicle deformation as shown in Figures 5.15 and 5.16, respectively.

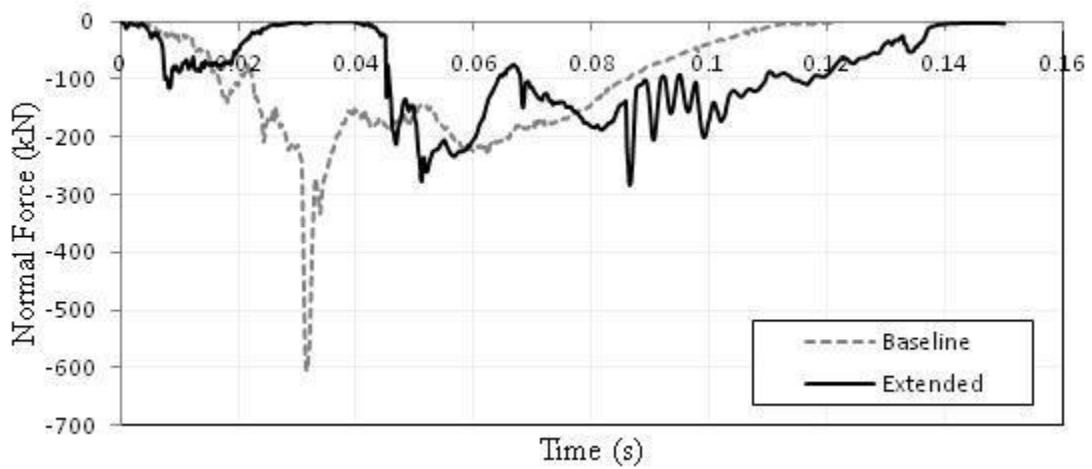


Figure 5.15: Comparison of the normal rigid wall force between the modified Geo-Metro and the baseline models at a 56.6 km/h impact speed.

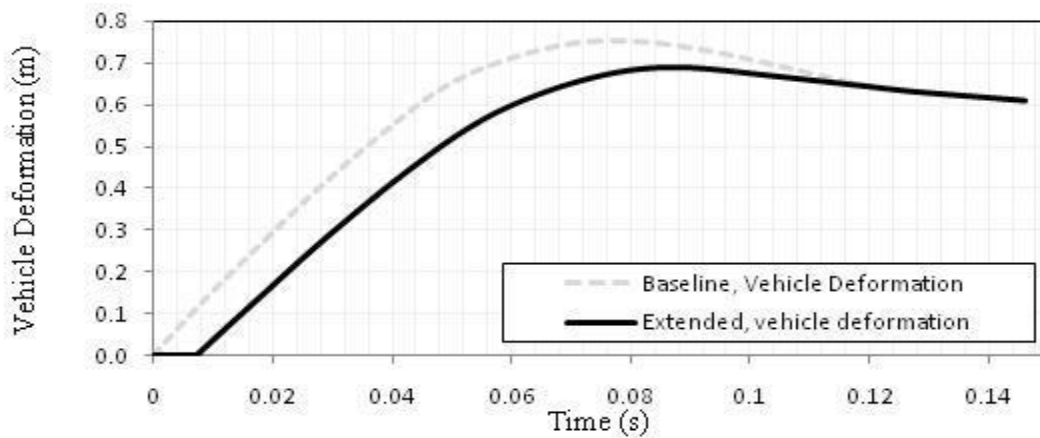


Figure 5.16: Comparison of the car structural deformation (Def) between the modified Geo-Metro FE and the baseline models at a 56.6 km/h impact speed

The degree of enhancements for both peak values of the normal rigid wall force and vehicle deformation achieved by the modified extended model and their comparison with those of the baseline model as provided in Table 5.5.

Table 5.5: Percentage of enhancement of both the normal rigid wall force and peak vehicle deformation (*Def*) at a 56.6 km/h impact speed

Model	Maximum normal RW force (kN)	Peak vehicle Deformation (m)
Baseline	605.004	0.7518
Extended	284.032	0.7061
% reduction	53.05 %	6.08 %

In order to obtain the energy absorbed by the structural members in the modified model, the energy absorbed by the CEM system must be subtracted from the total potential energy, which will be named as ‘net internal energy’. A comparison of the energy balance response between the baseline and the modified extended FE model clearly indicates a noticeable reduction of the energy absorbed by vehicle structure. The amount of energy dissipated by the add-on system has a significant effect in reduction of the energy absorbed (PE) by the structural members, which is about 9% reduction compared with the baseline model, as shown in Figure 5.18. Furthermore, the CEM system reduces the rate of decay of both kinetic energy (KE) and potential energy (PE) of the extended FE model compared with the baseline model, as shown in Figures 5.17 and 5.18. Additionally, both the hourglass energy (HGE); that represents energy dissipated due to meshing, type of joint and type of elements; and the sliding energy (SE) dissipated due to interaction between adjacent parts; are also reduced, for instance, the sliding

energy has reduced from 12.7 KJ to 6.3 KJ, as shown in Figure 5.17, compared with the sliding energy of the baseline shown in Figure 5.9.

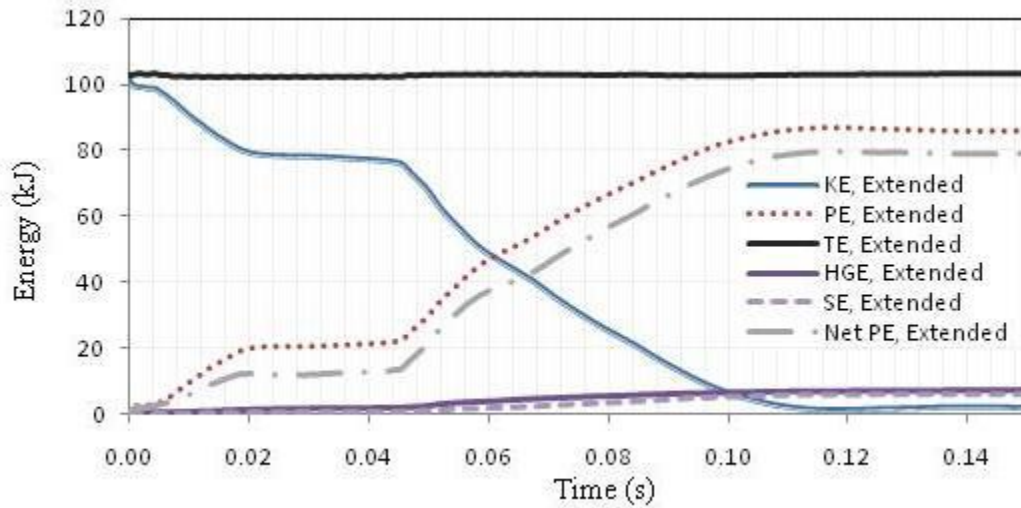


Figure 5.17: Energy balance response of Geo-Metro extended FE model at 56.6 km/h

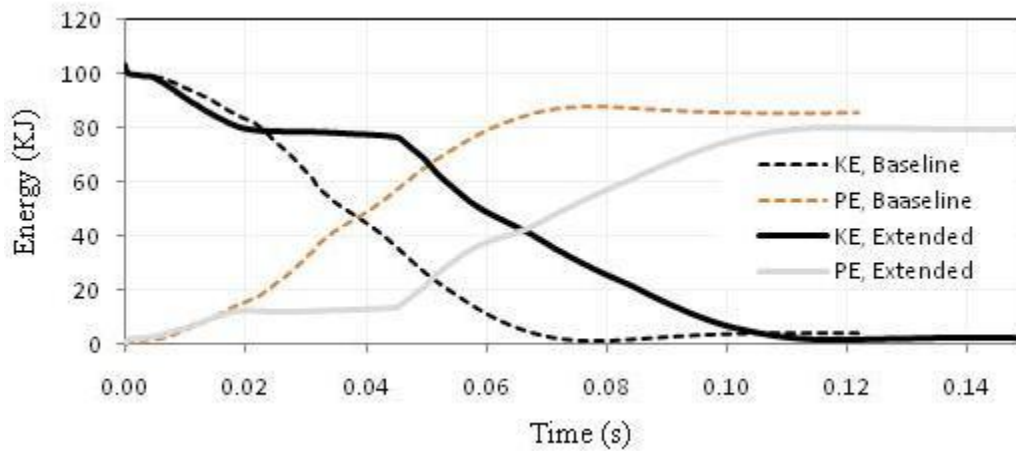


Figure 5.18: Comparison of the kinetic and internal energies between the baseline and extended FE Geo-Metro models at 56.6 km/h

5.4 Optimization of the Modified FE Model

Optimization techniques have evolved to reach a degree of maturity in the past few years, especially in the field of crashworthiness enhancement. With rapidly advancing computer technology, computers are becoming more powerful, and

correspondingly, the size and complexity of the problems that can be solved using optimization techniques are also increasing. The current modified FE model contains 194,261 elements and requires a computational time of about 5.5 hours on the cluster using 48 processors for the completion of just one simulation run for a 175 ms simulation time of a frontal impact with a rigid barrier.

Although optimization methods are generally effective in solving linear structural design problems, they lose their effectiveness in crashworthiness problems. Objective and constraint functions in crashworthiness optimization problems are often non-smooth and highly nonlinear in terms of their design variables, which yield high computational cost. It should be mentioned that there are two main types of optimization algorithms, namely gradient-based and non-gradient-based algorithms. In the first type, gradients of the objective and constraint functions are required, which may not be obtained analytically due to the complexity of the problem. Numerical evaluation of the gradients may also fail or generate spurious results due to the noisy nature of the responses in crash problems. On the other hand, when using non-gradient-based algorithms such as the genetic algorithms, a much larger number of iterations are required compared with gradient based techniques. Therefore, applying crashworthiness optimization directly to a nonlinear FE model is not practical due to high computational costs associated with simulations. This has prompted different researchers to conduct structural optimization using surrogate models through metamodel methods as an alternative method [32,33,199,200]. In the following subsection, the metamodel techniques are discussed to select the proper technique to be used for design optimization of crashworthiness problems.

5.4.1 Metamodeling Techniques (Space Mapping Technique)

As explained above, conducting optimization algorithm directly to a high fidelity FE model is practically impossible as it is a very time consuming and tedious process. Therefore, it is very important to represent the original FE model as a surrogate model using meta-modeling techniques. This, in turn, reduces the optimization's run time without a need to run LS-DYNA simulation since the optimization will be conducted directly on the response function obtained from the RSM technique instead of full nonlinear FE model.

A metamodel is simply defined as the steps required to extend and map the necessary information needed from a LS-DYNA simulation to form a mathematical model describing the response of the system. Metamodels are used as surrogate models for finite element models to describe the functional relationship between the physical parameters of a structure and its responses [201]. In order to implement the metamodeling technique, two main steps are needed: implementing the design-of-experiments (DoE) and selection of the appropriate type of the surrogate model, such as response surface method (RSM) or neural network models (NNM) [199]. In the following section, metamodel building using approximation techniques is described.

5.4.1.1 Design-of-Experiments Implementation

Decision making and DoE methods are extensively implemented in dynamic vehicle structural analysis to cope with the ever increasing demands on car manufacturers to lower production costs and withstand global competition in the car production market [201,203]. Design-of-experiments provides a systematic and formal way of defining a design matrix based on statistical methods to select the most controlling design points so

as to maximize the gain while using a minimum number of simulations. This is achieved by investigating which set of design variables in a process affects the performance most and then narrowing down the set to the required number of design points that guarantees satisfactory functional performance output in products. Different studies have discussed various DoE methods that are applicable in car crash analysis, like the Koshal, Optimal Latin Hypercube Sampling (OLHS), Monte Carlo techniques (preferable for large number of DVs) and D-optimal criterion [32,201,203,204]. Among different DoE techniques, the D-optimal criterion has been verified for its applicability to vehicle structural optimization, especially under crash simulations [33,205]. To understand the D-optimal concept, let:

$$y = \hat{y} + \varepsilon \quad (5.3)$$

where y : is the true optimization response, $\hat{y} = X\phi$ is the approximated DoE response function, X is the design matrix that relates system criteria with DVs, ϕ is the regression coefficients and ε is the error, defined as the difference between the simulation analysis and the approximate function.

To minimize overall error (ε), the least square method is used to obtain an accurate metamodel, the regression coefficients so that the metamodeling accurately represent the original model. This can be obtained if the determinant of $(X^T X)^{-1}$ is set to a minimum, which means that the set of regression coefficients ϕ that achieves minimum error can be represented as:

$$\phi = (X^T X)^{-1} (X^T \hat{y}) \quad (5.4)$$

which may be derived by differentiating the least square error with respect to ϕ . It is

recommended to use minimum number of design points for DoE specified as $\frac{(N+1)(N+2)}{2}$ when applying the D-optimal technique, where N is the number of design variables [205,206]. Additionally, it is recommended to use 1.5 times the minimum number of design points to guarantee the accuracy of the results [202].

The initial starting point is the optimal design variables obtained from section 3.4.1 for the simplified LMS model and applied in section 5.3 with the values of [$\lambda_2=0.1$, $\mu_2=3.345$, $\lambda_1=0.3$, $\mu_1=2.0$]. The values of design variables are allowed to be varied $\pm 20\%$ and $\pm 10\%$ of their initial values for the add-on EA Voigt elements in extendable and integrated positions, respectively. The design space that contains all the upper and lower bounds of the design variables is represented as follows: $\lambda_2=[0.08:0.12]$, $\mu_2=[2.748:4.122]$, $\lambda_1=[0.27:0.33]$, $\mu_1=[1.8:2.2]$. The number of design variables is four, which requires that the number of design points assigned to be 15 as a minimum and 23 as the recommended number of points for the D-optimal criterion. Henceforth, in this dissertation, the design points are set as 30 for more accurate model representation. The design matrix of the D-optimal criterion is provided in Table 5.6. It should be mentioned that these design points are generated from LS-OPT optimization software based on system design performance and design vector limits.

Table 5.6: Design matrix of metamodel for the modified Geo model

Design point	μ_2	μ_1	λ_2	λ_1
1	3.345	2.000	0.010	0.300
2	2.890	1.800	0.092	0.270
3	3.980	2.160	0.090	0.270
4	4.120	2.200	0.090	0.330
5	3.850	1.800	0.110	0.270
6	2.750	2.200	0.092	0.324
7	2.750	1.800	0.090	0.270
8	2.750	2.200	0.090	0.330
9	2.750	1.840	0.110	0.330
10	4.120	1.800	0.092	0.330
11	2.750	1.800	0.094	0.330
12	4.120	1.800	0.110	0.330
13	4.120	2.120	0.110	0.330
14	4.120	1.800	0.110	0.270
15	2.750	2.200	0.102	0.270
16	2.750	2.160	0.090	0.270
17	2.750	2.160	0.108	0.324
18	4.120	1.840	0.090	0.270
19	4.120	2.200	0.092	0.270
20	3.980	2.160	0.110	0.270
21	2.750	1.880	0.108	0.270
22	4.120	2.200	0.094	0.270
23	4.120	2.160	0.110	0.270
24	4.120	1.800	0.090	0.312
25	2.750	1.800	0.108	0.270
26	3.980	1.800	0.108	0.330
27	2.750	2.160	0.110	0.330
28	2.750	1.800	0.092	0.330
29	4.120	1.800	0.094	0.330
30	4.120	2.200	0.110	0.330

In order to implement metamodeling technique on the FE model, the assigned design variables, which are the damping and stiffness factors of the add-on EA system,

have to be represented as parametric multipliers to the ordinates of the corresponding look-up tables. It should be mentioned that the scaling factor is used to scale-down nominal values of the look-up table in order to be in the same order of design variables used in Chapter 3 and 4 for the sake of convenience.

5.4.1.2 Implementing Response Surface Method to Develop the Metamodel

The second step in the metamodeling process is to choose a suitable surrogate model. There are different suitable techniques that can be implemented in car optimization under dynamic and impact loads such as the response surface method (RSM), Kriging, simulated annealing, and neural networks [32,33,65,195]. Among different surrogate models, the RSM using a full term quadratic regression analysis model has shown to be very effective for crashworthiness optimization problems [33]. Therefore in this study, the full term quadratic RSM model is used where the response function \hat{y} for 4 design variables are represented as:

$$\begin{aligned} \hat{y} = & a_0 + a_1x_1 + a_2x_2 + a_3x_3 + a_4x_4 + a_{12}x_1x_2 + a_{13}x_1x_3 + a_{14}x_1x_4 \\ & + a_{23}x_2x_3 + a_{24}x_2x_4 + a_{34}x_3x_4 + a_{11}x_1^2 + a_{22}x_2^2 + a_{33}x_3^2 + a_{44}x_4^2 \end{aligned} \quad (5.5)$$

where x_1 to x_4 are the design variables and a_{ij} is the coefficients of the response function obtained from the metamodeling process. This quadratic model represents a hyper plane in the design space with a curvature due to the second degree interacting terms, and it is the default model of RSM application. It should be mentioned that the metamodel surrogate method using a quadratic RSM model can be run through an automated method using LS-OPT or manually by conducting the FE model at each design point of the D-optimal criterion provided in Table 5.6 using LS-DYNA. The output responses are then collected and used in regression analysis through which the unknown regression

parameters ϕ of the RSM models are determined from the model output response according to Eqn. (5.5).

5.4.2 Optimization of the Surrogate Model

Now, the optimization problem can be conducted using the response function obtained from metamodel implementation and there is no longer need to conduct optimization directly on nonlinear FE simulations. This makes the optimization problem manageable by any available optimization algorithms.

5.4.2.1 Single-objective optimization

There are two single objective function optimizations conducted under this investigation: the conceptual HIC, measured at the firewall accelerometer location, and the peak vehicle *Def*, which is the measured distance between the tip of the inner bumper and rear left seat. The surrogate model is optimized using an SQP algorithm as a single objective function by writing a program in MATLAB. Different initial design points have been used in an attempt to catch the global optima.. The iteration history for peak vehicle deformation '*Def*' and HIC are shown in Figures 5.19 and 5.20 respectively. The optimal results are also tabulated in Table 5.7.

As it can be realized from Table 5.7, the optimal results based on minimization of the HIC is very close to the starting points, which is the optimal set of design variables obtained for the simplified LMS model. Moreover, the optimal results based on minimization of the peak vehicle deformation (Def) is also close to those obtained based on the LMS model except the extendable Voigt element (μ_2) has increased from 3.345 to 4.12.

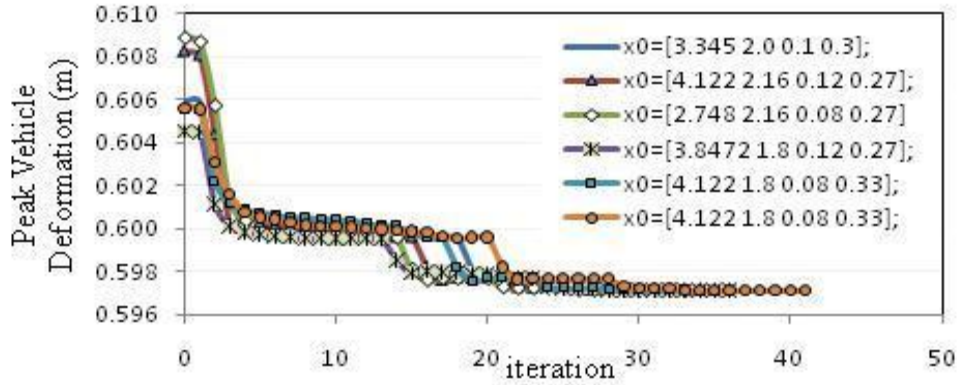


Figure 5.19: Convergence of single objective function: occupant HIC using SQP optimization algorithm

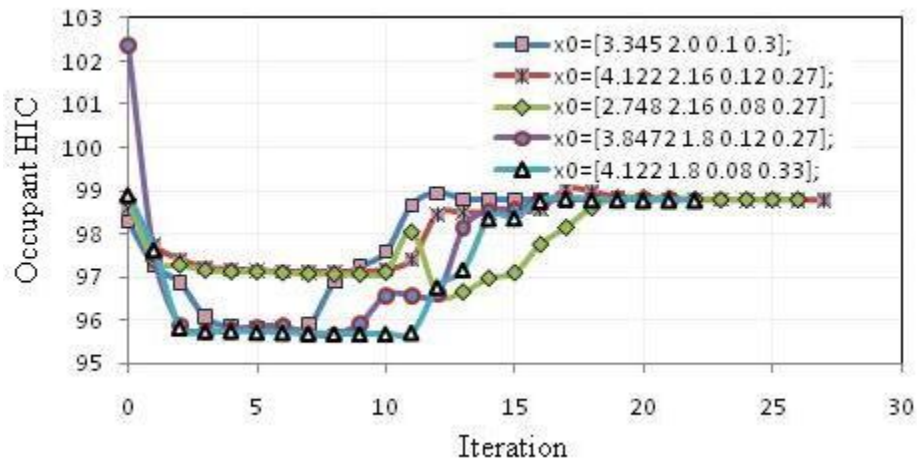


Figure 5.20: Convergence of single objective function: peak vehicle deformation (*Def*) using SQP optimization algorithm

Table 5.7: Comparison of the optimal HIC and Def values between the optimal and initial design variables

Objective function	value	μ_2	μ_1	λ_2	λ_1
HIC	Starting 97.75	3.345	2.0	0.1	0.3
	Optimal 98.78	3.52	1.9	0.12	0.3
Deform	Starting 60.66 (cm)	3.345	2.0	0.1	0.3
	Optimal 59.71 (cm)	4.12	1.92	0.12	0.27

5.4.2.2 Multi-Objective Optimization

The conceptual HIC and peak vehicle deformation (*Def*) are considered to be the two main objective functions for conducting multiobjective function (MOO). Additionally, different system performance are used as constraint functions or to measure system behavior such as toe intrusion, peak longitudinal deceleration at the rear seat locations, and maximizing the *SpAbsEng* of the proposed crash energy management (CEM) system. This is conducted using MOGA technique by writing a program in MATLAB based on the response quadratic function obtained from the metamodel technique, The Pareto front curve obtained from the MOGA technique is shown in Figure 5.21. In this figure, the system design performance using the optimal set of design variables obtained in section 5.3 is also shown for comparison with the system performance of different optimal points located on the PF curve. It should be mentioned that the design space assigned for the design variables used in conducting MOGA is the same as that used in section 4.5.1 with the upper and lower bounds as: $\lambda_2=[0.08:0.12]$, $\mu_2=[2.748:4.122]$, $\lambda_1=[0.27:0.33]$, $\mu_1=[1.8:2.2]$.

It should be mentioned that all the points located on the PF curve are optimal. However, the lower anchor points (AP) is the most desirable optimal point to be selected since it achieves minimum vehicle deformation (*Def*), which is considered to be one of the main goals for enhancing vehicle crashworthiness. Additionally, the HIC value recorded at this point is much lower than the HIC threshold value (350), which is according to the Abbreviated Injury Scale (AIS) represent the 3rd grade of injury level. The variation of DV values at the lower anchor points of the PF curve at each iteration point is shown in Figure 5.22, and the comparison between the initial DV values and optimal set is tabulated in Table 5.7.

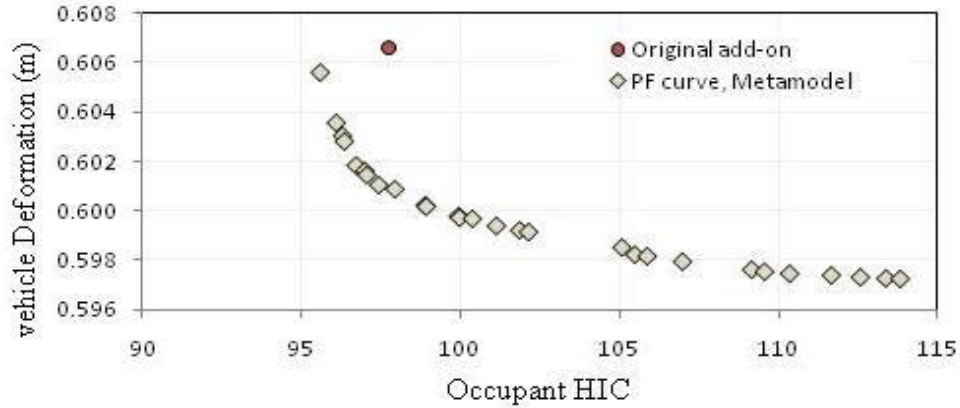


Figure 5.21: Comparison of system performance between MOO results of the surrogate FE and the initial design variables of the add-on configurations of the modified FE model at 56.6 km/h impact speed

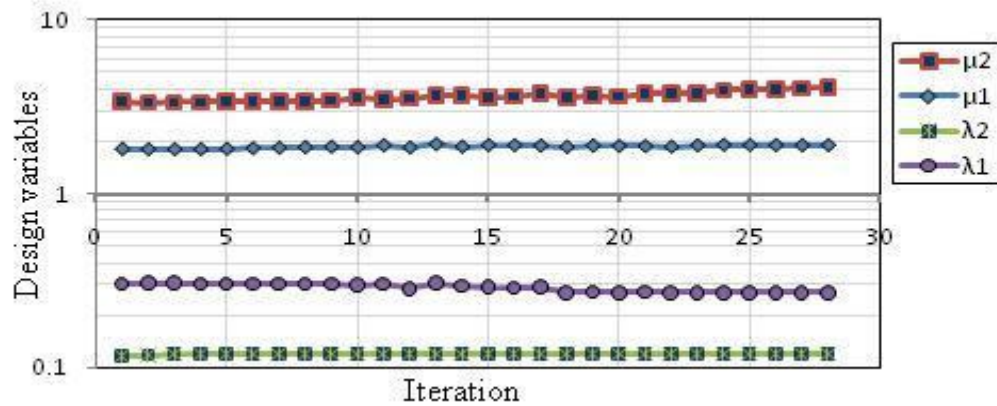


Figure 5.22: Variations of design variables of the lower anchor point of the PF curve with iteration number at 56 km/h impact speed in logarithmic scale of the y-axis.

As it can be realized, the optimal DVs based on LMS model agree well with those obtained the upper AP of the PF curve. Also the examination of the results reveals that the variation in the system performance as well as the corresponding values of the optimal DV sets are insignificant, as shown in Table 5.8. This implies that the variations of the objective functions at the APs are small and the value of the design parameters obtained at the optimal set of design variables are very close. This fortifies the hypothesis that the optimal design set obtained in section 3.4.1 is generally applicable to all passenger car sizes after proper scaling.

Table 5.8: Comparison between design criteria at the optimal sets obtained from LMS MOGA optimization and Metamodel MOGA optimization through LS-OPT at lower AP of Pareto Frontier curves

Description	HIC	Deformation (cm)	μ_2	μ_1	λ_2	λ_1
Optimal obtained from LMS Model	97.75	60.66	3.345	2.0	0.1	0.3
Optimal obtained from Metamodel/MOGA at UPR AP	95.76	60.55	3.326	1.812	0.11	0.305
Optimal obtained from Metamodel/MOGA at LWR AP	110.75	59.79	3.949	1.916	0.12	0.27

The computational time for conducting the metamodel technique using 30 design points for DoE is 38.45 hours using LS-OPT on the Concordia University server, which uses 48 processors. Another 0.5 hours is necessary to conduct multiobjective optimization using multiobjective genetic algorithm (MOGA) via writing a program in the Matlab with the population size of 55 and number of generations of 110. If the MOGA optimization is conducted directly on a FE model using LS-OPT with the default configurations (population size = 30 and number of generations = 100), it would take around 375 hours and require a 750 GB disk space using 64 processors. Even if these conditions are met, the results may not be valid and noisy nature of the response performances.

5.5 Summary

The FE model of Geo-Metro vehicle was modified and validated with the NCAP crash test results to be used in building the proposed CEM system and verify its applicability on different passenger car models. The proposed add-on EA system that represents the main pillar of the modified CEM system is scaled-down to cope with the

vehicle model's mass. Additionally, the proposed add-on EA system is implemented in the FE model, and the comparisons of different system performance between the modified and the baseline FE models showed great crashworthiness enhancement. It has been shown that using the proposed add-on system enhanced peak occupant deceleration at the rear seat, peak normal rigid wall force and peak vehicle deformation by 42.7%, 53.1% and 6.1%, respectively. Additionally, the absorbed energy by structural members has also reduced by 9%.

Furthermore, in order to verify the applicability of the optimal set of DVs using obtained previously for the LMS model on the detailed small-scale FE model, optimization process was conducted. This was achieved by investigating the variations of the design variables over a range of design space using the metamodeling technique. A surrogate model was obtained to practically conduct optimization without requiring the full FE vehicle model. Single and multi-objective optimization techniques were performed. It has been shown that the optimum results and associated system performance agree well with those at the initial designs.

CHAPTER 6

CONCLUSIONS, CONTRIBUTIONS, AND FUTURE RECOMMENDATIONS

6.1. Highlight and Conclusions of Dissertation Research

In this dissertation research, a systematic investigation using the lumped-parameter model was conducted to evaluate performance potential of alternate concepts in crash energy management (CEM) system. Through simulation results of vehicle models of varying complexities, it is illustrated that the proposed crash energy management (CEM) system comprising integrated and/or extendable add-on energy absorber can yield enhanced crashworthiness of vehicles in the frontal crash impact. Different performance measures were assigned to measure the degree of enhancements that could be achieved by the proposed concepts compared with the baseline vehicle model. These included the occupant HIC, peak vehicle deformation, specific absorbed energy and total deviation of the vehicle deceleration pulse from the target optimal crash pulse. The results attained for the vehicle models comprising the proposed add-on absorbers showed the superior effectiveness of the add-on elements over a wide range of impact speeds (35-80 km/h). It has been proven that the amount of energy absorbed by a vehicle's structure due to impact could be greatly reduced by the add-on elements over the specified range of impact speed. Furthermore, the proposed CEM system was implemented into a validated high fidelity full-scale FE model of a passenger car, while the optimal design parameters were identified using a simplified lumped-mass model of the vehicle. The identified optimal parameters, however, were observed to be valid, when the add-on elements were implemented to a detailed elasto-plastic lumped parameters

model and a comprehensive finite element model. The conclusions highlights of the dissertation research are summarized below:

- (a) Systematic parametric study was performed to identify the suitable damping force characteristics due to extended and integrated add-on absorbers to achieve lower HIC and deformation in both the arrangements.
- (b) Two new adaptive crash energy concepts were proposed and their effectiveness in enhancing vehicle crashworthiness evaluated through variable energy absorption properties was investigated over a range of impact speeds. The results obtained from a simplified lumped-parameter (LMS) vehicle-occupant model indicated that the extendable and integrated damped absorbers (EIDV model) configuration could yield superior performance, followed by the integrated absorber configuration (IV model).
- (c) Different optimization techniques were evaluated for identification of optimal design parameters over a range of impact speeds. The extendable add-on CEM system provided most significant enhancement of crashworthiness over the 35-80 km/h impact speed range. For instance, the dynamic crush distance and peak occupant deceleration were reduced by 54.1% and reduce 65.6% respectively at a 48 km/h impact speed, when compared to those of the baseline model.
- (d) Investigation of the applicability of the optimal add-on absorbers (EIDV and IV models), identified from the simplified vehicle model, to the detailed elasto-plastic lumped-parameter (LMS) model of vehicle revealed reasonably good validity of the optimal solutions. The proposed EIDV system resulted in significant enhancement of the crashworthiness of the elasto-plastic model for the specified

range of impact speeds, as observed for the simplified model. The vehicle dynamic crush, peak occupant deceleration, occupant HIC and the specific absorbed energy of the elasto-plastic model with EIDV absorbers were 68.3%, 15.5%, 35.1% and 90.4%, respectively, lower than those of the model without the absorbers.

- (e) The effectiveness of the proposed extendable CEM system was further evaluated using a high fidelity finite element model of an economy-size passenger car using the optimal set of design parameters, identified from the simplified model. At an 56 km/h impact speed, the FE model with the absorbers resulted in 42.68 % and 6% reductions in peak deceleration at the rear seat location and total crush distance, respectively, while the absorbed energy of vehicle structure was reduced by approximately 9%.
- (f) The metamodeling optimization technique was applied to the modified FE model using the LS-OPT software to obtain a simplified yet accurate surrogate model to facilitate optimization. Different optimization algorithms were implemented using the resulting surrogate model to identify optimal configurations of the add-on elements. The assigned design performance measures obtained from the Pareto Frontier curve were observed to be quite close to those obtained with the optimal design obtained from the simplified LMS model.
- (g) It can be concluded that the proposed CEM concepts with the optimal designs of the add-on absorbers would yield considerable improvements in all of the performance measures over the specified range of impact speeds and a barrier impact. Furthermore, the optimal solutions obtained from the simplified model were judged to be valid for the complex vehicle models.

6.2. Contributions

A new CEM concept was proposed to enhance crashworthiness and reduce occupant injury severity over a range of 35-80 km/h impact speeds. The effectiveness of the proposed extendable CEM system was demonstrated for the vehicle models of varying complexities including the simplified lumped-parameter, a detailed elasto-plastic lumped parameter and a comprehensive finite-element model. The add-on absorbers were designed to yield variable stiffness/damping properties with only a little effect on the original structural stiffness, which would result in improved the survivability envelope and reduced likelihood of a severe injury. Optimal parameters of the proposed CEM system were identified through formulations and solutions of a composite minimization function of various important measures of crashworthiness and occupant protection.

The optimal solutions, attained using the simplified vehicle-occupant model, were further evaluated in conjunction with the elasto-plastic and FE models of the vehicle. It was shown that optimal solutions derived on the basis of multiples performance measures would be equally valid for the three vehicle models considered in the study. This will definitely reduce the possibility of severe injury of the occupant. Apart from the above, the other key contributions of this dissertation research are summarized below:

- (a) Proposed different configurations of crash energy management (CEM) comprising add-on energy absorbers.
- (b) Assessment of the selected configurations of the CEM system using simplified, elasto-plastic and FE models of the vehicle;
- (c) Identifications of the optimal number of performance measures of the add-on absorbers through parametric sensitivity analyses.

- (d) Identification optimal design parameters through minimization of multiple objective function of different measures over a wide range of impact speeds, 35 to 80 km/h.
- (e) A scaling technique for adapting vehicle masses to the current designs of lower was further implemented.
- (f) Implementations of the proposed add-on CEM systems to more elaborate vehicle models, such as a validated FE model for their assessments. The proposed models were tested over a range of impact speeds varying from 35 to 80 km/h and verified their capabilities to enhance crashworthiness in frontal impact with a rigid barrier.
- (g) Applications of optimization techniques to the surrogate model obtained from metamodeling technique over the FE model using LS-OPT software.

6.3. Recommendations for Future Works

This dissertation research has introduced a new concept in CEM system that can enhance crashworthiness considerably by reducing the peak occupant HIC, vehicle deformation and amount of specific energy absorption of the vehicle structure. Fundamental investigations have been conducted to demonstrate the performance of the CEM concept using vehicle models of varying complexities. While the proposed concept has shown promising potentials to enhance crashworthiness of vehicles, far more studies would be essential for realizing an implementable design of the add-on elements. The major limitations of the proposed CEM concept are briefly discussed, which form the essential basis recommendations for more adaptive CEM system are addressed to ensure applicability for the future desirable studies.

This dissertation research concerned only with a full frontal rigid barrier impact, while the vehicle responses and effectiveness of the proposed CEM concept are not

evaluated under oblique and offset impacts. Furthermore, the performance potentials under different impact scenarios such as deformable (fixed or moving) barriers, impacts between two mating vehicles with different mass ratios need to be investigated. The study also lacks characterization of the properties of the restraint system and considerations of the nonlinear damping properties in the model. The effects of nonlinear damping properties such as quadratic and cubic term on the performance measures have not been thoroughly evaluated, nor are the design methods to achieve desired damping. In light of the above state recommendations, it is suggested that further studies be designed to address the following:

- The study should be extended to investigate vehicle-to-vehicle (VTV) impact with different mass ratios up to 1.6 to cover most probable severe impacts.
- The study should also be extended to investigate oblique and offset impacts with both rigid and deformable barriers.
- The triggering mechanisms required for initiation and deployment of the extended portion of the bumper need further investigations, which may employ short-range radar sensors for timely activation prior to a crash event.
- Implementation of suitable crush elements, such as honeycomb, to shield the proposed absorbers from higher shock loads should be considered.
- An extended study is needed to add different crash energy management concepts, such as the splitting the crash energy between the less affected structural members.

APPENDIX-A

Table A.1: Identification of design variables of the EIDV model with configuration # 2 corresponding to minimal deformation, HIC, total deviation error at different impact speeds

speed (km/h)	35	40	45	50	55	60	65	70	75	80
Minimal vehicle deformation										
	0.202	0.297	0.385	0.465	0.535	0.597	0.651	0.698	0.736	0.773
λ_1	0.3	0.3	0.3	0.3	0.3	0.3	0.3	0.3	0.3	0.3
μ_1	5.0	5.0	5.0	5.0	5.0	5.0	5.0	5.0	5.0	5.0
λ_2	0.3	0.3	0.3	0.3	0.3	0.3	0.3	0.3	0.3	0.3
μ_2	1.5	1.5	1.5	1.5	1.5	1.5	1.5	1.5	1.5	1.5
Occupant HIC	57.94	73.00	89.95	109.11	130.87	155.66	184.02	216.51	253.80	296.59
Specific energy absorbed	75.79%	72.24%	67.69%	63.66%	60.33%	57.55%	55.22%	53.26%	51.59%	50.15%
Total deviation error, Δ_{Err}	26.4	26.0	26.9	37.8	36.6	48.2	46.6	49.9	48.0	45.9
Minimal occupant HIC										
	27.8	27.6	27.5	41.4	40.3	51.7	49.4	59.0	108.4	117.6
λ_1	0.1	0.1	0.1	0.1	0.1	0.1	0.1	0.1	0.1	0.1
μ_1	5.0	5.0	5.0	5.0	5.0	5.0	5.0	5.0	5.0	5.0
λ_2	0.1	0.1	0.1	0.1	0.1	0.1	0.1	0.2	0.1	0.3
μ_2	0.4	0.6	0.8	1.1	1.4	1.5	1.5	1.5	1.5	1.5
Peak vehicle deformation	0.640	0.629	0.627	0.608	0.599	0.634	0.683	0.721	0.767	0.796
Specific energy absorbed	25.13%	30.00%	33.14%	37.65%	40.14%	38.09%	34.63%	32.50%	28.91%	28.22%
Total deviation error, Δ_{Err}	40.9	36.4	31.5	43.9	40.9	51.8	49.4	56.2	61.4	67.6
Minimal total deviation error										
	27.8	27.6	27.5	41.4	40.2	51.4	49.0	56.1	61.4	67.3
λ_1	0.1	0.1	0.1	0.3	0.3	0.3	0.3	0.3	0.3	0.3
μ_1	5.0	5.0	5.0	5.0	5.0	5.0	5.0	5.0	5.0	5.0
λ_2	0.2	0.3	0.3	0.3	0.3	0.3	0.3	0.3	0.1	0.1
μ_2	1.5	1.5	1.3	1.5	1.5	1.5	1.5	1.5	1.5	1.5
Peak vehicle deformation	0.177	0.219	0.333	0.341	0.397	0.449	0.496	0.539	0.609	0.642
Occupant HIC	23.8	35.6	42.2	65.2	84.4	107.3	134.4	166.2	189.7	231.2

Table A.2: Identification of design variables of the EVIS model corresponding to minimal deformation, HIC, total deviation error at different impact speeds

speed (km/h)	35	40	45	50	55	60	65	70	75	80
Minimal vehicle deformation										
	0.311	0.345	0.376	0.405	0.432	0.459	0.487	0.526	0.565	0.602
λ_2	0.1	0.1	0.1	0.1	0.1	0.1	0.1	0.1	0.1	0.1
μ_2	1.6	1.8	2.0	2.2	2.4	2.7	2.9	3.2	3.4	3.5
μ_1	1.1	1.1	1.2	1.2	1.2	1.2	1.2	1.2	1.2	1.2
Occupant HIC	4.90	7.81	11.66	17.60	24.94	35.11	48.75	62.36	79.19	100.60
Specific energy absorbed	94.88%	94.48%	93.67%	93.55%	92.97%	92.75%	93.08%	91.31%	89.59%	87.97%
Total deviation error, Δ_{Err}	29.5	28.5	27.8	40.6	39.2	50.1	48.0	58.8	58.4	61.9
Minimal occupant HIC										
	3.80	6.19	9.48	14.20	20.61	29.86	41.12	55.98	75.45	100.28
λ_2	0.1	0.1	0.1	0.1	0.1	0.1	0.3	0.3	0.3	0.3
μ_2	2.1	2.4	2.6	2.9	3.1	3.4	3.5	3.5	3.5	3.5
μ_1	1.2	1.2	1.2	1.2	1.2	1.2	1.2	1.2	1.2	1.2
Peak vehicle deformation	0.347	0.381	0.410	0.447	0.481	0.506	0.535	0.556	0.581	0.611
Specific energy absorbed	90.63%	89.91%	89.83%	89.01%	88.22%	88.25%	87.63%	87.77%	87.33%	86.38%
Total deviation error, Δ_{Err}	31.9	31.4	30.3	43.1	41.3	52.1	49.8	59.9	59.2	62.1
Minimal total deviation error										
	27.1	26.1	25.1	38.0	37.1	49.3	48.0	58.8	58.4	61.9
λ_2	0.1	0.1	0.2	0.3	0.3	0.3	0.3	0.3	0.3	0.3
μ_2	3.5	3.5	3.5	3.5	3.5	3.5	3.5	3.5	3.5	3.5
μ_1	1.2	1.2	1.2	1.2	1.2	1.2	1.2	1.2	1.2	1.2
Peak vehicle deformation	0.333	0.363	0.393	0.421	0.445	0.467	0.487	0.526	0.565	0.602
Occupant HIC	6.81	9.98	14.78	21.13	28.94	38.00	48.75	62.36	79.19	100.60

Table A.3: Identification of design variables of the IV model corresponding to minimal deformation, HIC, total deviation error at different impact speeds

speed (km/h)	35	40	45	50	55	60	65	70	75	80
Minimal vehicle deformation										
μ_1	0.140	0.156	0.172	0.186	0.200	0.213	0.224	0.235	0.245	0.255
λ_1	5.0	5.0	5.0	5.0	5.0	5.0	5.0	5.0	5.0	5.0
	0.8	0.8	0.8	0.8	0.8	0.8	0.8	0.8	0.8	0.8
Occupant HIC	145.91	206.09	279.74	368.04	472.24	593.49	733.16	892.22	1072.20	1274.48
Specific energy absorbed	0.48%	0.47%	0.46%	0.46%	0.45%	0.44%	0.43%	0.42%	0.41%	0.40%
Total deviation error, Δ_{Err}	57.0	65.5	74.3	67.0	76.5	76.5	86.7	93.7	105.0	116.8
Minimal occupant HIC										
	103.47	136.92	176.00	221.18	272.85	334.46	413.36	511.83	623.91	750.17
μ_1	1.6	1.8	1.9	2	2.1	1.9	1.7	1.7	1.7	1.8
λ_1	0.1	0.1	0.1	0.1	0.1	0.1	0.1	0.1	0.1	0.1
Peak vehicle deformation	0.324	0.337	0.355	0.371	0.385	0.427	0.471	0.490	0.508	0.512
Specific energy absorbed	5.04%	4.01%	3.73%	3.43%	3.12%	4.32%	5.91%	5.97%	5.99%	5.19%
Total deviation error, Δ_{Err}	26.0	33.0	39.6	30.7	37.4	35.5	35.8	38.8	43.5	52.6
Minimal total deviation error										
	22.0	20.6	19.3	27.9	27.2	35.1	35.3	38.2	41.3	46.7
μ_1	1.3	1.0	0.8	1.6	1.4	1.7	1.6	1.6	1.5	14.0
λ_1	0.3	0.1	0.1	0.1	0.1	0.1	0.1	0.1	0.1	0.1
Peak vehicle deformation										
Occupant HIC										

APPENDIX-B

Table B.1: Pareto Frontier (PF) results at four selected impact speeds over the specified range of impact speeds using multiobjective optimization using GA for the EIDV model (extended-integrated voigt elements) using only two design variables (μ_2, μ_1)

35 km/h				50 km/h				65 km/h				80 km/h			
μ_2	μ_1	HIC	Def	μ_2	μ_1	HIC	Def	μ_2	μ_1	HIC	Def	μ_2	μ_1	HIC	Def
1.491	1.196	4.47	0.3015	1.849	1.704	15.56	0.3980	2.389	1.789	40.22	0.4910	2.796	2.000	85.92	0.5614
1.491	1.196	4.47	0.3015	1.849	1.704	15.56	0.3980	2.389	1.789	40.22	0.4910	3.121	1.998	89.90	0.5405
1.471	1.345	4.67	0.2952	1.778	1.895	15.76	0.3903	2.540	2.000	42.97	0.4657	3.393	1.935	92.14	0.5284
1.596	1.257	4.87	0.2917	1.895	2.000	16.74	0.3745	2.753	1.908	44.41	0.4576	3.529	1.972	94.25	0.5177
1.623	1.400	5.15	0.2831	1.994	2.000	17.51	0.3674	2.837	1.842	45.14	0.4566	3.617	2.000	95.61	0.5105
1.466	1.771	5.19	0.2743	2.114	2.000	18.42	0.3590	2.934	2.000	46.89	0.4394	3.937	1.980	100.42	0.4935
1.429	2.000	5.38	0.2653	2.498	1.919	20.55	0.3389	3.291	2.000	50.80	0.4168	3.968	2.000	100.89	0.4904
1.563	2.000	5.81	0.2584	2.542	2.000	21.09	0.3329	3.438	2.000	52.30	0.4078	4.126	2.000	103.21	0.4815
1.721	2.000	6.28	0.2499	2.643	1.982	21.68	0.3297	3.821	1.821	54.54	0.4021	4.299	2.000	105.68	0.4719
1.883	2.000	6.83	0.2407	2.901	1.900	22.63	0.3242	3.929	2.000	56.07	0.3900	4.527	1.969	108.82	0.4617
2.135	1.899	7.26	0.2303	2.871	2.000	22.78	0.3202	3.929	2.000	56.07	0.3900	4.693	2.000	110.90	0.4543
2.161	1.999	7.60	0.2250	3.072	2.000	23.92	0.3143								
2.161	1.999	7.60	0.2250	3.072	2.000	23.92	0.3143								

Table B.2: Anti-Pareto Frontier (APF) results at four selected impact speeds over the specified range of impact speeds using MOGA for the EIDV model (extended-integrated voigt elements) using only two design variables (μ_2, μ_1)

APF 35 km/h				APF 50 km/h				APF 65 km/h				APF 80 km/h			
μ_2	μ_1	HIC	Def	μ_2	μ_1	HIC	Def	μ_2	μ_1	HIC	Def	μ_2	μ_1	HIC	Def
0.100	0.100	62.97	0.5046	0.100	1.975	42.28	0.7185	0.100	2.000	81.87	0.9829	0.101	1.950	172.70	1.1665
0.101	0.100	63.04	0.5045	0.100	1.975	42.28	0.7185	0.100	2.000	81.87	0.9829	0.101	1.950	172.70	1.1665
0.101	0.100	63.09	0.5044	0.104	0.453	74.32	0.6917	0.100	0.811	140.34	0.9091	0.159	1.422	241.223	1.0299
0.102	0.100	63.10	0.5043	0.106	0.392	82.70	0.6877	0.106	0.616	169.02	0.8820	0.120	0.788	343.88	1.0182
0.102	0.100	63.13	0.5043	0.103	0.228	121.92	0.6818	0.124	0.496	206.17	0.8527	0.124	0.582	421.55	0.9846
0.102	0.100	63.17	0.5042	0.100	0.186	139.00	0.6804	0.117	0.376	247.39	0.8427	0.132	0.372	564.35	0.9420
0.102	0.100	63.19	0.5042	0.100	0.158	155.33	0.6778	0.100	0.225	337.24	0.8298	0.157	0.280	682.32	0.9102
0.103	0.100	63.23	0.5041	0.100	0.127	175.90	0.6741	0.126	0.207	373.14	0.8111	0.121	0.170	858.49	0.9064
0.103	0.100	63.27	0.5041	0.100	0.116	185.43	0.6726	0.106	0.152	433.23	0.8105	0.191	0.171	955.42	0.8791
0.103	0.100	63.30	0.5040	0.100	0.100	201.50	0.6701	0.100	0.126	469.46	0.8069	0.161	0.106	1152.97	0.8757
0.104	0.100	63.31	0.5040	0.181	0.101	212.48	0.6505	0.103	0.100	532.46	0.7984	0.278	0.100	1214.74	0.8538
								0.196	0.100	552.62	0.7734				
								0.196	0.100	552.62	0.7734				

Table B.3: Pareto Frontier (PF) results at four selected impact speeds over the specified range of impact speeds using multiobjective optimization using GA for the EIDV model (extended-integrated voigt elements) using the four design variables (λ_2 , λ_1 , μ_2 , μ_1)

PF, 35 km/h						PF, 50 km/h						PF, 65 km/h						PF, 80 km/h					
λ_2	μ_2	μ_1	λ_1	HIC	Def	λ_2	μ_2	μ_1	λ_1	HIC	Def	λ_2	μ_2	μ_1	λ_1	HIC	Def	λ_2	μ_2	μ_1	λ_1	HIC	Def
0.201	1.384	1.298	0.105	4.19	0.3280	0.132	1.875	1.597	0.105	14.40	0.4247	0.105	2.285	1.887	0.102	36.77	0.5131	0.106	2.857	1.921	0.103	80.50	0.5832
0.201	1.384	1.298	0.105	4.19	0.3280	0.132	1.875	1.597	0.105	14.40	0.4247	0.105	2.285	1.887	0.102	36.77	0.5131	0.118	2.900	1.978	0.117	82.06	0.5739
0.199	1.381	1.314	0.132	4.25	0.3232	0.130	1.870	1.685	0.111	14.69	0.4177	0.129	2.332	1.887	0.110	37.66	0.5070	0.100	3.016	2.000	0.100	82.79	0.5679
0.197	1.381	1.351	0.149	4.35	0.3185	0.130	1.869	1.704	0.122	14.82	0.4149	0.100	2.255	2.000	0.147	37.67	0.5024	0.100	3.084	2.000	0.100	83.66	0.5636
0.100	1.316	1.898	0.101	4.50	0.3012	0.100	1.735	2.000	0.175	15.02	0.3996	0.100	2.277	2.000	0.174	38.27	0.4979	0.112	3.203	1.934	0.115	85.56	0.5590
0.145	1.405	1.507	0.227	4.66	0.2993	0.131	1.855	1.875	0.175	15.60	0.3968	0.100	2.273	2.000	0.217	38.84	0.4935	0.100	3.284	2.000	0.100	86.35	0.5514
0.100	1.355	1.758	0.240	4.73	0.2885	0.100	1.753	2.000	0.259	15.61	0.3894	0.132	2.445	1.925	0.155	39.82	0.4909	0.121	3.273	1.911	0.163	88.06	0.5507
0.100	1.309	2.000	0.198	4.81	0.2833	0.131	1.854	1.943	0.264	16.32	0.3822	0.135	2.473	1.942	0.174	40.54	0.4854	0.121	3.398	1.961	0.149	88.25	0.5411
0.100	1.366	2.000	0.300	5.14	0.2684	0.210	1.725	1.999	0.299	16.63	0.3759	0.155	2.484	1.949	0.195	41.28	0.4803	0.123	3.487	1.969	0.121	88.79	0.5381
0.100	1.409	2.000	0.300	5.31	0.2663	0.144	2.000	1.942	0.252	17.47	0.3719	0.206	2.443	1.987	0.194	41.71	0.4764	0.100	3.648	2.000	0.100	90.19	0.5299
0.100	1.545	2.000	0.300	5.74	0.2594	0.130	2.077	1.875	0.289	17.96	0.3682	0.112	2.740	1.938	0.189	42.85	0.4677	0.100	3.816	2.000	0.100	92.61	0.5202
0.100	1.626	2.000	0.300	6.04	0.2551	0.200	1.990	2.000	0.300	18.36	0.3586	0.131	2.882	1.864	0.230	45.02	0.4578	0.128	3.746	1.998	0.164	94.00	0.5160
0.100	1.702	2.000	0.300	6.22	0.2509	0.173	2.114	2.000	0.300	19.04	0.3528	0.131	2.869	1.889	0.267	45.59	0.4527	0.100	4.052	2.000	0.100	95.94	0.5069
0.100	1.779	2.000	0.300	6.49	0.2466	0.143	2.194	2.000	0.300	19.37	0.3500	0.100	2.884	2.000	0.300	46.31	0.4427	0.128	3.830	1.992	0.262	98.18	0.5013
0.100	1.838	2.000	0.300	6.68	0.2433	0.120	2.281	2.000	0.300	19.50	0.3461	0.100	3.075	2.000	0.300	48.48	0.4304	0.100	4.413	2.000	0.100	100.70	0.4869
0.100	1.907	2.000	0.300	6.81	0.2394	0.100	2.372	2.000	0.300	19.96	0.3418	0.100	3.087	2.000	0.300	48.60	0.4297	0.100	4.522	2.000	0.100	102.05	0.4810
0.188	1.858	1.988	0.296	7.07	0.2390	0.100	2.415	2.000	0.300	20.26	0.3391	0.100	3.304	2.000	0.300	50.93	0.4161	0.128	4.500	1.968	0.167	104.49	0.4758
0.100	1.990	2.000	0.300	7.08	0.2346	0.100	2.643	2.000	0.300	21.74	0.3289	0.100	3.670	2.000	0.141	51.57	0.4116	0.100	4.633	2.000	0.145	104.91	0.4701
0.100	2.050	2.000	0.300	7.26	0.2311	0.127	2.806	1.972	0.288	22.40	0.3251	0.100	3.672	2.000	0.173	52.19	0.4077	0.100	4.629	2.000	0.204	106.84	0.4640
0.157	2.081	1.994	0.300	7.56	0.2273	0.127	3.044	2.000	0.298	23.93	0.3152	0.217	3.768	1.995	0.293	55.81	0.3938	0.100	4.624	2.000	0.265	108.83	0.4579
0.157	2.081	1.994	0.300	7.56	0.2273	0.127	3.044	2.000	0.298	23.93	0.3152	0.217	3.768	1.995	0.293	55.81	0.3938	0.100	4.622	2.000	0.298	109.92	0.4547

Table B.4: Anti-Pareto Frontier (APF) results at four selected impact speeds over the specified range of impact speeds using MOGA for the EIDV model (extended-integrated voigt elements) using the four design variables ($\lambda_2, \lambda_1, \mu_2, \mu_1$)

APF, 35 km/h						APF, 50 km/h						APF, 65 km/h						APF, 80 km/h					
HIC	Def	λ_2	μ_2	μ_1	λ_1	HIC	Def	λ_2	μ_2	μ_1	λ_1	HIC	Def	λ_2	μ_2	μ_1	λ_1	HIC	Def	2	λ_2	μ_2	μ_1
<i>65.43</i>	<i>0.5375</i>	0.100	0.100	0.100	0.100	<i>43.92</i>	<i>0.7205</i>	0.104	0.101	1.061	0.106	<i>81.70</i>	<i>0.9861</i>	0.107	0.102	1.984	0.133	<i>170.18</i>	<i>1.1715</i>	0.111	0.102	1.973	0.104
<i>65.44</i>	<i>0.5375</i>	0.100	0.100	0.100	0.100	<i>43.92</i>	<i>0.7205</i>	0.104	0.101	1.061	0.106	<i>81.70</i>	<i>0.9861</i>	0.107	0.102	1.984	0.133	<i>170.18</i>	<i>1.1715</i>	0.111	0.102	1.973	0.104
<i>65.47</i>	<i>0.5375</i>	0.100	0.100	0.100	0.100	<i>49.98</i>	<i>0.7205</i>	0.100	0.100	0.825	0.100	<i>91.18</i>	<i>0.9752</i>	0.100	0.100	1.601	0.100	<i>204.56</i>	<i>1.1419</i>	0.100	0.100	1.505	0.100
<i>65.49</i>	<i>0.5375</i>	0.100	0.101	0.100	0.100	<i>49.98</i>	<i>0.7205</i>	0.100	0.100	0.825	0.100	<i>114.97</i>	<i>0.9465</i>	0.100	0.100	1.117	0.100	<i>230.53</i>	<i>1.1079</i>	0.113	0.105	1.303	0.120
<i>65.50</i>	<i>0.5375</i>	0.100	0.101	0.100	0.100	<i>58.48</i>	<i>0.7142</i>	0.106	0.102	0.634	0.104	<i>151.87</i>	<i>0.9163</i>	0.100	0.100	0.744	0.100	<i>294.30</i>	<i>1.0786</i>	0.100	0.100	0.917	0.100
<i>65.54</i>	<i>0.5374</i>	0.100	0.101	0.100	0.100	<i>111.24</i>	<i>0.7113</i>	0.100	0.100	0.266	0.100	<i>165.61</i>	<i>0.9083</i>	0.100	0.100	0.664	0.100	<i>396.08</i>	<i>1.0323</i>	0.100	0.100	0.603	0.100
<i>65.57</i>	<i>0.5374</i>	0.100	0.101	0.100	0.100	<i>116.11</i>	<i>0.7096</i>	0.104	0.101	0.251	0.103	<i>178.65</i>	<i>0.9003</i>	0.100	0.100	0.589	0.100	<i>419.12</i>	<i>1.0246</i>	0.100	0.100	0.558	0.100
<i>65.61</i>	<i>0.5373</i>	0.100	0.101	0.100	0.100	<i>122.84</i>	<i>0.7089</i>	0.105	0.101	0.234	0.103	<i>193.88</i>	<i>0.8929</i>	0.100	0.100	0.525	0.100	<i>502.41</i>	<i>1.0006</i>	0.100	0.100	0.431	0.100
<i>65.63</i>	<i>0.5373</i>	0.100	0.101	0.100	0.100	<i>140.03</i>	<i>0.7085</i>	0.100	0.100	0.195	0.100	<i>206.46</i>	<i>0.8780</i>	0.126	0.103	0.469	0.117	<i>509.53</i>	<i>0.9791</i>	0.119	0.119	0.443	0.108
<i>65.64</i>	<i>0.5373</i>	0.100	0.102	0.100	0.100	<i>142.52</i>	<i>0.7062</i>	0.106	0.102	0.190	0.103	<i>231.57</i>	<i>0.8659</i>	0.142	0.104	0.399	0.116	<i>590.06</i>	<i>0.9785</i>	0.100	0.100	0.329	0.100
<i>65.66</i>	<i>0.5373</i>	0.100	0.102	0.100	0.100	<i>158.74</i>	<i>0.7061</i>	0.100	0.100	0.164	0.100	<i>253.41</i>	<i>0.8615</i>	0.129	0.105	0.359	0.117	<i>608.04</i>	<i>0.9652</i>	0.122	0.105	0.313	0.127
<i>65.68</i>	<i>0.5373</i>	0.100	0.102	0.100	0.100	<i>160.06</i>	<i>0.7060</i>	0.100	0.100	0.162	0.100	<i>261.43</i>	<i>0.8612</i>	0.120	0.104	0.344	0.117	<i>657.76</i>	<i>0.9650</i>	0.100	0.100	0.274	0.100
<i>65.69</i>	<i>0.5373</i>	0.100	0.102	0.100	0.100	<i>167.12</i>	<i>0.7050</i>	0.100	0.100	0.152	0.100	<i>316.19</i>	<i>0.8549</i>	0.100	0.100	0.263	0.100	<i>739.88</i>	<i>0.9508</i>	0.100	0.100	0.220	0.100
<i>65.72</i>	<i>0.5372</i>	0.100	0.102	0.100	0.100	<i>173.36</i>	<i>0.7041</i>	0.100	0.100	0.144	0.100	<i>381.55</i>	<i>0.8435</i>	0.100	0.100	0.203	0.100	<i>826.28</i>	<i>0.9377</i>	0.100	0.100	0.174	0.100
<i>65.74</i>	<i>0.5372</i>	0.100	0.102	0.100	0.100	<i>179.58</i>	<i>0.7030</i>	0.100	0.100	0.133	0.100	<i>419.81</i>	<i>0.8373</i>	0.100	0.100	0.172	0.100	<i>877.33</i>	<i>0.9319</i>	0.100	0.100	0.155	0.100
<i>65.78</i>	<i>0.5372</i>	0.100	0.102	0.100	0.100	<i>189.14</i>	<i>0.7016</i>	0.100	0.100	0.122	0.100	<i>425.70</i>	<i>0.8325</i>	0.126	0.102	0.169	0.112	<i>899.92</i>	<i>0.9204</i>	0.123	0.112	0.156	0.143
<i>65.80</i>	<i>0.5371</i>	0.100	0.103	0.100	0.100	<i>201.09</i>	<i>0.6999</i>	0.100	0.100	0.110	0.100	<i>463.41</i>	<i>0.8318</i>	0.100	0.100	0.147	0.100	<i>1036.03</i>	<i>0.9198</i>	0.100	0.100	0.118	0.100
<i>65.82</i>	<i>0.5371</i>	0.100	0.103	0.100	0.100	<i>208.81</i>	<i>0.6989</i>	0.100	0.100	0.103	0.100	<i>490.11</i>	<i>0.8236</i>	0.133	0.105	0.136	0.117	<i>1118.23</i>	<i>0.9146</i>	0.100	0.100	0.102	0.100
<i>65.84</i>	<i>0.5371</i>	0.100	0.103	0.100	0.100	<i>220.24</i>	<i>0.6913</i>	0.100	0.123	0.100	0.100	<i>543.53</i>	<i>0.8235</i>	0.100	0.100	0.111	0.100	<i>1210.17</i>	<i>0.9002</i>	0.100	0.134	0.100	0.100
<i>65.87</i>	<i>0.5371</i>	0.100	0.103	0.100	0.100	<i>222.96</i>	<i>0.6729</i>	0.111	0.208	0.102	0.109	<i>573.95</i>	<i>0.8207</i>	0.100	0.100	0.100	0.100	<i>1246.36</i>	<i>0.8919</i>	0.100	0.164	0.100	0.100
<i>65.89</i>	<i>0.5370</i>	0.100	0.103	0.100	0.100	<i>222.96</i>	<i>0.6729</i>	0.111	0.208	0.102	0.109	<i>606.50</i>	<i>0.8033</i>	0.100	0.161	0.100	0.100	<i>1275.83</i>	<i>0.8754</i>	0.100	0.256	0.100	0.100

REFERENCES

- 1 J.L. Gerberding, H. Falk, and I. Arias, ‘CDC Injury Fact Book’, National Center for Injury Prevention and Control - Centers for Disease Control and Prevention, 2006, USA.
- 2 K.C. Chan, ‘Highway Safety Causes of Injury in Automobile Crashes’, United States General Accounting Office ‘GAO’ Report # GAO/PEMD-95-4, May 1995.
- 3 Paul Du Bois, C. C. Chou, B. B. Fileta, T. B. Khalil, A. I. King, H. F. Mahmood, H. J. Mertz, and J. Wismans, ‘Vehicle crashworthiness and occupant protection’, American Iron and Steel Institute (AISI) publications 2004, USA.
- 4 Y. Wei, H. Meng, H. Zhang, and X. Wang, ‘Vehicle Frontal Collision Warning System based on Improved Target Tracking and Threat Assessment’, Proceedings of the 2007 IEEE Intelligent Transportation Systems Conference, Sept. 30:Oct. 3, 2007, WA, Seattle- USA.
- 5 K. Wani, ‘Government Status Report of Japan’, presentation on the 20th International Technical Conference on the Enhanced Safety of Vehicles, June 18: 21, 2007, Lyon, France.
- 6 M. Shinohara, ‘Future Direction for Enhanced Safety’, report , Nissan Motor Co., Ltd, 20th International Technical Conference on the Enhanced Safety of Vehicles Conference (ESV) in Lyon, France, June 18-21, 2007.
- 7 R. Rajamani, *Vehicle Dynamics and Control*, Springer, 2006, ISBN: 0-387-26396-9, USA.
- 8 F. Scarpa, M. Hassan, and M. Ruzzene, ‘Modeling and testing of shape memory alloy chiral honeycomb structures’, Proceedings of SPIE, the International Society for Optical Engineering, Smart structures and materials. Conference, Vol. 6170, pp. 239-246, February 2006.

- 9 A. L. Browne, N. L. Johnson, and S. R. Webb, 'Smart impact management devices; experimental validation of impact triggered rapid expansion of aluminum honeycomb', Proceedings of SPIE, the International Society for Optical Engineering, Smart structures and materials Conference, , Vol. 6173, pp. 61730J.1-61730J.12, 2006.
- 10 R. Delivorias, 'Research on Smart Materials; Application of ER and MR fluid in an Automotive Crash Energy Absorber', Report# MT04.18, Internal traineeship under Supervision of Dr. W.J. Witteman, Eindhoven University of Technology - Department of Mechanical Engineering Vehicle Safety, Eindhoven March 16, 2004.
- 11 <http://www.eevc.org/publicdocs/publicdocs.htm>, 'EEVC WG 19 Primary Secondary Safety Interaction', European enhanced Vehicle Committee final report, 2006.
- 12 B. Pipkorn, H. Mellander, Y. Håland 'Car driver protection at frontal impacts up to 80 km/h (50 mph)', 19th International Technical Conference on the Enhanced Safety of Vehicles (NHTSA), report # 05-0102, 2005
- 13 M. P. Burke, *Forensic Medical Investigation of Motor Vehicle Incidents*, CRC Press, ISBN 0-8493-7859-1, 2007, USA.
- 14 A. C. Kim, 'A rapid method for identifying and characterizing structural impacts using distributed sensors: an application for automotive pedestrian protection', PhD dissertation, Stanford University, 2005, USA.
- 15 C. Klukowski and R.Meier, 'Adaptive linear crash systems, intelligent materials for passenger car steering columns', ThyssenKrupp techforum, 2006, No1, pp. 40-47, ISSN 1612-2771, Germany.
- 16 A. Brecher, 'A safety roadmap for future plastics and composites intensive vehicles', NHTSA, Report#: DOT HS 810 863, Sep 2007.

- 17 M. Avery, J. M. Nolan, M. Brumbelow, and D. S. Zuby, ‘Important Considerations in the Development of a Test to Promote Stable Bumper Engagement in Low Speed Crashes’, SAE paper #: 2004-01-1319.
- 18 W. J. Witteman, ‘Improved Vehicle Crashworthiness Design by Control of the Energy Absorption for Different Collision Situations’, PhD dissertation, Eindhoven University of Technology, The Netherlands, ISBN 90-386-0880-2, 1999.
- 19 D. W. Lee, ‘An innovative inflatable morphing body structure for Crashworthiness of military and commercial vehicles’, PhD dissertation, Michigan University, 2008.
- 20 http://www.who.int/violence_injury_prevention/publications/road_traffic/world_report/summary_en_rev.pdf, ‘World report on road traffic injury prevention: summary’, World Health Organization, ISBN: 92 4 156260 9, Geneva, 2004.
- 21 www.tc.gc.ca/roadsafety/tp/tp3322/2005/menu.htm, ‘Canadian Motor Vehicle Traffic Collision Statistics: 2005’, Transport Canada, report #3322, ISBN 0-662-49667-1, December 2006.
- 22 <http://www.tc.gc.ca/roadsafety/tp/tp14800/menu.htm>, Analysis and Estimation of the Social Cost of Motor Vehicle Collisions in Ontario (2007 Report).
- 23 ‘Traffic Safety Facts 2004’, A Compilation of Motor Vehicle Crash Data from the Fatality Analysis, NHTSA, Report #: DOT HS 809 919
- 24 FARS 2005, <http://www-fars.nhtsa.dot.gov/Main/reportslinks.aspx>, National Highway Traffic Safety Administration, Fatality Analysis Reporting System (FARS), USA, 2005.
- 25 H. Wallentowitz and H. Adam, ‘Predicting the crashworthiness of vehicle structures made by lightweight design materials and innovative joining methods’, Proceedings of ASME International Mechanical Engineering Congress and Exposition, 1995, Vol. 210, pp. 331-354.
- 26 J.L. Traets, ‘The effect of adaptive car structures on the crash behavior in different crash scenarios, Rapport#: MT 05.47, MSc. Thesis, Eindhoven University of

- Technology -Department of Mechanical Engineering Vehicle Safety, Eindhoven, December 2005.
- 27 R. Schram; F. J. W. Leneman; C. D. van der Zweep; J. S. H. M. Wismans; and W. J. Witteman, 'Assessment criteria for assessing energy absorbing front under-run protection on Trucks', *International Journal of Crashworthiness*, Vol. 11, Issue 6, pp: 597- 604, 2006.
 - 28 D.P. Wood and C.K. Simms, 'Car size and injury risk: a model for injury risk in frontal collisions', *Accident Analysis and Prevention*, Vol.34, Issue 1, pp:93–99, 2002.
 - 29 R. Gupta and A. D. Kelkar, 'Nonlinear crash dynamics simulation of novel airbag based next generation energy absorbing barrier', 9th International LS-DYNA Users Conference, June 2006, Michigan, USA.
 - 30 http://www.automotivetechgroup.com/FMVSS_Test_Summary.pdf,
FMVSS Test Summary and Estimated Costs, 2009, USA.
 - 31 K. Hamza and K. Saiou, 'Design Optimization of Vehicle Structures for Crashworthiness using equivalent mechanism approximations', *Journal of Mechanical Design*, ASME, May 2005, Vol.127, pp. 485-492.
 - 32 X. Liao, Q. Li, X. Yang, W. Zhang, and W. Li, 'Multiobjective optimization for crash safety design of vehicles using stepwise regression model', *Journal of Structural Multidisciplinary Optimization*, Vol. 35, No. 6, pp: 561–569, 2008.
 - 33 H. K. Ibrahim, Design optimization of vehicle structures for crashworthiness improvement, PhD dissertation, Concordia University, 2009, Canada.
 - 34 D. G. Buzemanjewkes, D. C. Viano, and P. Lovsund, 'A Multi-body Integrated Vehicle-Occupant Model for Compatibility Studies in frontal crash', *Journal of Crash Prevention and Injury Control*, Vol. 1, Issue. 2, pp. 143-154, 1999.
 - 35 H.S. Kim, S.Y. Kang, I.H. Lee, S.H. Park, and D.C. Han, 'Vehicle Frontal Crashworthiness Analysis by Simplified Structure Modeling using Nonlinear

- Spring and Beam Elements', *International Journal of Crashworthiness*, Vol. 2, Issue 1, pp: 107-117, 1996.
- 36 A. Elmarakbi, 'dynamic modeling and analysis of vehicle's smart front -end structure for frontal collision', PhD dissertation, University of Toronto, 2004.
- 37 S. Jawad, 'Smart structures for frontal collision mitigation', SAE paper #: 2002-01-0247.
- 38 K.H. Lin, J. Augustitus, and M. Kamal, 'Computer simulation of vehicle-to-barrier impact, a user's guide', General Motor research publication #: GMR-1943, 1975.
- 39 U. Seiffert and L. Wech, *Automotive safety handbook*, 2nd Edition, SAE International, ISBN: 978-1-86058-346-9, 2003.
- 40 A. Elmarakbi and J. Zu, 'Incremental harmonic balance method for analysis of standard/smart vehicle-to-rigid-barrier frontal collision', *Int. J. of Vehicle Safety*, Vol. 2, No. 3, pp: 288 – 315, 2007.
- 41 A. Elmarakbi and J. Zu, 'Mathematical modeling of a vehicle crash with emphasis on the dynamic response analysis of extendable cubic nonlinear dampers using the incremental harmonic balance method', *Proceedings of IMechE, Part D: Journal of Automobile Engineering*, Vol. 221, No.1,pp: 143-156, 2007.
- 42 A. Elmarakbi and J. Zu, 'Crash analysis and modeling of two vehicles in frontal collisions using two types of smart front-end structures: an analytical approach using IHBM', *International Journal of Crashworthiness*, Vol. 11, Issue 5 pp: 467–483, 2006.
- 43 H.G.Mooi and J.H.A.M. Huibers, 'Simple and effective lumped mass models for determining kinetics and dynamics of car-to-car crashes', *International Journal of crashworthiness*, Vol. 5, Issue 1, pp. 7–24, 2000.
- 44 M.M. Kamal, 'Analysis and simulation of vehicle to barrier impact', SAE paper # 700414.

- 45 R. A. Radwan and W. T. Hollowell, 'System identification of vehicle structure in crash loading environments, SAE paper # 900415.
- 46 M. Huang, R. Chen, and B. Margolin, 'Use of an advanced CRUSH model in estimating vehicle impact loading and energy absorption', ASME, AMD, Vol.210, pp: 273:285, crashworthiness and occupant protection in transportation systems, 1995.
- 47 F. M. Hikmat, and L. Chunhui, 'Front end design of vehicle structure subjected to frontal crash load', ASME, AMD-Vol.225, pp: 223:240, crashworthiness, occupant protection and biomechanics in transportation systems, 1997.
- 48 M. Balike, 'Enhancement of crashworthiness in car-truck collisions using damped under-ride guard and composite crush elements', PhD dissertation, Concordia University; 1998.
- 49 C.D. van der Zweep, F. Jenefeldt, and R. Thomson, 'Improvement of Vehicle Crash Compatibility through the Development of Crash Test procedures (VC-COMPAT)', Project #: GRD2-2001-50083, Chalmers University, 2006.
- 50 N. Jones, 'Several phenomena in structural impact and structural crashworthiness', European Journal of Mechanics A/Solids, Vol. 22, Issue 5, pp: 693–707, 2003.
- 51 M.A. Crisfield, *Non-linear Finite Element Analysis of Solids and Structures*, John Wiley & Sons Inc., 2000, ISBN 0 471 95649 X, USA.
- 52 S.R. Singiresu, *The finite element methods in engineering*, 4th Edition, Elsevier Science & Technology Books, 2004, ISBN: 0750678283.
- 53 R. Gupta and A. D. Kelkar, 'Nonlinear Crash Dynamics Simulation of Novel Airbag Based Next Generation Energy Absorbing Barrier', 9th International LS-DYNA Conference, June 2006, Michigan, USA.
- 54 W. Qi, X. L. Jin, and X. Y. Zhang, 'Improvement of energy-absorbing structures of a commercial vehicle for crashworthiness using finite element method',

- International Journal of Advanced Manufacturing Technology, Vol. 30, No.11-12, pp: 1001-1009, 2006.
- 55 W. J. Witteman and R.F.C. Kriens, ‘Numerical Optimization of Crash Pulses’, Proceedings PAM’99, 9th European Seminar on Advanced Finite Element Simulation Techniques, Darmstadt, Germany, 1999.
- 56 A. Gavelin, ‘Seat integrated safety belts, a parametric study using finite element simulations’, a Licentiate Thesis in Mechanical Engineering, Luleå University of Technology, Sweden, 2006.
- 57 U. K. Lee , S. B. Jang ,and S. S. Cheon , ‘Development of a Subframe Type Fuel Tank for Passenger Cars’, ASME, Journal of Mechanical Design, Vol. 132, Issue 4, pp: 44501-44508, April 2010.
- 58 M. Perneti and S. Scalera, ‘Development of validated finite element model of a passenger car suitable to simulate collisions against road safety barrier’, 4th International SIIV Congress, pp.12-14, September 2007, Palermo, Italy.
- 59 G.A. Aramayo and M.H. Koebbe, ‘Parametric Finite Element Model of a Sport Utility Vehicle – Development and Validation’, Proceedings of the 7th International Ls-Dyna Users Conference, 2002, pp. 11.43-11.52, Detroit, USA.
- 60 H Fang, K. Solanki, and M. F. Horstemeyer, ‘Numerical simulations of multiple vehicle crashes and multidisciplinary crashworthiness optimization’, International Journal of Crashworthiness, Vol. 10, Issue 2, pp. 161–171, 2004.
- 61 L. Wägström, R. Thomson; and B. Pipkorn, ‘Structural adaptivity in frontal collisions: implications on crash pulse characteristics’, International Journal of Crashworthiness, Vol. 10, Issue 4, pp. 371-378, 2005.
- 62 R.Tarazona and L.Castjon, ‘An innovative concept of energy absorption system for automotive collisions’, SAE paper #: 2004-01-1613.
- 63 M.L. McCoy and H. M. Lankarani, ‘Determination of the crush stiffness coefficients of a typical aftermarket frontal protective guard used in light trucks and

- vans with comparisons between guard stiffness and frontal vehicle crush coefficients', Proc. of IMechE, Vol. 220, No. 8, pp: 1073-1084, August 2006.
- 64 Y. Liu, H. Matsuhisa, H. Utsuno, and J.G. Park, 'Vibration control by a variable damping and stiffness system with Magnetorheological dampers', Journal of Sound and Mechanical Vibration, Vol. 49, No. 2, pp: 411-417, 2006.
- 65 F. Duddeck, 'Multidisciplinary optimization of car bodies', Journal of Structural and Multidisciplinary Optimization, Vol. 35, No. 4, pp. 375-389, April 2008.
- 66 X. Liao, Q. Li, X. Yang, W. Zhang, and W. Li, 'Multi-objective optimization for crash safety design of vehicles using stepwise regression model', Structural and Multidisciplinary Optimization, Vol. 35, No. 6, pp. 361-369, June 2008.
- 67 K. Hamza, 'Design for vehicle structural crashworthiness via crash mode matching', PhD dissertation, University of Michigan, 2008.
- 68 Q. Yu, N. Koizumi, H. Yajima, and M. Shiratori, 'Optimum design of vehicle frontal structure and occupant restraint system for crashworthiness', Japan Society of Mechanical Engineering (JSME), Special Issue on Novel Development and Applications in Finite Element Technologies, Vol.44, No.4, pp. 594:601, 2001.
- 69 H.S. Kim, S.Y. Kang, I.H. Lee; S.H. Park; and D.C. Han, 'Vehicle Frontal Crashworthiness Analysis by Simplified Structure Modeling using Nonlinear Spring and Beam Elements', International Journal of Crash, Vol. 2, No. 1, pp: 107-117, 1997.
- 70 W. S. Hwang and D. H. Lee, 'System identification of structural acoustic system using the scale correction', Journal of Mechanical Systems and Signal Processing Vol. 20, Issue 2, pp: 389-402, 2006.
- 71 M. Ahmadian and J. a. Norris, 'Experimental analysis of Magnetorheological dampers when subjected to impact and shock loading', Journal of Communications in Nonlinear Science and Numerical Simulation, Vol. 13, Issue 9, pp: 1978-1985, 2008.

- 72 M. Ahmadian, R.J. Appleton, and J.A. Norris; ‘Designing Magneto-Rheological Dampers in a Fire Out-of-Battery Recoil System’, IEEE Transactions on Magnetics, Vol. 39, No. 1, pp: 480-485, January 2003.
- 73 National Highway Traffic Safety Administration, FMVSS No. 208, http://www.access.gpo.gov/nara/cfr/waisidx_01/49cfr571_01.html.
- 74 J. K. Charles, ‘Correlation Of NCAP Performance with Fatality Risk in Actual Head-On Collisions’, NHTSA Technical Report: DOT HS 808 061, January 1994.
- 75 B. O’Neill, A. K. Lund, D. S. Zuby, and C. A. Preuss, ‘Offset Frontal Impacts- A Comparison of Real-World Crashes with Laboratory Tests’, Enhanced Safety of Vehicles (ESV) report # 94S-S4-O- 19, IIHS, 1994.
- 76 NHTSA, ‘Consumer Information; New Car Assessment Program; Notice’, Federal Register / Vol. 73, No. 134 / Friday, July 11, 2008 / Notices, Docket No. NHTSA–2006–26555.
- 77 N.L. Eindhoven, ‘EEVC WG15 Expectations from VC-Compat and Plans ‘EEVC WG15 Expectations from VC-Compat and Plans’, VC-Compat Final Workshop, October 17 - 18, 2006, Sweden.
- 78 J. T. Herridge and R. K. Mitchell, ‘Development of a computer simulation program for collinear car/car and car/barrier collisions’, ASME paper, No. 73-ICT-34, 1973
- 79 R. R. P. Rodenburg, C D van der Zweep, G Kellendonk, H G Mooi, and W J Witteman, ‘Development of a Generic Vehicle Modeling Procedure’, International Conference of Crash 4-7 July 2006, Athens Greece
- 80 M. Huang, *Vehicle Crash Mechanics*, CRC Press, ISBN: 0849301041, 2002, USA.
- 81 A.K. Zaouk, N. E. Bedewi, C. D. Kan, and D. Marzougui, ‘Validation of a nonlinear FE vehicle model using multiple impact data’, Proc. Of ASME International Mechanical Engineering Congress and Exposition, 1996, pp: 17-22.

- 82 D.W. Lee, Z. Dong, and N. Kikuchi, 'An innovative I-bumper concept for improved crashworthiness of military and commercial vehicles', SAE paper #: 2008-01-0512
- 83 J. Holnicki-Szulc, P. Pawłowski, M. Mikułowski, and C. Graczykowski, 'Adaptive impact absorption and applications to landing devices', Journal of Advances in Science and Technology, Vol. 56, pp: 609-613, 2008.
- 84 A. Elmarakbi and J. Zu 'Towards the Optimum Solution of Vehicle Compatibility: A Numerical Study Using a Fixed Smart Structure', proceedings of the FISITA World Automotive Congress, May 2004, Barcelona, Spain.
- 85 J. T. Wang, 'An extendable and retractable bumper', 19th International Technical Conference on the Enhanced Safety of Vehicles, Paper #: 05-0144, 2005
- 86 W.T. Hollowell, 'Adaptive time domain, constrained system identification of nonlinear structures', ASME, AMD, Applied Mechanics Division, Vol. 79, pp: 105-123, 1986.
- 87 R.T. Marler, C.H. Kim, and J. S. Arora, 'System identification of simplified crash models using multi-objective optimization', Computer Methods in Applied Mechanics and Engineering, Vol. 195, pp. 4383–4395, 2006.
- 88 E. Toccalino and D. Automotivei, 'Passenger Vehicle Safety Rating (Euro & US-NCAP, IIHS): Performance Overview and Energy Management Solutions', SAE paper #: 2003-01-0230.
- 89 http://www.radio.rai.it/cpu/archivio_2005/eventi/ERF.pdf, The European Union Road Federation (ERF), 'The dynamics of vehicle – guardrail collisions and their impact on occupant safety', ERF information brief, October 2005.
- 90 D. Woo, S.B. Choi, Y.T. Choi, and N.M. Wereley, 'Frontal Crash Mitigation using MR Impact Damper for Controllable Bumper', J. of Intelligent Material Systems and Structures, Vol. 18, Issue 12, pp:1211-1215, 2007.

- 91 http://www.iihs.org/ratings/protocols/pdf/measures_frontal.pdf, IISH, Frontal Offset Crashworthiness Evaluation Guidelines for Rating Injury Measures, June 2009.
- 92 W. J. Witteman, 'Adaptive frontal structure design to achieve optimal deceleration pulses', 19th International Technical Conference on the Enhanced Safety of Vehicles, June 2005, Washington, D.C., USA.
- 93 R. C. Herdman, *Advanced Automotive Technology, Visions of a Super-Efficient Family Car*, Business/Technology Books, ISBN-10: 0899343228, 1995, USA.
- 94 J. Banhart, 'Aluminum foams for lighter vehicles', *International Journal of Vehicle Design*, Vol. 37, No. 2/3, pp: 114-125, 2005.
- 95 D.H. Guston and D. Sarewitz, 'Real-Time Technology Assessment', *Technology in Society*, Vol. 24, Issue 1/2, pp: 93-109, 2002.
- 96 R. Brantman, 'Achievable Optimum Crash Pulses for Compartment Sensing and Airbag Performance', 13th International Technical Conference on Experimental Safety Vehicles (ESV), Paper S9-O-22, pp. 1134-1138, November 1991, Paris, France.
- 97 J. Kral, 'Yet another look at crash pulse analysis', SAE paper #: 2006-01-0958
- 98 Z. Cheng and J.A. Pelletiere, 'Optimal Crash Pulse for Minimization of Peak Occupant Deceleration in Frontal Impact', SAE paper #: 2006-01-0670
- 99 Z. Cheng, J.A. Pelletiere, and A. Joseph, 'Optimal Restraint Characteristics for Minimization of Peak Occupant Deceleration in Frontal Impact', SAE paper #: 2006-01-0913
- 100 Y. Motozawa and T. Kamei, 'A new concept of occupant deceleration control in a crash', SAE paper #: 2001-01-0881.
- 101 Y. Motozawa, M.Tsurruta, Y. Kawamura, and J. Noguchi, 'A new concept of occupant deceleration control in a crash, part-2, SAE paper #: 2003-01-1228.

- 102 J.Wu, G.S. Nusholtz, and S. Bilkhu, 'Optimization of vehicle crash pulses in relative displacement domain', International Journal of Crashworthiness, Vol. 7, No. 4, pp.397-411, 2002.
- 103 W. Beek, 'Alternative lower rail design to lower injury level of occupant caused by frontal crash', Internal traineeship under Supervision of Dr. W.J. Witteman, Eindhoven University of Technology -Department of Mechanical Engineering Vehicle Safety, May 2006.
- 104 W. J. Witteman and R.F.C. Kriens, 'The Necessity of an Adaptive Vehicle Structure to Optimize Deceleration Pulses for Different Crash Velocities', SAE paper #: 2001-06-0171.
- 105 N Sharpe, R Vendrig, and K Houtzager, 'Improved design for frontal protection', SAE paper #: 2001-06-0137.
- 106 M. Walters, 'Literature survey on advanced materials in crash safety applications', Rapport #: MT04.07, Internal traineeship under Supervision of Dr. W.J. Witteman, Eindhoven University of Technology, February 2004.
- 107 D. Gabauer and H. C. Gabler, 'Evaluation of Threshold Values of Acceleration Severity index by using event data recorder technology', Journal of the Transportation Research Board, Vol. 1904, pp: 37-45, 2005.
- 108 P. Gridkevičius and A. Žiliukas, 'The crash energy absorption of the vehicles front structure', Journal of the Transportation, Vol. XVIII, No. 2, pp. 97:101, 2003.
- 109 H. Wallentowitz and H. Adam, 'Predicting the crashworthiness of vehicle structure made by lightweight design materials and innovative joining methods', Crashworthiness and occupant protection in transportation systems, ASME, AMD, Vol. 210, pp: 331-354, 1995.
- 110 D. F. Shanahan, 'Human Tolerance and Crash Survivability', proceedings of Pathological Aspects and Associated Biodynamics in Aircraft Accident Investigation paper-6 "RTO-EN-HFM-113", November 2004, Germany.

- 111 Y.B. Cho, C.H. Bae, M.W. Suh, and H. C. Sin ‘Maximisation of crash energy absorption by crash trigger for vehicle front frame using the homogenization method’, *International Journal of Vehicle Design*, Vol. 46, No. 1, pp. 23-50, 2008.
- 112 L. Wägström, R. Thomson, and B. Pipkorn, ‘Structural adaptivity for deceleration level reduction in passenger car frontal collisions’, *International Journal of Crashworthiness*, Vol. 9 No. 2, pp. 121–127, 2004.
- 113 H. S. Kim, W. Chen, and T. Wierzbicki, ‘Weight and crash optimization of foam-filled three-dimensional ‘S’ frame’, *Computational Mechanics* Vol. 28, No. 5, pp: 417-424, 2002.
- 114 A.L. Browne, J.D. Mcclary, C.S. Namuduri, and S.R. Webb, ‘Impact performance of Magnetorheological fluids’, *Journal of Intelligent Material Systems and Structures*, Vol. 20, pp. 723-728, April 2009.
- 115 J. B. Heyerman, ‘On the Crashworthiness of Foam-Filled Ultralight Automotive Structures’, MSc. thesis, University of Toronto, 2000.
- 116 S.M. Sohn, B.J. Kimb, K.S. Parkb and Y.H. Moon, ‘Evaluation of the crash energy absorption of hydroformed bumper stays’, *Journal of Materials Processing Technology*, Vol. 187–188, pp.283–286, 2007.
- 117 D. Lehmus, ‘Metallic Foams as Energy Absorbing Materials – Status and Prospects’, *Advanced Passive Safety Network - APSN 27*, Report: D121 – Workshop on Energy Absorbing Structures and Materials in Railway and Aerospace, pp. 27-30, 2006.
- 118 M.J.A.M. Walters, ‘Designing and analyzing Kagome structures for crash safety applications’, MSc thesis, Eindhoven University of Technology-Department of Mechanical Engineering, Automotive Engineering, 2005.
- 119 M. Ostrowski, J. H.Szulc, and P. Griskevicius, ‘Adaptive Crashworthiness of Front-End Structure of Motor Vehicles’, SAE paper # 2007-01-1180.

- 120 M. Ostrowski, P. Griškevičius, and J. Holnicki-Szulc, 'Feasibility study of an adaptive energy absorbing system for passenger vehicles', CMM-2005 – Computer Methods in Mechanics conference June 2005, Częstochowa, Poland
- 121 W.J. Witteman and R.F.C. Kriens, 'Modeling of an innovative frontal car structure: similar deceleration curves at full overlap, 40 per cent offset and 30 degrees collisions, Eindhoven University of Technology-Laboratory for Automotive Engineering, Eindhoven, The Netherlands, Paper Number 98-S 1-0-04, pp. 194:212.
- 122 B. Pipkorn; Y. Håland, 'Proposed variable stiffness of vehicle longitudinal frontal members', Int. J. of Crashworthiness, Vol. 10, No. 6, pp: 603–608, 2005.
- 123 S. S Deshmukh and G. H. McKinley, 'Adaptive energy-absorbing materials using field-responsive fluid-impregnated cellular solids', Smart Material and Structure Vol. 16, pp: 106-113, 2007.
- 124 G. Bettin, 'High-rate deformation behavior and applications of fluid filled reticulated foams', PhD dissertation, Massachusetts Institute of technology, 2007.
- 125 A. A. Berlin, 'Active Control of Buckling using Piezo-Ceramic Actuators', Proceedings of SPIE -The International Society for Optical Engineering Smart Structures and Materials, Vol. 2447, pp: 141-154, 1995.
- 126 J.Holnicki-Szulc, *Smart technologies for safety engineering*, John Wiley & Son Ltd, ISBN: 9780470058466, 2008, USA.
- 127 J. Holnicki-Szulc, P. Pawłowski, M. Mikułowski, and C. Graczykowski, 'Adaptive impact absorption and applications to landing devices', Advances in Science and Technology, Vol. 56, pp: 609-613, 2008.
- 128 J.Holnicki-Szulc, C. Graczykowski, G. Mikułowski, A. Mróz, and P. Pawłowski 'Smart Technologies for Adaptive Impact Absorption', Journal of Solid State Phenomena, pp: 187-194, April, 2009.

- 129 T. Bielecki, J. H. Szulc, L. Jezequel, 'Adaptive Car Buffer-The Concept, Design Tools and Perspectives', 2001 IEE/ASME International Conference on Advanced Intelligent Mechatronics Proceedings, July 2001, Como, Italy.
- 130 T. Bielecki, J. H. Szulc, and L. Jezequel, 'Adaptive Impact Absorbers, the Concept, Design Tools and Applications', proceedings of 3rd World Conference on Structural Control, April 2002, Como, Italy.
- 131 P. G. Kit, 'Hydraulic Bumpers for the Protection of Buildings, Cranes and Operators From Impact Damage', Iron and Steel Engineer, Vol. 74, Issue 9, pp: 47-54, Sep 1997.
- 132 R. Delivorias, 'The Potential of Magneto-Rheological Fluid in Crashworthiness Design', MSc. Thesis, Department of Mechanical Engineering Automotive Engineering, Eindhoven University of Technology, 2005.
- 133 Y.T. Choi and N. M. Wereley, 'Vibration control of a landing gear system featuring Electrheological/Magnetorheological fluids', Journal of aircraft Vol. 40, No. 3, May-June 2003.
- 134 D. C. Batterbee, N D Sims, R Stanway, and Z. Wolejsza, 'Magnetorheological Landing Gear-1, A Design Methodology', J. of Smart Material and Structure, Vol. 16, No. 6, pp: 2429-2440, 2007.
- 135 D. C. Batterbee, D. C. Batterbee, N. D. Sims, R. Stanway, and M. Rennison, 'Magnetorheological Landing Gear-2, Validation Using Experimental Data', Journal of Smart Material and Structure, Vol. 16, No. 6, pp: 2441-2452, 2007.
- 136 E. L. Kathe, 'Recoil Considerations for Railguns', IEEE Transactions on Magnetics, Vol. 37, Issue 1, pp: 425-430, January 2001.
- 137 J. A. Norris, 'Behavior of Magneto-Rheological Fluids Subject to Impact and Shock loading', MSc. Thesis, Virginia University, 2003.

- 138 D. H. Kim, J. W. Park, G. S. Lee , and K. I. Lee, ‘Active Impact Control System Design With A Hydraulic Damper’, *Journal of Sound and Vibration*, Vol. 250, No. 3, pp. 485-501, 2002.
- 139 C.C. Clark and W.A. Young, ‘Car Crash Theory and Tests of Airbag Bumper Systems’, SAE Paper # 951056.
- 140 B. Pipkorn, R. Fredriksson, and J. Olsson, ‘Bumper Bag for SUV to Passenger Vehicle Compatibility and Pedestrian Protection’, Paper # 0056-O, Proceedings of 20th International Technical Conference on the enhanced safety of Vehicles (ESV), NHTSA, 2007, Lyon, France.
- 141 H. De Haven, ‘Accident Survival-Airplane and Passenger Automobile’, in ‘Accident research; methods and approaches’ by W. Haddon, E.A. Suchman, and D. Klein, (New York, Harper and Row), 1964, pp: 562-568.
- 142 R. Grzebieta, ‘Tram and Rail Crashworthiness Principles’, Advanced Passive Safety Network-APSN, Report #: D121, Workshop on Energy Absorbing Structures and Materials in Railway and Aerospace, July 2006, Netherlands.
- 143 <http://www.defense-update.com/products/r/reaps.htm>, Rotorcraft External Airbag Protection System (REAPS)
- 144 C.H. Kim, A.R. Mijar, and J.S. Arora, ‘Development of simplified models for design and optimization of automotive structures for crashworthiness’, *Structural and Multidisciplinary Optimization*, Vol. 22, No. 4, pp: 307–321, 2001.
- 145 C.H. Kim, ‘Development of simplified models for automotive crashworthiness simulation and design using optimization’, PhD dissertation, University of Iowa, 2002
- 146 X. Liaoa; Q. Li, X. Yang, W. Lib, and W. Zhang ‘A Two-Stage Multi-Objective Optimization of Vehicle Crashworthiness under Frontal Impact’, *International Journal of Crashworthiness*, Vol. 13, Issue 3, pp: 279–288, June 2008.

- 147 <http://www.csrl.org/reports/Innovation.pdf>, R. Cirincione, ‘Innovation and Stagnation in Automotive Safety and Fuel Efficiency’, Center for the Study of Responsive Law, ISBN: 0-936758-41-4, 2006, USA.
- 148 Y. Liu, H. Matsuhisa, and H. Utsuno, ‘Semi-Active Vibration Isolation System with Variable Stiffness and Damping Control’, *Journal of Sound and Vibration*, Vol. 313, Issue 1-2, pp: 16–28, 2008.
- 149 Y. Liu, H. Matsuhisa, H. Utsuno, and J.G. Park, ‘Variable damping and stiffness vibration control with Magnetorheological fluid dampers for 2 DOF system’, *Journal of Sound and Mechanical Vibration*, Vol. 49, No. 1, pp:156–162, 2006.
- 150 H. Porumamilla, A.G.Kelkar, and J.M. Vogel, ‘Modeling and Verification of an Innovative Active Pneumatic Vibration Isolation System’, *Journal of Dynamic Systems, Measurement, and Control*, Vol. 130, Issue 3, pp: 03001-031012, May 2008.
- 151 R. D. Nayeri, S. F. Masri, and J. P. Caffrey, ‘Studies of The Performance of Multi-Unit Impact Dampers under Stochastic Excitation’, *Journal of Vibration and Acoustics*, ASME, Vol. 129, Issue 2, pp: 239-251, 2007.
- 152 I. Iskhakov and Y. Ribakov, ‘Semi-Active Friction-Damped Reinforced Concrete Structures with Self-Variable Stiffness’, the structural design of tall and special building, Vol.17, Issue 2, pp: 351-365, 2008.
- 153 M. Kleinberger, E. Sun, R. Eppinger, S. Kuppa, R. Saul, ‘Development of Improved Injury Criteria for the Assessment of Advanced Automotive Restraint Systems’, NHTSA, September 1998.
- 154 R. Eppinger, E. Sun, F. Bandak, M. Haffner, N. Khaewpong, M. Maltese, S. Kuppa, T. Nguyen, E. Takhounts, R. Tannous, and A. Zhang, R. Saul, ‘Development of Improved Injury Criteria for the Assessment of Advanced Automotive Restraint Systems-II’, NHTSA, November 1999.

- 155 G. Toganel and A. Soica, 'Aspects Regarding the Impact Speed, AIS and HIC Relationship for Car-Pedestrian Traffic Accidents', Published in ANNALS of the Oradea University, Fascicle of Management and Technological Engineering, Vol. VI (XVI), 2007.
- 156 D. B. Jewkes , 'Vehicle Acceleration and Compartment intrusion for Far-Sided Occupants v. Near-Sided Occupants in Frontal Offset Collisions', SAE paper #: 2003-01-0159.
- 157 J. C. Dixon, *The Shock Absorber Handbook*, 2nd Edition, John Wiley & Sons Inc., ISBN: 978-0-470-51020-9, 2007, U.K.
- 158 J. Holnicki-Szulc and P. Pawłowski, 'The concept of multifoldig and its Experimental Validation', 21st International Congress of Theoretical and Applied Mechanics (ICTAM), August 2004, Warsaw, Poland
- 159 S. R. Singiresu, *Engineering Optimization-Theory and Practice*, Fourth Edition, John Wiley & Sons Inc., 2009, ISBN 978-0-470-18352-6, USA.
- 160 K. C. Tan, T. H. Lee and E. F. Khor, 'Evolutionary Algorithms for Multi-Objective Optimization: Performance Assessments and Comparisons', proceedings of the 2001 IEEE Congress on Evolutionary Computation, May 2001, Soul, Korea.
- 161 Y. Zhang, P. Zhu, and G. Chen, 'Lightweight Design of Automotive Front Side Rail Based on Robust Optimization', *Journal of Thin-Walled Structures*, Vol. 45, Issue 7-8, pp: 670–676, 2007.
- 162 H. Agarwal and J. E. Renaud, 'Reliability Based Design Optimization For Multidisciplinary Systems Using Response Surfaces', *Journal of Engineering Optimization*, Vol. 36, No. 3, pp. 291–311, June 2004.
- 163 A. Abraham and L. C. Jain, R. Goldberg, *Evolutionary Multiobjective Optimization, Theoretical Advances and Applications*, Springer, ISBN 1852337877, 2005, USA.

- 164 G. V. Reklaitis, A. Ravindran, and K. M. Ragsdell, *Engineering Optimization, Methods and Applications*, 2nd Edition, John Wiley & Sons Inc., ISBN: 978-0-471-55814-9, 2006, USA.
- 165 R.N. Cadete, J.P.Dias, and M.S. Pereira, ‘Optimization in vehicle crashworthiness design using surrogate models’, 6th World Congresses of Structural and Multidisciplinary Optimization, Rio de Janeiro, May/June 2005, Brazil
- 166 Matlab online help, Optimization Toolbox Documentation-R2009a, <http://www.mathworks.com/help/toolbox/optim/?BB=1>.
- 167 M. Affenzeller, S. Winkler, S. Wagner, and A. Beham, , *Genetic Algorithms and Genetic Programming, Modern Concepts and Practical Applications*, CRC press-Taylor & Francis Group, 2009, ISBN 978-1-58488-629-7, USA.
- 168 R. L. Haupt and S. E. Haupt, *Practical Genetic Algorithms, Second Edition* John Wiley & Sons Inc., ISBN: 0-471-45565-2, 2004, USA.
- 169 N. S. Ermolaeva, K. G. Kaveline, and J. L. Spoomaker, ‘Materials Selection Combined with Optimal Structural Design: Concept and Some Results’, *Materials and Design* Vol. 23, Issue 8, pp: 459–470, 2002.
- 170 J. R. Figueira, S. Greco, and M. Ehrgott, *Multiple Criteria Decision Analysis: State of the Art Surveys (International Series in Operations Research & Management Science)*, Springer Science Inc., ISBN: 038723067-x, 2005, USA.
- 171 C. A. Mattson and A. Messac, ‘Pareto Frontier Based Concept Selection under Uncertainty, with Visualization’, *Journal of Optimization and Engineering*, Vol. 6, No. 1, pp: 85-115, March 2005.
- 172 N. Jones, *Structural impact*, Cambridge University Press, ISBN 0521628903, 1997, U.K.
- 173 G.J. Simitises, J.H. Starnes, and J. Rezaeepazhand, ‘Structural similitude and scaling laws for plates and shells: a review’, *Advances in the Mechanics of Plates and Shells*, Vol. 88, pp: 295–310, 2002.

- 174 T.A. Duffey, M.C. Cheres, and S.H. Sutherland, 'Experimental verification of Scaling Laws for Punch-Impact-Loaded Structures', *International Journal of Impact Engineering*. Vol. 2, Issue 1, pp: 103-117, 1984.
- 175 H.J. Mertz, 'A Procedure for Normalizing Impact Response Data', SAE paper #: 840884
- 176 R. E. Oshiro, M. Alves, 'Scaling Impacted Structures', *J. of Applied Mechanics*, Vol. 74, No. 1-2, pp: 130-145, 2004.
- 177 M. M. Kamal and J. A. Wolf, *Modern Automotive Structural Analysis*, Van Nostrand Reinhold Company, ISBN: 0-44224-839-3, 1982, USA.
- 178 K. H. Ni and K.H. Lin, 'A Mixed Method of Analysis for Vehicle Structure', *Proceedings of the AIAA/ASME 18th structures, structural dynamics and materials conference*, Paper #.77-370, San Diego, March 1977, USA.
- 179 D. Kecman, 'An Engineering Approach to Crashworthiness of Thin-Walled Beams and Joints in Vehicle Structures', *Journal of Thin-Walled Structures* Vol. 28, Nos. 3/4, pp: 309-320, 1997.
- 180 M.J. Dolan and J.F. Oilar, 'How Seat Design Characteristics Affect Impact Injury Criteria', SAE paper #: 860638
- 181 S.K.Kim, S.W. White, A.K. Bajaj, and P.Davies, 'Simplified Models of the Vibration of Mannequins in Car Seats', *Journal of sound and vibration*, Vol. 26, Issue 1, pp: 49-99, 2003.
- 182 R.K.Ippili, P.Davies, A.K. Bajaj, and L.Hagenmeyer, 'Nonlinear Multi-Body Dynamic Modeling of Seat-Occupant System with Polyurethane Seat and H-Point Predication', *International Journal of Industrial Ergonomics*, Vol.33, No. 5-6, pp: 368-383, 2008.
- 183 G.E. Bertocci, S.Szobota, D. Ha, and L. Roosmalen, 'Development of Frontal Impact Crashwothy Wheelchair Seating Design Criteria using Computer

- Simulation’, Journal of Rehabilitation Research and Development Vol. 37, No. 5, pp: 565-572, 2000.
- 184 R. D. Cook, D. S. Malkus, M. E. Plesha, and R. J. Witt, *Concepts and Applications of Finite Element Analysis*, 4th Edition, John Wiley & Sons Inc., ISBN: 0 471 25605 0, 2002.
- 185 Vehicle Database: Catalog Sorted by NHTSA Test Number, test #: 2239, http://www-nrd.nhtsa.dot.gov/database/asp/vehdb/veh_catalog_by_tstno.aspx
- 186 <http://imechanica.org/node/5396>, iMechanica web of mechanics and mechanician.
- 187 C. A. Felippa, ‘Nonlinear finite element methods’, lecture notes for the course Nonlinear Finite Elements Methods, offered since 1987 to Colorado University, USA, <http://www.colorado.edu/engineering/CAS/courses.d/NFEM.d/Home.html>
- 188 T. Belytschko, W. K. Liu, and B. Moran, *Nonlinear Finite Elements for Continua and Structures*, John Wiley & Sons Inc., ISBN: 978-0-471-98774-1, 2000.
- 189 J. O. Hallquist, *LS-DYNA Theory Manual*, Livermore Software Technology Corporation, 2006.
- 190 <http://www.ncac.gwu.edu/vml/models.html>, NCAC website, Finite element models archive
- 191 W. Wu and R. Thomson, ‘Effects of front wheels and steering-suspension systems during vehicle oblique collisions with a flared guardrail terminal’, International Journal of Crash, Vol. 10, No. 5, pp: 495–503, 2005.
- 192 Website of NHTSA Vehicle Database, Test : V02239, Geo-Metro: <http://www-nrd.nhtsa.dot.gov/database/asp/vehdb/testseries.aspx?level=5&test=2239>
- 193 J.H.Smith, *An Introduction to Modern Vehicle Design*, Butterworth-Heinemann, ISBN 07506 5044 3, 2002, U.K.
- 194 J. Reimpell, H. Stoll, and J. W. Betzler, *The Automotive Chassis; Engineering Principles*, 2nd Edition, Butterworth-Heinemann, ISBN 0 7506 5054 0, 2001, U.K.

- 195 S. Heimbs, F. Strobl, P. Middendorf, S. Gardner, B. Eddington, and J. Key, 'Crash Simulation of an F1 Racing Car Front Impact Structure', 7th European LS-DYNA Conference, May 2009, Salzburg, Austria.
- 196 V. Nagabhushana, National Crash Analysis Center (NCAC), power point presentation file for Geo-Metro FE simulation report transferred through personal email, June, 14 2010.
- 197 L.E. Schwer, 'A Primer on the DYNA/NIKE Linear Viscoelastic Material Model', available on LS-DYNA website: <http://schwer.net/SECS/Materials.htm>
- 198 LS-DYNA support website, Contact modeling in LS-DYNA, <http://www.dynasupport.com/tutorial/ls-dyna-users-guide/contact-modeling-in-ls-dyna/?searchterm=patches>
- 199 R. J. Yang, N. Wang, C. H. Tho, J. P. Bobineau, and B. P. Wang, 'Metamodeling Development for Vehicle Frontal Impact Simulation', Journal of Mechanical Design, Vol. 127, No. 5, pp: 1014 -1020, 2005.
- 200 F. Qingguo and Z. Lingmi, 'Application of experimental design techniques to structural simulation meta-model building using neural network', Journal of Earthquake Engineering and Engineering Vibration, Vol.3, No.2, pp: 293-298, December 2004.
- 201 N.Stander, D.A. Dooge, S. Varadappa, 'Automotive crashworthiness design using response surface-based variable screening and optimization', J. of Engineering Computations, Vol. 22, No. 1, pp. 38-61, 2005.
- 202 M. Redhe, J. Forsberge, T. Janssone, P. O. Marklund, and L. Nilsson, 'Using the response surface methodology and the D-optimality criterion in crashworthiness related problems', J. of Structural and Multidisciplinary Optimization, Vol. 24, No. 3, pp. 185-194, 2002.

- 203 G.G.Wang and S.Shan, 'Review of Metamodeling Techniques in Support of Engineering Design Optimization', *Journal of Mechanical Design*, Vol. 129, No. 4, pp. 370-80, April 2007.
- 204 J. Marczyk, R. Ho_mann, and P. Krishnaswamy, 'Uncertainty Management in Automotive Crash, from Analysis to Simulation', proceedings of ASME Conference, September 2000, Baltimore, USA.
- 205 H. Kurtaran, A. Eskandarian, D. Marzougui, and N. E. Bedewi, 'Crashworthiness design optimization using successive response surface approximations', *Journal of Computational Mechanics*, Vol. 29, Issue 4/5, pp: 409–421, 2002.
- 206 X. Qu and R.T. Haftka, 'A Reliability-Based Structural Optimization using Response Surface Approximations and Probabilistic Sufficiency Factor', PhD dissertation, Florida University, 2004.